Plasma Physics Reports, Vol. 26, No. 9, 2000, pp. 721–736. Translated from Fizika Plazmy, Vol. 26, No. 9, 2000, pp. 771–787.

TOKAMAKS

Electrostatic Plasma Turbulence and Spitzer Longitudinal Conductivity in Tokamaks

S. N. Gordienko* and É. I. Yurchenko**

**Landau Institute for Theoretical Physics, Russian Academy of Sciences, Chernogolovka, Moscow oblast, 142432 Russia*

***Russian Research Centre Kurchatov Institute, pl. Kurchatova 1, Moscow, 123182 Russia*

Received December 23, 1999

Abstract—An analysis has revealed that there may be three radically different steady states of a tokamak plasma: (i) discharges in which the electron and ion transport can be described by neoclassical theory; (ii) discharges with the Spitzer longitudinal conductivity, neoclassical ion transport, and "anomalous" electron transport; and (iii) discharges in which the electron transport and ion transport are both "anomalous." The dimensionless parameters responsible for the occurrence of the three types of discharges are determined. In accordance with the criteria derived for the achievement of different steady states, discharges of the second type are most typical of modern tokamaks and discharges of the third type can occur only if the turbulence is sufficiently strong. Discharges of the first type cannot occur in the range of the working parameters of present-day tokamaks and future tokamak reactors, but they can be ignited in a large class of magnetic confinement systems. The physical reason for the onset of different types of discharges is associated with the fact that turbulent fluctuations play very different roles in the dynamics of the ion and electron components of a finite-size magnetized plasma. The question of the self-consistency between the profiles is considered. A law is derived according to which the thermal diffusivity increases toward the plasma edge. © *2000 MAIK "Nauka/Interperiodica".*

1. INTRODUCTION

It is well known that, in some tokamak experiments, the plasma electron heat conductivity was anomalously high and could exceed the neoclassical value by several orders of magnitude [1]. However, in the same experiments, the longitudinal plasma conductivity was often very close to the Spitzer conductivity and the ion conductivity was more or less neoclassical [1]. In other experiments in modern-day large tokamaks, the ion thermal conductivity was also observed to be anomalous [2]. It is even more surprising that, in many experiments, the thermal diffusivity was found to depend on the radial profiles of the temperature and current density [1]. In order to explain the nonlocal nature of heat transport, it is necessary to self-consistently follow the mutual relations between the local values of transport coefficients and the global changes in the heat transport profile due to the onset of instabilities. Tokamak experiments also revealed operating modes with different radial profiles of the plasma parameters, i.e., different confinement modes. In some confinement modes, the temperature profile has a steeper drop at the plasma edge than the density profile, and, in other confinement modes, vice versa.

In order to explain these phenomena, which play key roles in tokamak physics, various approaches have been proposed in the literature. For example, Kadomtsev [1] attempted to theoretically describe the principle of profile consistency by applying a variational approach in order to minimize the plasma energy functional and by using phenomenological considerations in order to find the relation between the anomalous thermal conductivity and deviations from the optimum (canonical) profile. Coppi [3] tried to attribute the principle of profile consistency to the temperature dependence of the thermal diffusivity χ, $\chi \sim 1/T$. In our papers [4, 5], this principle was explained by the methods of the theory of strong turbulence.

However, we emphasize that the microscopic mechanisms responsible for the occurrence of different modes of confinement have not been revealed in the cited papers. Of course, the formation of different temperature and density profiles can be affected by such factors as atomic processes, edge phenomena, and the way in which the impurities are generated. In our study, we show that, even if these factors are completely disregarded (which corresponds to a fully ionized plasma), the model of turbulent heat transport [4, 5] can be used to reveal the parameter describing the relative steepness of the decreasing temperature and density profiles in the edge plasma and to determine the transport parameters of the discharge. We show that, because of the finite dimensions and toroidal geometry of a tokamak, the turbulent properties can differ strongly between the plasma ions and electrons and that it is the extent to which the turbulent properties are different that governs which type of turbulence occurs in a discharge plasma.

1063-780X/00/2609-0721$20.00

2. KINETIC EQUATIONS FOR DIFFERENT CONFINEMENT MODES

An accurate description of turbulent plasmas requires that turbulent fluctuations be included in the kinetic equation. Unfortunately, Boltzmann-like kinetic equations (such as the Vlasov equation with the Lenard–Balescu or Landau collision integral) are incapable of incorporating turbulent fluctuations correctly [6, 7]. These kinetic equations, which can be derived in a standard way from the hierarchy of the Born–Green–Kirkwood–Bogolyubov–Yvon (BGKBY) equations, are sufficient (because of the smallness of the parameter $1/N_D$) for describing a hypothetical fluctuation-free media consisting of the particles undergoing Coulomb interactions [5]. To avoid misunderstanding, we emphasize that fluctuations of the mean (large-scale) electric field in a plasma can also be introduced correctly into the Vlasov equation; however, such an approach is inapplicable to fluctuations of the real (rather than mean) electric field and surely cannot be used to study strongly unstable nonequilibrium plasmas. One of us [8] proposed the method for deriving kinetic equations that systematically takes into account turbulent fluctuations in an unbounded plasma in the absence of a magnetic field. In our paper [11], these equations were generalized to the case of infinitely long confinement systems with a straight magnetic field. The generalized equations incorporate the total electric field, in contrast to the Vlasov equation, which assumes a "smoothed" electric field. In fact, in the kinetic equations proposed in [11], the total electric field serves as a variable in the distribution functions, so that there is no need to represent the real electric field as a superposition of the smoothed and fluctuating components, as is done in the standard theories. In other words, the new kinetic approach makes it possible not only to solve Poisson's equation but also to calculate the electron and ion densities by means of the distribution functions evaluated from the kinetic equations that exactly account for the real electric field. In comparison with the Vlasov and Fokker–Planck equations, which contain only a smoothed electric field and thereby cannot be used to describe certain nonequilibrium plasma states correctly, the new approach significantly extends the applicability range of kinetic treatments in plasma theory.

Clearly, taking into account the finite dimensions of a tokamak plasma can substantially change the structure of the kinetic equations that account for fluctuation electric fields in a tokamak. Now, we qualitatively describe such kinetic equations under different plasma conditions and discuss a new concept of the confinement modes.

According to [8, 11], the properties of the operators

$$\hat{L} = \mathbf{V}\frac{\partial}{\partial \mathbf{R}} + \left(\mathbf{A} + \frac{Ze}{M}[\mathbf{V}, \mathbf{H}(\mathbf{R})]\right)\frac{\partial}{\partial \mathbf{V}}, \quad (1)$$

$$\hat{l} = \mathbf{v}\frac{\partial}{\partial \mathbf{r}} + \left(\mathbf{a} - \frac{e}{m}[\mathbf{v}, \mathbf{H}(\mathbf{r})]\right)\frac{\partial}{\partial \mathbf{v}} \quad (2)$$

are of fundamental importance in deriving the kinetic equations with allowance for fluctuations.

Note that the following formal interpretation of these operators makes them far simpler to analyze. Operator (1) can be regarded as a Liouville operator for a system consisting of a single particle with mass M and charge eZ that propagates in a magnetic field $\mathbf{H}(\mathbf{R})$ and experiences a constant uniform force $M\mathbf{A}$; i.e., the particle moves in the potential $\phi = -M(\mathbf{A}, \mathbf{R})$. Operator (2) can be interpreted in a similar manner. However, it should be kept in mind that the particles described by the Liouville operators (1) and (2) have nothing in common with real plasma electrons and ions.

Let us dwell on this point in more detail. The dynamics of a multiparticle system can be described by different formal approaches, the most simple being a hydrodynamic description in which the treatments carried out with the Eulerian and Lagrangian variables lead to the same results. A variety of treatments is also typical of the kinetic description: the particle dynamics can be studied in a real three-dimensional coordinate space, in a six-dimensional phase space of a particle, and even in an extended nine-dimensional (three coordinates of the position vector, three velocity components, and three acceleration components) phase space of a particle. All of these treatments are certainly equivalent in solving the basic equations of motion exactly, but each offers its own significant advantages in a model description of the dynamic system.

Using operators (1) and (2) as one-particle Liouville operators, we follow the dynamics of different real particles with given accelerations rather than the dynamics of a given physical particle. In other words, we number the particles in a Hamiltonian system and, at each instant, we renumber them so as to assign the same numbers to different (at different instants) particles with fixed accelerations (we can say that the particles are numbered by their accelerations) and follow the dynamics of the particles with a fixed number (or acceleration). Below, for brevity, we will call such fictitious particles "electrons" and "ions," because we can do so without causing confusion. The kinetic equations derived in [8, 11] are based on the equalities

$$\lim_{\tau \to +\infty} e^{-\tau \hat{L}} F_1(\mathbf{R}, \mathbf{V}, \mathbf{A}) = 0,$$
$$\lim_{\tau \to +\infty} e^{-\tau \hat{l}} f_1(\mathbf{r}, \mathbf{v}, \mathbf{a}) = 0 \quad (3)$$

at $(\mathbf{H}, \mathbf{A}) \neq 0$ and $(\mathbf{H}, \mathbf{a}) \neq 0$, respectively. In (3), f_1 and F_1 are the generalized one-particle electron and ion distribution functions. Actually, the kinetic equations [8, 11] can be obtained under conditions that are less stringent in comparison with (3): it is sufficient to require

the existence of the time scales τ_i and τ_e such that

$$e^{-\tau_i \hat{L}} F_1(\mathbf{R}, \mathbf{V}, \mathbf{A}) \ll F_1(\mathbf{R}, \mathbf{V}, \mathbf{A}) \text{ and } e^{-\tau_e \hat{l}} f_1(\mathbf{r}, \mathbf{v}, \mathbf{a}) \ll f_1(\mathbf{r}, \mathbf{v}, \mathbf{a}), \quad (4)$$

respectively.

In the case of infinitely long confinement systems with a straight magnetic field, conditions (3) and (4) hold automatically, thereby imposing no restrictions. The situation with tokamaks is radically different: the potential forces $m\mathbf{a}$ and $M\mathbf{A}$, which are described by the operators $\hat{l}$ and $\hat{L}$, act to periodically increase and decrease the velocities of the particles because of particle circulation along the torus. Hence, conditions (3) definitely fail to hold and we may only hope to satisfy conditions (4) for certain values of the plasma parameters.

Let us determine the parameter range in which the tokamak plasma can be described by the kinetic equations with fluctuations [8, 11]. In situations in which the kinetic equations derived in [8, 11] are applicable, the energy density of the fluctuation electric fields in strongly nonequilibrium plasma states (such that $\Delta S/N \gg 1$, where ΔS is the amount by which the plasma entropy differs from its equilibrium value and N is the total number of plasma particles) in large aspect ratio tokamaks can be written as (see Appendix 1)

$$\frac{W}{nT_e} = C_2 D^2 \left(\frac{r_D}{\rho_e}\right)^2, \quad (5)$$

where r_D is the Debye radius, ρ_e is the Larmor radius, D is the nonquasineutrality parameter, and N_D is the number of particles inside the Debye sphere.

For conditions (4) to hold, it is necessary to satisfy the inequalities

$$\sqrt{\frac{T_i}{M}} \ll \sqrt{RA_{ch}}, \quad \sqrt{\frac{T_e}{m}} \ll \sqrt{Ra_{ch}}. \quad (6)$$

With the characteristic electron and ion accelerations a_{ch} and A_{ch} estimated from (5) and for $T_e \sim T_i$, inequalities (6) can be reduced to the condition

$$\zeta_e = \max\left[\frac{1}{N_D^{2/3}}\left(\frac{R}{r_D}\right)^2, D^2\left(\frac{R}{\rho_e}\right)^2\right] \gg 1 \quad (7)$$

on the electron fluctuation parameter ζ_e, which reflects the allowed loss of accuracy when the electron dynamics is described in terms of smoothed electric fields rather than in terms of real plasma electric fields.

We can see that, because of the first term in the square brackets in (7), the necessary condition (6) can be satisfied at fairly large values of R. In fact, for a fusion plasma with the parameters $n \sim 10^{14}$ cm^{-3} and $T \sim$ 10 keV and for a tokamak with the major radius $R \sim 10$ m, we have

$$\left(\frac{R}{r_D}\right)^2 \gg N_D^{2/3}, \quad (8)$$

which is enough to ensure condition (7). In this connection, we will work under condition (7) below.

The parameter ζ_e has a clear physical meaning: it characterizes the role of fluctuation electric fields in the kinetics of a tokamak plasma. For $\zeta_e \gg 1$, the role of fluctuation electric fields is substantial, so that they cannot be neglected in the analysis. For $\zeta_e \ll 1$, the fluctuation electric fields play a minor role, so that the plasma can be regarded as a fluctuation-free medium consisting of particles undergoing Coulomb interactions, in which case we can use, e.g., the Vlasov equation with the Landau collision integral. Note that, according to (8), the inequality

$$N_D \gg \left(\frac{R}{r_D}\right)^3 \text{ or } \frac{\lambda_{st}}{R} \gg N_D^{2/3} \quad (9)$$

(where λ_{st} is the electron mean free path with respect to Coulomb collisions) serves as a necessary condition for the applicability of the "fluctuation-free" tokamak plasma approximation.

Recall that the standard way to derive kinetic equations with the Landau or Lenard–Balescu collision integral is to consider a homogeneous plasma in the limit of large N_D. Relationships (7) and (9) imply that the limiting transitions are not always commutative: passages to the limit of a homogeneous plasma and to the limit $N_D \longrightarrow +\infty$ do not necessarily yield the same results if performed in the opposite order.

Let us analyze the fluctuation-dominated (turbulent) modes of plasma confinement in tokamaks more thoroughly. Under condition (7), a toroidal confinement system is characterized not only by the time scales

$$\tau_e \geq \frac{1}{a_{ch}}\sqrt{\frac{T_e}{m}} \text{ and } \tau_i \geq \frac{1}{A_{ch}}\sqrt{\frac{T_i}{M}}, \quad (10)$$

which were introduced in (4), but also by the time τ_R required for a fictitious electron to complete a revolution in the toroidal direction under the action of the force described by the operator $\hat{l}$,

$$\tau_R \sim \Gamma\sqrt{\frac{R}{a_{ch}}}, \quad (11)$$

where the factor $\Gamma = (1 + \epsilon^2/q^2)^{1/4}$ reflects the magnetic field geometry, q is the safety factor, and $\epsilon = r/R$. The relationship among the time scales τ_R, τ_e, and τ_i governs the type of discharge in a tokamak, i.e., the type of turbulence in the confinement mode. Note that the kinetic equations derived in [11] can be applied to tokamaks only on time scales shorter than the time interval after which the force described by the operator $\hat{l}$ starts to lower the velocities of fictitious electrons down to their

initial values, i.e., on time scales such that

$$\tau_R \longrightarrow +\infty. \tag{12}$$

This limiting condition is undoubtedly satisfied under the inequalities

$$\tau_e \ll \tau_R, \quad \tau_i \ll \tau_R, \tag{13}$$

which can be rewritten as

$$\Gamma^4\zeta_e \gg 1, \quad \Gamma^4\zeta_Z = \Gamma^4\frac{Z^4m^2}{M^2}\left(\frac{T_e}{T_i}\right)^2\zeta_e \gg 1. \tag{14}$$

Note that, in tokamaks, the safety factor is larger than unity; i.e, we have $\Gamma \sim 1$. For this reason, we will neglect the geometric factor Γ in further analysis.

Physically, conditions (14) imply that both the electron and ion transport should be treated with allowance for fluctuations. To save space, we will refer to the plasma states in which the turbulence of both the ion and electron components is important as the ion–electron type of turbulence or simply (*i*, *e*)-turbulence. The (*i*, *e*)-turbulence was first investigated in our papers [4, 5] in the electrostatic approximation.

The first inequality in (13) follows from condition (7), which can also be satisfied for confinement modes such that

$$\tau_i \gg \tau_R. \tag{15}$$

In other words, we arrive at the conditions

$$\zeta_e \gg 1, \quad \zeta_Z \ll 1, \tag{16}$$

which indicate that the electron transport should be treated with allowance for turbulent fluctuations, while the ion component can be described in an almost ideal, fluctuation-free plasma approximation. Below, such plasma states will be referred to as the electron type of turbulence or simply (*e*)-turbulence. It is these plasma states with a pure (*e*)-turbulence that are the subject of our analysis. Note that the plasma states with a pure ion turbulence cannot occur in the range of electron-to-ion temperature ratios that are of interest from the standpoint of tokamaks.

We emphasize that the transition from (*i*, *e*)-turbulence to (*e*)-turbulence is describe by the ion fluctuation parameter

$$\zeta_Z = \frac{Z^4m^2}{M^2}\left(\frac{T_e}{T_i}\right)^2\zeta_e, \tag{17}$$

which reflects the role of turbulent fluctuations in the ion conductivity. It is of interest to note that, if a plasma contains ions of different species, then some of the ion components can be described in the fluctuation-free approximation, while the remaining ion components possess anomalous properties and their dynamics is strongly affected by fluctuation electric fields in a plasma.

Recall that, in a bounded plasma, the ion dynamics can differ fundamentally from the electron dynamics because of the small value of the factor $(m/M)^2$ in (17).

3. KINETIC EQUATIONS FOR (*e*)-TURBULENCE

In our papers [4, 5], we derived and partially analyzed the kinetic equations for (*i*, *e*)-turbulence. In other words, we studied ion–electron turbulence, for which the electron and ion fluctuation parameters are both large ($\zeta_e \gg 1$ and $\zeta_Z \gg 1$). In this section, we obtain the kinetic equations for (*e*)-turbulence, i.e., for the case in which the electron fluctuation parameter is large ($\zeta_e \gg 1$) and the ion fluctuation parameter is small ($\zeta_Z \ll 1$). For discharges with (*e*)-turbulence, the fluctuation electric fields should be systematically taken into account only in describing the electron dynamics, while the plasma ions can be treated in the fluctuation-free approximation.

With the formalism developed in [8, 9, 11], a straightforward way of deriving kinetic equations is to introduce the generalized distribution functions, which depend on the coordinates, velocities, and accelerations of the particles. The problem at hand differs fundamentally from the problem treated in [9] in that the kinetic equations should be obtained under the conditions $\zeta_Z \ll 1 \ll \zeta_e$; in other words, we must take into account the condition $\tau_e \ll \tau_R$ for the electrons (in this sense, we have $\tau_R = +\infty$) and the condition $\tau_i \gg \tau_R$ for the ions (in this sense, we have $\tau_R = 0$).

The method of generalized distribution functions is advantageous in that it enables us to decouple infinite hierarchies of equations for the multiparticle distribution functions on infinitely long time scales. This possibility stems from the fact that the formalism of generalized distribution functions makes it possible to explicitly take into account the irreversible character of the evolution of a multiparticle system (the particles "forget" the initial conditions) before we proceed to decoupling the hierarchy of equations for the multiparticle distribution functions. We are thus faced with the justification of the decoupling procedure only for states in which the particles forget the initial correlations and the interaction between the particles gives rise to new correlations between them rather than for arbitrary states of the system. The possibility of carrying out the decoupling procedure for a smaller class of the states of the system makes the desired closed kinetic equation far simpler to derive [9], the more so because this class can be characterized explicitly.

Note that, if in studying the (*e*)-mode of confinement we introduce the generalized two-particle distribution function $f_2(t, 1_e, 2_e)$ in the same manner as in [8], then we can immediately write out the desired kinetic equation for the plasma electrons:

$$\left(\frac{\partial}{\partial t} + \hat{l}_1 + \hat{l}_2\right)f_2(t, 1_e, 2_e) = f_1(t, 1_e)d(t, 2_e) + f_1(t, 2_e)d(t, 1_e). \tag{18}$$

Here, $1_e = (\mathbf{r}_1, \mathbf{v}_1, \mathbf{a}_1)$, $1_i = (\mathbf{R}_1, \mathbf{V}_1, \mathbf{A}_1)$, etc., where the lowercase letters stand for the coordinates, velocities,

and accelerations of the electrons and the uppercase letters mean the same for the ions. Further,

$$f_1(t, 1_e) = \int_0^{+\infty} e^{-\tau \hat{l}_1} d(t-\tau, 1_e) d\tau, \tag{19}$$

$$\hat{l}_j = \mathbf{v}_j \frac{\partial}{\partial \mathbf{r}_j} + \left(\mathbf{a}_j - \frac{e}{mc}[\mathbf{v}_j, \mathbf{H}] \right) \frac{\partial}{\partial \mathbf{v}_j}, \quad j = 1, 2,$$

$$d(t, 1_e) = \int \hat{q}(1_e, 3_e) f_2(t, 1_e, 3_e) d3_e + \int \hat{q}^*(1_e, 1_i) \Phi(t, 1_e, 1_i) d1_i, \tag{20}$$

$$\hat{q}(1_e, 2_e) = -\mathbf{q}(1_e, 2_e) \frac{\partial}{\partial \mathbf{a}_1},$$

$$\hat{q}^*(1_e, 1_i) = -\mathbf{q}^*(1_e, 1_i) \frac{\partial}{\partial \mathbf{a}_1},$$

where

$$\mathbf{q}(1_e, 2_e) = \frac{e^2}{m} \frac{1}{|\mathbf{r}_1 - \mathbf{r}_2|^3} \times \left[\mathbf{v}_1 - \mathbf{v}_2 - 3 \frac{(\mathbf{v}_1 - \mathbf{v}_2, \mathbf{r}_1 - \mathbf{r}_2)}{|\mathbf{r}_1 - \mathbf{r}_2|^2} (\mathbf{r}_1 - \mathbf{r}_2) \right], \tag{21}$$

$$\mathbf{q}^*(1_e, 1_i) = -\frac{Ze^2}{m} \frac{1}{|\mathbf{r}_1 - \mathbf{R}_1|^3} \times \left[\mathbf{v}_1 - \mathbf{V}_1 - 3 \frac{(\mathbf{v}_1 - \mathbf{V}_1, \mathbf{r}_1 - \mathbf{R}_1)}{|\mathbf{r}_1 - \mathbf{R}_1|^2} (\mathbf{r}_1 - \mathbf{R}_1) \right], \tag{22}$$

and Φ is the two-particle electron–ion distribution function. Note that the interval of integration over τ in (19) is actually extended to a time τ_0 such that $\tau_e \ll \tau_0 \ll \tau_R$ rather than to infinity.

Analyzing Eqs. (18) and (19) in the limit $m \ll M$, we can neglect $\mathbf{V}_1$ in comparison with $\mathbf{v}_1$ in (22) and can rewrite the integral over the ion coordinates, velocities, and accelerations in the expression for $d(t, 1_e)$ in the form

$$\int \hat{q}^*(1_e, 1_i) \Phi(t, 1_e, 1_i) d1_i = \left[\frac{\partial}{\partial \mathbf{a}_1} f_e(t, \mathbf{r}_1, \mathbf{v}_1, \mathbf{a}_1) \right] \times \left[-\frac{Ze^2}{m} \int \frac{1}{|\mathbf{r}_1 - \mathbf{R}_1|^3} \times \left(\mathbf{v}_1 - 3 \frac{(\mathbf{v}_1, \mathbf{r}_1 - \mathbf{R}_1)}{|\mathbf{r}_1 - \mathbf{R}_1|^2} (\mathbf{r}_1 - \mathbf{R}_1) \right) F_1(t, 1_i) d\mathbf{R}_1 d\mathbf{V}_1 \right]. \tag{23}$$

We emphasize that the correctness of the decoupling procedure (23) is not based on the relationship

$$\Phi(t, 1_e, 1_i) = F_1(t, 1_i) f_e(t, 1_e), \tag{24}$$

which nevertheless serves as a sufficient condition for relationship (23). In fact, in accordance with the formalism of generalized distribution functions, a sufficient condition for the decoupling relationship (23) to be justified is the fact that, in the interval $\tau_e \ll \tau_0 \ll \tau_R$, we can describe the electron–ion interaction in an "averaged" fashion in the sense of (23) [9]. Note that the electron kinetic equation derived in such a way is valid only on time scales t such that $\tau_0 \ll t \ll \tau_R$, because it is these time scales on which the integral representation (19) allows us to apply the averaged description of the electron–ion interaction in accordance with (23) [9].

The averaged description has a clear physical meaning. With allowance for fluctuations on certain time scales, the terms describing two-particle interactions in the kinetic equations for generalized distribution functions vanish; in other words, the particle dynamics on these time scales is correctly described by appropriately defining the averaged interaction. This assertion was proved on the basis of the integral representations for the generalized distribution functions (the H-theorem in a gentle formulation) [9]. In Appendix 2, we present a particular example in order to explicitly illustrate the phenomenon of the averaged interaction.

Now, we can readily take the limit $\tau_R \longrightarrow +\infty$ in the kinetic equation for the electron plasma component because this equation is valid on arbitrary time scales t rather than over the interval $\tau_0 \ll t \ll \tau_R$. Hence, the electron dynamics in tokamaks is also characterized by the time scale τ_R, which stems from the fact that fictitious electrons forget the initial conditions because of their circulation along the torus. Consequently, the distribution of the electric field fluctuations (i.e., the electron acceleration distribution) should be established on time scales shorter than τ_R and should adiabatically follow the possible processes that occur on longer time scales.

Relationship (23) is easy to interpret: light electrons move in the field of heavy ions, which, in a first approximation, can be assumed to be immobile in studying the electron dynamics. According to (23), the dynamics of the electron plasma component is governed only by the mean field of the plasma ions (the second factor on the right-hand side of this relationship describes how the acceleration of an electron changes as it moves in the mean field of the ions). For a uniform ion distribution, integral (23) vanishes, so that Eq. (18) is a closed equation for the distribution function $f_2(t, 1_e, 2_e)$, in which case the one-particle electron distribution function is uniquely determined by (19). Consequently, in the lowest order approximation in m/M, the ions play the role of a neutralizing background in the formation of the electron distribution function in a plasma with (e)-turbulence.

We can readily see that the symmetry group generated by the closed equation derived above for the function $f_2(t, 1_e, 2_e)$ coincides with the group of turbulent

dimensionalities [4, 8, 11] so that, following [11], we can introduce the nonquasineutrality parameter D, which reflects the symmetry properties of the system. After solving the corresponding functional equations, we can use the groups of turbulent and physical dimensionalities in order express the transverse electron thermal diffusivity $\chi_\perp^{(e)}$ and the energy density W of the fluctuation electric fields (see Appendix 1) in terms of the nonquasineutrality parameter [4, 11]:

$$\chi_\perp^{(e)} = \chi_{cl} + C_3 D^2 \frac{cT_e}{eH}, \tag{25}$$

$$\frac{W}{nT_e} = C_2 D^2 \left(\frac{r_D}{\rho_e}\right)^2, \tag{26}$$

where Ω_{ce} is the electron gyrofrequency and χ_{cl} is the neoclassical electron thermal diffusivity. The fixed numbers C_i ($i = \overline{2, 3}$) cannot be evaluated by the method proposed here.

Now, we consider plasma states with an essentially steady turbulence and focus primarily on the kinetics of the ion plasma component. Since the plasma turbulence in the initial state is almost steady, the ion velocity distribution function is close to that in the steady turbulent state. Recall that the distribution of the fluctuation electric field in a plasma should be established on time scales of about τ_R. However, by virtue of the condition $\zeta_Z \ll 1$, the fluctuation electric fields cannot significantly change the ion velocity distribution function and, after the formation of the steady-state distribution of the fluctuation electric field, the ion velocity distribution function remains almost unchanged because both plasma electrons and ions are almost steady. The above considerations allow us to ignore the influence of the turbulence-induced fluctuation electric field on the ion dynamics in the limit $\zeta_Z \ll 1$. Since our approach cannot describe how the electron motion is affected by fluctuations, we can represent the generalized multiparticle distribution functions for the plasma ions as a product of two functions: one dependent only on the coordinates, velocities, and time and the other dependent only on the coordinates, accelerations, and time [9]. This factorization immediately yields the Fokker–Planck equation for the ions [9]. However, for further analysis, we must consider this problem in more detail.

Note that, for $D^2 \ll 1$, we must treat the transport conditions (25) and (26) as being dependent on the nonquasineutrality parameter. However, the one-particle distribution function $f_e(t, 1_e)$ is almost insensitive to D^2, because it changes markedly only when D changes by an amount of order unity. An analogous situation, which was thoroughly analyzed in [5], is examined in Appendix 1. Therefore, we can assume that, in the limit of the small values of the nonquasineutrality parameter D, the electron velocity distribution function is nearly Maxwellian. This assumption and the fact that, in describing the (e)-mode of confinement, the plasma ions should be treated in the fluctuation-free approximation immediately yield the following equation for the one-particle ion distribution function:

$$\left(\frac{\partial}{\partial t} + \mathbf{V}\frac{\partial}{\partial \mathbf{R}} + \frac{Ze}{M}\left(\mathbf{E} + \frac{1}{c}[\mathbf{V}, \mathbf{H}]\right)\right)F_1(t, \mathbf{V}, \mathbf{R}) = St_{ie} + S_{t_{ii}}, \tag{27}$$

where $F_1(t, \mathbf{V}, \mathbf{R})$ is the ion distribution function, the Landau collision integral St_{ie} describes collisions between the ions and electrons that obey a Maxwellian distribution function, and the term St_{ii} in the Landau collision integral accounts for ion–ion collisions. In fact, in deriving the closed equation for the electrons in a plasma with (e)-turbulence, the smallness of the electron-to-ion mass ratio m/M enabled us to describe the electrons in terms of the mean field of the ions. Since the ion plasma component should be described with the same accuracy, we cannot apply the method of renumbering the ions and must integrate (over accelerations) the hierarchy of equations coupling the generalized distribution functions. This procedure leads to the BGKBY hierarchy, which should be decoupled in a standard way. Note that, in the case of (e)-turbulence, the electrons should be treated by correctly accounting for the total fluctuation electric field in the plasma, while the ions can be described in terms of the smoothed electric field, which enters the Vlasov and Fokker–Planck equations.

Recall that kinetic equations of the form of Eq. (27), in which the fluctuations are neglected, are valid on time scales $t \geq 1/\omega_{pe}$, beginning with the instant at which the plasma starts to evolve, i.e., on time scales required for the two-particle correlation function to form [10].

In order to find the longitudinal plasma conductivity, it is sufficient to determine the relative velocity $\mathbf{u}$ at which the friction force due to Coulomb collisions between ions and electrons with the distribution function $f_e^{(0)}(\mathbf{v} - \mathbf{u}, \mathbf{r})$ is equal to the force exerted by the electric field on the plasma electrons. Consequently, according to Eq. (27), we find that the longitudinal plasma conductivity is exactly equal to the Spitzer conductivity:

$$\sigma_\parallel = \sigma_{Sp}. \tag{28}$$

Note that expression (28) was derived in the same way as the expression for the Spitzer conductivity in a thermodynamically equilibrium plasma because the inequality $\zeta_Z \ll 1$ guarantees that the ion component is in a turbulence-free state.

Relationship (28) shows that, in a straight magnetic field, the ion thermal diffusivity is classical and, in a curved magnetic field, it is neoclassical. Based on what was said above, we can conclude that, on the whole, the

ions in a plasma with (*e*)-turbulence may be treated in the neoclassical approximation.

Hence, correct to numerical factors, our approach provides all of the transport coefficients required to study the radial profiles of the plasma parameters in tokamaks.

4. RADIAL PROFILES OF THE TRANSVERSE THERMAL DIFFUSIVITY IN A PLASMA WITH (*e*)-TURBULENCE

Here, we study (*e*)-turbulence ($\zeta_e \gg 1$, $\zeta_Z \ll 1$) using the methods developed in [4, 5] to describe the phenomenon of self-consistency between the profiles in a plasma with (*i*, *e*)-turbulence ($\zeta_e \gg 1$, $\zeta_Z \gg 1$). We discuss a large aspect ratio tokamak under the condition that ion heat losses are negligible in comparison with electron heat losses.

We assume that the radial profile of the safety factor $q(r)$ and the torus loop voltage $U = 2\pi RE$ are both prescribed and consider a tokamak plasma with a pure Ohmic current. In this case, according to (28), we obtain

$$T_e(r) = \text{const} T_* \left[\frac{2 - S(r)}{q(r)}\right]^{2/3}, \tag{29}$$

where

$$T_*^{3/2} = \frac{e^2 H}{U}\sqrt{mc^2}, \quad S(r) = \frac{rq'(r)}{q(r)},$$

and the constant in (29) stems from the expression for the Spitzer longitudinal conductivity. In what follows, we will often denote by const various factors that are independent of plasma parameters, because the procedure for finding these factors, although straightforward, leads to fairly involved expressions which make the physical meaning of the profiles to be obtained more difficult to understand.

Thus, in a plasma with (*e*)-turbulence, the temperature profile turns out to be uniquely related to the Ohmic current profile and this relationship is universal. It is this point in which the (*e*)-turbulence differs fundamentally from the (*i*, *e*)-turbulence: according to the analysis made in [4, 5], the (*i*, *e*)-turbulence is characterized by a universal relationship between the nonquasineutrality parameter and the radial profile of the safety factor, whereas the radial temperature profile is governed by the requirement that the plasma column in a tokamak be macroscopically stable. These considerations imply, in particular, that the radial temperature and density profiles differ radically between (*i*, *e*)-turbulence and (*e*)-turbulence; in other words, the types of plasma turbulence and self-consistent profiles can actually be controlled by the ion fluctuation parameter ζ_Z.

We illustrate this conclusion by taking as an example discharges in which the ideal ballooning modes are most dangerous for MHD plasma stability. The (*i*, *e*)-turbulence in such discharges was considered in [4, 5]. Under the assumption that neoclassical ion heat losses are much smaller than "anomalous" electron heat losses, we investigate (*e*)-turbulence in discharges whose macroscopic stability is governed by the ideal MHD ballooning modes using the formalism that was developed in [4, 5] to study (*i*, *e*)-turbulence and taking into account the specific features of (*e*)-turbulence that were discussed above. In this connection, we do not repeat the analysis of [4, 5] and immediately write out the final expressions for the radial profiles of plasma parameters (for clarity, we consider the limit $T_e \gg T_i$, in which the ion pressure can be neglected):

$$p(r) = \frac{H^2}{8\pi}P(r), \quad P(r) = \frac{1}{R}\int_a^r \frac{S(r)}{q^2(r)}dr, \tag{30}$$

$$n(r) = \frac{p(r)}{T_e(r)} = \text{const}\frac{H^2}{8\pi T^*}\left[\frac{q(r)}{2 - S(r)}\right]^{2/3} P(r), \tag{31}$$

$$D^2(r) = \text{const}\frac{He}{8p^2 RT_* c}\frac{Q(r)}{rp(r)}\left[\frac{2 - S(r)}{q(r)}\right]^{1/3} \times \frac{q^2(r)}{S'(r)q(r) + q'(r)[2 - S(r)]}, \tag{32}$$

$$\chi_\perp = \chi_\perp^{(e)} = -\frac{3Q(r)}{8\pi^2 Rrp(r)}\left(\frac{d}{dr}\ln\left[\frac{2 - S(r)}{q(r)}\right]\right)^{-1}, \tag{33}$$

where $Q(r)$ is a power deposited in the plasma at a distance r from the chamber axis. Note that, in the case of pure electron turbulence, the dependence of the nonquasineutrality parameter on the plasma parameters differs radically from that in the case of ion–electron turbulence, which was studied in [4, 5].

Following [4, 5], we assume that the power $Q(r)$ is a sum of the injected neutral beam power $Q_0 = \text{const}$ and the Ohmic heating power:

$$Q_{Ohm} = 4\pi^2 RE\int_0^r j(r)rdr = \frac{4\pi^2 RE^2 T_*^{3/2}}{e^2\sqrt{m}}\int_0^r \frac{2 - S(r)}{q(r)}rdr. \tag{34}$$

The function $q(r)$ can be found from the principle of maximum entropy, as was done in [4, 5]. However, for simplicity, we obtain the radial profile of the safety factor variationally in order to provide reliable information on the discharge structure by properly choosing the trial function. Let us seek $q(r)$ in the form

$$q(r) = q_0[1 + (r/r_0)^2], \quad q_0 \geq 1, \tag{35}$$

with the only parameter r_0.

Assuming that $r_0 \ll a$ and that the total number N_e of electrons in the plasma column is fixed, we find from (31)

$$N_e = \frac{\text{const}}{q_0^{4/3}} \frac{H^2 r_0^3}{T_*}, \tag{36}$$

which can be rewritten as

$$r_0 = \text{const} q_0^{4/9} \left(\frac{\bar{\beta} R}{a} \right)^{1/3} a, \tag{37}$$

where $\bar{\beta} = 8\pi T_* \bar{n}/H^2$, with $\bar{n} = N_e/2\pi^2 R a^2$ being the plasma density averaged over the entire volume of the tokamak chamber. It is important to note that

$$n(0) \sim \left(\frac{1}{\bar{\beta}} \frac{a}{R} \right)^{2/3} \bar{n}, \tag{38}$$

which indicates that $n(0) \gg \bar{n}$ under the condition

$$\bar{\beta} \ll \frac{a}{R}. \tag{39}$$

Hence, the (*e*)-turbulence is characterized by the following temperature, density, and pressure profiles:

$$T(r) = \frac{T(0)}{[1 + (r/r_0)^2]^{4/3}}, \quad n(r) = \frac{n(0)}{[1 + (r/r_0)^2]^{1/6}}, \tag{40}$$
$$p(r) = \frac{p(0)}{[1 + (r/r_0)^2]^{3/2}},$$

in which case the thermal diffusivity in the region $r > r_0$ is equal to

$$\chi_\perp \sim (r/r_0)^3. \tag{41}$$

5. COMPARISON BETWEEN SELF-CONSISTENT PROFILES IN TOKAMAK PLASMAS WITH (*i*, *e*)- AND (*e*)-TYPES OF TURBULENCE

Recall that the ion dynamics is very sensitive to the value of the parameter ζ_Z, so that the self-consistent profiles can change radically. According to [4, 5], in the limit $\zeta_Z \gg 1$, which corresponds to the (*i*, *e*)-turbulence, we have

$$n(r) \sim 1/r^2, \quad T(r) \sim 1/r, \quad \chi_\perp(r) \sim r^3. \tag{42}$$

In contrast, in the limit $\zeta_Z \ll 1$, which corresponds to (*e*)-turbulence, we have

$$n(r) \sim 1/r^{1/3}, \quad T(r) \sim 1/r^{8/3}, \quad \chi_\perp(r) \sim r^3. \tag{43}$$

It is noteworthy that plasmas with different types of turbulence, namely, ion–electron turbulence and pure electron turbulence, are characterized by precisely the same radial behavior of the transverse thermal diffusivity in the edge region, the temperature and density profiles being extremely different. The reason for this can be explained based on expression (33): in the region $r \gg r_0$ and for the safety factor whose radial profile is described by (35), we have

$$\chi_\perp = \text{const} \frac{Q_{\text{tot}}}{p(r)}, \tag{44}$$

where Q_{tot} is the total input power and the pressure profile is governed by the most dangerous macroscopic instability. Therefore, the radial profile of the transverse thermal diffusivity will differ between plasmas with (*i*, *e*)-turbulence and (*e*)-turbulence only when different plasma conditions result in different most dangerous instabilities, more precisely, the instabilities that occur near marginal stability for turbulent fluctuations but do not affect turbulent transport. Consequently, our model allows us to hope to derive a more or less favorable radial profile of the transverse thermal diffusivity only in a plasma column whose macroscopic structure is "organized" so as to change the kind of most dangerous instability.

Note that the ion fluctuation parameter ζ_Z changes when approaching the plasma boundary. This circumstance allows us to conclude that in tokamaks a part of the plasma column may be in a state with the developed (*i*, *e*)-turbulence, while the state of the remaining part may be characterized by (*e*)-turbulence. We can readily see that ζ_Z increases toward the boundary. Consequently, we may expect discharges with a hybrid structure, such that (*e*)-turbulence dominates in the central plasma and (*i*, *e*)-turbulence occurs predominantly in the edge region.

Of course, the type of confinement mode is governed by many parameters: $Q(r)$, U, $\bar{n}$, H, R, a, etc. For simplicity, we restrict ourselves to considering discharges with Ohmic heating alone. Using (32), we can apply the approach of [4, 5] to estimate ζ_Z for plasmas with the (*e*)- and (*i*, *e*)-types of turbulence. As a result, the functional dependence of the estimated quantities ζ_Z and ζ_e on the parameters of the plasma column will differ strongly between the (*e*)- and (*i*, *e*)-types of turbulence. We can readily show that the parameter range in which (*i*, *e*)-turbulence and (*e*)-turbulence can occur simultaneously satisfies the condition

$$\zeta_Z^{(e)} \ll 1 \ll \zeta_Z^{(e,i)}, \tag{45}$$

where $\zeta_Z^{(e)}$ and $\zeta_Z^{(e,i)}$ are the values of ζ_Z for the (*e*)- and (*i*, *e*)-types of turbulence, respectively. This possible property of the discharges—to exhibit a sort of bistability—is very important and illustrative.

We do not present here the explicit expressions that we derived for the parameter ζ_Z for different types of turbulence using the above model, in which ballooning modes are regarded as the most dangerous macroscopic instability, because, in what follows, we will show that this model is unrealistic for tokamaks. On the other

hand, our model is of particular importance, because it yields some universal (i.e., independent of the kind of most dangerous instability) results and is the main subject of our analysis. The results that are strongly sensitive to the kind of most dangerous instability will be analyzed below in a qualitative way. Let us illustrate the above-said with the following examples. First, we can expect that, regardless of the kind of most dangerous instability, tokamak discharges in a certain parameter range will also exhibit a sort of bistability governed by the type of ion turbulence (the change in the parameters changes the solution to the kinetic equations, but the number of equations remains unchanged). Second, the thermal diffusivity should also remain unchanged, because, as was noted above, it is only associated with the kind of most dangerous instability rather than with the real fastest growing mode and also depends on such a "rough" parameter as the pressure profile [see (44)]. Finally, we expect that the real temperature and density profiles will be intermediate between the profiles in (42) and (43).

6. PHYSICAL INTERPRETATION AND CONSEQUENCES OF THE RESULTS OBTAINED

Note that the pure electron and ion–electron types of turbulence that occur at different levels of ion turbulence can be interpreted in a simple and illustrative way. Since, in the limit $\zeta_e \gg 1$, which is of interest to us, the electrons always behave in a more or less anomalous fashion, the electron thermal diffusivity is definitely anomalous, whereas the ions may exhibit neoclassical behavior. The longitudinal conductivity is more difficult to describe, because it is governed by the states of both the electron and ion components. In the (i, e)-mode of confinement, the ions exhibit turbulent behavior ($\zeta_Z \gg 1$), in which case the ion distribution at each instant is strongly nonuniform, so that the ion background gives rise to significant spatial variations of the electrostatic potential. As the longitudinal current flows through the plasma, the plasma electrons can be efficiently scattered by the electrostatic potential produced by the ions; therefore, the longitudinal conductivity is also anomalous [4, 5]. In the (e)-mode, the ion turbulence is absent ($\zeta_Z \ll 1$): the ions are distributed uniformly in space and the electrostatic potential experiences no macroscopic fluctuations, which efficiently scatter the electrons. As a result, the longitudinal plasma conductivity is exactly equal to the Spitzer conductivity. Recall that, in early tokamak experiments, the longitudinal plasma conductivity was often significantly lower than the Spitzer conductivity, whereas more recent experiments have revealed that the longitudinal conductivity is close to the Spitzer conductivity.

On the other hand, we must keep in mind that our model cannot pretend to explain real tokamak experiments, because it neglects finite β values (i.e., the nonpotential nature of the plasma) and self-consistent macroscopic electric fields, which give rise to the rotation of the plasma column.

7. ABSOLUTE VALUE OF THE TRANSVERSE THERMAL DIFFUSIVITY

Note that the above results on the physics of transverse transport in tokamaks have widely different statuses. Some of the results, namely, those that are insensitive to the kind of most dangerous instability, are universal in character. Other results differ markedly between discharges with different kinds of the most dangerous instability. Among the most important universal results, we can mention the conclusions about the nature of the radically different behavior of the ions and electrons in finite-size plasmas, the assertion that the transverse thermal diffusivity increases toward the plasma boundary, and the explanation for the possible existence of hybrid discharges with a Spitzer longitudinal conductivity, the roughly neoclassical behavior of the ions, and the strongly anomalous transverse electron thermal diffusivity. However, the absolute value of the transverse thermal diffusivity is not a universal quantity: it is very sensitive to the kind of most dangerous macroscopic instability. Consequently, a comparison between the absolute values of the calculated and experimental transverse thermal diffusivities makes it possible to reveal the kind of macroscopic instability that occurs near the marginal stability for turbulent fluctuations.

In our study, we assume that the role of the most dangerous instability is played by ballooning modes, because the stability criterion for these modes is suitable for our purposes, one of which is to compare different types of turbulence (electron turbulence and ion–electron turbulence) in the problem as formulated (see [4]). This approach can be justified by the fact that our formulation of the problem makes it possible to reveal some universal characteristic features of the transverse transport (we do not pretend here to describe its specific properties). On the other hand, in order to better understand the physics of transverse transport, it is helpful to compare the calculated results with experimental data and to analyze (at least, preliminarily) how other kinds of dangerous instabilities will affect the results.

We start by noting that, regardless of the kind of most dangerous instability, formula (25) and the conditions for the discharge to be steady yield the following universal radial profile of the transverse thermal diffusivity:

$$\chi_\perp = \frac{Q(r)}{4\pi^2 R r n(r) |dT_e/dr|}. \quad (46)$$

Moreover, for expression (46) to be valid, the main channel for energy losses should be associated with anomalous electron thermal diffusivity and the inequalities $\chi_{cl} < \chi_\perp \ll \chi_{\text{Bohm}}$ should be satisfied. To avoid misunderstanding, we emphasize that expression (46) has

no singularity at $r \longrightarrow 0$, because the quantity $Q(r)$ in the numerator in (46) approaches zero as $r \longrightarrow 0$.

Expression (46) itself is physically meaningless, because it is nothing more than a formal consequence of the definition of the thermal diffusivity. Physically, the only meaningful points here are the assertion that the energy is lost mainly due to the anomalous electron thermal diffusion and the existence of the lower and upper bounds, χ_{cl} and χ_{Bohm}, on the electron thermal diffusivity.

Note that both kinetic and hydrodynamic processes (macroscopic plasma displacements) can also contribute to the electron thermal diffusivity. Our approach is capable of incorporating only the contribution of the kinetic phenomena. In this context, the conductivity differs fundamentally from the thermal diffusivity in that it arises entirely from the kinetic processes (to significantly change the conductivity requires that there be hydrodynamic motions during which the macroscopic parameters of a medium experience strong variations, while a substantial change in the thermal diffusivity can be ensured by hydrodynamic motions such that the density and temperature fluctuate only slightly). Consequently, regardless of whether the hydrodynamic processes in a tokamak plasma are taken into account or not, an adequate kinetic theory should give a correct value of the conductivity.

Expression (46) demonstrates that the approach developed here is capable of obtaining transverse thermal diffusivities that agree with the experimentally measured values. However, to calculate the discharges self-consistently (i.e., to determine the relations among the temperature gradient, the plasma density, and the profile of the total heating power) requires the most dangerous macroscopic instability to be specified, in which case the final results are strongly sensitive to the kind of the most dangerous instability.

In our model, the role of the most dangerous instability is assumed to be played by ballooning modes. Under this assumption, we have demonstrated that our approach to describing transport in tokamaks can be used to calculate discharges self-consistently. However, the transverse thermal diffusivities obtained from our model turn out to be too small in comparison with the experimentally measured values. We emphasize that this circumstance does not discredit our approach but simply demonstrates that either the ballooning modes are unlikely to play the role of the most dangerous instability or the real transport in tokamaks should be described with allowance for hydrodynamic processes. We must also keep in mind that, in real tokamaks, the β values are finite.

8. CONCLUSION

In conclusion, we summarize the main results of our work, using notation suitable for comparison with the experimental data and theoretical results obtained in other papers.

Under the conditions

$$\zeta_Z = Z^4\left(\frac{R}{r_D}\right)^2\left(\frac{m}{M}\right)^2\left(\frac{T_e}{T_i}\right)^2 \max\left(\frac{1}{N_D^{2/3}}, \frac{W}{nT_e}\right) \ll 1, \quad (47)$$

$$\zeta_e = \left(\frac{R}{r_D}\right)^2 \max\left(\frac{1}{N_D^{2/3}}, \frac{W}{nT_e}\right) \ll 1, \quad (48)$$

electrons and ions can both be treated without allowance for nonequilibrium fluctuations, i.e., in the neoclassical approximation.

However, for present-day tokamaks, conditions (47) and (48) may fail to hold. From a practical standpoint, the most interesting case is that described by the conditions

$$\zeta_Z \ll 1, \quad \zeta_e \gg 1, \quad (49)$$

where the ions can be modeled in the fluctuation-free approximation, the electron dynamics should be studied with allowance for fluctuations, the longitudinal conductivity of a tokamak plasma coincides with the Spitzer conductivity, and the transverse ion thermal diffusivity is neoclassical. Note again that, under conditions (49), fluctuations should be taken into account in describing the electron dynamics. However, the fluctuations may affect the transverse electron transport in different ways: if conditions (49) and the extremely restrictive condition

$$\frac{W}{nT_e} \sim \frac{1}{N_D}\left(\frac{r_D}{\rho_e}\right) \quad (50)$$

are both satisfied, then the fluctuations change the transverse electron transport but in a way that does not differ greatly from the neoclassical predictions. Note that condition (50) differs fundamentally from conditions (47)–(49) in that it is independent of the tokamak dimensions. If condition (50) fails to hold because of the high level of turbulent noises but conditions (49) are satisfied, then the transverse electron transport is anomalously high, the longitudinal plasma conductivity remains equal to the Spitzer conductivity, and the ions can be described roughly in terms of neoclassical theory.

With the prescribed kind of the most dangerous instability that occurs near the marginal stability for turbulent fluctuations, our approach is capable of describing discharges self-consistently. In the present paper, we apply this approach to examine a particular case such that the role of the most dangerous instability is played by ballooning modes.

We now explain why conditions (49) are most representative of the last generation of tokamaks. We can readily see that the condition $\zeta_e \gg 1$ holds for modern

devices because

$$\Delta_e = \frac{1}{N_D^{2/3}}\left(\frac{R}{r_D}\right)^2 \gg 1, \quad (51)$$

in which case, however, we have

$$\Delta_Z = Z^4\left(\frac{m}{M}\right)^2\left(\frac{T_e}{T_i}\right)^2\Delta_e \ll 1. \quad (52)$$

This indicates that, according to (49), confinement modes with a Spitzer longitudinal conductivity can occur only when turbulent noise is below a critical level W_{cr} such that

$$\frac{W_{cr}}{nT_e} = \frac{1}{Z^4}\left(\frac{r_D}{R}\right)^2\left(\frac{M}{m}\right)^2\left(\frac{T_i}{T_e}\right)^2. \quad (53)$$

We illustrate relationships (51)–(53), taking as an example a large tokamak with the major radius $R \sim 10$ m and assuming a hydrogen plasma under fusion reactor conditions: $n = 10^{14}$ cm^{-3}, $T_i = T_e = 10$ keV, $\Delta_e = 10^4$, $\Delta_Z = 2.5 \times 10^{-3}$, and $W_{cr}/nT_e = 10^{-4}$ (the electric field corresponding to this value of W_{cr} is very strong: $E_{cr} = 20$ kV/cm). Hence, we see that plasmas with a Spitzer longitudinal conductivity in discharges with a lower noise level are representative of present-day tokamaks and future tokamak reactors.

This example indicates that, for modern tokamaks, the condition $\zeta_e < 1$ is of interest only from a theoretical viewpoint, because $\zeta_e > \Delta_e$. It is this respect in which tokamaks differ radically from other magnetic confinement systems for which the condition $\zeta_e < 1$ can be satisfied and thus the plasma can surely be described in the fluctuation-free approximation. In fact, according to [13], a plasma-filled betatron with $R = 20$ cm is capable of creating a plasma with $n = 5 \times 10^{10}$ cm^{-3} and $T_e > 10$ keV, i.e., with $\Delta_e = 2 \times 10^{-5}$. The fluctuation-free approximation undoubtedly applies to such a plasma.

Note that, under conditions (49), the state of the plasma column is such that turbulent processes should be taken into account in describing the electron component but can be neglected in treating the ions. Thus, we arrive at the notion of electron turbulence, or (*e*)-turbulence.

A third possible case is that in which

$$\zeta_Z \gg 1, \quad \zeta_e \gg 1. \quad (54)$$

Under these conditions, both the electrons and ions should be described with allowance for fluctuations. For real tokamaks, these conditions should correspond to discharges with bad confinement properties: the longitudinal conductivity is far below the Spitzer conductivity, the turbulent noise is relatively intense, and the transverse thermal diffusivity is high. In such discharges, turbulent processes affect both the electron and ion plasma components. The properties of this ion–electron turbulence, or (*i*, *e*)-turbulence, were already studied in our paper [11].

Two possible types of turbulence, namely, (*e*)-turbulence and (*i*, *e*)-turbulence, make it possible to ignite bistable discharges with different sorts of radial profiles of the plasma temperature and plasma density. Such discharges are characterized by a universal behavior of the transverse thermal diffusivity: it increases when approaching the plasma boundary. With our model, the self-consistency of the profiles can be explained in a natural way. Of course, the physics of plasma confinement in tokamaks is far more complicated and cannot be adequately described by the electrostatic plasma model, in particular, because it is necessary to take into account finite β values.

ACKNOWLEDGMENTS

We would like to thank all the participants of the OGRA Seminar on Similarity Methods in Plasma Physics. We are especially grateful to A.A. Skovoroda, A.A. Timofeev, and V.V. Arsenin, whose questions have been mostly answered in this paper. We also wish to express our appreciation for helpful discussions with V.I. Kogan, who pointed out that it is necessary to incorporate the Holtsmark fluctuating electric field into the problems of plasma physics.

APPENDIX 1

Here, we consider some properties of the developed turbulence in a plasma. First, we determine the amplitude of the fluctuation electric fields excited in a turbulent plasma. Note that the mean squared electric field calculated by averaging over the plasma volume diverges, because, in the vicinity of each point charge, the electric field increases according to the law $1/r^2$. The electric field averaged over the plasma "particles," i.e., the quantity proportional to the mean squared acceleration of particles in a plasma, is free of this singularity (this will be especially clear if we note that the electric fields diverging in the vicinities of point charges make no contributions that cause the mean squared acceleration to diverge), but it nevertheless diverges because of the large contribution that comes from close collisions (at least in a zeroth approximation, in which the plasma is treated as an ideal gas and binary collisions between particles are regarded as being completely stochastic and independent). For this reason, it is convenient to characterize the intensity of fluctuation electric fields in a plasma by the quantity

$$W^* = \frac{1}{48\pi}(W_{ee}^* + W_{ii}^* + W_{ei}^*). \quad (A1.1)$$

Here,

$$W^*_{ee} = \int\left(\frac{m\mathbf{a}_1}{e} + \frac{m\mathbf{a}_2}{e}\right)^2 f_2(t, 1_e, 2_e)d1_e d2_e \times \left[\int f_2(t, 1_e, 2_e)d1_e 2_e\right]^{-1},$$

$$W^*_{ei} = \int\left(\frac{m\mathbf{a}_1}{e} - \frac{M\mathbf{A}_1}{Ze}\right)^2 \Phi(t, 1_e, 1_i)d1_e d1_i \times \left[\int \Phi(t, 1_e, 1_i)d1_e d1_i\right]^{-1},$$

$$W^*_{ii} = \int\left(\frac{M\mathbf{A}_1}{Ze} + \frac{M\mathbf{A}_2}{Ze}\right)^2 F_2(t, 1_i, 2_i)d1_i d2_i \times \left[\int F_2(t, 1_i, 2_i)d1_i d2_i\right]^{-1},$$

where f_2, F_2, and Φ are the generalized two-particle distribution functions. Collisions between particles with very small impact parameters make no contributions that cause the quantity W^* introduced in such a manner to diverge. The denominator $1/48\pi$ on the right-hand side of (A1.1) stems from the fact that the energy density of the "collective" component of the plasma electric field is accounted for six times and the remaining part of the denominator (8π) comes from the definition of the energy density of the electric field. We can readily see that the quantity W^*, which naturally appears in equations describing plasma dynamics, has a clear physical meaning: it characterizes the role of the collective interaction between particles. In fact, this quantity is nondivergent, because it is not contributed to by small-impact parameter collisions (since the statistical weighting factor of three-body collisions is small, simple estimates show that they do not cause the second moments to diverge), and completely incorporates the collective electric fields in a plasma.

Plasma with a developed turbulence is characterized by the group of transformations $K_D \times G_2$; i.e., the quantity

$$w_D = \frac{W^*}{e^2 n^{4/3}} n^{-4D/3(2D+3)}$$

should depend on the quantities

$$x_D = \frac{\Omega_{ce}}{\omega_{pe}},\ y_D = \frac{T}{e^2 n^{1/3}} n^{-2D/3(2D+3)}.$$

Moreover, this dependence should be invariant under the transformations from the group $K_D \times G_2$, while the quantities x_D, y_D, and w_D themselves are not invariant and are transformed as $1/t$, v^2, and $(v/t)^2$, respectively (see [5] for details). Physically, this result, which was thoroughly examined in [5], can be explained as follows. Each state of a turbulent plasma is characterized by a certain group of transformations of the kinetic equations with fluctuations. Each plasma state is invariant under the transformations from "its own" group. In other words, each state of a plasma with a developed turbulence is characterized by a certain dynamic symmetry that imposes fairly stringent restrictions on the relationships between the quantities describing this turbulent plasma state. Recall that the nonquasineutrality parameter D, on the one hand, reflects the symmetry properties of the plasma states and, on the other hand, characterizes fluctuations on spatial scales of about the Debye length, thereby clarifying the role of the effects associated with the plasma nonquasineutrality [5]. It is an easy matter to show that, for $D \neq 0$, the requirements for the above relationship among the quantities x_D, y_D, and w_D to be invariant uniquely determine the functional dependence $w_D = C(D)y_D x_D^2$; i.e.,

$$\frac{W^*}{nT} = C(D)\left(\frac{r_D}{\rho_e}\right)^2, \qquad \text{(A1.2)}$$

where $C(D)$ is an unknown function of the parameter D.

We emphasize that expression (A1.2) is valid only for $D \neq 0$. For $D = 0$, the above symmetry considerations fail to give a unique relationship between the quantity W^* and the plasma parameters. The reason is that, for $D = 0$, the group $K_0 \times G_2$ is degenerate, thereby generating an infinite class of relationships among the parameters x_D, y_D, and w_D. That is why the solutions characterized by the symmetry group K_0 require special treatment. To study this degenerate case, the dynamic plasma state should be described using the approach based on equations that are invariant under the transformations from the group K_0. In other words, we must construct a kinetic equation such that the full family of its solutions is invariant under these transformations. The steady solution to this kinetic equation will correspond precisely to the desired solution with the symmetry group K_0, because, under the transformations from this group, the desired solution passes over to the steady solution and, moreover, satisfies the equation that possesses the relevant symmetry properties. In other words, solutions that are close to the desired solution and are transformed by the operators of the group K_0 are again solutions to the same equation. Consequently, the desired solution is the limiting (at $D \longrightarrow 0$) solution of the family of solutions describing the developed turbulence. We can readily show that the desired equation is the Vlasov equation with the Landau collision integral (the Fokker–Planck equation) and that the limit $D \longrightarrow 0$ corresponds simply to a thermally equilibrium plasma state. Hence, for $D = 0$, the quantity W^* is equal to $C_1 e^2 n^{4/3}$ (the constant C_1 is uninteresting for further analysis).

Note that, for turbulent noises, the quantity W^* should be continuous in the limit $D = 0$. However, the noise level determined by (A1.2) differs from that at $D = 0$ by a power of the quantity $T/e^2 n^{1/3}$, which is a

large parameter of the problem because the number of particles inside the Debye sphere $N_D = (T/e^2 n^{1/3})^{3/2}$ is large. In our approach, all of the quantities are expanded in powers of the small parameter introduced above (the reciprocal of the number of particles inside the Debye sphere). If the lowest order terms in expansions vanish, then the next-order nonvanishing terms come into play. These considerations immediately yield the conclusion that, at $D = 0$, the unknown function $C(D)$ equals zero. On the other hand, the requirement that the noise level W^* be positive regardless of the value of D gives

$$C(D) = C_2 D^2, \tag{A1.3}$$

where C_2 is a nonnegative constant. Therefore, for $D \le 1$, we have

$$\frac{W^*}{nT} = \frac{C_1}{N_D^{2/3}} + C_2 D^2 \left(\frac{r_D}{\rho_e}\right)^2. \tag{A1.4}$$

The expressions for the transverse thermal diffusivity and conductivity of the plasma can be derived in an analogous fashion:

$$\chi_\perp = \chi_{cl} + C_3 D^2 \chi_{\text{Bohm}}, \tag{A1.5}$$

$$\frac{1}{\sigma_\parallel} = \frac{1}{\sigma_{Sp}} + C_4 \frac{D^2}{\Omega_{ce}}, \tag{A1.6}$$

where C_3 and C_4 are nonnegative constants, σ_{Sp} is the Spitzer conductivity, and χ_{cl} is the classical transverse thermal diffusivity.

Expressions (A1.5) and (A1.6) refine the results of [11], where the limiting value of the thermal diffusivity at $D = 0$ was determined under the assumption that the plasma state with $D = 0$ is insensitive to the magnetic field strength.

Since the term $C_1/N_D^{2/3}$ in (A1.4) comes from the contribution of the Holtsmark fluctuating electric field to (A1.1), it is convenient to introduce the quantity W,

$$\frac{W}{nT} = C_2 D^2 \left(\frac{r_D}{\rho_e}\right)^2,$$

which accounts for the purely turbulent component of the plasma electric field.

The results obtained show that the limiting (at $D \longrightarrow 0$) solution in the full family of solutions to the kinetic equations with fluctuations (this family is parameterized by the nonquasineutrality parameter D) describes a thermodynamically equilibrium plasma state. It is of interest to analyze these solutions in the model with a large parameter $\Delta S/N$, i.e., to consider strongly nonequilibrium solutions. Note that, in an almost ideal plasma in a thermally equilibrium state, the entropy per particle is proportional to the logarithm of the number of particles inside the Debye sphere. Therefore, if in some nonequilibrium state the change in the entropy per particle is a finite fraction of its equilibrium value, then in the limit of an infinite number of particles inside the Debye sphere this change is infinitely large, of course, under the condition that the above finite fraction be nonzero. Consequently, analyzing the order of limiting transitions makes it possible to understand why the solution corresponding to a thermally equilibrium state is a limiting one in the family of solutions describing strongly nonequilibrium plasma states.

In other words, the large value of the Coulomb logarithm in a turbulent plasma results in plasma states in which, on the one hand, the plasma particle distribution function can be regarded as being nearly Maxwellian and, on the other hand, the plasma can be regarded as a strongly nonequilibrium medium. Let us illustrate this seemingly paradoxical situation using a simple example. We consider the distribution function of the form

$$f = f_0 + \delta f, \quad \delta f = \epsilon e^{-\psi} f_0 \ln f_0, \tag{A1.7}$$

where f_0 is a Maxwellian distribution function, ϵ is a small quantity, and an arbitrary velocity-dependent function ψ ensures that the correction δf decreases sufficiently sharply at high velocities. The entropy of a plasma with the distribution function f has the form

$$S_B = -\int f \ln f \, d\mathbf{v}, \tag{A1.8}$$

so that we have

$$\begin{aligned} S_B[f] - S_B[f_0] &= -\epsilon \int e^{-\psi} f_0 \ln^2 f_0 \, d\mathbf{v} \\ &\quad - \epsilon \int e^{-\psi} f_0 \ln f_0 \, d\mathbf{v} + O(\epsilon^2), \end{aligned} \tag{A1.9}$$

which indicates that the correction to the distribution function is on the order of $\epsilon f_0 \ln f_0$, while the entropy changes due to this correction by an amount $\epsilon f_0 \ln^2 f_0$. Consequently, at large values of the Coulomb logarithm, i.e., of the quantity $\ln(1/f_0)$, a situation is possible in which the correction to the distribution function is small and the change in the entropy is large.

However, we should make an important remark. For the prescribed mean kinetic energy and plasma density, the plasma entropy is maximum in the thermally equilibrium state. In other words, for each variation of the distribution function such that the mean kinetic energy and the plasma density both remain unchanged, the first variation of the entropy vanishes. Consequently, the first variation δf of the distribution function in (A1.7) should certainly change either the plasma temperature or the plasma density. However, this circumstance is unimportant for the above analysis, the more so since, in a turbulent plasma, these plasma parameters experience strong fluctuations.

We thus arrive at the following fundamentally important conclusion: in the range $D \ll 1$, the distribution functions of plasma particles can be assumed to be

Maxwellian, in which case, according to (A1.5) and (A1.6), the transport coefficients may exceed their thermodynamically equilibrium values by many orders of magnitude because of the large number of particles inside the Debye sphere.

APPENDIX 2

We consider a test particle with charge Z_0, mass M, and velocity v directed along the z-axis. Let the test particle move in a plasma consisting of electrons with charge e and mass m_e and ions with charge Z and mass m_i. For brevity, we assume that the particle velocity v is much higher than both the electron and ion thermal velocities. According to [14], on time scales τ such that $\tau < r_D/v$, where r_D is the Debye radius, the distribution function describing the change $\Delta\mathbf{p}$ in the momentum of a test particle on the time scale τ has the form

$$f_\tau(\Delta\mathbf{p}) = \int p(\mathbf{u})\exp[i(\mathbf{u}, \Delta\mathbf{p})]\frac{d\mathbf{u}}{(2\pi)^3}, \qquad \text{(A2.1)}$$

where $p(\mathbf{u}) = \exp[nU_e(\mathbf{u})]\exp[nU_i(\mathbf{u})]$ and

$$U_e = -\frac{2\pi Z_0^2 e^4 \tau}{v}u_z^2$$

$$-\frac{\pi Z_0^2 e^4 \tau}{v}(u_x^2 + u_y^2)\ln\left[\frac{v^4\tau^2}{Z_0^2 e^4 (u_x^2 + u_y^2)}\right],$$

$$U_i = -\frac{2\pi Z_0^2 Z^2 e^4 \tau}{v}u_z^2$$

$$-\frac{\pi Z_0^2 Z^2 e^4 \tau}{v}(u_x^2 + u_y^2)\ln\left[\frac{v^4\tau^2}{Z_0^2 Z^2 e^4 (u_x^2 + u_y^2)}\right].$$

Expression (A2.1) was derived exclusively from Newton's second law by evaluating the momentum transferred from plasma particles to the test particle [14] under the assumption of straight-line motion of the test particle (this assumption is valid on time scales much shorter than the mean free time of a test particle). Since the characteristic function of the test particle is represented as a product of the characteristic functions describing its scattering by electrons and ions, the scattering events by electrons are statistically independent of those by ions. For this reason, we restrict ourselves to considering the distribution function for the momentum transferred only from the electrons to the test particle:

$$f_\tau^{(e)} = \int \exp[nU_e(\mathbf{u}) - i(\mathbf{u}, \Delta\mathbf{p})]\frac{d\mathbf{u}}{(2\pi)^3}. \qquad \text{(A2.2)}$$

For completeness, note that, since the distribution function $f_\tau^{(i)}$ for the momentum transferred from the ions is similar in form to (A2.2),

$$f_\tau^{(i)} = \int \exp[nU_i(\mathbf{u})/Z - i(\mathbf{u}, \Delta\mathbf{p})]\frac{d\mathbf{u}}{(2\pi)^3},$$

the distribution function $f_\tau(\Delta\mathbf{p})$ for the total momentum transferred to the test particle is defined as a convolution of the distribution functions for the momenta transferred from electrons and ions:

$$f_\tau(\Delta\mathbf{p}) = \int f_\tau^{(i)}(\Delta\mathbf{p} - x) f_\tau^{(e)}(\mathbf{x})d\mathbf{x}.$$

The function $f_\tau^{(e)}$ can be investigated analytically. After performing the necessary manipulations, we can see that a portion of this function is Gaussian in shape,

$$f_\tau^{(e)}(\Delta\mathbf{p}) = \frac{1}{(2\pi)^{3/2}p_0^2 p_1}\exp\left(-\frac{p_z^2}{2p_1^2} - \frac{p_x^2 + p_y^2}{2p_0^2}\right), \qquad \text{(A2.3)}$$

where $p_x^2 + p_y^2 < 2p_0^2\ln(\Lambda/4)$, Λ is defined as a solution to the equation $\Lambda = \ln[2\pi\Lambda n(v\tau)^3] \gg 1$, $p_0^2 = (2\pi n Z_0^2 e^4 \Lambda\tau)/v$, and $p_1^2 = 2p_0^2/\Lambda$. The tail of this function characterizes the transfer of the transverse momentum and obeys the power law

$$f_\tau^{(e)}(\Delta\mathbf{p}) = \frac{1}{\pi\sqrt{2\pi}}\exp\left(-\frac{p_z^2}{2p_1^2}\right)\frac{p_1}{(p_x^2 + p_y^2)^2}, \qquad \text{(A2.4)}$$

where $p_x^2 + p_y^2 > 2p_0^2\ln(\Lambda/4)$ and $\Delta\mathbf{p} = (p_x, p_y, p_z)$.

The Gaussian portion of the distribution function (A2.3) and the power-law tail (A2.4) form via different mechanisms. The Gaussian portion stems from numerous scattering events each characterized by a small amount of the momentum transferred, i.e., from the scattering of the test particle by fluctuations of the electric self-field of the plasma. The power-law tail is governed by binary collisions between particles with small impact parameters, so that the tail is actually extended to the maximum possible amount of the momentum transferred in a binary collision event (i.e., an amount of about $p^* \sim 2m_e v$) rather than to infinity. Parenthetically, if $p^{*2} < 2p_0^2\ln(\Lambda/4)$, then the power-law tail is completely absent.

Note that, for the Gaussian portion of the distribution function (A2.3), the second moment of the momentum transferred is equal to

$$\langle(\Delta\mathbf{p})^2\rangle_G = \frac{4\pi n Z_0^2 e^4 \tau}{v}\ln[2\pi\Lambda n(v\tau)^3]. \qquad \text{(A2.5)}$$

The power-law tail is governed by a very small fraction of the total number of plasma particles (on the order of $1/\Lambda\ln(\Lambda/4)$); however, this fraction makes a large contribution to the second moment:

$$\langle(\Delta\mathbf{p})^2\rangle_t = \frac{4\pi n Z_0^2 e^4 \tau}{v}\ln\left[\frac{m_e^2 v^3}{\pi n e^4 Z_0^2 \tau\Lambda\ln(\Lambda/4)}\right]. \qquad \text{(A2.6)}$$

Let us calculate the distribution function for the momentum transferred on time scales $\tau \gg r_D/v$, on which it is necessary to take into account Debye screening. In other words, under the assumption that the electric field at a given point is created by the particles that occur at distances shorter than the Debye radius from it, the distribution function can be calculated at most to logarithmic accuracy. A simple analysis shows that, in calculations, it is sufficient to replace the functions U_e and U_i in (A2.1) and (A2.2) with the new functions $U_e^{(D)}$ and $U_i^{(D)}$ defined as

$$U_e^{(D)} = -\frac{\pi Z_0^2 e^4 \tau}{v}(u_x^2 + u_y^2)\ln\left(\frac{r_D^2 v^2}{Z_0^2 e^4 (u_x^2 + u_y^2)}\right), \quad \text{(A2.7)}$$

$$U_i^{(D)} = -\frac{\pi Z_0^2 Z^2 e^4 \tau}{v}(u_x^2 + u_y^2) \times \ln\left[\frac{r_D^2 v^2}{Z_0^2 Z^2 e^4 (u_x^2 + u_y^2)}\right]. \quad \text{(A2.8)}$$

The distribution function $f_\tau^{(e)}$ for the momentum transferred from the electrons can be calculated in an explicit form:

$$f_\tau^{(e)}(\Delta\mathbf{p}) = \frac{1}{2\pi p_0^2}\delta(p_z)\exp\left(-\frac{p_x^2 + p_y^2}{2p_0^2}\right), \quad \text{(A2.9)}$$

where $p_x^2 + p_y^2 < 2p_0^2 \ln(L/4)$, $L = \ln(2\pi L r_D^2 v\tau) \gg 1$, and $p_0^2 = (2\pi n Z_0^2 e^4 L\tau)/v$. The power-law tail, which characterizes the transfer of the transverse momentum, has the form

$$f_\tau^{(e)}(\Delta\mathbf{p}) = \frac{2}{\pi L}\delta(p_z)\frac{p_0^2}{(p_x^2 + p_y^2)^2}, \quad \text{(A2.10)}$$

where $p^{*2} > p_x^2 + p_y^2 < 2p_0^2 \ln(L/4)$ and $\Delta\mathbf{p} = (p_x, p_y, p_z)$.

On time scales $\tau > \tau^* = m_e^2 v^3/[L\ln(L/4)\pi n e^4 Z_0^2]$ such that $p^{*2} < 2p_0^2 \ln(L/4)$, the power-law tail of the asymptotic distribution function (A2.10) is completely absent.

We emphasize that the time scale τ^* is parametrically shorter than the mean free time of a test particle in a plasma. This circumstance guarantees the applicability of our approach on such time scales. We draw attention to the factor $\delta(p_z)$ in (A2.9) and (A2.10). This δ-function has a clear physical meaning: inside the Debye sphere, the plasma potential experiences fluctuations, thereby changing the kinetic energy of a particle and leading to a Gaussian distribution over p_z in (A2.3) and (A2.4). However, the fluctuations of the kinetic energy and p_z, which are driven by the fluctuating plasma potential, do not grow on time scales τ such that $\tau > r_D/v$. When these fluctuations become much less intense than the transverse fluctuations of the momentum, the above δ-function appears in the corresponding approximate expressions. The energy losses (the friction force) should be calculated with allowance for both the fluctuation and polarization electric fields; i.e., the losses should be calculated to higher orders in the coupling constant [16].

On time scales $r_D/v < \tau < \tau^*$, the calculated second moments associated with the Gaussian portion of the distribution function (A2.9) and with the power-law tail have the form

$$\langle(\Delta\mathbf{p})^2\rangle_G = \frac{4\pi n Z_0^2 e^4 \tau}{v}\ln(2\pi L n r_D^2 v\tau), \quad \text{(A2.11)}$$

$$\langle(\Delta\mathbf{p})^2\rangle_t = \frac{4\pi n Z_0^2 e^4 \tau}{v}\ln\left[\frac{m_e^2 v^3}{\pi n Z_0^2 \tau L\ln(L/4)}\right]; \quad \text{(A2.12)}$$

on time scales $\tau > \tau^*$, the second moments are

$$\langle(\Delta\mathbf{p})^2\rangle_G = \frac{4\pi n Z_0^2 e^4 \tau}{v}\ln(2\pi L n r_D^2 v\tau) \quad \text{(A2.13)}$$

and $\langle(\Delta\mathbf{p})^2\rangle_t = 0$ (the latter stems from the fact that, on such time scales τ, the power-law tail is completely absent).

The total second moment of the momentum transferred is a sum of the contributions from the Gaussian portion of the distribution function and its power-law tail:

$$\langle(\Delta\mathbf{p})^2\rangle = \frac{4\pi n Z_0^2 e^4 \tau}{v}\ln\left(\frac{2m_e^2 v^6 \tau^2}{e^4 Z_0^2 \ln(\Lambda/4)}\right) \quad \text{(A2.14)}$$

for $\tau < r_D/v$,

$$\langle(\Delta\mathbf{p})^2\rangle = \frac{4\pi n Z_0^2 e^4 \tau}{v}\ln\left(\frac{2m_e^2 v^4 r_D^2}{e^4 Z_0^2 \ln(L/4)}\right) \quad \text{(A2.15)}$$

for $r_D/v < \tau < \tau^*$,

$$\langle(\Delta\mathbf{p})^2\rangle = \frac{4\pi n Z_0^2 e^4 \tau}{v}\ln(2\pi L n r_D^2 v\tau) \quad \text{(A2.16)}$$

for $\tau^* < \tau$.

According to (A2.14)–(A2.16), the process of momentum transfer can be regarded as being Markovian only on time scales $r_D/v < \tau < \tau^*$. The momentum transfer on short time scales $\tau < r_D/v$ is always strongly non-Markovian. On long time scales $\tau > \tau^*$, the contribution of non-Markovian effects to the second moment of the momentum transferred is governed by the value of the parameter $M^2\ln(L/4)/m_e^2$; however, we will not consider this point in more detail. The non-Markovian

behavior is always associated with a certain memory effect. The non-Markovian (nondiffusive) character of scattering on short time scales was first discovered by Kogan [15], who attributed this effect to the fact that the plasma particles remember information about their mean free paths. The non-Markovian behavior on long time scales [see (A2.16)] is explained by the fact that the Gaussian portion of the distribution function remembers the mean free time of a particle. On long time scales $\tau > \tau^*$, the Gaussian portion extends over the entire region of the power-law tail, which "shadows" the role of the non-Markovian character of the scattering of majority particles on intermediate time scales $r_D/v < \tau < \tau^*$.

It is of interest to note that the factors $\ln(\Lambda/4)$, $\ln(L/4)$, and L (which are parameters rather than numbers) in formulas (A2.14)–(A2.16) clearly demonstrate the collective character of the argument of the Coulomb logarithm; moreover, keeping these factors in the arguments of the logarithmic functions does not imply going beyond the accuracy adopted in our study.

From the standpoint of our problem, of fundamental importance is the fact that, for mean free times longer than τ^*, the power-law tail, which reflects the role of binary collisions, completely disappears and the process by which the test particle acquires its transverse momentum can be described in terms of collective interactions with allowance for fluctuations. This is an illustrative example of a gentle formulation of the H-theorem, which was proved by one of us [9] and was used to derive relationship (23). The above simple example also illustrates the effect of long-term memory of the particles, which is an important issue because this effect naturally introduces time scales τ_R into problems of the theory of tokamak plasmas.

REFERENCES

1. B. B. Kadomtsev, Fiz. Plazmy **13**, 771 (1987) [Sov. J. Plasma Phys. **13**, 443 (1987)].
2. Yu. V. Gott and É. I. Yurchenko, Fiz. Plazmy **20**, 853 (1994) [Plasma Phys. Rep. **20**, 769 (1994)].
3. B. Coppi, Comments Plasma Phys. Controlled Fusion **5**, 261 (1980).
4. S. N. Gordienko and É. I. Yurchenko, Pis'ma Zh. Éksp. Teor. Fiz. **67**, 640 (1998) [JETP Lett. **67**, 668 (1998)].
5. S. N. Gordienko and É. I. Yurchenko, Fiz. Plazmy **25**, 752 (1999) [Plasma Phys. Rep. **25**, 689 (1999)].
6. *Reviews of Plasma Physics*, Ed. by M. A. Leontovich (Gosatomizdat, Moscow, 1963; Consultants Bureau, New York, 1963), Vol. 1.
7. J. Keiser, *Statistical Thermodynamics of Nonequilibrium Processes* (Springer-Verlag, Heidelberg, 1987; Mir, Moscow, 1990).
8. S. N. Gordienko, Fiz. Plazmy **23**, 754 (1997) [Plasma Phys. Rep. **23**, 698 (1997)].
9. S. N. Gordienko, Usp. Fiz. Nauk **169**, 653 (1999).
10. A. Shelest, *Bogolyubov's Method in the Dynamic Theory of Kinetic Equations* (Nauka, Moscow, 1989).
11. S. N. Gordienko and É. I. Yurchenko, Fiz. Plazmy **25**, 531 (1999) [Plasma Phys. Rep. **25**, 481 (1999)].
12. S. V. Mirnov, *Physicas Processes in Tokamak Plasmas* (Énergoatomizdat, Moscow, 1983).
13. A. M. Stefanovskiĭ, Yad. Sint. **5**, 217 (1965).
14. S. N. Gordienko, Pis'ma Zh. Éksp. Teor. Fiz. **70**, 469 (1999) [JETP Lett. **70**, 583 (1999)].
15. V. I. Kogan, Dokl. Akad. Nauk SSSR **135**, 1374 (1960) [Sov. Phys. Dokl. **5**, 1316 (1960)].
16. D. V. Sivukhin, in *Reviews of Plasma Physics*, Ed. by M. A. Leontovich (Atomizdat, Moscow, 1964; Consultants Bureau, New York, 1968), Vol. 4.

Translated by G. Shepekina

Plasma Physics Reports, Vol. 26, No. 9, 2000, pp. 737–740. From Fizika Plazmy, Vol. 26, No. 9, 2000, pp. 788–792.

TOKAMAKS

Could Reversed-Field Pinches and Quasi-Helical Stellarators Benefit from Transport Suppression in Tokamaks?[1]

V. V. Yankov* and J. Nycander

Department of Technology, Euratom-NFR Fusion Association, Uppsala University, Box 534, 75121 Uppsala, Sweden

**Permanent address: Russian Research Centre Kurchatov Institute, pl. Kurchatova 1, Moscow, 123182 Russia*

Received May 28, 1997; in final form, April 24, 2000

Abstract—The trapped particle theory of turbulent transport successfully explains key features of tokamak transport: the canonical L-mode, supershort plasma profiles, and the transport suppression by negative magnetic shear and poloidal rotation. Here, this theory is applied to reversed-field pinch (RFP) profiles, which can be justified if the magnetic fluctuations are suppressed, and to stellarators. A canonical density profile for RFPs is suggested, and it is found that no analogue of the transport suppression by negative shear in tokamaks is possible in RFPs. In quasi-helical stellarators, on the other hand, it appears possible to create an analogue of the tokamak reversed shear mode in the entire plasma volume. © *2000 MAIK "Nauka/Interperiodica".*

1. INTRODUCTION

Tokamaks, quasi-helical stellarators, and reversed-field pinches (RFP) have different MHD stability properties but similar magnetic topology: the magnetic field lines are placed on nested tori, and the drift Hamiltonian has one invariant direction. This means that the turbulent transport due to drift instabilities probably has a common nature in these devices [1]. Recently, a dramatic improvement of the confinement was observed in tokamaks with reversed magnetic shear [2–6]. The aim of the present paper is to discuss whether a similar confinement mode could also be realized in stellarators and RFPs. We find that this should be possible in stellarators but not in RFPs.

There is a wide variety of turbulent transport models for tokamaks, and agreement about many principal questions is absent (see reviews [1, 7]). Our basic assumption is that turbulent transport (like collisional transport) is dominated by trapped particles, as was suggested by Kadomtsev and Pogutse [8] and supported by recent simulations [9]. Together with the hypothesis that the plasma is frozen in the poloidal magnetic field, this gives simple and natural explanations of three confinement modes in tokamaks.

(i) The particle pinch and the canonical profiles in L-mode and supershots in a tokamak with conventional positive magnetic shear are explained by the expansion of a plasma parcel as it drifts outward [10, 11].

(ii) The transport suppression by reversed shear is a result of the plasma being in a minimum energy state, because, in this case, it is compressed as it drifts outward [12].

(iii) The H-mode is explained by the absence of trapped ions in a poloidally rotating plasma [13–15].

The trapped particles are poorly confined because they are not frozen in the toroidal magnetic field and can drift outward under the influence of electrostatic forces even in a perfect magnetic field [8]. The result of this convection is a kind of attractor, or marginally stable relaxed state, which we call turbulent equipartition (TEP) [10, 11]. In general, TEP is a state in which the Lagrangian invariants are uniformly mixed. (The well-known Taylor theory of plasma relaxation in RFPs is based on the conservation of helicity [16], but since helicity is not a Lagrangian invariant, that model is not a case of TEP.)

The frozen-in law of the poloidal magnetic field implies the existence of a Lagrangian invariant L. A rigorous formulation can be obtained from the drift Vlasov equation [11, 17]:

$$dL/dt = 0, \quad L = \frac{rn_{\mu,J}}{B_\theta}, \tag{1}$$

where $n_{\mu,J}$ is the volume density of trapped particles with fixed values of μ and J (the two first adiabatic invariants of the trapped particles) and r is the minor radius. Uniform mixing of the Lagrangian invariant leads to the radial profile $n_{\mu,J} \sim B_\theta/r$ (L = const).

The same result can be formulated in fluid language. It is known that even a small deviation from the potential nature of the pressure forces violates the ideal frozen-in law on the transport time scale. The poloidal direction is not invariant in a tokamak, and the poloidal torque destroys the toroidal component of the frozen-in law. The fluid Lagrangian invariant follows from Eq. (1) by eliminating indices:

$$L = nr/B_\theta. \tag{2}$$

The Lagrangian invariant (2), as well as its counterpart in RFPs and stellarators, is the principal tool of our

[1] This article was submitted by the authors in English.

1063-780X/00/2609-0737$20.00 © 2000 MAIK "Nauka/Interperiodica"

consideration. As opposed to Eq. (1), it has not been rigorously derived, but we believe that its use in simple considerations is still justified by the success of this procedure in explaining the three tokamak confinement modes, as will now be described.

Mixing of L leads to the TEP profile

$$n \sim B_\theta / r. \tag{3}$$

Another interpretation of this result can be useful. If the mechanical part of the toroidal momentum $p_\varphi = mv_\varphi + eA_\varphi/c$ is neglected, profile (3) represents the quasilinear plateau on the toroidal distribution function, $df(p_\varphi)/dp_\varphi = 0$ [17].

In tokamaks, the toroidal magnetic field varies little and the poloidal magnetic field can be expressed through the safety factor. Profile (3) can then be written as $n \sim B_\theta/r \sim q^{-1}$. This formula is well supported by experimental data, which are presented in [17, 18]. More data are collected in [19]. For TFTR supershots, which are not flattened by sawtooth oscillations, nq is constant to within 10–20% [18, 19]. A correlation between the L-mode q-profiles and the density and temperature profiles (the peaking of the density and temperature profile increases with increasing $1/q$ peaking) is a typical feature of many tokamaks and was observed long ago [20].

An additional indication of the crucial role of trapped particles for turbulent transport is the strong suppression of transport by reversed magnetic shear that has been observed in simulations [9] and several recent tokamak experiments [2–4]. This is easily understood from the invariance of $L = (nr/B_\theta) \approx nq$, which implies that the density and, as a result of adiabatic compression, the temperature of a plasma parcel increase outward instead of inward if the shear is reversed [12, 17]. This analogue of a magnetic well suppresses turbulent convection.

Usually only the shear of the $\mathbf{E} \times \mathbf{B}$ drift [21] is discussed as the reason for the transport suppression in the H-mode [22, 23] and for internal transport barriers [24]. However, if the trapped ions (which are the reason for transport) are eliminated by poloidal rotation [13, 14], a transport barrier is the natural consequence. This prediction is in agreement [15] with observations, which supports our view that the transport is dominated by the trapped particles.

2. REVERSED-FIELD PINCHES

According to a widely accepted explanation, magnetic fluctuations are the principal reason for transport in RFPs. Recently, improved confinement in RFP plasmas was achieved by suppression of sawtooth oscillations in the Madison Symmetric Torus (MST) [25] and by suppression of magnetic field fluctuations in TPE-1RM20 [26]. In both experiments, the energy confinement time was three times larger than the usual value. If the magnetic fluctuations can be suppressed, weaker mechanisms like drift instabilities, which are assumed to be the principal reason for turbulent transport in tokamaks [8, 9], will have a significant impact. In this section, we study how models for drift turbulence transport in tokamaks can be applied to current or future RFP experiments, assuming that the magnetic turbulence can be suppressed.

Taylor's theory of plasma relaxation [16] gives the following minimum magnetic energy configuration for RFPs:

$$B_\theta = \alpha J_1(r), \quad B_\phi = \alpha J_0(r), \tag{4}$$

where J_0 and J_1 are the Bessel functions. This solution is well supported by experiments. The Lagrangian invariant (2) is the same as in tokamaks, and we obtain the TEP profile

$$n \sim B_\theta/r \sim J_1(r)/r\,. \tag{5}$$

Unlike in tokamaks, the toroidal field varies significantly over the plasma cross section, and the density profile (5) therefore does not have a simple relation to the magnetic shear.

How does (5) compare with observations? The experimental density profiles in RFPs vary strongly and are generally assumed to be dominated by magnetic activity [27]. In two recent experiments, magnetic activity was suppressed [25, 26], but density profiles were reported only for TPE-1RM20 [26]. It was observed that the plasma electron density profiles are bell-shaped (Fig. 11 of [26]) and the central-chord averaged electron density increases with the pinch parameter $B_\theta(a)/\langle B_\varphi \rangle$ (the ratio of the poloidal magnetic field at the plasma surface to the volume averaged toroidal magnetic field, cf. Fig. 4 of [26]). This does not contradict profile (5), but having only three chord measurements does not allow a detailed comparison.

As noted above, a dramatic improvement of confinement has recently been observed in tokamaks with negative magnetic shear. However, the fundamental factor is not the sign of the magnetic shear *per se* but rather the sign of the radial derivative of the TEP density profile, since this determines whether a plasma parcel is compressed or expands if it drifts outward. For RFPs, the TEP profile (5) decreases outward and they are therefore analogous to tokamaks with the conventional positive shear.

To summarize, the canonical density profile $n \sim J_1(r)/r$ based on trapped particle theory does not contradict RFP experiments with suppressed magnetic activity. The transport suppression by negative magnetic shear observed in tokamaks would correspond to changing the sign of the derivative $d(J_1(r)/r)dr$ in RFPs, which does not seem realistic.

3. QUASI-HELICAL STELLARATORS

The magnetic field in stellarators is in general three dimensional and has no invariant direction. In this case,

there are two kinds of trapped particles: "toroidally trapped" and "helically trapped." In quasi-helical stellarators, which were suggested in [28], the canonical momentum has an invariant component and only one kind of trapped particle exists. Along the invariant direction, the magnetic field strength is constant. This leads to tokamak-like confinement of trapped particles and other advantages [29].

Since the drift Hamiltonian is invariant in one direction, we may assume that there is no net force in this direction, analogously to the absence of a net toroidal force in tokamaks. This leads to the suggestion that the plasma is frozen in the component $B_\perp$ of the magnetic field that is directed perpendicular to the invariant direction (analogously to the poloidal field in a tokamak). Then, the Lagrangian fluid invariant corresponding to (2) is

$$L = na/B_\perp, \quad (6)$$

where a is the minor radius defined as the square root of the volume inside the magnetic surface. (As for tokamaks, we have no rigorous derivation of this fluid invariant, but an invariant corresponding to Eq. (1) can be derived from the drift Vlasov equation for trapped particles.) The quantity $a/B_\perp$ is a specific volume, defined by the frozen-in law for $B_\perp$. Hence, if the analogue of magnetic shear in a tokamak is positive (i.e., $d(a/B_\perp)da > 0$, as in a conventional tokamak), a plasma parcel that drifts outward will expand adiabatically. The released energy can drive an instability. Parcels of trapped particles that are displaced inward by the resulting turbulence are compressed, which should lead to the following TEP profile in quasi-helical stellarators:

$$n \sim B_\perp/a. \quad (7)$$

The analogue of reversed magnetic shear in a tokamak is

$$d(a/B_\perp)/da < 0. \quad (8)$$

If this is satisfied, a plasma parcel is compressed while drifting outward and its energy decreases inward instead of outward. Hence, if the pressure profile is peaked in the center, the plasma is in a minimum energy state. This leads to stability, as observed in tokamaks with negative magnetic shear.

Unfortunately, the quantity $a/B_\perp$ is a weak function of the magnetic surface in typical stellarators. Our recommendation is to create profiles where condition (8) is fulfilled globally. Perhaps, this would require a current in the plasma core. At the magnetic axis, a and $B_\perp$ both vanish. A strong gradient of the specific volume and particularly strong stability could be achieved by having $B_\perp = 0$ at an additional point near the axis or in the plasma core.

In the considerations above, the component $B_\perp$ of the magnetic field perpendicular to the invariant direction was not presented explicitly. Many coordinates are used in stellarators (a review is given in [30]). The condition of quasi-symmetry is that the magnetic field strength is constant along the quasi-symmetry direction. The unit vector **n** in this direction is given by [31]

$$\mathbf{n} = (F(\psi)\mathbf{B} + \mathbf{B} \times \nabla\psi)/|F(\psi)\mathbf{B} + \mathbf{B} \times \nabla\psi|. \quad (9)$$

Here, ψ and $F(\psi)$ are the external poloidal magnetic flux and the electric current, respectively.

If $B_\perp = 0$, then **B** is parallel to **n**, so that the magnetic field strength is constant along the magnetic field. This means that, on a magnetic surface where $B_\perp = 0$, there are very few trapped particles, which allows us to suggest an alternative beneficial regime for quasi-helical stellarators. If we have $B_\perp = 0$ near the plasma edge, a transport barrier without trapped particles can be created there. This is entirely analogous to the H-mode in tokamaks. (In that case, the absence of trapped particles in the transport barrier is caused by poloidal rotation.) If $B_\perp = 0$ near the plasma edge, the TEP profile (7) will be strongly peaked, which is also beneficial (but very different from the minimum energy state that would be possible if condition (8) were satisfied).

Modern stellarators are not quasi-symmetric. Nevertheless, we can try to check the TEP profile. The reason is that the approximate symmetries (both the helical and toroidal symmetries, which are essential for the two groups of trapped particles) have approximately constant $a/B_\perp$ and, therefore, lead to flat density profiles. Flat density profiles are really rather typical of stellarators [1], in contrast to tokamaks and RFPs.

4. CONCLUSION

Predictions of confinement in RFPs and quasi-helical stellarators have been carried out for the trapped particle dominated regime, as in tokamaks. The frozen-in law in the appropriate magnetic field component is the tool of analysis. The assumptions of the theory are poorly met in present RFPs and stellarators; nevertheless, the density profiles are typically bell-shaped in RFPs and flat in stellarators, in accordance with the theory.

If magnetic field fluctuations can be suppressed in future RFPs, the trapped particle instability can lead to the universal TEP profile (5). However, the stabilization by negative magnetic shear observed in tokamaks is not relevant for RFPs.

Quasi-helical stellarators are promising in many respects [29]. If, additionally, condition (8) is fulfilled, the radial dependence of the specific volume is reversed and the plasma is in a minimum energy state. The analogue of the magnetic shear stabilization in tokamaks is then possible in the entire plasma volume (whereas, in tokamaks, the shear cannot be reversed near the boundary). In this case, the turbulent transport could be suppressed globally. This is the principal suggestion of the present paper.

A different possibility for quasi-helical stellarators is to have $B_\perp = 0$ near the plasma edge (here, $B_\perp$ is the field component perpendicular to the invariant direction). In this way, one could create a transport barrier with very few trapped particles, analogously to the H-mode in tokamaks. As in tokamaks, trapped ions could also be eliminated by rotation, both in RFPs and in stellarators.

ACKNOWLEDGMENTS

V.V. Yan'kov is grateful to V.D. Pustovitov for discussion of Boozer's coordinates and quasi-helical symmetry. This work was supported by the Russian State Program "Fundamental Problems of Nonlinear Dynamics" and the European Communities under associated contract between Euratom and the Swedish Natural Science Research Council (NFR), grant nos. F-AA/FU/GU 09917-311 and F-AA/FU/GU 09917-312. This work was completed while V.V. Yan'kov was a guest researcher at the Department of Technology in Uppsala. He is grateful to the Swedish Institute for the support that made it possible to perform this study.

REFERENCES

1. F. Wagner and U. Stroth, Plasma Phys. Controlled Fusion **35**, 1321 (1993).
2. M. Hugon, P. Ph. van Milligen, P. Smeulders, *et al.*, Nucl. Fusion **32**, 33 (1992).
3. E. J. Strait, L. L. Lao, M. E. Mauel, *et al.*, Phys. Rev. Lett. **75**, 4421 (1995).
4. F. M. Levinton, M. C. Zarnstorff, S. H. Batha, *et al.*, Phys. Rev. Lett. **75**, 4417 (1995).
5. G. M. D. Hogeweij, A. A. M. Oomens, C. J. Barth, *et al.*, Phys. Rev. Lett. **76**, 632 (1996).
6. Y. Neyatani and the JT-60 Team, Plasma Phys. Controlled Fusion **38**, A181 (1996).
7. J. W. Conner and H. R. Wilson, Plasma Phys. Controlled Fusion **36**, 719 (1994).
8. B. B. Kadomtsev and O. P. Pogutse, in *Reviews of Plasma Physics*, Ed. by M. A. Leontovich (Atomizdat, Moscow, 1967; Consultants Bureau, New York, 1970), Vol. 5.
9. C. Kessel, J. Manickam, G. Rewoldt, and W. M. Tang, Phys. Rev. Lett. **72**, 1212 (1994).
10. V. V. Yankov, Pis'ma Zh. Éksp. Teor. Fiz. **60**, 169 (1994) [JETP Lett. **60**, 171 (1994)].
11. J. Nycander and V. V. Yankov, Phys. Plasmas **2**, 3874 (1995).
12. V. V. Yankov and J. Nycander, Comments Plasma Phys. Controlled Fusion **18**, 1 (1997).
13. H. L. Berk and A. A. Galeev, Phys. Fluids **10**, 441 (1967).
14. A. A. Galeev, R. Z. Sagdeev, and H. V. Wong, Phys. Fluids **10**, 1535 (1967).
15. J. Nycander and V. V. Yankov, Pis'ma Zh. Éksp. Teor. Fiz. **63**, 427 (1996) [JETP Lett. **63**, 448 (1996)].
16. J. B. Taylor, Phys. Rev. Lett. **33**, 1139 (1974).
17. V. V. Yankov, Fiz. Plazmy **21**, 759 (1995) [Plasma Phys. Rep. **21**, 719 (1995)].
18. V. V. Yankov and J. Nycander, Phys. Rev. Lett. **75**, 3582 (1995).
19. V. V. Yankov and J. Nycander, Phys. Plasmas **4**, 2907 (1997).
20. Yu. V. Esipchuk and K. A. Razumova, Plasma Phys. Controlled Fusion **28**, 1253 (1986).
21. H. Biglari, P. H. Diamond, and P. W. Terry, Phys. Fluids B **2**, 1 (1990).
22. F. W. Wagner, G. Becker, K. Behringer, *et al.*, Phys. Rev. Lett. **49**, 1408 (1982).
23. K. H. Burrell, T. N. Carlstrom, E. J. Doyle, *et al.*, Plasma Phys. Controlled Fusion **34**, 13 (1992).
24. Y. Koide, M. Kikuchi, M. Mori, *et al.*, Plasma Phys. Controlled Fusion **38**, 1011 (1996).
25. B. E. Chapman, A. F. Almagri, M. Cekic, *et al.*, Phys. Plasmas **3**, 709 (1996).
26. Y. Hirano, Y. Maejima, T. Shimada, *et al.*, Nucl. Fusion **36**, 721 (1996).
27. S. Hokin, private communication.
28. C. Nuhrenberg and R. Zille, Phys. Lett. A **129**, 113 (1988).
29. A. H. Boozer, Plasma Phys. Controlled Fusion **35**, A103 (1995).
30. V. D. Pustovitov and V. D. Shafranov, in *Reviews of Plasma Physics*, Ed. by V. V. Kadomtsev (Énergoizdat, Moscow, 1987; Consultants Bureau, New York, 1989), Vol. 15.
31. M. Yu. Isaev, M. I. Mikhaĭlov, and V. D. Shafranov, Fiz. Plazmy **20**, 357 (1994) [Plasma Phys. Rep. **20**, 319 (1994)].

Plasma Physics Reports, Vol. 26, No. 9, 2000, pp. 741–744. Translated from Fizika Plazmy, Vol. 26, No. 9, 2000, pp. 793–796.

MAGNETIC CONFINEMENT SYSTEMS

Plasma Equilibrium in Axisymmetric Open Divertor Configurations

V. V. Arsenin and A. Yu. Kuyanov

Institute of Nuclear Fusion, Russian Research Centre Kurchatov Institute, pl. Kurchatova 1, Moscow, 123182 Russia

Received December 23, 1999

Abstract—The equilibrium of a plasma with isotropic pressure in a periodic divertor configuration with a poloidal magnetic field is calculated. The issue of how the plasma equilibrium changes as the parameter $\beta \equiv 8\pi p/B^2$ increases is considered for a fairly representative class of pressure profiles $p(\psi)$ (where ψ is the flux coordinate). It is shown that the plasma can be in equilibrium up to β values (in terms of the vacuum magnetic field at the divertor axis) on the order of unity. © *2000 MAIK "Nauka/Interperiodica".*

1. INTRODUCTION

In the simplest (axisymmetric) version of open magnetic confinement systems (simple mirrors), a plasma can be in equilibrium up to $\beta = 8\pi p/B^2 \sim 1$; moreover, because of the symmetry, there are no neoclassical transverse transport in the plasma. This circumstance has stimulated interest in alternative confinement devices based on simple mirrors. Among such devices, there are open-ended systems, in which the longitudinal losses are fairly efficiently reduced by, e.g., electrostatic plugs (in a tandem mirror device), and closed systems with simple mirror cells aimed at confining the main plasma. In order to maintain the plasma in equilibrium and to reduce transverse losses, closed systems with mirror cells should be equipped with specially designed toroidal linking sections, but we do not consider this issue here. In axisymmetric confinement devices, the key problem is how to ensure MHD-stable equilibrium. Several methods have been proposed for plasma stabilization. The advantage of one of the simplest methods—divertor stabilization—is the possibility of placing stabilizers (divertors) at desired positions along the system [1–3]. In this connection, it is necessary to determine β values above which the divertor fails to stabilize the plasma. Since the magnetic field in the divertor region is depressed and there is a magnetic null line at the plasma boundary, the question regarding the maximum possible β values consistent with equilibrium naturally arises. Knowledge of the picture of equilibrium is also required to study the plasma stability.

Two approaches are customarily used to describe plasma equilibrium in axisymmetric systems. The first approach is based on the Grad–Shafranov equation in "rigid" (e.g., cylindrical) coordinates (see review [4]). Note that the magnetic configuration of an axisymmetric open system is purely poloidal (the toroidal magnetic field is absent). This approach, which is generally used to solve the problems with prescribed external currents, is convenient for calculating plasma equilibria in specific confinement systems. The second approach involves "inverse" flux coordinates (see, e.g., [5]), which are adequate for solving the MHD stability problem, and is better suited for studying problems with a prescribed outer boundary.

In this paper, we analyze plasma equilibrium produced by a prescribed set of ring current-carrying coils in a poloidal magnetic configuration with divertors. We treat the problem in the Grad–Shafranov formulation. We examine the equilibrium of a plasma with isotropic pressure, keeping in mind a system with longitudinal tandem plugging or a closed system. We reconstruct the picture of equilibrium for a fairly representative class of pressure profiles $p(\psi)$ (where ψ is the flux coordinate) and investigate how the plasma equilibrium changes as β increases. In order to simplify the boundary conditions imposed at the open ends (which, however, have essentially no impact on plasma equilibrium), we present the numerical results obtained for a periodic configuration.

2. FORMULATION OF THE PROBLEM

We describe a magnetic field configuration by the Grad–Shafranov equation for the flux function $\psi = rA_\theta$, where A_θ is the component of the vector potential:

$$\frac{\partial^2\psi}{\partial r^2} - \frac{1}{r}\frac{\partial\psi}{\partial r} + \frac{\partial^2\psi}{\partial z^2} = -4\pi r^2\frac{dp}{d\psi} - \frac{4\pi r}{c}j_{\text{ext}}. \qquad (1)$$

Here, the plasma pressure $p = p(\psi)$ is a given function and j_{ext} is the prescribed current density in the external coils. The external currents govern the vacuum configuration $\psi = \psi_v$. We represent the field as a superposition of the vacuum field and the field generated by the

1063-780X/00/2609-0741$20.00

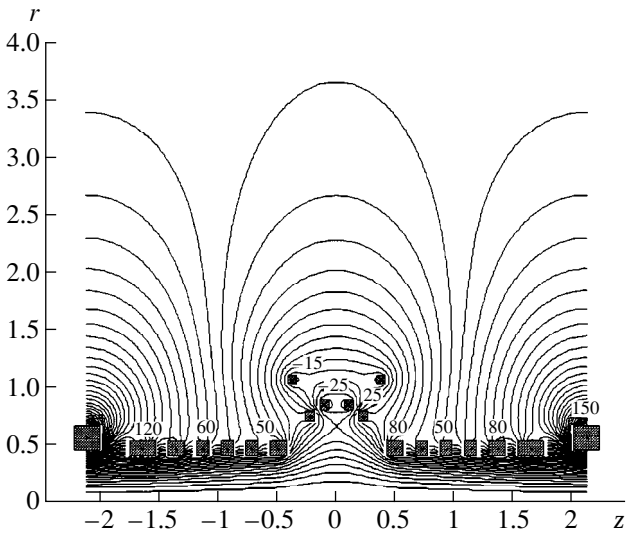

Fig. 1. Arrangement of ring current-carrying coils over a period along the z-axis and the lines ψ = const of the vacuum magnetic field. The current magnitudes in each coil are indicated.

plasma currents, $\psi = \psi_v + \psi_p$, to obtain the following equation for ψ_p:

$$\frac{\partial^2\psi_p}{\partial r^2} - \frac{1}{r}\frac{\partial\psi_p}{\partial r} + \frac{\partial^2\psi_p}{\partial z^2} = -4\pi r^2\frac{dp}{d\psi}, \qquad (2)$$

where $p = p\left(\dfrac{\psi_v + \psi_p}{\psi_s}\right)$ and the boundary value ψ_s is such that $p(\xi) = 0$ for $\xi \geq 1$.

If the system has finite dimensions along the z-axis, then the function $\psi_p(r, z)$ falls off to zero with distance from the plasma and has no singularities at the positions of the external coils:

$$\psi_p(\infty) = 0. \qquad (3)$$

If the system is periodic in z, then the spectrum of the field B_z can contain the zeroth Fourier harmonic, corresponding to the field of a uniform solenoid, in which case we have

$$\psi_p\big|_{r\to\infty} = \text{const}, \qquad (4)$$

with an unknown constant to be determined. Instead of (4), it is more convenient to impose another boundary condition. We consider a surface $r = R$ such that R is larger than the period L of the system. The nonzeroth Fourier harmonics of the field produced by plasma currents fall off exponentially toward this surface. For the zeroth Fourier harmonic, we have $\partial\langle\psi_p\rangle/\partial r = 0$. We supplement Eq. (2) with the boundary condition

$$\left.\frac{\partial\psi_p}{\partial r}\right|_{r=R} = 0. \qquad (5)$$

Calculations show that, even for $r = R$, the final results are weakly sensitive to the position $R \sim L$ of the surface.

At the system axis, the flux functions satisfy the conditions

$$\psi_v(0, z) = 0, \quad \psi_p(0, z) = 0. \qquad (6)$$

We assume that the configuration is symmetric about the $z = 0$ plane, where the field vanishes at a circle of radius $r = r_s$, which is the intersection of the plasma surface $\psi = \psi_s$ with the plane, so that we have

$$\left.\frac{\partial\psi}{\partial r}\right|_{z=0} = 0 \text{ for } \psi = \psi_s. \qquad (7)$$

In a prescribed vacuum field, the position of the circle, $r = r_s$, is known for $\beta = 0$.

We also assume that the configuration is symmetric about the $z = \pm L/2$ planes, so that

$$\left.\frac{\partial\psi}{\partial z}\right|_{z=\pm L/2} = 0. \qquad (8)$$

In order to cover a fairly broad class of pressure profiles, we choose

$$p(\psi) = p_0[1 - (\psi/\psi_s)^\gamma]^\alpha, \qquad (9)$$

which describes, in particular, a stable pressure profile near the separatrix at $\beta = 0$, $\gamma = 1$, and $\alpha \approx 0.55$ [2]. The parameter values presented below correspond to the ranges $\gamma, \alpha \geq 1$. In our analysis, we do not consider the limitations imposed by the plasma equilibrium on the power index α.

Maximum values of β_0 and $\beta_{L/2}$ and the relative displacement of the magnetic null line for these β values from the positions of the magnetic null line at $\beta = 0$ for different pressure profiles (9)

γ	α	β_0	$\beta_{L/2}$	$\delta r_s/r_s$
1	1	0.865	0.054	0.086
1	2	1.114	0.069	0.040
2	1	0.629	0.039	0.113
2	2	0.793	0.049	0.068

3. RESULTS OF CALCULATIONS

We calculated the vacuum field from the prescribed currents in discrete coils (Fig. 1). The magnetic null line was ensured by reversing the currents in the coils near the $z = 0$ plane.

Assuming that the system is periodic in z, we solved a difference analogue of Eq. (2) with the boundary conditions (5) and (6) iteratively with respect to the nonlinearity in the right-hand side. At each iteration step, we solved the corresponding linear equation using a method of expansion in Fourier series in the variable z and a sweep method in the radial direction and recalcu-

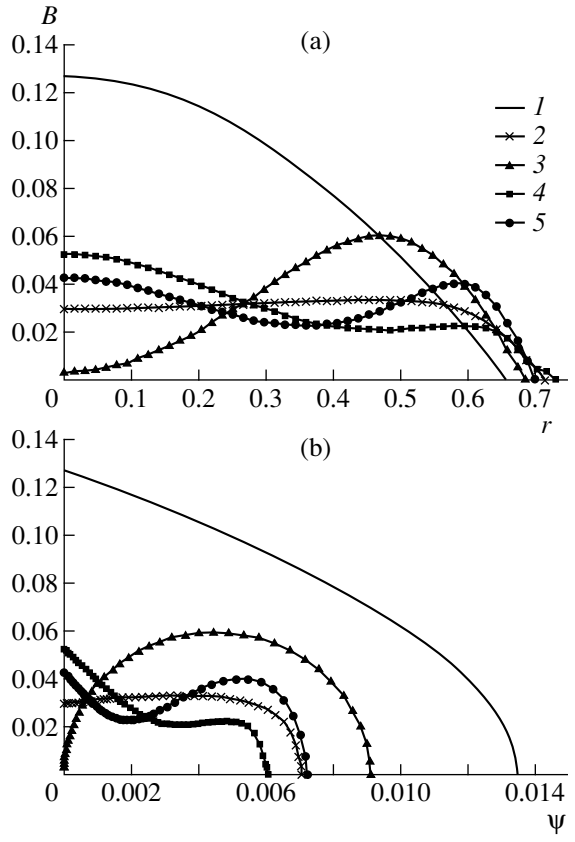

Fig. 2. Profiles of the magnetic field in the equatorial plane of a divertor as functions of (a) r and (b) ψ for different pressure profiles (9) with (*2*) $\gamma = 1$ and $\alpha = 1$ at $\beta_0 = 0.86$, (*3*) $\gamma = 1$ and $\alpha = 2$ at $\beta_0 = 1.114$, (*4*) $\gamma = 2$ and $\alpha = 1$ at $\beta_0 = 0.62$, and (*5*) $\gamma = 2$ and $\alpha = 2$ at $\beta_0 = 0.79$. Also shown are the vacuum field profiles (curves *1*).

lated the value of ψ_s in accordance with condition (7). The maximum possible β consistent with equilibrium was determined as a maximum value above which the iteration procedure started to diverge.

Calculations show that the plasma can be in equilibrium up to the value $\beta_0 \equiv 8\pi p_0/B_v^2(0, 0)$, which is on the order of unity. The maximum possible values of β_0 for several pressure profiles (9) and for a vacuum field shown in Fig. 1 are listed in the table, which also presents the relevant β values in terms of the vacuum field at the axis in mirror cells between the divertors, $\beta_{L/2} \equiv 8\pi p_0/B_v^2(0, L/2)$. Figure 2 shows profiles of the magnetic field in the equatorial plane of a divertor as functions of r (Fig. 2a) and ψ (Fig. 2b) for the same pressure profiles and for β close to its maximum value. In Fig. 3, we plot the magnetic field lines ψ = const for one of the pressure profiles.

As β increases, the magnetic null line is displaced in the radial direction. The displacement δr_s may be important from a practical standpoint because the increase in β makes it necessary to appropriately adjust

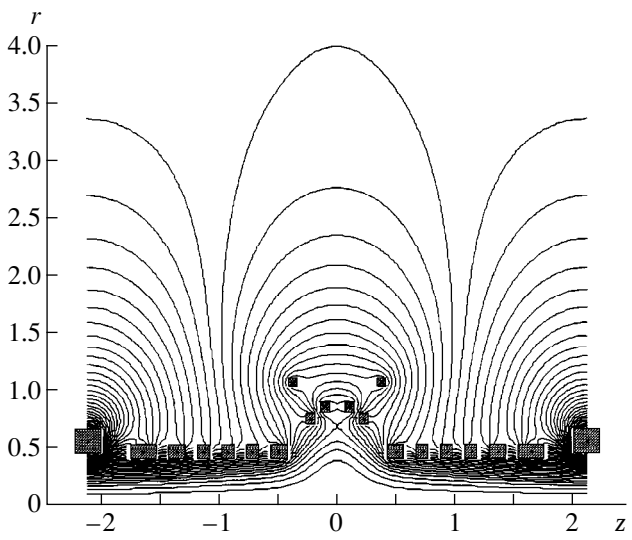

Fig. 3. Magnetic field lines for the pressure profile (9) with $\gamma = 1$ and $\alpha = 2$ at $\beta_0 = 1.11$.

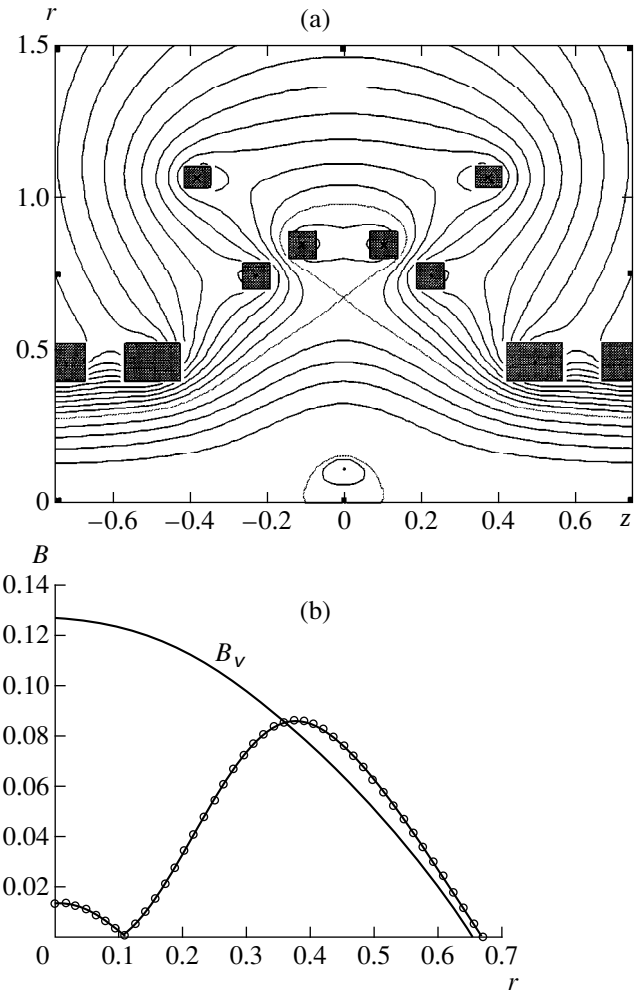

Fig. 4. Configuration with a reversed field for $\alpha = 4$ and $\gamma = 1$ at $\beta_0 = 1.265$: (a) field lines ψ = const and (b) radial profile of the magnetic field in the $z = 0$ plane. The vacuum field B_v is the same as in Fig. 1.

the injection system in order to control the spatial positions of the local regions where the plasma is heated. For the magnetic configuration under analysis, the displacement δr_s was found to be relatively small because of the fixed positions of closely spaced "divertor" coils with reversed currents (see the last column in the table). An increase in $\delta r_s/r_s$ with increasing γ can be explained as follows: the closer the region where the pressure gradient (and, accordingly, the diamagnetic current in the plasma) is maximum to the separatrix, the greater the extent to which the diamagnetic current distorts the vacuum field near the magnetic null line $\mathbf{B}_v = 0$. The separatrix can be made "undisplaced" (or fixed at, e.g., $r_s|_{z=0}$ or $r_s|_{z=L/2}$) by means of feedback from the currents in the external coils to the β value.

Calculations carried out for peaked pressure profiles ($\alpha = 4$, 5, and 6) also demonstrate the existence of equilibrium configurations with a magnetic field that is reversed in the vicinity of the point ($r = 0$, $z = 0$). Such equilibria were found to exist in a narrow range of beta values close to the maximum value of β_0. Figure 4 shows an example of an equilibrium configuration with $\alpha = 4$ and $\gamma = 1$. The ability to calculate equilibrium configurations with a reversed field indicates that our code, which was initially devised to describe "simple" equilibria analogous to those in Figs. 2 and 3 (without vanishing points for the magnetic field at the axis), can be successfully applied to calculate nonparaxial equilibrium plasma configurations in axisymmetric open systems.

4. CONCLUSION

We have established that, within the chosen class of pressure profiles $p(\psi)$, the maximum β values that can be achieved in equilibrium configurations are on the order of unity.

For peaked pressure profiles, we have calculated equilibrium configurations with a magnetic field that is reversed at the axis.

It remains a challenge to find out whether MHD stable configurations with $\beta \sim 1$ can exist.

ACKNOWLEDGMENTS

This work was supported in part by the Russian Foundation for Basic Research, project no. 96-15-96815 (under the program "Leading Scientific Schools").

REFERENCES

1. B. Lane, R. S. Post, and J. Kesner, Nucl. Fusion **27**, 277 (1987).
2. V. P. Pastukhov and A. Yu. Sokolov, Fiz. Plazmy **17**, 1043 (1991) [Sov. J. Plasma Phys. **17**, 603 (1991)]; A. Yu. Sokolov, Fiz. Plazmy **18**, 657 (1992) [Sov. J. Plasma Phys. **18**, 343 (1992)].
3. R. S. Post, K. Brau, J. Casey, *et al.*, in *Proceedings of the 12th International Conference on Plasma Physics and Controlled Nuclear Fusion Research, Nice, 1988* [Nucl. Fusion Suppl. **2**, 493 (1989)].
4. V. D. Shafranov, in *Reviews of Plasma Physics*, Ed. by M. A. Leontovich (Gosatomizdat, Moscow, 1963; Consultants Bureau, New York, 1966), Vol. 2.
5. L. M. Degtyarev and V. V. Drozdov, Comput. Phys. Rep. **2**, 341 (1985).

Translated by O. Khadin

Plasma Physics Reports, Vol. 26, No. 9, 2000, pp. 745–758. Translated from Fizika Plazmy, Vol. 26, No. 9, 2000, pp. 797–810.

PLASMA DYNAMICS

Study of Hydrodynamic Instabilities of a Z-Pinch during a High-Current Explosion of a Thin Wire

S. Yu. Gus'kov*, G. V. Ivanenkov*, A. R. Mingaleev*, V. V. Nikishin, S. A. Pikuz*, V. B. Rozanov*, W. Stepniewski***, V. F. Tishkin**, D. A. Hammer****, and T. A. Shelkovenko***

** Lebedev Institute of Physics, Russian Academy of Sciences, Leninskiĭ pr. 53, Moscow, 117924 Russia*

*** Institute of Mathematical Modeling, Russian Academy of Sciences, Miusskaya pl. 4a, Moscow, 125047 Russia*

**** Kaliski Institute of Plasma Physics and Laser Microfusion, Warsaw 49 Hery 23, Poland*

***** Laboratory of Plasma Studies, 369 Upson Hall, Cornell University, Ithaca, NY 14853 USA*

Received April 22, 1999; in final form, January 17, 2000

Abstract—Results are presented from laboratory and numerical experiments on the influence of the core and associated hydrodynamic instabilities on the high-current implosion of a plasma of exploding metal wires. The experimental investigation of the discharge structure was carried out using the multiframe X-ray backlighting technique with high temporal and spatial resolution (<1 ns and 1 μm, respectively); X-pinches were used as small-sized radiation sources. The implosion of a dense Z-pinch was modeled by the free-point method with the use of a two-dimensional radiative MHD code. The onset of instabilities at the corona–core boundary was modeled by the NUTCY Eulerian code. The results show that hydrodynamic processes in the core are primarily responsible for the formation of small bright regions observed in X-rays. After the reflection of a shock wave from the axis, the rapid onset of hydrodynamic instabilities can occur at the corona–core boundary. © *2000 MAIK "Nauka/Interperiodica"*.

1. INTRODUCTION

Exploding-wire discharges have been investigated for a long time. Here, we only mention the relevant work [1] and the studies on high-current radiating discharges related to laser engineering (see, e.g., [2]). Modern high-voltage generators make it possible to carry out experiments with dense Z-pinches in which a high-temperature radiating plasma is produced with multiterawatt megaampere current pulses. Among all the types of loads, the highest plasma parameters have been achieved in discharges through thin metal wires (solitary filaments, multiple-wire liners, and X-pinches). This makes it possible to use discharges such as hard UV and soft X-ray sources, thereby extending the capabilities of the spectroscopy of multiply charged ions, X-ray optics, and lithography. Their applications in controlled fusion, laboratory modeling of the action of high-power X-ray pulses, and production of inverse-population media for short-wavelength lasers are also studied. In particular, a number of methods were proposed for laser pumping with the help of dense Z-pinches. Finally, X-pinches have recently found a new application as small-sized short-duration X-ray sources in the backlighting technique used to diagnose dense Z-pinches; this technique is also used in this study. The demand for comprehensive studies of nanosecond exploding-wire discharges is also supported by the fact that the processes occurring in such discharges are closely related to the dynamics of laser plasmas.

The studies [3] carried out with the help of a novel technique of multiframe X-ray backlighting have revealed a number of interesting features of nanosecond electric explosions of thin (several tens of microns in diameter) wires, clearly demonstrating the heterogeneous structure of such discharges. It turned out that deep in the plasma corona, arising during the shunting breakdown of the products of metal evaporation (which is usually studied by optical methods), there is a dense cold core formed on the axis of the discharge at the beginning of the explosion.[1] The corona–core boundary is rather sharp. Further studies have shown that the core is a liquid column boiling over its entire volume during the breakdown [4]. At the corona–core boundary, strong perturbations with amplitudes comparable to the core radius arise [5]. These perturbations are interpreted as a consequence of the Rayleigh–Taylor and Richtmayer–Meshkov hydrodynamic instabilities, which, in the nonlinear stage, give rise to the Kelvin–Helmholz instability. Along with these perturbations, constrictions typical of pinches are formed.

Because of the complicated dynamic structure, the exploding wires occupy a special place in the class of dense pinches. The study of such a complicated structure, may provide a new way of investigating the behavior of a plasma with high density gradients by examin-

[1] Only the best conductors, such as Al, Cu, Ag, and Au, can be completely evaporated during an explosion.

1063-780X/00/2609-0745$20.00 © 2000 MAIK "Nauka/Interperiodica"

ing hydrodynamic instabilities. High densities of released energy (100 TW/cm^2 and higher) and a short discharge duration ($\simeq$100 ns) are similar to the relevant characteristics of laser plasmas. However, unlike the planar or spherical symmetry of targets, the cylindrical geometry of Z-pinches is more convenient for diagnosing the regions where the instabilities arise. In comparison with shock tubes, pinches are advantageous because they permit studies of instabilities under conditions of intense electron and radiative heat transport.

Hence, the problem of the hydrodynamic stability of heterogeneous Z-pinches becomes important for a general understanding of the physics of processes occurring not only in thin-wire discharges. Below, we employ two different models. The first model describes the compression of the central core by the pressure pulse arriving from the hot plasma, and the second one describes the surface effects. Currently, there is no unified approach for studying both global and surface effects. Hence, the analysis of the latter effects, associated with the forward and backward passage of a shock wave through the core, is of interest even if the problem is formulated in the simplest way. This is why we restrict ourselves to such a simple model.

2. GENERAL DESCRIPTION OF THE EFFECTS

In experiments, we used the X-ray backlighting technique. A detailed description of this technique is presented in [3, 5, 6]; here, we only outline its general characteristics. The experiments were carried out with the XP device at Cornell University (the pulse duration is 100 ns, and the current attains 500 kA) with a diagnostic complex for studying wire-discharge plasmas by the scheme mentioned above. A pair of X-pinches placed inside a diode was used as the source, and the load under study was placed in the return-current circuit. The choice of the material for X-pinches and the optimization of the source sizes allowed us to achieve a spatial resolution from one to several μm and a time resolution better than 1 ns in the spectral range from 1 to 5 Å.

A typical picture observed is illustrated in Fig. 1, which presents the images of the core of an exploded Ti wire (50 μm in diameter) and the surrounding coronal plasma. The images were obtained 49 and 68 ns from the start of the current. On both sides of the node, specially tied to fix the position, one can see the development of the core inhomogeneities. There are inhomogeneities with two characteristic scale lengths: "ripples" with wavelengths of 20–30 μm are modulated by the outer "envelope" (with a scale length of $\simeq$1 mm) of the corona–core boundary and the compression front. The enlarged fragments of the images (which are presented in the same figure) demonstrate the internal structure of the core. In the upper fragment (49 ns), the front moves toward the axis; behind the front, one can see perturbations of the boundary. At 68 ns, the front moves back after reflection from the axis and the perturbations inside are less pronounced than those ahead of it. In the lower fragment, the irregularities are seen only at the edge; one can also see a frontal cone arriving at the surface. With time, this area contracts, whereas in the expanded region where the front has already left the core mixing of the dense core substance with the corona plasma is observed.

This phenomenon can be explained by the prolonged existence of a heterogeneous structure in nanosecond wire discharges [3]. Its development for initial diameters of 10–50 μm was considered in [7]. This structure produces no effects, except for emission in the visible and soft UV spectral regions, until the front of MHD compression of the corona reaches the core. According to [5], the interaction between this wave and the core plays an important role in the formation (and, consequently, emission) of hot points emitting intense soft X radiation from regions 20–30 μm in size on the plasma axis. Further studies [4] showed that the core substance is in the state of a boiling liquid metal. As before, we can see in Fig. 2 how the shock-wave front propagates through the core; however, due to a more detailed resolution of the structural elements, we can detect the presence of many vapor bubbles and capillary effects. Splashes of liquid at the points where the bubbles arrive at the corona–core boundary are also seen. This leads us to the conclusion that such effects may be attributed to the generation of perturbations during the interaction between the core and the compression front.

This interaction begins when the compressed coronal plasma collides with the dense core, which expands slowly by inertia after the initial explosion. In gasdynamics, a similar process is known as a particular case of the decay of a discontinuity: instead of a single shock wave incident from the corona side, a shock wave passing to the core and a shock wave reflected from the boundary appear. The boundary is then transformed into a contact discontinuity moving toward the axis. The megabar pressure in the corona is high enough for hydrodynamic compression of the dense central region to occur. After the reflection of the shock wave from the axis, conditions arise under which the boundary becomes unstable. The details of this process depend largely on the initial irregularities present at the corona–core boundary and compression front. As a whole, this situation is similar to the acceleration of targets by laser pulses, when the hot corona evaporated from the target surface accelerates the cold internal core [8].

Obviously, this scheme is simplified and needs to be studied more thoroughly. Recent calculations [9, 10] by a modified free-point method have partly confirmed and complemented this scheme. However, the underlying physical model that provides a rather complete description of the processes of dissipation, ionization kinetics, and radiation transfer in a nonideal plasma cannot be regarded as being perfect. In this model, the

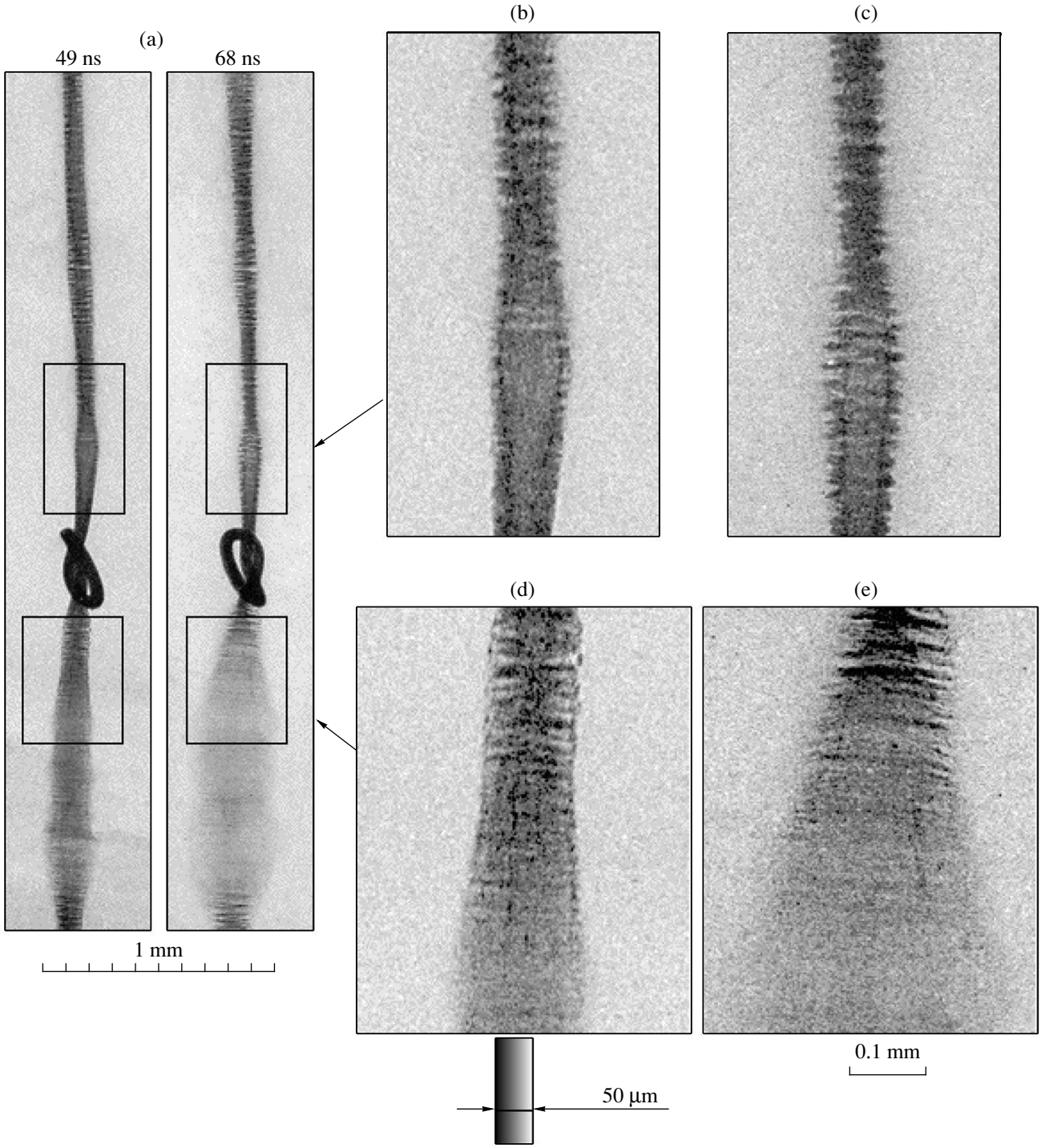

Fig. 1. X-ray backlighting images of the core of the exploded 50-μm-diameter Ti wire: (a) the images obtained in one shot at two different instants and (b–e) enlarged fragments of these images.

core is introduced inadequately to the experiment (the drop of the density is only tenfold and rather diffuse; instead of a liquid–vapor mixture, the substance is regarded as a dense plasma whose state corresponds to a thermodynamic point that lies above the binodal curve). There is also the problem of how to specify the precise conditions at the boundaries and describe the radiation transfer in a moderately dense plasma (in particular, for relatively light elements such as Ti). As a result, the calculations did not allow the authors to

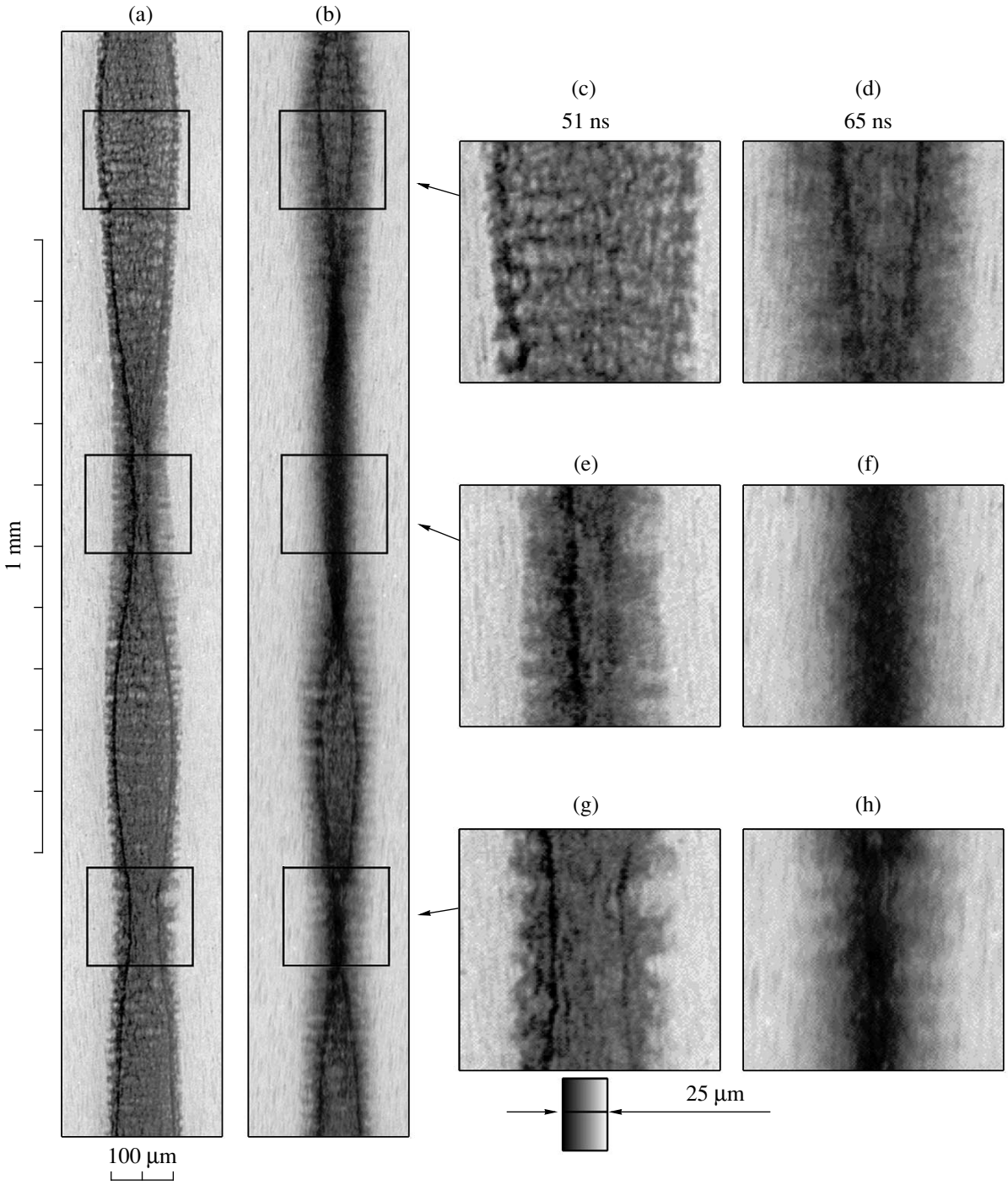

Fig. 2. X-ray backlighting images of the core and the surrounding corona in the Ni-wire discharge.

obtain compression parameters comparable with the experiment or to attain the stage in which the surface instabilities come into play. However, it is important that the model has demonstrated the role of the structure of a wide front of the shock wave arriving at the core. Recently, the calculation algorithm has been improved; below, we consider the current state of the model.

3. CALCULATION OF THE COMPRESSION OF A Z-PINCH WITH AN INTERNAL CORE

When calculating the compression of a plasma with a central core, we used a fairly detailed (from the standpoint of the number of incorporated processes) radiative MHD model [9] (see also [10]) of exploding wires. Note that, in its current state, the model still cannot adequately describe a two-phase core substance, because

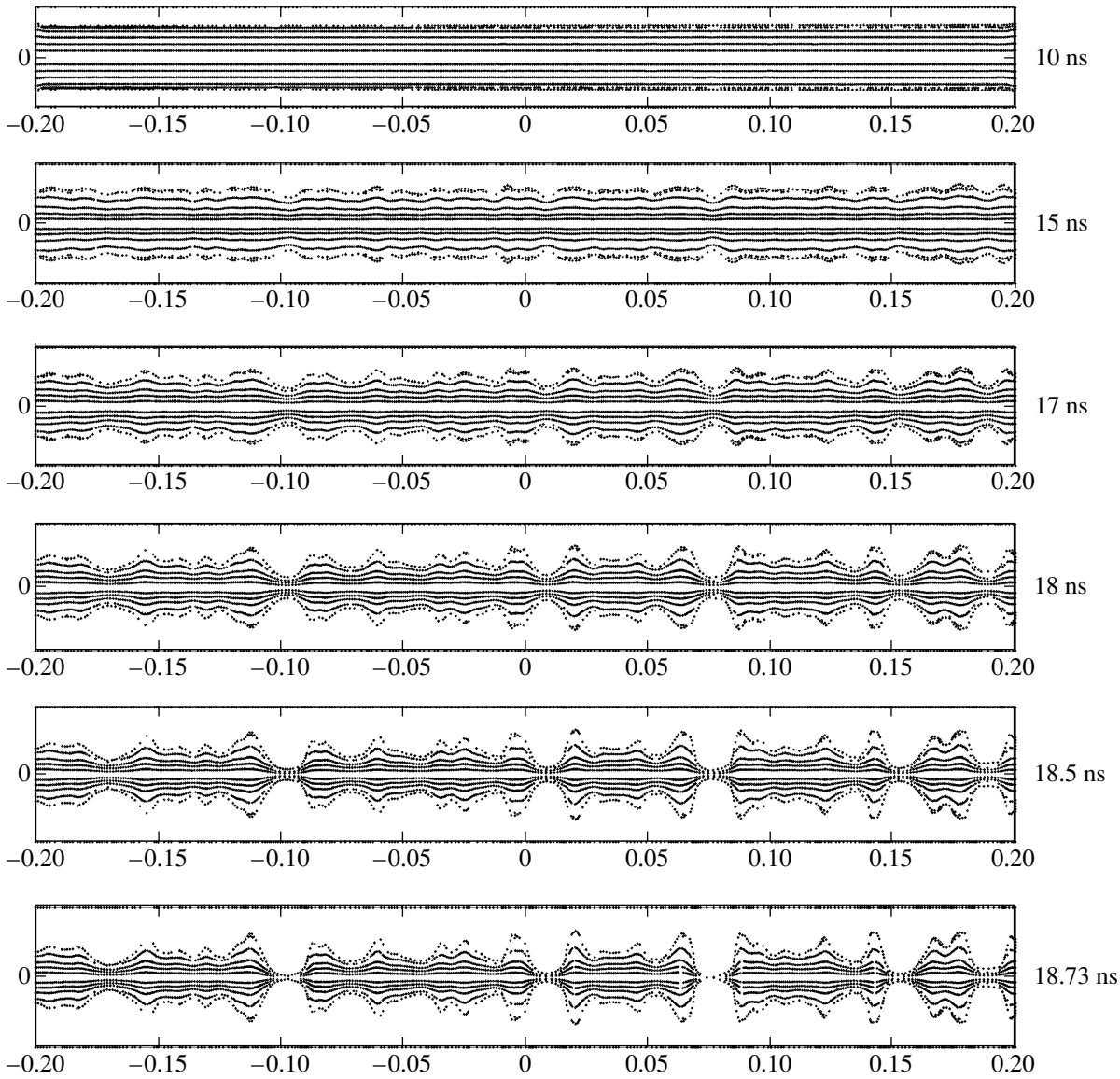

Fig. 3. Results of MHD calculations of the propagation of the compression wave through the core in a Ti-wire discharge. The distribution of the calculation points.

the problem of describing the "cold start" of a discharge is as yet unresolved. For this reason, we will start from a specific state corresponding to the maximum expansion of the products of an electric explosion of a metal wire. Similar to [9, 10], which dealt with tungsten, in our model, the core was simulated by a multifold increase in the density in the region with a 90-μm radius and a plasma corona extended to 300 μm outside this region. In our calculations for Ti, the relative increase in the density (which was previously equal to 10) varied from 10 to 50. However, as before, the initial state of the core was taken beyond the region where two-phase states can exist. Initially, the core had a smooth surface and the perturbations in the core and corona were produced by introducing the initial scatter in the parameters at a level of 1%.

Such a simulation successfully reproduced the implosion process for a Ti wire (the wire diameter was 24 μm, the core-to-corona density ratio was 40, and the mesh consisted of 13×500 cells). Initially, a compression shock wave was formed in the plasma corona. The extension of the shock wave over the radius attained 80 μm (a value comparable with the core radius) and was determined by the processes of emission and electron heat conduction and smoothing of the jumps in the densities of ions with different charge numbers. The resulting wide front is seen in the spatial distributions of both calculation points shown in Fig. 3 and the electron density n_e and temperature T_e shown in Fig. 4 for a

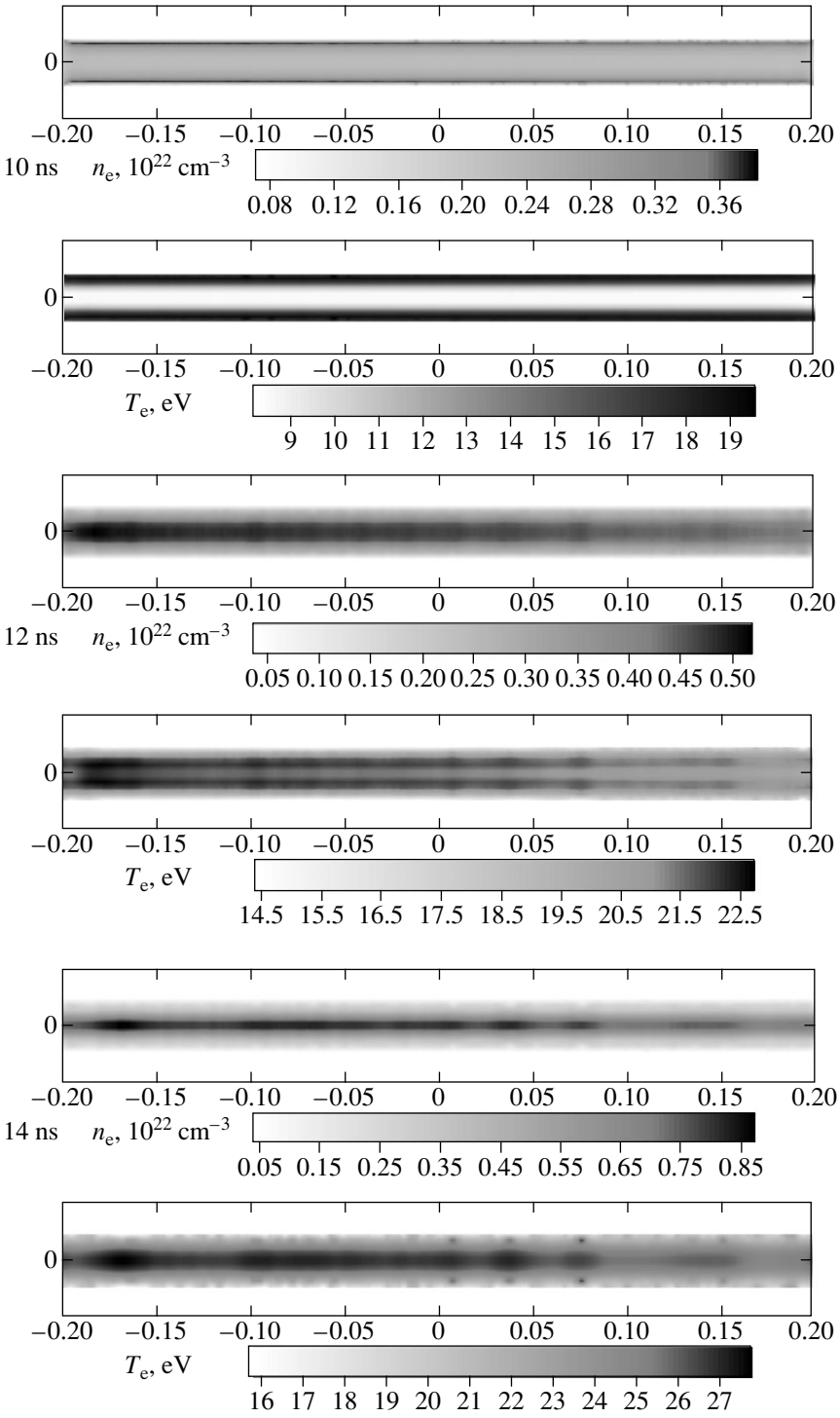

Fig. 4. Results of MHD calculations of the propagation of the compression wave through the core in a Ti-wire discharge. The density and electron-temperature distributions.

time of 10 ns. At as early as 12 ns, one can see the interaction of the compression wave with the core; 2 ns later, the entire core region is involved in the process of heating, which is initially almost uniform along the axis, because both the radiation and electron heat waves penetrate into the core before the shock. At the same time, we see that a chain of perturbations arises in the corona, increasing markedly by 15 ns. In one nanosecond, the character of heating changes sharply: the wide front of the implosion wave affects the core, which leads to the

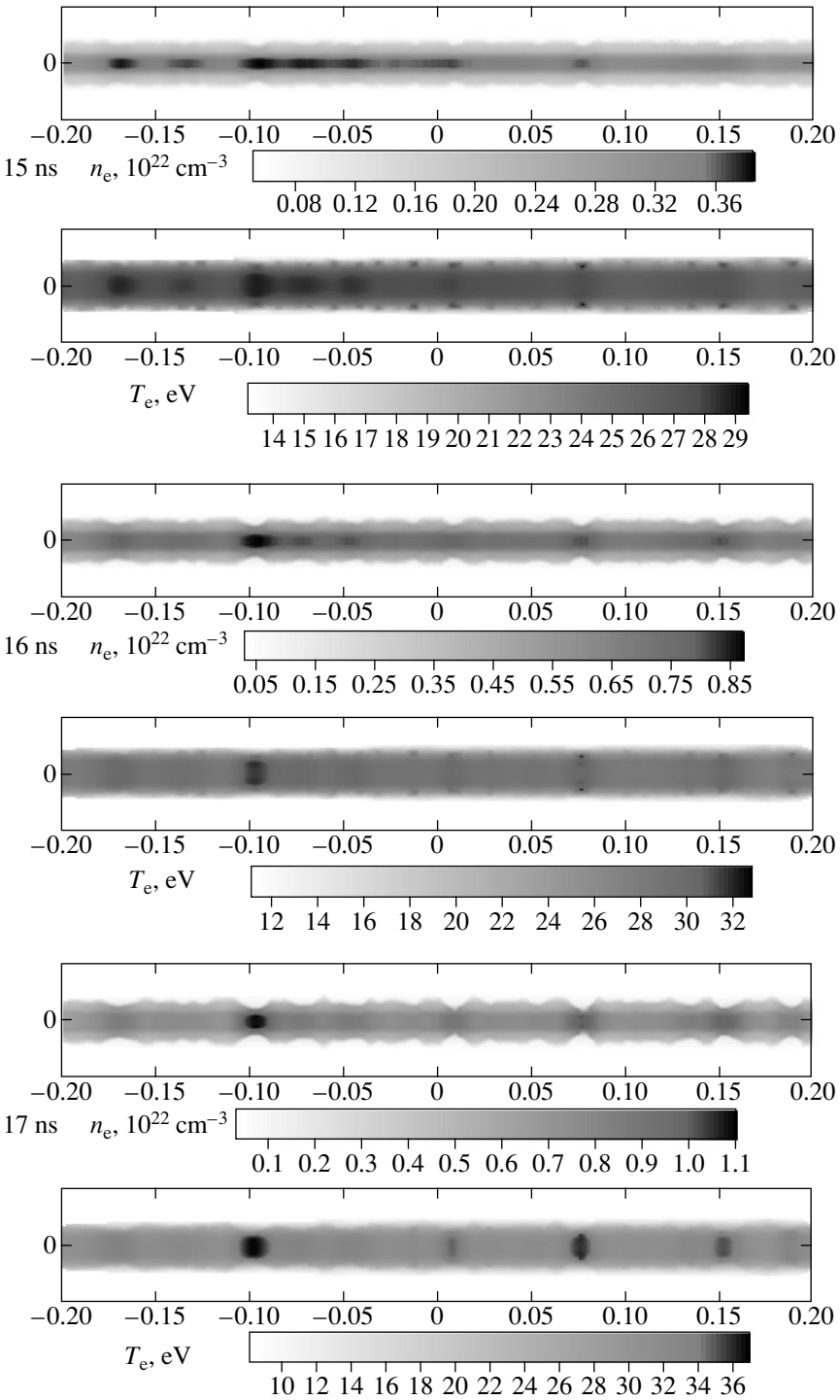

Fig. 4. (Contd.)

formation of individual hot spots in which further compression occurs. The axial inhomogeneity of heating and compression becomes more pronounced at 16 and 17 ns, between which the traces of the chain of perturbations disappear in the corona plasma. After 18 ns, the process changes fundamentally: against the background of the almost unchanged bulk of the plasma column, compression occurring at a growing rate is observed only locally, namely, at the constriction points clearly seen in Fig. 3. Heating and compression are most pronounced during deceleration in the final stage of implosion. Thus, for about 30 ps after 18.70 ns, the

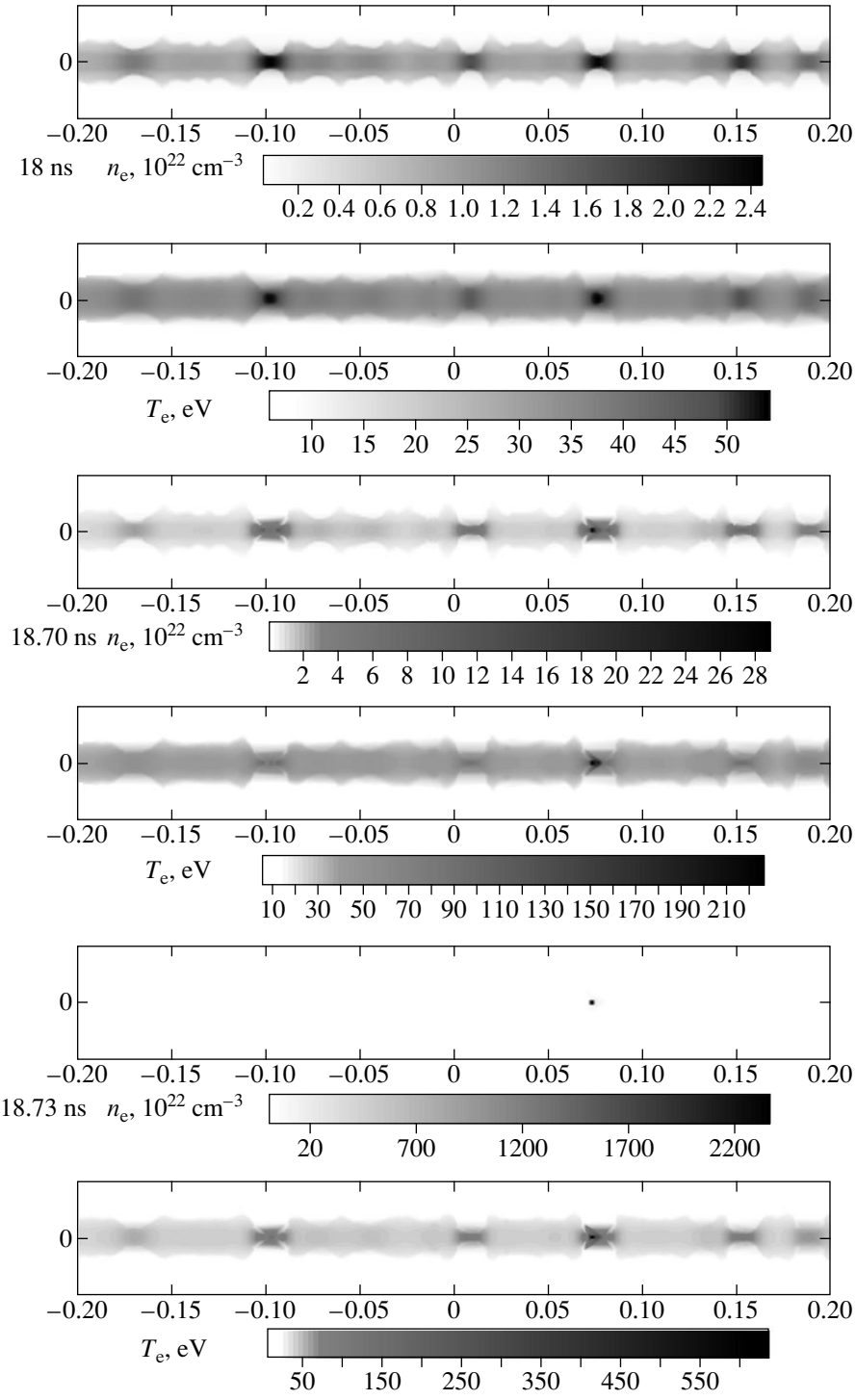

Fig. 4. (Contd.)

maximum value of n_e increases by one order of magnitude and T_e increases more than three times. The process ends with the formation of very thin constrictions containing one or more hot points. The calculations yield the following plasma parameters: the pinch radius is equal to 0.1 μm, which is close to the Rosseland mean free path for photons; the electron density is equal to $n_e \simeq 10^{25}$ cm^{-3}; the temperature is equal to T_e = 0.8–0.9 keV; and the ion charge is 18.5. The radiation pressure contributes appreciably to the force balance.

All of this resembles the results obtained previously for an X-pinch constriction [10] (of course, taking into account the difference in the load material).

In calculations, we also varied the ratio between the densities on both sides of the corona–core boundary. With the load mass being conserved, an increase in this ratio resulted in a decrease in the fraction of the corona substance. This led to an enhancement of the shock wave arising in the corona; to the intensification of the processes occurring in the core; and, consequently, to an increase in the density and temperature of the compressed plasma.

Unfortunately, the computation of the next stage of implosion for Ti requires much more time and leads to problems that still remain unresolved. Among physical circumstances, it is sufficient to mention a high (in comparison with tungsten) transmittance of the plasma in the model using the radiation temperature in addition to the ion and electron temperatures. (It is seen from Fig. 1 that turbulence must also be taken into account.) Nevertheless, the simulation of this stage reflects the main specific features of implosion in a heterogeneous corona–core system: since the front of the shock wave arriving from the corona at the core surface is rather wide, the core falls completely in the relaxation zone and the shock wave in the core simply has no time to form. Nevertheless, as is seen from Figs. 1 and 2, a narrow compression front in the core is observed experimentally. Thus, it is necessary to correct the conclusions drawn from the model of a dense plasma core. In the model of a two-phase medium containing vapor bubbles, the compression front in the core can form due to the change in compressibility of the core substance. However, in this case too, a wide compression front (rather than an abrupt jump) arrives at the core surface.

Despite the importance of the implosion processes under consideration, our interest extends further. The problems that emerge in simulating the implosion process after a shock wave moving away from the axis has been formed (either due to reflection from the axis or in an explosion, as in an X-pinch [10]) hamper investigations of instabilities at the corona–core boundary. In this stage, an intense turbulent mixing of the core substance and the corona plasma occurs behind the front of the shock wave reflected from the axis. For this reason, we now turn to another, simplified model, but it is helpful first to perform a preliminary analysis.

4. INSTABILITY OF THE CORONA–CORE BOUNDARY

Instabilities of the boundary between media with different densities may be primarily attributed to classical hydrodynamic effects. This is promising for constructing (for lack of better models) simplified models of the phenomenon, without posing the question as to whether they have any bearing on the structure of wire discharges: in essence, there is no peculiar MHD features in them. It is seen from the above simulations that the shock front in the corona of an exploding wire is fairly broad and the pressure is rather uniform in space. At the corona–core boundary, one can expect the onset of the Rayleigh–Taylor instability (quasi-monotonic acceleration of a dense substance by a less dense substance) and the Richtmayer–Meshkov instability (the passage of a shock wave through the boundary between media with different densities). As an example, we consider the former instability. According to [8], its linear growth rate is defined by the expression

$$\gamma_{RT} = \sqrt{\frac{Agk_z}{1 + k_z L}}.$$

Here, k_z is the wavenumber of the initial perturbation at the corona–core boundary, g is the boundary acceleration taken with the opposite sign, L is the scale length of variations in the substance density, and $A = (\rho_c - \rho_p)/(\rho_c + \rho_p)$ is the Attwood number (where ρ_c and ρ_p are the mass densities of the core and coronal plasma, respectively).

As was mentioned above, in the course a high-current explosion, a sharp boundary arises between the plasma corona ($\rho_p = 10^{-3}$–10^{-2} g/cm^3) and the liquid central core ($\rho_c = 10^{-1}$–1 g/cm^3). The Attwood number is equal to $A \simeq 1$, and we obtain the following estimates: $L \simeq a_0\rho/\Delta\rho \simeq a_0/A \simeq a_0$, and $g \simeq P_p/\rho_c L \simeq P_p/\rho_c a_0$, where a_0 is the initial perturbation amplitude and P_p is the coronal plasma pressure. From here, we obtain the instability growth rate

$$\gamma_{RT} \simeq \frac{k_z\sqrt{P_p/\rho_c}}{\sqrt{k_z a_0(1 + k_z a_0)}}. \quad (1)$$

The experimental data lead to the values $(P_p/\rho_c)^{1/2} \simeq (3–6) \times 10^5$ cm/s, and, for wavelengths of 20–30 μm and $k_z a_0 \simeq 1$, we obtain a typical value, $\gamma_{RT} \simeq (2–5) \times 10^8$ s^{-1}. This indicates a rapid growth of instabilities during the discharge.

Hypothetically, the initial perturbations can be related to (i) irregularities of the wire shape, (ii) the effect that explosive bubbles arriving at the core surface have on the pressure distribution in the corona during the volume boiling and surface evaporation of the core substance, and (iii) perturbations due to MHD instabilities of the plasma compressed by the corona current. Through the corona, the first two types of initial perturbations (both are characterized by scale lengths of tens of microns, which is on the order of the initial wire radius) affect the shape of both the core and the shock front, whereas the third type of perturbation (with a scale length of several hundreds of microns) affects only the front. Our data on the boiling of the liquid core allow us to argue for the dominant role of the second type of perturbation, which enables the onset of both the Rayleigh–Taylor and Richtmayer–Meshkov insta-

bilities of the boundary between the media with different densities.

As time elapses, the growth of perturbations becomes markedly nonlinear: in the case of the Rayleigh–Taylor instability, this is accompanied by the formation of jets; i.e., the coronal plasma penetrates the core. Perturbations of the lateral surfaces of the jets can also grow with time due to the Kelvin–Helmholz instability, whose growth rate depends on the velocity with which the liquids flow with respect to one another. Allowing for a cumulative increase in the jet velocity during the cylindrical compression of the core substance toward the axis, we can roughly estimate this velocity in the nonlinear stage of the Rayleigh–Taylor instability as $u \simeq r_c\gamma_{RT}(r_c/r)^2$, where $r_c \simeq 100$ μm is the initial core radius. Substituting this velocity into the classical expression for the growth rate of the Kelvin–Helmholz instability $\gamma_{KH} \simeq uk_r(\rho_p/\rho_c)^{1/2}$, we obtain

$$\gamma_{KH} \simeq \gamma_{RT}k_r r_c(\rho_p/\rho_c)^{1/2}(r_c/r)^2. \qquad (2)$$

It follows from here that, for $r_c = 50$–100 μm and $\rho_p/\rho_c \simeq 10^{-2}$, both growth rates entering (2) become comparable as soon as the jet covers a distance approximately equal to two-thirds of the core radius. We can also find out how the instabilities are related to the subsequent turbulence responsible for the mixing of the core and corona substances.

5. MODELING OF THE INSTABILITIES OF THE CORONA–CORE BOUNDARY

We assume that the instabilities under study are primarily related to classical hydrodynamic effects and are not too sensitive to the peculiarities of a radiative MHD plasma. Therefore, we will only use gas-dynamic equations supplemented with a qualitative description of a few of the discharge features needed for our analysis. It is of interest to consider what will happen if the density jump in the core (which was "lost" in the previous simulations) is taken into consideration.

We use a NUTCY two-dimensional cylindrical code [11] created for solving the set of gas-dynamic equations. Its important part is the block for solving the balance equations for the mass densities of the interacting substances or parts of the system distinguished by certain properties that are chosen for each particular problem. This allows us to use this code efficiently to correctly simulate the evolution of the boundary between two substances with different initial properties in various problems, such as the decay of a discontinuity and the onset of various hydrodynamic instabilities. The code is based on the method of quasi-monotonic difference schemes with higher order approximation. The algorithm employs the principle of splitting between particular physical processes and uses economical, locally one-dimensional difference schemes [12]. The program was successfully used to simulate the onset of hydrodynamic instabilities in experiments with shock tubes [13] and experiments on the acceleration and compression of the materials of targets of different geometries by a laser pulse [14].

The code implies that the plasma is ideal, neutral, and isothermal and that there are only external forces and energy sources. Among dissipative processes, it includes only electron heat conduction. Among the effects of ionization and radiation cooling, the heat balance incorporates only volume losses due to bremsstrahlung. The ion charge numbers are taken to be constant in both the core and the corona and correspond to their averaged (throughout the entire process) values in each medium. The absence of Joule heating is compensated by the constancy of the temperature at the external plasma boundary.

Computations were performed for a cylindrical plasma fragment with axial and radial dimensions of 500 μm, which roughly complied with the conditions of MHD compression of the Z-pinch. To model the situation close to the experiment [3, 5] (wires were made of Ti, and the atomic weight was 47.9), two versions of the problem were examined. The first version corresponded to modeling the propagation of a shock wave from the pinch corona into a dense core. The initial conditions were chosen as follows (Fig. 5a): near the axis of the dense core, the temperature, density, pressure, and ion charge number were specified as $T = T_0 = 3$ eV, $\rho_0 = 0.1$ g/cm^3, $P_0 = 1.81 \times 10^{-2}$ Mbar, and $Z_0 = 2$, respectively; in the outer region of the hot corona, the plasma parameters were specified as $T_0 = 100$ eV, $\rho_0 = 10^{-3}$ g/cm^3, $P_0 = 2.21 \times 10^{-2}$ Mbar, and $Z_0 = 10$. The boundary between these regions was 100 μm away from the axis. A sinusoidal initial perturbation with a wavelength of 30 μm and amplitude of 5 μm was imposed on the boundary. Behind the front of the shock wave, the plasma parameters were specified as $T = 316$ eV, $\rho = 2.85 \times 10^{-3}$ g/cm^3, and $P = 1.99 \times 10^{-1}$ Mbar. At $t = 0$, the front was 20 μm away from the corona–core boundary.

The second version of the problem corresponded to modeling the propagation of a shock wave through a dense core directly from the corona–core boundary. Here, in contrast to the previous version, the boundary was assumed to be smooth, whereas a sinusoidal perturbation with the same parameters was imposed on the front (Fig. 6a). The core and corona parameters behind the front of the shock wave were the same for both versions. In both cases, the boundary conditions were the following: the rigid-surface reflection condition on the axis and end-face boundaries of the calculation domain and the conditions for conservation of the parameters behind the shock front on the immobile outer cylindrical surface.

Results of simulations for the first version are presented in Figs. 5b–5d, in which the radial profiles of the pressure, density, and plasma temperature at different instants are shown. At the instant $t = 2$ ns counted from a certain zero time, the shock wave arrives at the axis.

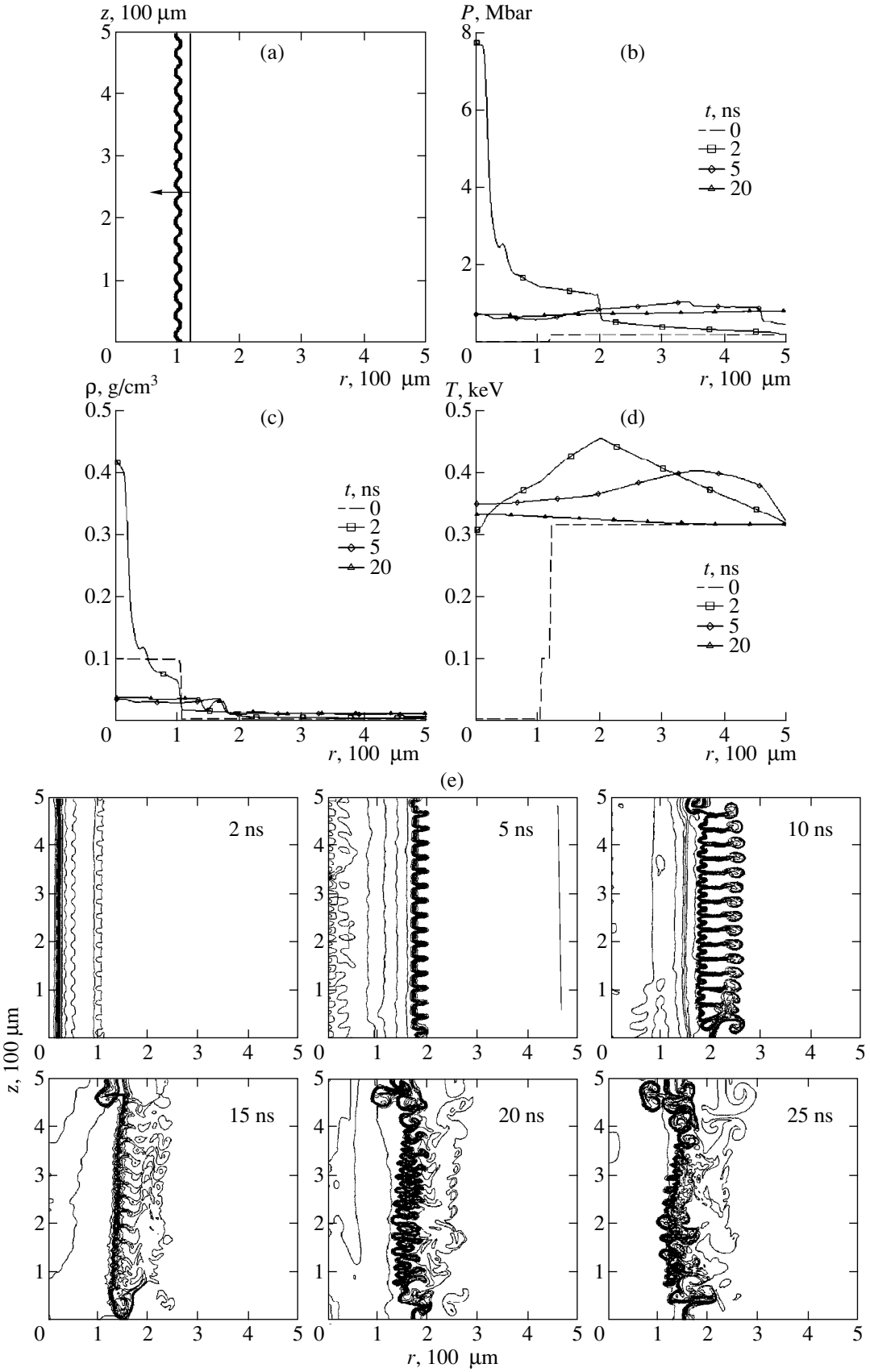

Fig. 5. (a) The initial position of the boundary; the radial profiles of (b) the pressure, (c) density, and (d) temperature; and (e) the density contours at different instants for the problem of the passage of a shock wave through the corona–core boundary.

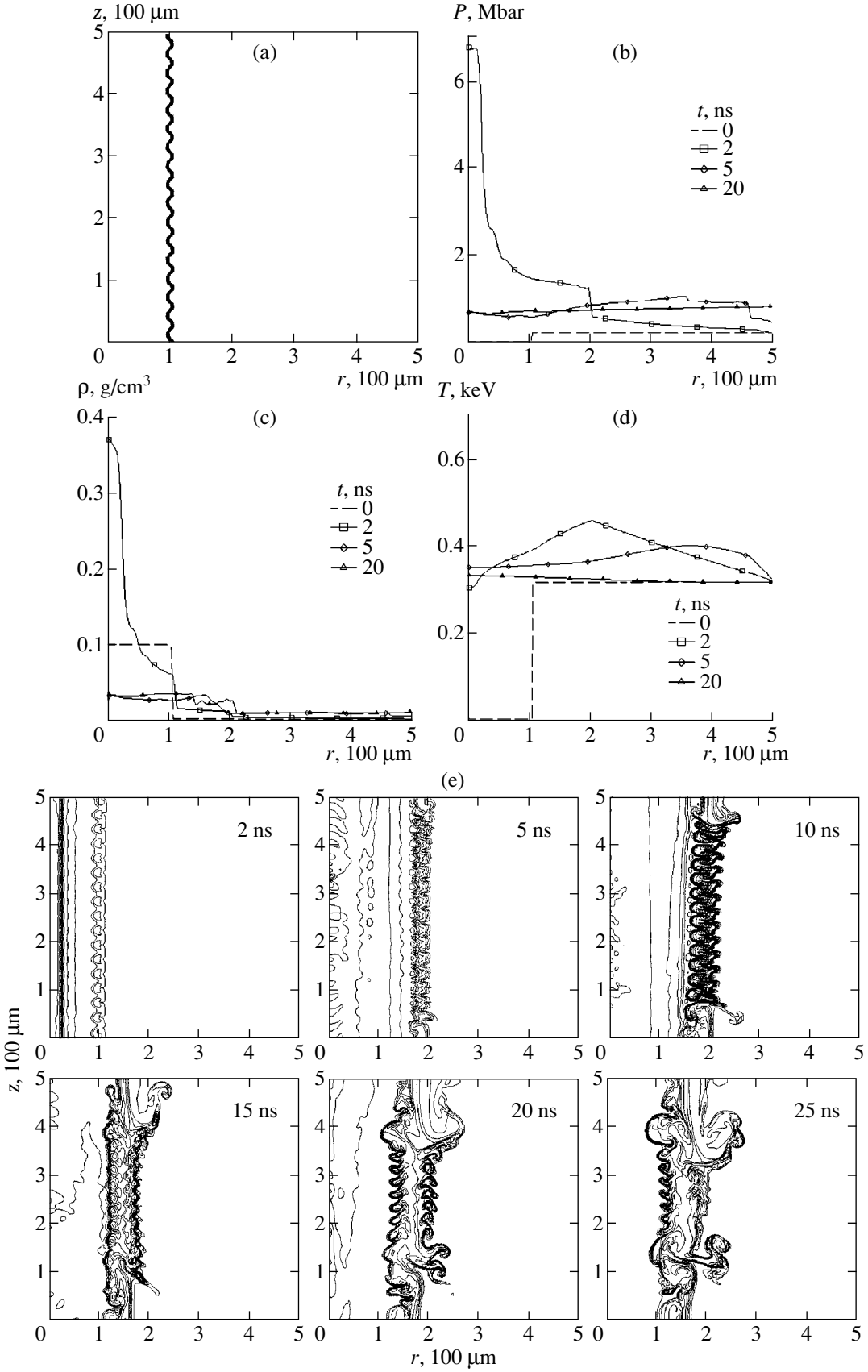

Fig. 6. (a) The initial position of the boundary; the radial profiles of (b) the pressure, (c) density, and (d) temperature; and (e) the density contours at different instants for the problem of the decay of the discontinuity at the corona–core boundary.

Near the axis, the plasma pressure is ≃7.8 Mbar and the density is ≃0.42 g/cm^3. By the instant t = 5 ns, the shock front, which has been reflected from the axis and has passed once more through the corona–core boundary, approaches the outer boundary; the density decreases to 0.02–0.05 g/cm^3; and the temperature varies within the range 300–450 eV.

Figure 5e shows the density contours at certain characteristic instants of the evolution of the corona–core boundary. They give evidence for a rapid growth of hydrodynamic perturbations at the boundary. By 5 ns (i.e., after the reflection from the axis), the onset of the Richtmayer–Meshkov instability is seen, which can be recognized by the change in the positions of points where the perturbations are maximum (a typical effect of the Richtmayer–Meshkov instability when the shock wave passes from a heavy substance to a light substance). A nearly threefold increase in the perturbation amplitude shows that the inverse growth rate is close to 5 ns, which is in good agreement with the analytical estimates made in the previous section.

By 10 ns, the Richtmayer–Meshkov instability arrives at the nonlinear stage accompanied by the formation of a characteristic fungous-like perturbation of the boundary. In addition, the evolution of the boundary layer is significantly influenced by the Kelvin–Helmholz instability caused by high velocity gradients on both sides of the boundary. This influence manifests itself as a destruction of plasma jets, which terminates by 15 ns with the formation of a transition layer consisting of the mixed substance. It is interesting that, by 20 ns, perturbations with wavelengths smaller than the initial ones arise because of the deformation of the boundary in the nonlinear stages of the Richtmayer–Meshkov and Kelvin–Helmholz instabilities. Note that, after 10 ns (i.e., once the fungous structure begins to form), the position of the contact boundary is stabilized at a distance of 150–200 μm from the axis. After this time, the width of the transition layer also remains almost constant and is equal to 100–120 μm.

In the second version of the problem, the conditions correspond to a simultaneous onset of the Richtmayer–Meshkov and Rayleigh–Taylor instabilities. The results of calculations show that, in this case, the linear growth rates of radial hydrodynamic instabilities are close to each other and the instabilities develop in a similar manner in the linear stage (Figs. 6b–6d). The main distinction from the previous version is that the Kelvin–Helmholz instability begins at an earlier time, grows more rapidly, and almost suppresses the effects of the Richtmayer–Meshkov and the Rayleigh–Taylor instabilities in the nonlinear stage. This explains the absence of a pronounced fungous structure and the formation of a more compact transition layer 60–80 μm wide (Fig. 6e). At the same time, the position of the transition layer is close to that in the first version (≃120–150 μm from the axis).

What does all this mean in the case of exploding wires? Due to the high effective compressibility, a specific shock front arises in the bubble-containing media. According to the above consideration, during the front propagation toward the core axis and then backward, hydrodynamic instabilities can grow rapidly at the corona–core boundary. In this case, the conditions of the problem (a sharp boundary between the high- and low-density substances and a diffuse shock front arriving at the boundary) enable the onset of both the Richtmayer–Meshkov and Rayleigh–Taylor instabilities. In the nonlinear stages of these instabilities, liquid flows with high velocity gradients can arise on the perturbed boundary, which leads to the onset of the Kelvin–Helmholz instability. The growth rates of all these instabilities in a high-current thin-wire discharge turn out to be fairly high: their inverse values amount to several nanoseconds against the background of compression lasting several tens of nanoseconds. As a result, the hydrodynamic instabilities can affect the whole process of the Z-pinch implosion (e.g., they can lead to the formation of regular radial perturbations at the corona–core boundary with amplitudes comparable with the pinch size).

The results agree qualitatively with the observed picture of mixing of the core and corona substances after the return of the shock front. However, in the present formulation, the problem does not take into consideration the magnetic field or real Joule heating and the mixing can also be attributed to the heterogeneous structure of the two-phase core. Therefore, the construction of an adequate model calls for further detailed simulations.

6. CONCLUSION

Computer simulations of the interaction between the hot corona and the core of an exploding wire have demonstrated a number of important features in which this object differs from the conventional model of a plasma column. These features are attributed to the high density of the cold core and to the diffuse front of a shock wave generated in the corona. We have also revealed that the two-phase state of the core cannot be ignored; as a consequence, the model of the dynamics of heterogeneous (the corona–core boundary and vapor bubbles in the liquid core) pinches calls for further generalization. Calculations using this model might answer the question regarding the nature of mixing of the pinch substance after the shock front returns from the core to the corona.

ACKNOWLEDGMENTS

We thank S.L. Nedoseev for a critical review of the article. This work was supported in part by the DE-FG02-98ER54496 grant and the BD-9356 contract of Sandia National Laboratory (USA).

REFERENCES

1. W. G. Chace, Phys. Fluids **2**, 230 (1959).
2. F. A. Nikolaev, V. B. Rozanov, and Yu. P. Sviridenko, Tr. Fiz. Inst. Akad. Nauk SSSR **76**, 36 (1974).
3. G. V. Ivanenkov, A. R. Mingaleev, S. A. Pikuz, *et al.*, Zh. Éksp. Teor. Fiz. **114**, 1216 (1998) [JETP **87**, 663 (1998)].
4. S. A. Pikuz, G. V. Ivanenkov, T. A. Shelkovenko, and D. Hammer, Pis'ma Zh. Éksp. Teor. Fiz. **69**, 349 (1999) [JETP Lett. **69**, 377 (1999)]; S. A. Pikuz, T. A. Shelkovenko, D. B. Sinars, *et al.*, Phys. Rev. Lett. **83**, 4313 (1999).
5. S. Yu. Gus'kov, G. V. Ivanenkov, A. R. Mingaleev, *et al.*, Pis'ma Zh. Éksp. Teor. Fiz. **67**, 531 (1998) [JETP Lett. **67**, 559 (1998)].
6. G. V. Ivanenkov, A. R. Mingaleev, S. A. Pikuz, *et al.*, Fiz. Plazmy **25**, 851 (1999) [Plasma Phys. Rep. **25**, 783 (1999)].
7. G. V. Ivanenkov, A. R. Mingaleev, T. A. Novikova, *et al.*, Zh. Tekh. Fiz. **65** (4), 40 (1995) [Tech. Phys. **40**, 312 (1995)].
8. V. B. Rozanov, C. P. Verdon, V. Decroisette, *et al.*, in *Energy from Inertial Fusion* (IAEA, Vienna, 1995), p. 21.
9. G. V. Ivanenkov, A. R. Mingaleev, S. A. Pikuz, *et al.*, in *Proceedings of 4th International Conference on Dense Z-Pinches, Vancouver, 1997* (AIP, New York, 1997), p. 253; G. V. Ivanenkov and W. Stepniewski, Fiz. Plazmy **26**, 24 (2000) [Plasma Phys. Rep. **26**, 21 (2000)].
10. G. V. Ivanenkov and W. Stepniewski, J. Mosc. Phys. Soc. **9**, 337 (1999).
11. V. V. Nikishin, V. F. Tishkin, I. V. Popov, and A. P. Favorskiĭ, Mat. Model. **7** (5), 15 (1995).
12. A. A. Samarskiĭ, *The Theory of Difference Schemes* (Nauka, Moscow, 1983).
13. I. V. Popov, V. F. Tishkin, V. V. Nikishin, *et al.*, in *Proceedings of 23th European Conference on Laser Interaction with Matter, Oxford, 1994*, p. 43.
14. S. Yu. Gus'kov, V. B. Rosanov, I. G. Lebo, *et al.*, in *Proceedings of 12th International Conference in Laser Interaction Research and Plasma Physics, Osaka, 1995*, p. 219.

Translated by N. Larionova

Plasma Physics Reports, Vol. 26, No. 9, 2000, pp. 759–771. Translated from Fizika Plazmy, Vol. 26, No. 9, 2000, pp. 811–823.

PLASMA DYNAMICS

Collisionless Expansion of a Plasma Cloud with Doubly Charged Ions in a Rarefied Magnetized Plasma

S. T. Surzhikov

Institute for Problems of Mechanics, Russian Academy of Sciences, pr. Vernadskogo 101, Moscow, 117526 Russia

Received March 18, 1999; in final form, November 15, 1999

Abstract—The collisionless interaction between an expanding cylindrical plasma cloud containing singly and doubly charged ions and a magnetized background plasma is investigated numerically using a method combining the kinetic and hydrodynamic approaches. The results presented were obtained from simulations carried out under conditions corresponding to active space experiments on the expansion of plasma clouds in the Earth's ionosphere. © *2000 MAIK "Nauka/Interperiodica".*

1. INTRODUCTION

Collisionless interactions between plasma streams have attracted much interest in connection with active space experiments [1, 2], the investigation of plasma dynamics in fusion devices [3, 4], the laboratory modeling of a laser plasma in an external magnetic field [5, 6], and the interpretation of astrophysical observations [5, 7, 8].

In this paper, we focus on the specific features of electromagnetic interactions between rarefied plasma streams at the initial stage of active space experiments similar to those described in [9] and laboratory experiments with laser-produced plasmas [5]. The numerical models developed to study such interaction processes are based on kinetic [10], magnetohydrodynamic (MHD) [14–19], and combined kinetic and hydrodynamic approaches [11–13]. Kinetic models, which are capable of describing high-frequency parameters of the interaction processes associated with small-scale electron motions, are the most laborious and have not yet been widely used in practical applications. The models combining kinetic and hydrodynamic approaches make it possible to describe the structure of collisionless shock waves on time scales governed by the motion of the ions of both an expanding plasma and a background plasma, but they are also fairly involved. The most economical MHD models cannot in principle predict the structure of collisionless shock waves driven by an expanding plasma, but they can nevertheless fairly accurately describe the structure of the perturbed magnetic field and such global parameters of the interaction process as the mean velocity of the shock wave and the averaged jumps in the parameters inside the shock front [20–22].

The structure of collisionless shock waves driven by an expanding plasma in both magnetized and unmagnetized background plasmas has been investigated in detail in [11–13, 17–19]. Here, we use a hybrid model to study the characteristic features of the interaction of an expanding plasma cloud containing singly and doubly charged ions with the ions of the ionospheric plasma. Our investigation is motivated by the circumstance that, in the stage of collisionless interaction between a background plasma and an expanding plasma, the latter should contain ions with different charge numbers (this circumstance was pointed out in some theoretical [23] and experimental [5, 6] papers). Our aim here is to clarify how the structures of both the plasma cloud and collisionless shock waves change in the course of interaction. This issue is especially important for interpreting laboratory experiments.

2. FORMULATION OF THE PROBLEM

In order to describe the collisionless interaction between an expanding plasma (EP) ejected from a plasma source or created as a result of the explosion of matter and a rarefied background plasma (BP) with a frozen-in magnetic field, we use a hybrid model in which the ion velocity distribution functions are determined by solving the Vlasov kinetic equation and the electron plasma component is treated using the fluid approach. The first series of simulations was carried out for an EP containing only singly charged ions ($\alpha = 1$). In the second series of simulations, half of the EP ions were assumed to be singly charged and the rest of the EP ions were assumed to be doubly charged ($\alpha = 2$). In both series of simulations, the BP was assumed to contain only singly charged ions ($\alpha = 3$). We denote the ion velocity distribution functions by $f_\alpha \equiv f_\alpha(\mathbf{r}, \mathbf{v}, t)$ and write the Maxwell–Vlasov equations describing the self-consistent behavior of the ions in a rarefied plasma in electromagnetic fields [25–27]:

$$\frac{\partial f_\alpha}{\partial t} + \mathbf{v}\frac{\partial f_\alpha}{\partial \mathbf{r}} + \frac{e_\alpha}{m_\alpha}\left(\mathbf{E} + \frac{1}{c}[\mathbf{v}\times\mathbf{H}]\right)\frac{\partial f_\alpha}{\partial \mathbf{v}} = 0, \quad \alpha = 1, 2, 3, \tag{1}$$

1063-780X/00/2609-0759$20.00 © 2000 MAIK "Nauka/Interperiodica"

$$\operatorname{curl}\mathbf{E} = -\frac{1}{c}\frac{\partial \mathbf{H}}{\partial t}, \tag{2}$$

$$\operatorname{curl}\mathbf{H} = \frac{4\pi}{c}\mathbf{J} + \frac{1}{c}\frac{\partial \mathbf{E}}{\partial t}, \tag{3}$$

$$\operatorname{div}\mathbf{E} = 4\pi\rho_e, \quad \operatorname{div}\mathbf{H} = 0, \tag{4}$$

where the independent variables ($\mathbf{r}$, $\mathbf{v}$, t) denote the coordinate, velocity, and time; $\mathbf{E}$ and $\mathbf{H}$ are the electric and magnetic fields; e_α and m_α are the charge and mass of an ion of species α; c is the speed of light; ρ_e is the space charge density; and $\mathbf{J}$ is the current density.

Knowing the distribution functions, we can determine the densities and macroscopic velocities of the ions of each species, $n_\alpha(\mathbf{r}, t) = \int f_\alpha d\mathbf{v}$ and $\mathbf{u}_\alpha(\mathbf{r}, t) = 1/n_\alpha \int \mathbf{v} f_\alpha d\mathbf{v}$, and (if necessary) their mean temperatures, $T_\alpha(\mathbf{r}, t) = m_\alpha/(3n_\alpha)\int f_\alpha (\mathbf{v} - \mathbf{u}_\alpha)^2 d\mathbf{v}$. The total density, velocity, and temperature of the ions and the total charge and current densities are represented by the formulas

$$n(\mathbf{r}, t) = \sum_\alpha^{N_\alpha} n_\alpha(\mathbf{r}, t), \quad n(\mathbf{r}, t)\mathbf{V}(\mathbf{r}, t) = \sum_\alpha^{N_\alpha} n_\alpha \mathbf{u}_\alpha(\mathbf{r}, t),$$
$$n(\mathbf{r}, t)T(\mathbf{r}, t) = \sum_\alpha^{N_\alpha} n_\alpha T_\alpha(\mathbf{r}, t), \tag{5}$$

$$\rho_e = \sum_\alpha^{N_\alpha} e_\alpha n_\alpha - e n_e(\mathbf{r}, t),$$
$$\mathbf{J} = \sum_\alpha^{N_\alpha} e_\alpha n_\alpha \mathbf{u}_\alpha(\mathbf{r}, t) - e n_e \mathbf{V}_e(\mathbf{r}, t), \tag{6}$$

where $\mathbf{V}_e$ is the mean electron velocity and N_α is the number of ion components (in the case at hand, $N_\alpha = 3$).

We neglected all ionization processes that might have affected plasma expansion: radiation ionization, anomalous ionization due to electron heating in collective interactions, ionization of atoms by electrons with sufficiently high energies, etc.

The mean electron velocity and electron density were determined from the following considerations. Since the mass of an electron is low, the electron gyroradius $R_{H,e}$ is much smaller than the ion gyroradii $R_{H,i}$. Consequently, it is natural to average the electron distribution function, which can change sharply on the short spatial scale $R_{H,e}$, over the period of Larmor electron gyration and to examine only the guiding center motion of the electrons. This approach implies that the electrons should be treated as a fluid and the electron motion should be described in terms of the mass velocity $\mathbf{V}_e$ and mass density n_e in the hydrodynamic approximation.

According to the estimates made in [11, 14], the plasma is to a large degree electrically neutral, $\rho_e = 0$, except for very narrow zones. Consequently, with sufficient accuracy, we can set $n_e = \sum_\alpha^{N_\alpha} e_\alpha n_\alpha$.

If we neglect the electron pressure and (naturally) collision-induced electron–ion friction (the latter is justified by the results obtained in [17, 18]), the equation of electron motion takes the form

$$m_e \frac{d\mathbf{V}_e}{\partial t} = -e\left(\mathbf{E} + \frac{1}{c}[\mathbf{V}_e \times \mathbf{H}]\right). \tag{7}$$

Neglecting electron gyration is equivalent to the assumption that the electron gyroradius is zero (or $m_e = 0$). In this approximation, the total force acting on the electrons should clearly be zero:

$$\mathbf{E} + \frac{1}{c}[\mathbf{V}_e \times \mathbf{H}] = 0. \tag{8}$$

In solving the problem, we also assumed that the plasma is ideally conducting. Since at a height of about $h \simeq 350$ km in the Earth's magnetosphere the characteristic plasma conductivity is $\sigma \simeq 10^{11}$ s^{-1}, the magnetic field penetrates diffusively into the plasma on a time scale of about $\tau_m = \dfrac{4\pi R_{H,i}^2 \sigma}{c^2} \simeq 1.4 \times 10^{-9} R_{H,i}^2$. Under the conditions $V_0 \sim 6 \times 10^7$ cm/s and $R_{H,i} \sim 0.2 \times 10^6$ cm, which are typical of the expansion process under consideration, the diffusion time of the magnetic field, $\tau_m = 0.56 \times 10^2$ s, is appreciably longer than the characteristic expansion time. This circumstance justifies the use of the ideally conducting plasma approximation.

The above assumptions underlie the equations of the hybrid model that was developed in [24] and is used here:

$$\frac{\partial f_\alpha}{\partial t} + \mathbf{v}\frac{\partial f_\alpha}{\partial \mathbf{r}} + \frac{1}{m_\alpha}(\mathbf{E} + [\mathbf{v} \times \mathbf{H}])\frac{\partial f_\alpha}{\partial \mathbf{v}} = 0, \quad \alpha = 1, 2, 3, \tag{9}$$

$$\mathbf{E} + [\mathbf{V}_e \times \mathbf{H}] = 0, \quad \operatorname{curl}\mathbf{E} = -\frac{\partial \mathbf{H}}{\partial t},$$
$$\operatorname{curl}\mathbf{H} = M_A^2 n(\mathbf{V} - \mathbf{V}_e), \tag{10}$$

where the quantities are nondimensionalized by analogy with [11]:

$$t = \tilde{t}\Omega_{H_*}, \quad r = \frac{\tilde{r}}{R_{H_*}}, \quad v = \frac{\tilde{v}}{V_0},$$

$$n_\alpha = \frac{\tilde{n}_\alpha}{n_*}, \quad H = \frac{\tilde{H}}{H_*}, \quad E = \frac{\tilde{E}}{V_0 H_*/c},$$

$$m_\alpha = \frac{\tilde{m}_\alpha}{m_*}, \quad M_A^2 = \frac{4\pi n_* m_* V_0^2}{H_*^2} = \frac{4\pi\rho_* V_0^2}{H_*^2}.$$

We choose the following normalizing parameters: V_0 is the initial velocity of the EP, n_* is the ion density of the unperturbed BP, H_* is the unperturbed magnetic field strength, $\Omega_{H_*} = eH_*/m_*c$ is the cyclotron frequency of the BP ions, and $R_{H_*} = V_0/\Omega_{H_*}$ is their gyroradius. The tilde marks the quantities to be nondimensionalized.

Since our problem is one-dimensional and axisymmetric, we can set $\mathbf{E} = (E_r, E_\varphi, E_z = 0)$ and $\mathbf{H} = (H_r = 0, H_\varphi = 0, H_z = H)$.

3. NUMERICAL METHOD

The basic set of equations was solved by the particle method [11, 25–27]. Instead of integrating the Vlasov kinetic equation, we traced the trajectories of a large number of particles, $N_p = \sum_\alpha^{N_\alpha} N_{p,\alpha}$, where $N_{p,\alpha}$ is the number of particles that simulate the behavior of the αth plasma species. If we denote the position vector and the radial and azimuthal velocities of the pth particle by r_p, $v_{p,r}$, and $v_{p,\varphi}$, then, in cylindrical coordinates, the motion of this particle can be described by the equations

$$\frac{dr_p}{dt} = v_{p,r}, \quad p = 1, 2, \ldots, N_p, \tag{11}$$

$$\frac{dv_{p,r}}{dt} = \frac{v_{p,\varphi}^2}{r} + \frac{E_r + v_{p,\varphi}H}{m_p}, \quad p = 1, 2, \ldots, N_p, \tag{12}$$

$$\frac{dv_{p,\varphi}}{dt} = -\frac{v_{p,r}v_{p,\varphi}}{r_p} + \frac{E_\varphi - v_{p,r}H}{m_p}, \quad p = 1, 2, \ldots, N_p. \tag{13}$$

The equations of the hybrid model can be solved in three stages, each having a clear physical meaning. In the first stage (which can be referred to as the kinetic stage), we solve equations (11)–(13) for each particle by determining its position at each time step with allowance for its interaction with the electric and magnetic fields. In the second stage, we find the mean macroscopic velocities of the plasma medium and its density. Finally, we evaluate the electric and magnetic fields self-consistently with the mean plasma parameters.

We solved the kinetic equations by the following explicit two-step scheme of second-order accuracy.

The equations solved at the *first step* are

$$y_1^{k+1/2} = y_1 + \frac{\tau}{2}y_2,$$

$$y_2^{k+1/2} = y_2 + \frac{\tau}{2}\left\{\frac{y_3^2}{y_1} + \frac{1}{m_\alpha}[y_3 H(y_1) + E_r(y_1)]\right\},$$

$$y_3^{k+1/2} = y_3 + \frac{\tau}{2}\left\{-\frac{y_2 y_3}{y_1} + \frac{1}{m_\alpha}[-y_1 H(y_1) + E_\varphi(y_1)]\right\},$$

where $y = (y_1, y_2, y_3) = (r_p, v_{p,r}, v_{p,\varphi})$, τ is the time step, and the functions on the right-hand sides are taken from the kth time step. Writing $H(y_1)$, $E_r(y_1)$, and $E_\varphi(y_1)$ means that the related field magnitudes are interpolated from the position $y_1 = r_p$ of the pth particle on the Eulerian grid $\omega_r = \{r_i, i = 1, 2, \ldots, N_i; h = r_i - r_{i-1} = \text{const}\}$.

The equations solved at the *second step* are

$$y_1^{k+1} = y_1 + \tau y_2^{k+1/2},$$

$$y_2^{k+1} = y_2 + \tau\left\{\frac{(y_3^{k+1/2})^2}{y_1^{k+1/2}} + \frac{1}{m_\alpha}[y_3^{k+1/2}H(y_1^{k+1/2}) + E_r(y_1^{k+1/2})]\right\},$$

$$y_3^{k+1} = y_3 + \tau\left\{-\frac{y_3^{k+1/2}y_2^{k+1/2}}{y_1^{k+1/2}} + \frac{1}{m_\alpha}[y_2^{k+1/2}H(y_1^{k+1/2}) + E_\varphi(y_1^{k+1/2})]\right\}.$$

Note that this scheme differs from those adopted in [11, 12]. Golubev *et al.* [11] applied an analogous scheme only to find r and v_r. Instead of the above equation for the azimuthal velocity, they used the conservation condition for the canonical momentum of each particle:

$$r\left(v_\varphi + \frac{A_\varphi}{m_\alpha}\right) = \text{const}, \tag{14}$$

where the vector potential A_φ defines the magnetic field as $H = r^{-1}\dfrac{\partial(rA_\varphi)}{\partial r}$.

One can readily see that differentiating condition (14) with respect to time yields an equation equivalent to Eq. (13).

We assumed that, at the initial instant, the EP is homogeneous and is bounded by a cylindrical surface

of radius R_0 and that all of the quasi-particles of the EP and BP are distributed uniformly in space (at equal distances). The initial velocities of the quasi-particles were defined as

$$v_{p_\alpha, r}^{k=0} = \frac{r_{p_\alpha}^{k=0}}{R_0}, \quad \alpha = 1, 2, \quad p_\alpha = 1, 2, \ldots, N_{p_\alpha},$$

$$v_{p_\alpha, \varphi}^{k=0} = v_{p_3, r}^{k=0} = 0, \quad \alpha = 1, 2, 3, \quad p_\alpha = 1, 2, \ldots, N_{p_\alpha},$$

where $r_{p_\alpha}^{k=0}$ is the initial coordinate of the pth quasi-particle, which contains ions of species α.

In the second stage, we had to determine the distribution function of the plasma particles. Since the method of quasi-particles implies that each of them has finite dimensions, we wrote the distribution function in the form

$$\tilde{f}(\mathbf{r}, \mathbf{V}) = \sum_p \Phi(\mathbf{r}, \mathbf{r}_p)\delta(\mathbf{V} - \mathbf{V}_p), \tag{15}$$

where the function $\Phi(\mathbf{r}, \mathbf{r}_p)$ defines the density distribution of the actual particles over the pth quasi-particle with velocity $\mathbf{V}_p$ and δ is the Dirac delta function.

Expression (15) implies that, in the vicinity of the point r, the number of quasi-particles per unit volume is

$$n(\mathbf{r}) = \int \tilde{f}(\mathbf{r}, \mathbf{V})d\mathbf{V} = \sum_p^{N_p} \Phi(\mathbf{r}, \mathbf{r}_p). \tag{16}$$

To find the number of actual particles in a quasi-particle, we must integrate the relevant term in (16) over space,

$$\beta_p = \int \Phi(\mathbf{r}, \mathbf{r}_p)d\mathbf{r}, \tag{17}$$

which yields the normalization condition

$$\int \varphi(\mathbf{r}, \mathbf{r}_p)d\mathbf{r} = 1, \tag{18}$$

where $\varphi(\mathbf{r}, \mathbf{r}_p) = \Phi(\mathbf{r}, \mathbf{r}_p)/\beta_p$ is the normalized function describing the density distribution of the actual particles over the pth macroparticle.

As was mentioned in [25, 27], the choice of this function governs which particular version of the method of quasi-particles is used. In this paper, we assume that the normalized function is $\varphi(\mathbf{r}, \mathbf{r}_p) = \frac{1}{2}\pi r h$ in the region $|\mathbf{r} - \mathbf{r}_p| \le \frac{h}{2}$ and equals zero outside this region.

The density of the plasma particles in the vicinity of the point $\mathbf{r}_i$ is equal to

$$n_i = \sum_p^{N_p} \Phi(\mathbf{r}_i, \mathbf{r}_p) = \frac{1}{2\pi r_i h h_z} \sum_p^{N_p} \beta_p \chi_p(r_i), \tag{19}$$

where $2\pi r_i h h_z$ is the volume of a cell in the vicinity of the point r_i and h_z is the height of the cell in the z-direction. The function $\chi_p(r_i)$ is equal to unity in the region $|\mathbf{r}_i - \mathbf{r}_p| \le \frac{h}{2}$ and equals zero outside this region.

In expression (19), we pass over to dimensionless variables and set $h_z = R_{H_*}$. As a result, we obtain

$$n_i = \frac{1}{r_i} \sum_\alpha^{N_\alpha} \sum_{p_\alpha}^{N_{p_\alpha}} \gamma_{p_\alpha} \chi_{p_\alpha}(r_i), \tag{20}$$

where $\gamma_{p_\alpha} = \frac{\rho_{p_\alpha}^0 r_{p_\alpha}^0}{n_* m_* N_{p_\alpha}}$, $\rho_{p_\alpha}^0$ is the density of the plasma particles that constitute the pth quasi-particle, and $r_{p_\alpha}^0$ is its coordinate.

Using expressions (19) and (20), we can derive the distribution function of the actual particles in a quasi-particle:

$$\Phi_{p_\alpha}(r_i, r_p) = \frac{n_* \gamma_{p_\alpha} \chi_{p_\alpha}(r_i)}{r_i}. \tag{21}$$

The mean ion and electron velocities and the kinetic energy of the particles of the EP and BP can be deduced in a natural way:

$$\begin{aligned} \mathbf{V}(r_i) &= \frac{1}{n} \sum_p^{N_p} \mathbf{V}_p \gamma_p \chi_p(r_i), \\ \mathbf{V}_e(r_i) &= -\mathbf{V}(r_i) - \frac{1}{M_a^2 n_e} \operatorname{curl}\mathbf{H}, \\ E_{1,2} &= \sum_{\alpha = 1, 2} \frac{m_\alpha}{2} \sum_{p_\alpha}^{N_{p_\alpha}} \gamma_{p_\alpha} (v_{p_\alpha, \varphi}^2 + v_{p_\alpha, r}^2), \\ E_3 &= \frac{m_3}{2} \sum_{p_3}^{N_{p_3}} \gamma_{p_3} (v_{p_3, \varphi}^2 + v_{p_3, r}^2). \end{aligned} \tag{22}$$

Calculations according to formulas (20) and (22) complete the second stage of the solution of the problem. The third stage consists of evaluating the electric and magnetic fields self-consistently with the plasma parameters by solving the equations

$$\begin{aligned} \frac{\partial H}{\partial t} + \frac{1}{r}\frac{\partial (r V_{e,r} H)}{\partial r} &= 0, \quad E_\varphi = V_{e,r} H, \\ E_r &= -V_{e,\varphi} H - \frac{H}{n M_a^2}\frac{\partial H}{\partial r}, \end{aligned} \tag{23}$$

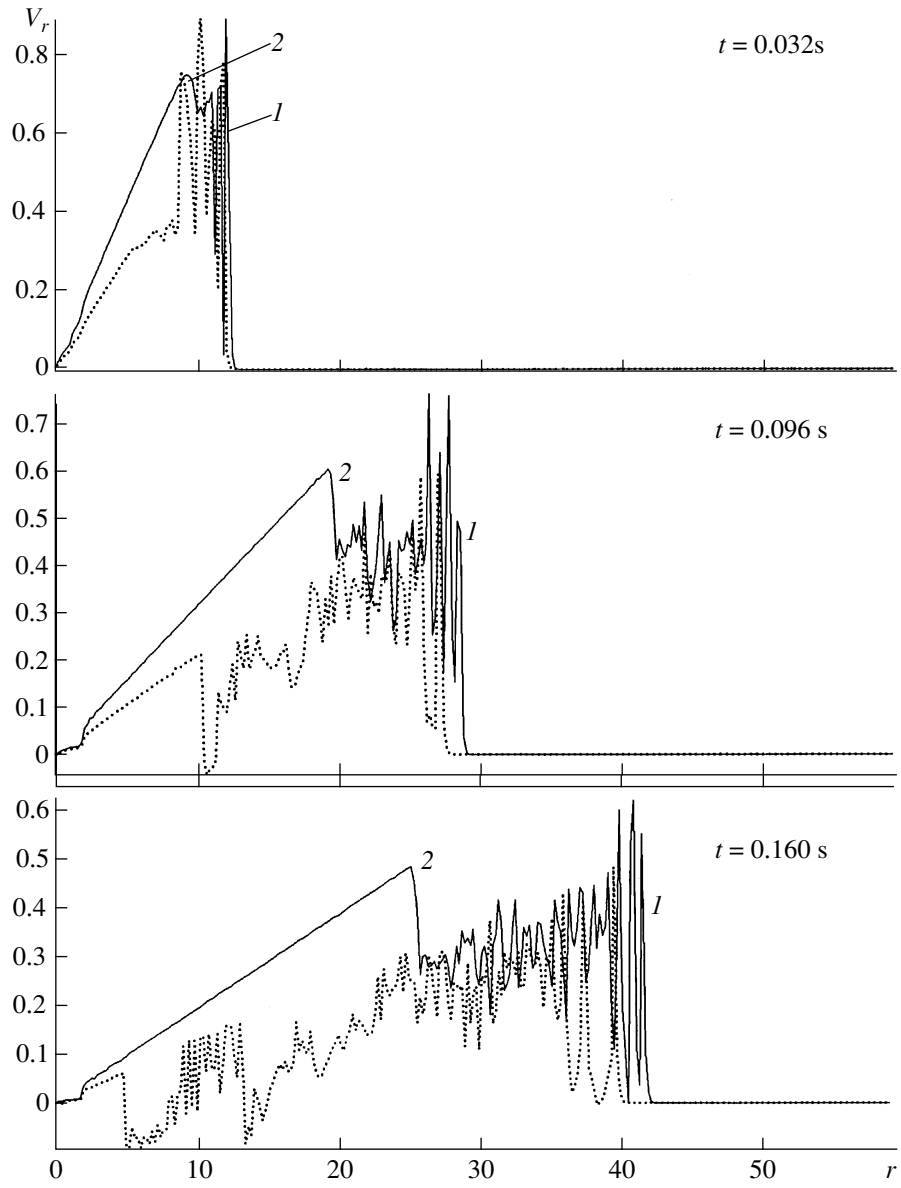

Fig. 1. Mean radial plasma velocity at different instants after the plasma cloud starts to expand: (*1*) the CSW front in the BP and (*2*) the boundary between the EP and BP. The solid and dashed curves illustrate the expansion of singly and doubly charged plasma clouds, respectively.

where $V_{e,r}$ and $V_{e,\varphi}$ are the radial and azimuthal components of the mean electron velocity $\mathbf{V}_e$.

The equation for the magnetic field strength was solved by the MacCormack explicit two-step scheme of second-order accuracy [28]:

$$\tilde{H}_i = H_i^p - \frac{\tau}{O_i}(S_i^+ G_{i+1}^p - S_i^- G_i^p), \quad G = V_{e,r} H,$$

$$\hat{H}_i = H_i^p + \tilde{H}_i - \frac{\tau}{2}\frac{S_i^+ \tilde{G}_i - S_i^- \tilde{G}_{i-1}}{O_i}, \quad \tilde{G} = V_{e,r}\tilde{H},$$

where $O_i = 2\pi\dfrac{r_i - r_{i-1}}{2}\dfrac{r_{i-1} + 2r_i + r_{i+1}}{4}$, $S_i^+ = 2\pi\dfrac{r_i + r_{i+1}}{2}$, and $S_i^- = 2\pi\dfrac{r_i + r_{i-1}}{2}$.

The fluxes through the boundaries of the grid cells were corrected numerically using the Zhmakin–Fursenko method [29]:

$$H_i^{p+1} = \hat{H}_i - \frac{\varphi^*_{i+1/2} - \varphi^*_{i-1/2}}{O_i},$$

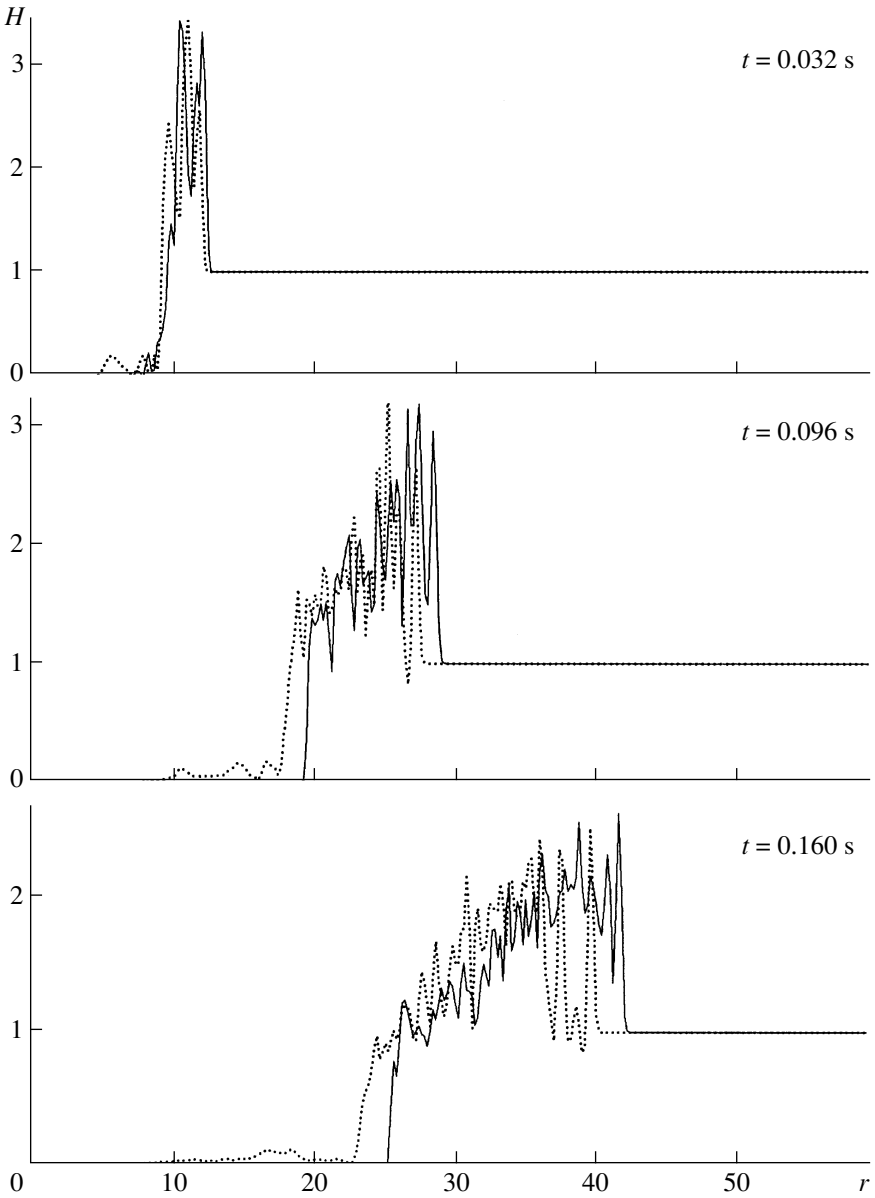

Fig. 2. Magnetic field strength at different instants after the plasma cloud starts to expand. The solid and dashed curves illustrate the expansion of singly and doubly charged plasma clouds, respectively.

where $\varphi^*_{i+1/2} = \varphi_{i+1/2}$ if $\{\delta\hat{H}_{i+1/2}\delta\hat{H}_{i-1/2} < 0$ or $\delta\hat{H}_{i+3/2}\delta\hat{H}_{i+1/2} < 0\}$ (otherwise, these functions equal zero) and

$$\varphi_{i+1/2} = \nu\delta H^p_{i+1/2}\phi(V_{e,r,i+1}, V_{e,r,i}),$$

$$\phi(V_{e,r,i+1}, V_{e,r,i}) = \frac{V_{e,r,i} + V_{e,r,i+1}}{2},$$

$$\delta H_{i+1/2} = H_{i+1} - H_i, \quad \delta H_{i+3/2} = H_{i+2} - H_{i+1},$$

where $\varphi^*_{i-1/2} = \varphi_{i-1/2}$ if $\{\delta\hat{H}_{i-1/2}\delta\hat{H}_{i-3/2} < 0$ or $\delta\hat{H}_{i-1/2}\delta\hat{H}_{i+1/2} < 0\}$ (otherwise, these functions equal zero). Here, ν is the artificially introduced viscosity.

The time step should be chosen from the condition for our numerical algorithm to converge:

$$\tau \le \frac{1}{h^{-1} + 2\nu/h^2}.$$

Varying the artificial viscosity ν in test simulations, we adjusted it to be fairly low (about 0.01). The parameters of the difference grid were chosen so that the second

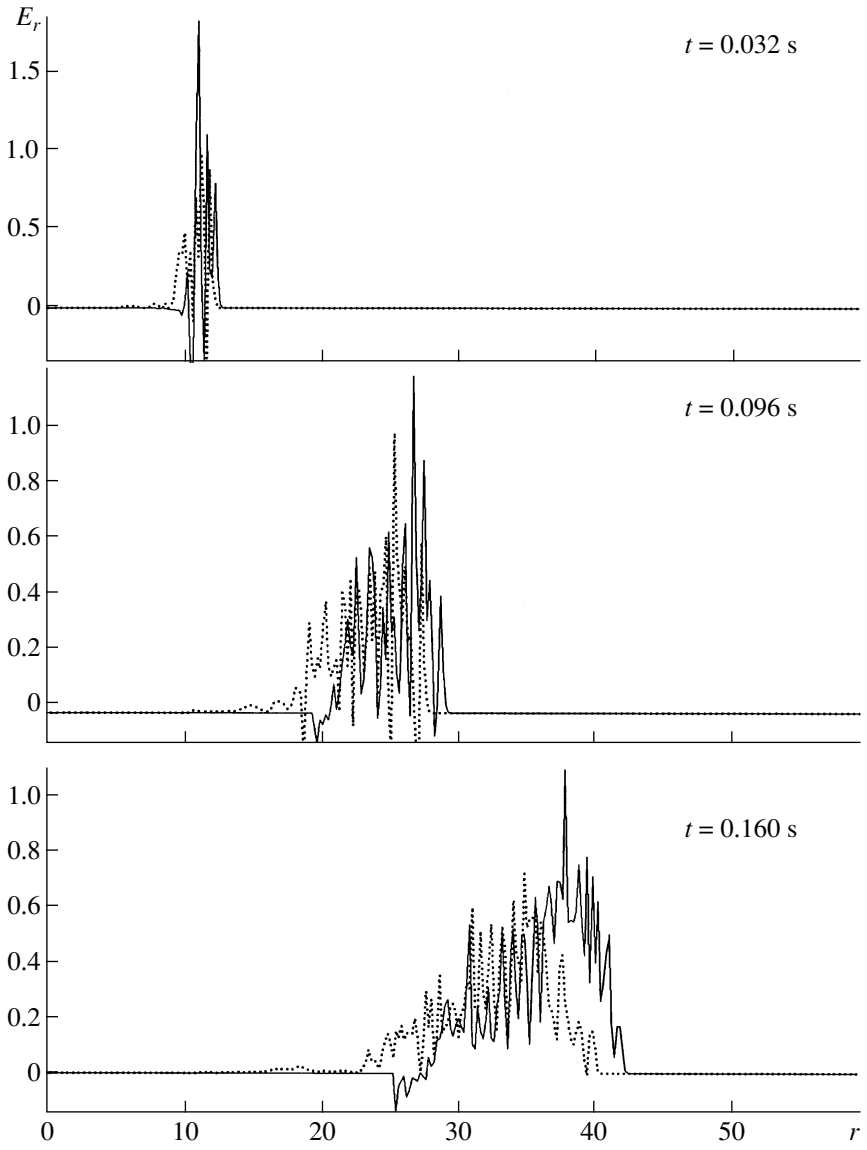

Fig. 3. Radial component of the solenoidal electric field at different instants after the plasma cloud starts to expand. The solid and dashed curves illustrate the expansion of singly and doubly charged plasma clouds, respectively.

term in the denominator on the right-hand side of the convergence condition was less than the first term.

4. SIMULATION RESULTS

At the initial instant, a homogeneous cylindrical plasma cloud containing either singly charged ions or both singly and doubly charged ions of mass $m_{\alpha=1,2}$ = 27 amu and total density $n_1 + n_2 = 2.7 \times 10^8$ cm^{-3} was assumed to start expanding in the radial direction with the velocity

$$V_r = \frac{r}{R_0} V_0,$$

where $V_0 = (0.035\text{–}0.35) \times 10^9$ cm/s, which corresponds approximately to the experimental conditions of [9]. Both series of simulations were carried out for the same density and mass of the BP ions and the same magnetic field H_*: $n_* = 0.96 \times 10^7$ cm^{-3}, m_* = 16 amu, and H_* = 0.5 Oe. These parameter values correspond to the following ranges of Alfvén–Mach numbers and BP ion gyroradii: $M_A \approx$ 4–40 and $R_{H_*} \approx (0.01\text{–}0.1) \times 10^7$ cm. In both series of simulations, the cyclotron frequency of the BP ions was set to be $\Omega_{H_*} \approx 300$ s^{-1}. The initial radius of the plasma cloud was chosen to be $R_0 = 2R_{H_*}$.

For a fixed initial expansion velocity, we simulated the expansion of both a plasma cloud containing only

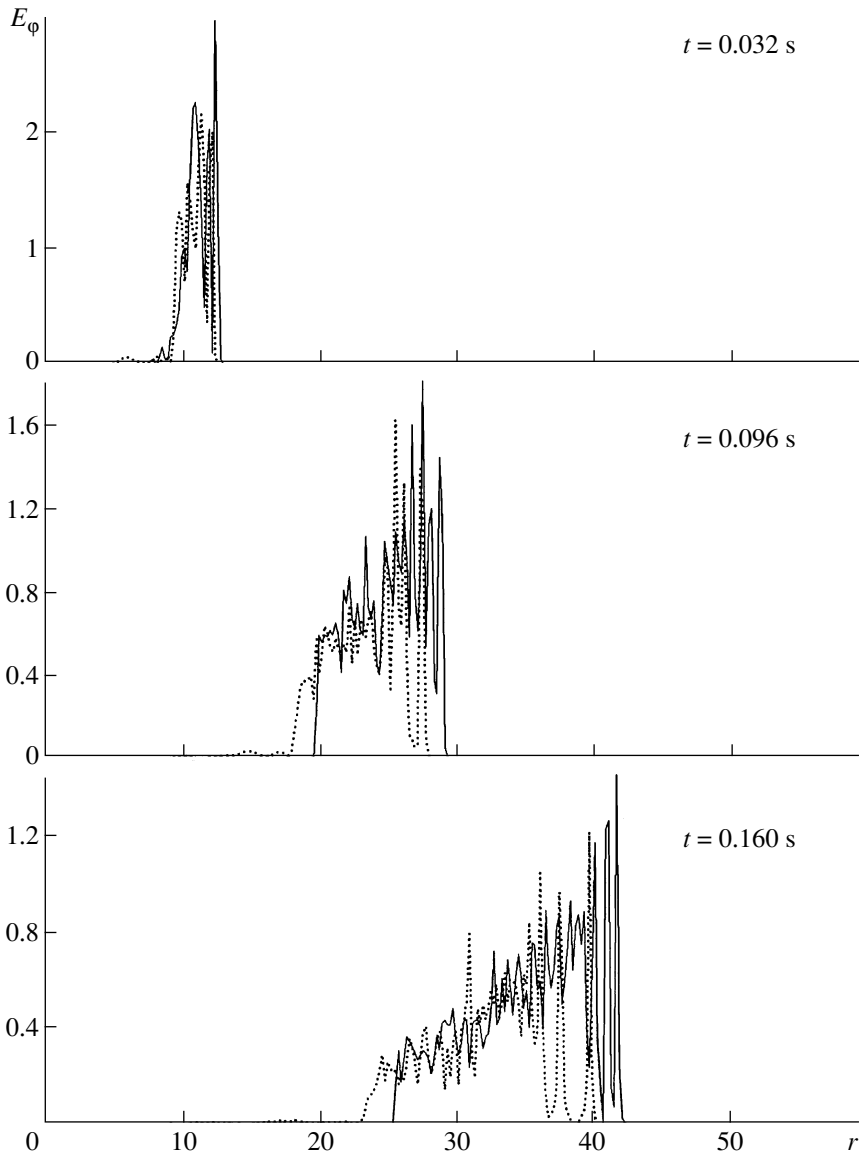

Fig. 4. Azimuthal component of the solenoidal electric field at different instants after the plasma cloud starts to expand. The solid and dashed curves illustrate the expansion of singly and doubly charged plasma clouds, respectively.

singly charged ions and a cloud containing both singly and doubly charged ions (below, we will refer to these clouds as "singly charged" and "doubly charged" plasma clouds, respectively). At the initial instant, the magnetic field was assumed to be expelled from the region occupied by the EP. The dynamics of the EP and BP was modeled by tracing the motion of $N_{p,1} = 6000$, $N_{p,2} = 6000$, and $N_{p,3} = 18000$ particles on a uniform spatial Eulerian grid consisting of $N_i = 300$ points, so that, on average, each Eulerian cell contained about 60 particles of the BP and from 20 to 40 particles of the EP.

The kinetic equations (11)–(13) were integrated with a time step of about 1/100 of the cyclotron period of the BP ions.

Although the expansion scenarios are very different for different initial expansion velocities (or, in fact, for different initial energies of the EP), we concentrated on revealing the most important points in which the expansion of a multicharged plasma differs from that of a plasma cloud containing only singly charged ions. The basic calculation version was chosen to be that with $V_0 = 0.35 \times 10^9$ cm/s; the simulation results for this version are illustrated in Figs. 1–9.

Each of these figures shows the computation results obtained at three subsequent times, 0.032, 0.096, and 0.16 s, after the plasma cloud started to expand; these times correspond to 1000, 3000, and 5000 time steps.

Figures 1–5 display the mean radial ion velocity, the magnetic field strength, the radial and azimuthal com-

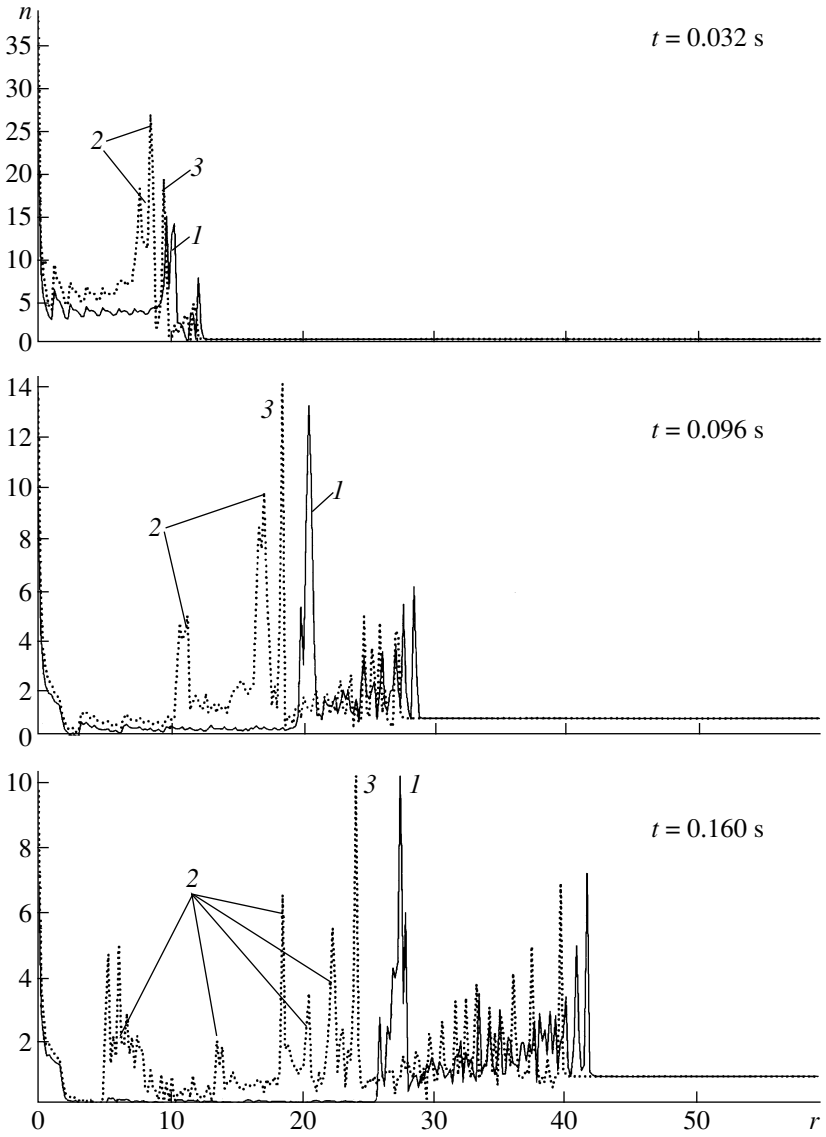

Fig. 5. Particle density of the EP and BP at different instants after the plasma cloud starts to expand: (*1*) the outer boundary of a singly charged plasma cloud, (*2*) local peaks in the density profiles of the doubly charged ions in a doubly charged EP cloud, and (*3*) local peaks in the density profiles of the singly charged ions in a doubly charged EP cloud. The solid and dashed curves illustrate the expansion of singly and doubly charged plasma clouds, respectively.

ponents of the solenoidal electric field, and the total density of the EP and BP ions, respectively. In each figure, the solid and dashed curves illustrate the simulation results for singly and doubly charged plasma clouds, respectively.

We point out the following features of the expansion processes.

(i) The EP gives rise to a collisionless shock wave (CSW) in the BP. In Fig. 1, the outer boundary of the shock front driven by an expanding, singly charged ion cloud is denoted by the symbol *1* and the outer boundary of the EP is marked by the symbol *2*. The distance between these boundaries is distinctly seen to increase as time elapses. The reason is that the ions at the outer boundary of the expanding cloud are decelerated, in which case part of the kinetic energy of the EP is transferred to the BP ions via electromagnetic interactions.

(ii) Inside the shock front (i.e., in the region between the outer boundaries of the CSW and the EP), the BP is seen to experience a complicated multistream motion. This is illustrated in Fig. 6, which shows the phase portrait of the BP ions in the case of expansion of a doubly charged cloud. The points in Fig. 6 correspond to every sixth particle. Inside the shock front, there are regions where a significant number of particles move either in the positive or negative direction. At the outer boundary of the CSW, we see the formation of periodic wavelike structures, i.e., the regions where the ions are alterna-

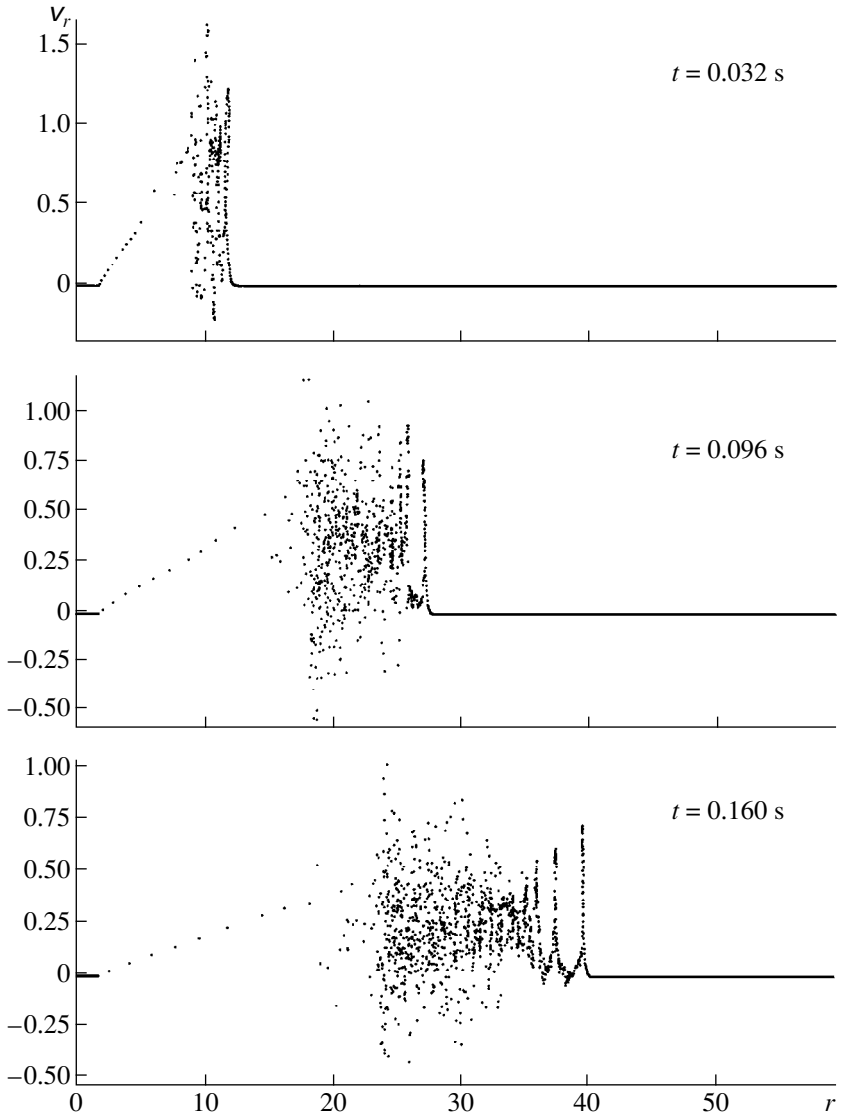

Fig. 6. Dynamics of particles of the BP during the expansion of a doubly charged plasma cloud.

tively accelerated and decelerated. These structures are seen most vividly at the time t = 0.16 s over distances (35–40)R_{H_*}. The upper part of the figure (which corresponds to the time t = 0.032 s) clearly illustrates the structure of the CSW front: the particles that started to move under the action of the solenoidal electric field form a loop in which the ions that were initially closer to the symmetry axis and started to move earlier turn out to be located at larger distances from the axis than the ions that started to move at later times. In fact, we observe the breaking of the CSW front. At first glance, the ion motion inside the CSW is stochastic. However, analyzing the overall dynamic picture of the processes, we can see that the looplike motion repeats over and over again. However, we must keep in mind that the particles not only experience radial motion but also rotate in the azimuthal direction (around the symmetry axis).

(iii) The magnetic field is expelled from the region into which the plasma cloud expands. Figure 2 shows that, at subsequent times, the magnetic field is displaced by distances of about 9, 19, and 25R_{H_*}. In the course of expansion, the magnetic field strength is observed to oscillate stochastically inside the shock front; the peak strengths of the magnetic field are larger than the background magnetic field strength by a factor of three. Due to the displacement of the magnetic field, the perturbed region is essentially free of the electric field. From Figs. 3 and 4, we can see that the solenoidal electric field is generated preferentially inside the shock front and that the peak azimuthal component exceeds the peak radial component by a factor of more

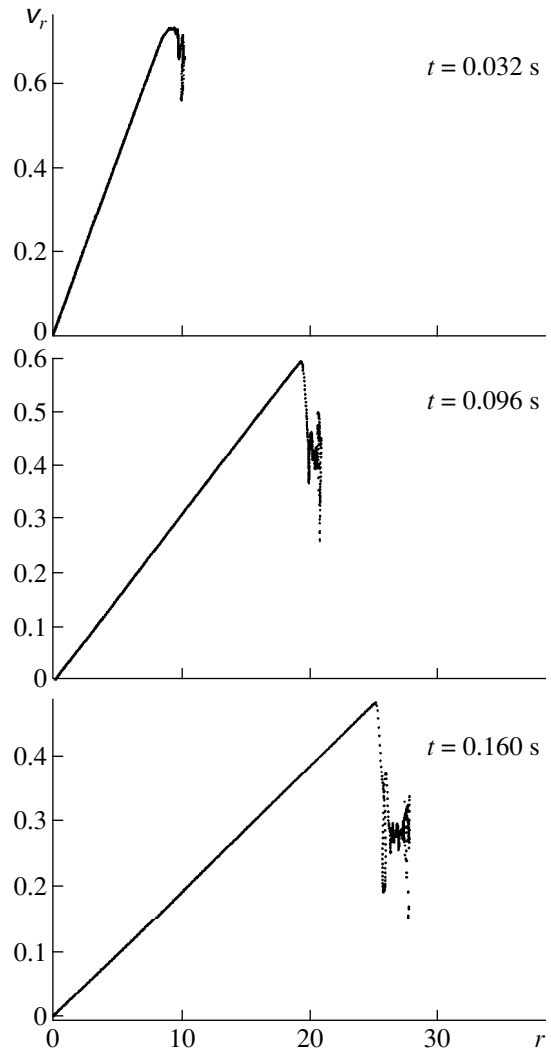

Fig. 7. Dynamics of particles of a singly charged EP cloud.

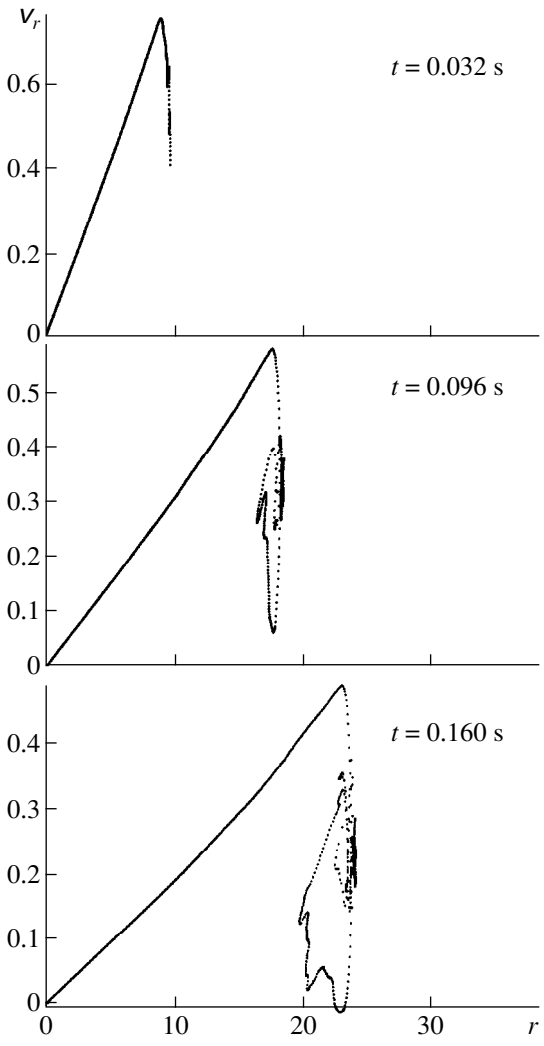

Fig. 8. Dynamics of singly charged particles during the expansion of a doubly charged plasma cloud.

than two. The peak azimuthal component is maximum at the outer boundary of the CSW, while the peak radial component is maximum at the symmetry axis. This result is consistent with the physical mechanism for the generation of the solenoidal electric field: according to equations (23), the solenoidal electric field is excited by the EP ions that enter the region occupied by the magnetic field.

(iv) In the course of expansion, an initially homogeneous plasma cloud evolves into a plasma shell. In Fig. 5, which illustrates the evolution of the total density of the EP and BP ions, the boundary of the singly charged plasma cloud is marked by the symbol *1*. At large radial distances from the symmetry axis, only the density of the BP ions oscillates. We can clearly see that, in contrast to the case of a singly charged plasma cloud (illustrated by solid curves), an expanding doubly charged plasma cloud does not evolve into a plasma shell. The dynamics of a doubly charged cloud is characterized by the separation of ions of different species: doubly charged ions (marked by the symbol *2* in Fig. 5) are mostly concentrated inside the cloud, while singly charged ions (marked by the symbol *3*) are accumulated at the outer boundary of the cloud. Such behavior of the ions in the doubly charged EP cloud is illustrated in Fig. 1, which shows the profiles of the mean radial velocity. We can see the regions where doubly charged ions move back to the symmetry axis, thereby making the mean plasma velocity negative. At times later than those designated in Fig. 1, singly charged ions also start to move back to the symmetry axis, but doubly charged ions again start to expand. Comparing the expansion of singly and doubly charged plasma clouds, we emphasize that, on the whole, a doubly charged cloud is slowed down at a higher rate and drives a slower CSW. In Fig. 1, we can see that, at the time $t = 0.16$ s, the outer boundary of the CSW driven by a singly charged EP

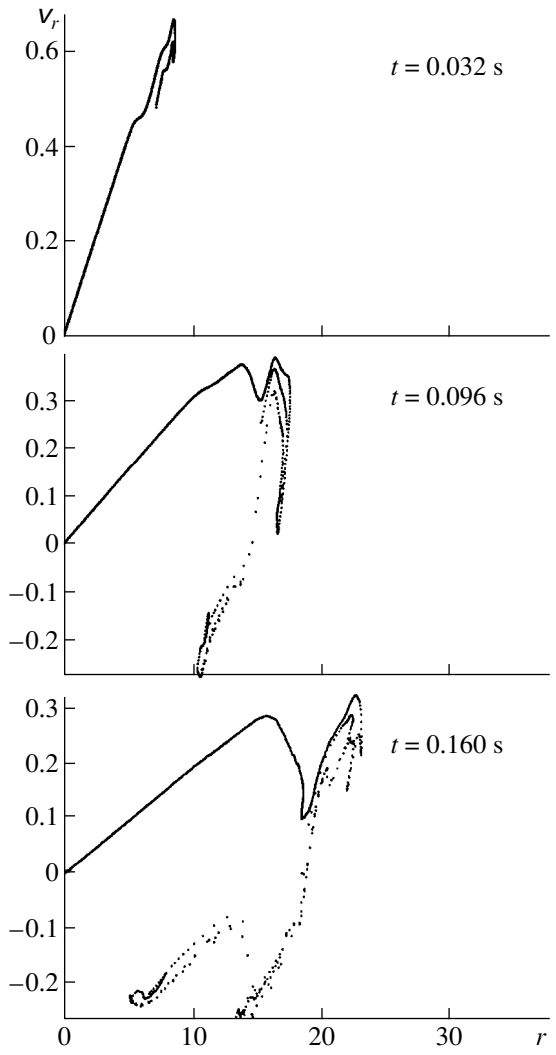

Fig. 9. Dynamics of doubly charged particles during the expansion of a doubly charged plasma cloud.

cloud is farther from the symmetry axis than the outer boundary of the CSW driven by a doubly charged EP cloud, the distance between the outer boundaries being about $\sim 2.5 R_{H_*}$. The structures of singly and doubly charged plasma clouds are demonstrated in Figs. 7–9. Figure 7 illustrates the expansion of a singly charged plasma cloud, and Figs. 8 and 9 refer to a doubly charged cloud. We can see that, at the times indicated, singly charged ions move preferentially in the radial direction away from the symmetry axis, while doubly charged ions move mostly back to the axis. A comparison between Figs. 7 and 8 clearly shows that, on the whole, the ion motion in a doubly charged EP cloud becomes stochastic earlier than that in a singly charged cloud.

Plasma clouds that start to expand at lower initial velocities evolve in an analogous manner. We point out another characteristic feature of the expansion processes: if the magnetic field is not initially expelled from the region occupied by the plasma cloud, then doubly charged ions start to decelerate earlier than singly charged ions. The remaining features of the expansion of doubly charged plasma clouds are as described above.

5. CONCLUSION

Using a hybrid numerical model (i.e., a model combining the kinetic and hydrodynamic approaches), we have solved the problem of the collisionless slowing down of the expansion of a cylindrical, doubly charged plasma cloud in a magnetized ionospheric plasma.

We have carried out a comparative analysis of the slowing down of the plasma steams of both singly charged ions and singly and doubly charged ions. Simulations performed for Alfvén–Mach numbers ranging between 4 and 40 revealed the following characteristic feature of the initial stage of the slowing down of a doubly charged EP cloud: doubly charged ions are mostly concentrated inside the cloud, while singly charged ions are accumulated at the outer boundary of the cloud. On the whole, a doubly charged plasma cloud is slowed down on shorter time scales and gives rise to slower CSWs in the ionospheric plasma.

REFERENCES

1. *Physics of Space and Laboratory Plasmas*, Ed. by A. G. Ponomarenko (Nauka, Novosibirsk, 1989).
2. V. V. Adushkin, Yu. I. Zetser, Yu. N. Kiselev, *et al.*, Dokl. Akad. Nauk **331**, 486 (1993).
3. V. S. Imshennik, in *Two-Dimensional Numerical Plasma Models*, Ed. by K. V. Brushlinskiĭ (Keldysh Inst. of Applied Mathematics, USSR Acad. Sci., Moscow, 1979), p. 120.
4. A. G. Sgro and C. W. Nielson, Phys. Fluids **19**, 126 (1976).
5. Yu. P. Zakharov, A. M. Orishich, and A. G. Ponomarenko, *Laser Plasma and Laboratory Modeling of Nonsteady Processes in Space* (Inst. of Theoretical and Applied Mechanics, Siberian Division, USSR Acad. Sci., Novosibirsk, 1988).
6. B. A. Bryunetkin, U. Sh. Begimkulov, V. M. Dyakin, *et al.*, Kvantovaya Élektron. (Moscow) **19**, 246 (1992).
7. R. Z. Sagdeev, in *Reviews of Plasma Physics*, Ed. by M. A. Leontovich (Atomizdat, Moscow, 1964; Consultants Bureau, New York, 1968), Vol. 4.
8. M. M. Leroy, Phys. Fluids **26**, 2742 (1983).
9. *Operation "Argus"* (Atomizdat, Moscow, 1960); *Operation "Sea-Star"* (Atomizdat, Mocsow, 1964).
10. V. A. Enal'skiĭ and V. S. Imshennik, Zh. Prikl. Mekh. Tekh. Fiz., No. 1, 3 (1965).
11. A. I. Golubev, A. A. Solov'ev, and V. A. Terekhin, Zh. Prikl. Mekh. Tekh. Fiz., No. 5, 33 (1978).
12. V. P. Bashurin, A. I. Golubev, and V. A. Terekhin, Zh. Prikl. Mekh. Tekh. Fiz., No. 5, 10 (1983).

13. Yu. A. Berezin, V. A. Vshivkov, and V. N. Snytnikov, Chislennye Metody Mekh. Sploshnoĭ Sredy **15** (3), 26 (1984).
14. Yu. P. Raĭzer, Zh. Prikl. Mekh. Tekh. Fiz., No. 6, 19 (1963).
15. S. M. Bakhrakh, E. V. Gubkov, V. A. Zhmaĭlo, *et al.*, Zh. Prikl. Mekh. Tekh. Fiz., No. 4, 146 (1974).
16. Yu. A. Berezin and P. V. Khenkin, Fiz. Plazmy **11**, 263 (1985) [Sov. J. Plasma Phys. **11**, 155 (1985)].
17. Yu. A. Berezin, V. A. Vshivkov, Yu. P. Zakharov, *et al.*, Fiz. Plazmy **14**, 45 (1988) [Sov. J. Plasma Phys. **14**, 28 (1988)].
18. Yu. A. Berezin, M. P. Fedoruk, and P. V. Khenkin, Fiz. Plazmy **14**, 463 (1988) [Sov. J. Plasma Phys. **14**, 272 (1988)].
19. K. G. Gus'kov, Yu. P. Raĭzer, and S. T. Surzhikov, Mat. Model. **4** (7), 49 (1992).
20. Yu. P. Raizer and S. T. Surzhikov, AIAA J. **33**, 486 (1995).
21. S. T. Surzhikov, AIAA Paper, No. 95-2000 (1995).
22. S. T. Surzhikov, AIAA Paper, No. 96-2301 (1996).
23. Yu. P. Raĭzer, Zh. Éksp. Teor. Fiz. **37**, 580 (1959) [Sov. Phys. JETP **10**, 411 (1959)].
24. S. T. Surzhikov, AIAA Paper, No. 97-2361 (1997).
25. Yu. A. Berezin and V. A. Vshivkov, *Particle Method and the Dynamics of Rarefied Plasmas* (Nauka, Novosibirsk, 1980).
26. Ch. K. Birdsall and A. B. Langdon, *Plasma Physics via Computer Simulation* (McGraw-Hill, New York, 1985; Énergoatomizdat, Moscow, 1989).
27. R. Hockney and J. Eastwood, *Computer Simulation Using Particles* (McGraw-Hill, New York, 1984; Mir, Moscow, 1987).
28. R. W. MacCormack, AIAA J. **20**, 1275 (1982).
29. A. I. Zhmakin and A. A. Fursenko, Zh. Vychisl. Mat. Mat. Fiz. **20**, 1021 (1980).

Translated by O. Khadin

Plasma Physics Reports, Vol. 26, No. 9, 2000, pp. 772–780. Translated from Fizika Plazmy, Vol. 26, No. 9, 2000, pp. 824–832.

PLASMA OSCILLATIONS AND WAVES

Splitting of the Spectra of MHD Waves and the Structure of a Satellite Alfvén Resonance in a Cold Plasma in a Strong Axial Magnetic Field and a Weak Helical Field

I. A. Girka

Karazin National University, Kharkov, Ukraine

Received February 15, 1999; in final form, December 3, 1999

Abstract—The possibility is demonstrated of splitting the eigenfrequencies of MHD plasma waves in a stellarator with a weakly rippled helical confining magnetic field. The distribution of the fields of an Alfvén wave in the satellite Alfvén resonance region is investigated when the influence of the helical ripple in a confining magnetic field on the resonance structure is comparable with the effects of the finite ion Larmor radius, electron inertia, and collisions between plasma particles. *© 2000 MAIK "Nauka/Interperiodica".*

1. INTRODUCTION

The effect of the helical ripple in a confining magnetic field on the MHD eigenmodes in stellarator plasmas is of interest in connection with the problem of plasma heating by these modes. Girka and Kovtun [1] showed that the helical field ripple generally causes the eigenfrequency of MHD waves to shift by an amount that is second order in the small parameter characterizing the deviation of the magnetic surfaces from being circular.

It is well known that the spectra of MHD oscillations of a plasma cylinder in an axial magnetic field are degenerate with respect to the sign of the axial wavenumber. Unlike in the case of an axial magnetic field, in which each MHD eigenmode propagates independently, the helical ripple in a stellarator magnetic field causes the eigenmodes to propagate as a wave envelope that contains (in addition to the fundamental harmonic proportional to $\propto \exp i(k_z z + m\vartheta - \omega t)$) satellite harmonics proportional to $\propto \exp i[(k_z - jk_s)z + (m + jl)\vartheta - \omega t]$ (here, m is the azimuthal mode number; k_z is the axial wavenumber of the fundamental mode; l is the polarity of a stellarator; and $j = \pm 1, \pm 2, \ldots, k_s = 1\alpha$ with $\alpha = 2\pi/L$ and L the pitch of the helical winding). The methods developed in [1] and the results obtained there may turn out to be inapplicable to investigating the propagation of MHD waves such that the axial wavelength of the fundamental mode is two times longer than the helical pitch and the azimuthal wavenumber of the fundamental mode is two times smaller than the polarity of the stellarator; specifically,

$$k_s = 2k_z, \quad l = 2m. \tag{1}$$

The reason is that the fundamental mode and one of the satellite modes are characterized by the same $|k_z|$. In contrast to the case of a rippled toroidal magnetic field [2], in a helical stellarator magnetic field, the azimuthal wavenumbers of the satellite modes differ from the azimuthal wavenumber of the fundamental mode. For MHD waves, the nonreciprocity effect (which indicates that eigenmodes with azimuthal wavenumbers of opposite signs have different frequencies) is often insignificant. In Section 3, we investigate the MHD eigenmodes of an inhomogeneous plasma cylinder under the resonance conditions (1), which can be satisfied in a stellarator with an even polarity and even number of helical magnetic field periods. Since the helical magnetic field is weak, we can describe degenerate spectra using perturbation theory.

Girka *et al.* [3] demonstrated the possibility of additional heating of stellarator plasmas in the satellite Alfvén resonance (SAR) regions $r = r_A^{(\pm)}$, in which we have

$$\varepsilon_1^{(0)}(r) \equiv 1 - \sum \omega_{pi}^2(r)/(\omega^2 - \omega_{ci}^{(0)2}) = (N_z \mp N_s)^2. \tag{2}$$

where $\omega_{c\sigma}$ and $\omega_{p\sigma}$ are the cyclotron and plasma frequencies of particles of species σ ($\sigma = i$ for ions and $\sigma = e$ for electrons), $N_z = ck_z/\omega$ is the axial refractive index, and the correction N_s to this index is $N_s = ck_s/\omega$. In the case of induced oscillations, the axial wavenumber k_z is assumed to be prescribed (it is governed by the spectral characteristics of the antenna). The ion cyclotron frequency $\omega_{ci}^{(0)} = eB_0/m_i c$ in (2) is defined in terms of the unrippled axial magnetic field B_0.

In the vicinity of resonances (2), the satellite harmonics of the electromagnetic field of MHD waves grow in amplitude and are converted into small-scale "kinetic" Alfvén waves. Paper [3] was aimed at investigating the case that is most favorable for Alfvén heating: the SAR region was assumed to be located deep in the plasma core, where the helical confining magnetic field of a straight stellarator is weakly rippled and the

1063-780X/00/2609-0772$20.00

plasma is hot. In this case, the extent to which the magnetic surfaces deviate from being circular due to the inhomogeneity of the axial magnetic field $\mathbf{B}_0$ is smaller than the width δr of the SAR region,

$$\delta r \sim (\rho_{Li}^2 a^*)^{1/3}, \tag{3}$$

which is defined in terms of the finite ion Larmor radius $\rho_{Li} = v_{Ti}/\omega_{ci}$, where $v_{Ti} = \sqrt{T_i/m_i}$ is the ion thermal velocity and T_i is the ion temperature. The quantity $a^* = \left|\partial \ln \varepsilon_1^{(0)}/\partial r\right|^{-1}_{r_A^{(\pm)}}$ in (3) is the characteristic distance in which the plasma density varies. In the SAR region, the radial profiles of the amplitudes of the satellite modes are governed just by the finite ion Larmor radius ρ_{Li} and electron inertia (see, e.g., [4–6]).

In Section 4, we study the SAR structure in the edge plasma, where the deviation of the magnetic surfaces from being circular is most pronounced and the plasma is usually colder than in the core.

2. FORMULATION OF THE PROBLEM

We consider the propagation of a wave with the frequency $\omega \ll \omega_{pe}, |\omega_{ce}|$ in a straight stellarator, assuming that the plasma pressure is low in comparison with the magnetic field pressure. In the paraxial approximation, the magnetic field $\mathbf{B}_0 = \mathbf{e}_r B_{0r} + \mathbf{e}_\vartheta B_{0\vartheta} + \mathbf{e}_z B_{0z}$ of an $l \geq 2$ stellarator can be described by the single harmonic [7]

$$B_{0r} = \bar{\Delta}_l B_0 \alpha r \sin(l\theta), \quad B_{0\vartheta} = \Delta_l B_0 \cos(l\theta), \quad B_{0z} = B_0 - \Delta_l B_0 \alpha r \cos(l\theta), \tag{4}$$

where

$$\bar{\Delta}_n = \frac{n b_n I_n'(k_s r)}{B_0 \alpha r}, \quad \Delta_n = \frac{n b_n I_n(k_s r)}{B_0 \alpha r},$$

$$b_n = 8 J a k_s^2 K_n'(k_s a)(nc)^{-1}, \quad \theta = \vartheta - \alpha z,$$

a is the radius of a cylindrical surface that a filamentary helical coil with current J is wound on, $K_n(\xi)$ and $I_n(\xi)$ are the modified Bessel functions, and the prime denotes the derivative with respect to the argument. The equilibrium plasma density is a function of magnetic surfaces, $n(r, \theta) = n(r_0)$, where

$$r_0 = r - 0.5 r \bar{\Delta}_l \cos(2\theta) + O(\bar{\Delta}_l^2). \tag{5}$$

We introduce the orthonormal coordinate vectors $(\mathbf{e}_1, \mathbf{e}_2, \mathbf{e}_3)$ associated with the lines of the magnetic field $\mathbf{B}_0$: $\mathbf{e}_3 = \mathbf{B}_0/|\mathbf{B}_0|$, $\mathbf{e}_1 = \mathrm{grad}(r_0)/|\mathrm{grad}(r_0)|$, and $\mathbf{e}_2 = \mathbf{e}_3 \times \mathbf{e}_1$. We solve the Maxwell equations in these coordinates, taking into account the following relationship between the electric induction vector $\mathbf{D}$ and the electric field $\mathbf{E}$ of the wave:

$$\mathbf{D} = \varepsilon_1 (E_1 \mathbf{e}_1 + E_2 \mathbf{e}_2) + \varepsilon_3 E_3 \mathbf{e}_3 - i\varepsilon_2 \mathbf{e}_3 \times \mathbf{E}. \tag{6}$$

The components of the permittivity tensor of a cold, weakly collisional plasma have the form

$$\varepsilon_1 = 1 - \sum_i \omega_{pi}^2(r_0)/(\omega^2 - \omega_{ci}^2), \quad \varepsilon_2 = \sum_i \omega_{pi}^2(r_0)\omega/[(\omega^2 - \omega_{ci}^2)\omega_{ci}]. \tag{7}$$

In (6), the integral operator ε_3 determines the absolute value of the longitudinal component of the vector $\mathbf{D}$.

Solving the Maxwell equations in the small electron inertia limit ($|\varepsilon_3| \longrightarrow \infty$), we find that the longitudinal component E_3 of the wave electric field vanishes over the entire plasma column, $E_3 = (B_{0r}E_r + B_{0\vartheta}E_{0\vartheta} + B_{0z}E_z)/|\mathbf{B}_0| \longrightarrow 0$. With this relationship between the components of the wave electric field, we can neglect the effects of collisions, electron inertia, and the finite ion Larmor radius in order to reduce the Maxwell equations to the following set of equations for the components of the wave electromagnetic field in cylindrical coordinates:

$$\left[\frac{1}{r}\frac{\partial B_z}{\partial \vartheta} - \frac{\partial B_\vartheta}{dz}\right] + \bar{\Delta}_l \sin(l\theta)\left[\frac{\partial B_r}{\partial z} - \frac{\partial B_z}{\partial r}\right] - \alpha r \bar{\Delta}_l \sin(l\theta)\left[\frac{1}{r}\frac{\partial (rB_\vartheta)}{\partial r} - \frac{1}{r}\frac{\partial B_r}{\partial \vartheta}\right] = \frac{\omega \varepsilon_1}{ic}\{E_r + E_\vartheta \bar{\Delta}_l \sin(l\theta)\} + \frac{\omega \varepsilon_2}{c}\{-E_r \bar{\Delta}_l \sin(l\theta) + E_\vartheta\},$$

$$-\bar{\Delta}_l \sin(l\theta)\left[\frac{1}{r}\frac{\partial B_z}{\partial \vartheta} - \frac{\partial B_\vartheta}{\partial z}\right] + \left[\frac{\partial B_r}{\partial z} - \frac{\partial B_z}{\partial r}\right] - \Delta_l \cos(l\theta)\left[\frac{1}{r}\frac{\partial (rB_\vartheta)}{\partial r} - \frac{1}{r}\frac{\partial B_r}{\partial \vartheta}\right] = \frac{\omega \varepsilon_1}{ic}\{-E_r \bar{\Delta}_l \sin(l\theta) + E_\vartheta\} - \frac{\omega \varepsilon_2}{c}\{E_r + E_\vartheta \bar{\Delta}_l \sin(l\theta)\}, \tag{8}$$

$$B_r = \frac{ic}{\omega r}\frac{\partial}{\partial \vartheta}[E_r \alpha r \bar{\Delta}_l \sin l\theta + E_\vartheta \Delta_l \cos l\theta] + \frac{ic}{\omega}\frac{\partial E_\vartheta}{\partial z},$$

$$B_\vartheta = \frac{c}{i\omega}\frac{\partial E_r}{\partial z} + \frac{c}{i\omega}\frac{\partial}{\partial r}[E_r \alpha r \bar{\Delta}_l \sin l\theta + E_\vartheta \Delta_l \cos l\theta],$$

$$B_z = \frac{c}{i\omega r}\frac{\partial}{\partial r}(rE_\vartheta) + \frac{ic}{\omega r}\frac{\partial E_r}{\partial \vartheta}.$$

To solve Eqs. (8), we need to know the first-order expressions for the tensor components ε_1 and ε_2:

$$\varepsilon_{1,2}(r,\theta) = \varepsilon_{1,2}^{(0)}(r) + \varepsilon_{1,2}^{(1)}(r)\cos(l\theta) + O(\Delta_l^2), \quad (9)$$

where $|\varepsilon_{1,2}^{(1)}| \sim |\Delta_l \varepsilon_{1,2}^{(0)}|$,

$$\varepsilon_2^{(0)}(r) \equiv \varepsilon_2(r,\theta)|_{\Delta_l = 0} = \sum_i \omega_{pi}^2(r)\omega/[(\omega^2 - \omega_{ci}^{(0)2})\omega_{ci}^{(0)}], \quad (10)$$

$$\varepsilon_1^{(1)}(r) = \left.\frac{\partial \omega_{pi}^2}{\partial r}\right|_{\Delta_l = 0} \frac{r\bar{\Delta}_l}{2}\sum_i \frac{1}{\omega^2 - \omega_{ci}^{(0)2}} + 2\sum_i \frac{\omega_{pi}^2(r)\omega_{ci}^{(0)2}}{(\omega^2 - \omega_{ci}^{(0)2})^2}\alpha r\Delta_l, \quad (11)$$

$$\varepsilon_2^{(1)}(r) = -\left.\frac{\partial \ln(\omega_{pi}^2)}{\partial r}\right|_{\Delta_l = 0} \frac{r\bar{\Delta}_l}{2}\varepsilon_2^{(0)} + \sum_i \frac{\omega_{pi}^2(r)\omega(3\omega_{ci}^{(0)2} - \omega^2)}{\omega_{ci}^{(0)}(\omega^2 - \omega_{ci}^{(0)2})^2}\alpha r\Delta_l. \quad (12)$$

3. SPLITTING OF THE SPECTRA OF MHD PLASMA WAVES IN A WEAKLY RIPPLED HELICAL MAGNETIC FIELD

In the problem of eigenmodes, the solution to Eqs. (8) should satisfy the following boundary conditions. The wave field inside a metal chamber should be finite, and the tangential component of the electric field should vanish at the inner surface of the chamber ($E_2|_{r=a} = 0$). If there is a vacuum gap between the plasma column and the chamber, then the tangential component $\mathbf{E}_2$ of the electric field and the longitudinal component $\mathbf{B}_3$ of the wave magnetic field should be continuous at the plasma–vacuum boundary. Further analysis in this section refers to an $l = 2$ stellarator.

The symmetry properties of the problem [see relationship (9)] allow us to seek a solution to Eqs. (8) for the axial component of the magnetic field of an MHD wave using the well-known procedure for deriving the secular equation (i.e., for applying perturbation theory to the case in which the spectrum is degenerate):

$$B_z = [(C_0^{(+)}\psi_1^{(0)}(r) + C_1^{(+)}\psi_1^{(+)}(r))e^{i\theta} + (C_0^{(-)}\psi_1^{(0)}(r) + C_1^{(-)}\psi_1^{(-)}(r))e^{-i\theta} + C_3^{(+)}\psi_3^{(+)}(r)e^{3i\theta} + C_3^{(-)}\psi_3^{(-)}(r)e^{-3i\theta}]\exp(-i\omega t), \quad (13)$$

where $|C_{1,3}^{(\pm)}\psi_{1,3}^{(\pm)}| \sim |\Delta_2 C_0^{(\pm)}\psi_1^{(0)}|$. The expressions for the remaining components of the magnetic and electric fields of an MHD wave are similar to (13).

3.1. Solution to Eqs. (8) in the Zeroth Approximation

In the absence of current-carrying helical coils ($\Delta_2 = 0$), the radial profile $\psi_j^{(0)}(r)$ ($j = 1, 3$) of the axial component of the magnetic field of an MHD wave satisfies the equation

$$\frac{1}{r}\frac{\partial}{\partial r}\frac{r}{k_j^2}\frac{\partial \psi_j^{(0)}}{\partial r} + q_j\psi_j^{(0)} = 0, \quad (14)$$

where

$$q_j \equiv q(j\alpha, r) = 1 - \frac{m^2}{k_j^2 r^2} + \frac{m}{r}\frac{\partial}{\partial r}\left(\frac{\mu_j}{k_j^2}\right), \quad (15)$$

$$k_j^2 \equiv k_\perp^2(j\alpha, r) = (\omega/c)^2(\varepsilon_1^{(0)} - j^2N^2)(1 - \mu_j^2), \quad (16)$$

$$\mu_j \equiv \mu(j\alpha, r) = \varepsilon_2^{(0)}/(\varepsilon_1^{(0)} - j^2N^2), \quad (17)$$

with $N = c\alpha/\omega$ being the axial refractive index for the fundamental mode.

The distribution of the RF fields of MHD waves in a plasma cylinder with a radially nonuniform density profile can be obtained numerically from Eq. (14) (see, e.g., [8]). Consequently, the solutions $\psi_j^{(0)}(r)$ to Eq. (14) that are finite at $r = 0$ and the solutions $\tilde{\psi}_j^{(0)}(r)$ that have a singularity at $r = 0$ and correspond to waves with the axial wavenumber $j\alpha$ can be assumed to be known. In this section, the plasma density profile is assumed to be such that the fundamental Alfvén resonance (AR), for which

$$\varepsilon_1^{(0)}(r) = N^2, \quad (18)$$

holds, and the SAR (2) are both absent. Under these assumptions, the functions $\psi_j^{(0)}(r)$ and $\tilde{\psi}_j^{(0)}(r)$ can be chosen to be real.

The dispersion relation for MHD oscillations of a plasma cylinder in an axial magnetic field is well known. The solution $\omega = \omega_0$ to the dispersion relation describes MHD waves in a stellarator plasma in the zeroth approximation. An analysis of the dispersion relation shows that, for small-scale fast magnetosonic (FMS) waves propagating nearly perpendicular to the magnetic field in a plasma cylinder, the nonreciprocity effect is weak:

$$\frac{\omega_0(+|m|) - \omega_0(-|m|)}{\omega_0} \approx \frac{2(1 + \omega/\omega_{ci})|m|}{(\pi n_r)^2}, \quad (19)$$

where n_r is the number of half-waves whose total length is equal to the radius of the plasma column. It is the eigenfrequency of waves with the azimuthal wavenumber $m = \pm 1$ and axial wavenumber $k_z = \mp\alpha$ that is expected to be split by the helical ripple in a stellarator confining magnetic field.

3.2. Solution to Eqs. (8) in the First Approximation

Linear inhomogeneous differential equations for the amplitudes $\psi_j^{(\pm)}(r)$ can be derived by substituting the wave field components (13) into Eqs. (8) and collecting terms proportional to $\propto \exp(ij\alpha z)$:

$$\left(\frac{1}{r}\frac{\partial}{\partial r}\frac{r}{k_j^2}\frac{\partial}{\partial r} + q_j\right)C_j^{(\pm)}\psi_j^{(\pm)} = -\hat{G}_j^{(\pm)}C_0^{(\pm)}\psi_1^{(0)}, \quad (20)$$

where the operator $\hat{G}_j^{(\pm)}$ is defined as

$$\hat{G}_j^{(\pm)}C_0^{(\pm)}\psi_1^{(0)} = \frac{\omega}{cr}\frac{\partial}{\partial r}\left[\frac{r}{k_j^2}(F_j^{(\pm)} + \mu_j A_j^{(\pm)})\right] + \frac{\omega m}{crk_j^2}(A_j^{(\pm)} + \mu F_j^{(\pm)}). \quad (21)$$

The quantities $A_j^{(\pm)}$ and $F_j^{(\pm)}$ with $j = 3$ in (21) have the form

$$A_j^{(\pm)} = \frac{-j}{2}N^2E_r^{(\pm)}\frac{d}{dr}(r\bar{\Delta}) - (j-1)N^2r\bar{\Delta}\frac{dE_r^{(\pm)}}{dr} + \frac{\varepsilon_1^{(1)}}{2}E_r^{(\pm)} + \frac{i\varepsilon_2^{(1)}}{2}E_\vartheta^{(\pm)} \pm \frac{jcN}{2i\omega}\frac{d}{dr}(\Delta E_\vartheta^{(\pm)}) \quad (22)$$
$$\mp\frac{\bar{\Delta}\varepsilon_2^{(0)}}{2}E_r^{(\pm)} \mp \frac{i\varepsilon_1^{(0)}\bar{\Delta}}{2}E_\vartheta^{(\pm)} \pm \frac{\bar{\Delta}c}{2\omega}\frac{d}{dr}C_0^{(\pm)}\psi_1^{(0)},$$

$$F_j^{(\pm)} = \mp\frac{j^2N^2\bar{\Delta}}{2}E_r^{(\pm)} - \frac{j^2Nc\Delta i}{2\omega r}E_\vartheta^{(\pm)} \pm \frac{\varepsilon_1^{(0)}}{2}\bar{\Delta}E_r^{(\pm)} - \frac{\varepsilon_2^{(1)}}{2}E_r^{(\pm)} - \frac{i}{2}\varepsilon_1^{(1)}E_\vartheta^{(\pm)} \pm \frac{i}{2}\varepsilon_2^{(0)}\bar{\Delta}E_\vartheta^{(\pm)} + \frac{\bar{\Delta}c}{2\omega r}C_0^{(\pm)}\psi_1^{(0)} \quad (23)$$
$$\mp\frac{\bar{\Delta}}{2}N^2E_r^{(\pm)} \mp \frac{\Delta cN}{2\omega}\frac{d}{dr}E_r^{(\pm)} - \frac{ic\Delta N}{2\omega r}E_\vartheta^{(\pm)}.$$

For simplicity, here and below, we omit the subscript 2 in Δ_2 and $\bar{\Delta}_2$. To find a small first-order correction to the amplitudes $\psi_j^{(\pm)}(r)$ of the fundamental harmonics, we set $j = 1$ in expressions (22) and (23) for $A_j^{(\pm)}$ and $F_j^{(\pm)}$ and replace the superscripts $(\pm) \longrightarrow (\mp)$ on the right-hand sides of these expressions. As a result, we obtain the amplitudes of the fundamental harmonics of the radial and azimuthal components ($E_{r0}^{(\pm)}$ and $E_{\vartheta 0}^{(\pm)}$) of the electric field:

$$E_{r0}^{(\pm)} = C_0^{(\pm)}u^{(\pm)}(r) - \frac{\omega^2}{c^2k_1^2}(A_1^{(\pm)} + \mu_1F_1^{(\pm)}), \quad (24)$$

$$E_{\vartheta 0}^{(\pm)} = iC_0^{(\pm)}v^{(\pm)}(r) - \frac{i\omega^2}{c^2k_1^2}(F_1^{(\pm)} + \mu_1A_1^{(\pm)}), \quad (25)$$

where

$$u^{(\pm)}(r) = \frac{-\omega}{ck_1^2}\left(\frac{\pm 1}{r}\psi_1^{(0)} + \mu_1\frac{\partial\psi_1^{(0)}}{\partial r}\right), \quad (26)$$

$$v^{(\pm)}(r) = \frac{-\omega}{ck_1^2}\left(\frac{\pm\mu_1}{r}\psi_1^{(0)} + \frac{\partial\psi_1^{(0)}}{\partial r}\right). \quad (27)$$

To calculate the operator $\hat{G}_j^{(\pm)}$, it is sufficient to collect terms that are zero order in Δ in expression (21) taken with the amplitudes $E_{r0}^{(\pm)}$ and $E_{\vartheta 0}^{(\pm)}$.

The solutions to Eq. (20) that are finite at $r = 0$ have the form

$$C_j^{(\pm)}\psi_j^{(\pm)} = H_j^{(\pm)}\psi_j^{(0)} + \psi_j^{(0)}\int_r^{a_p} W_j^{-1}k_j^2\tilde{\psi}_j^{(0)}\hat{G}_j^{(\pm)}C_0^{(\pm)}\psi_1^{(0)}dr - \tilde{\psi}_j^{(0)}\int_0^r W_j^{-1}k_j^2\psi_j^{(0)}\hat{G}_j^{(\pm)}C_0^{(\pm)}\psi_1^{(0)}dr, \quad (28)$$

with the Wronskian $W_j = \psi_j^{(0)}d\tilde{\psi}_j^{(0)}/dr - \tilde{\psi}_j^{(0)}d\psi_j^{(0)}/dr$. The integration constants $H_3^{(\pm)} \sim \Delta C_0^{(\pm)}$ are determined from the condition when amplitudes $E_{\vartheta 1}^{(\pm)}$ [which are proportional to $\exp(\pm 3i\theta)$] of the satellite harmonics of the azimuthal electric field of an MHD wave vanish at the metal surface of the chamber ($E_{\vartheta 1}^{(\pm)}(a) = 0$), where

$$E_{\vartheta 1}^{(\pm)} = \frac{\omega^2}{ic^2k_3^2}\left(\frac{c}{\omega}C_3^{(\pm)}\frac{\partial\psi_3^{(\pm)}}{\partial r} + F_3^{(\pm)}\right) - \frac{i\mu_3\omega^2}{c^2k_3^2}\left(\frac{cm}{\omega r}C_3^{(\pm)}\psi_3^{(\pm)} + A_3^{(\pm)}\right). \quad (29)$$

The integration constants $H_1^{(\pm)} \sim \Delta C_0^{(\pm)}$ are found from the condition

$$\int_0^a \psi_1^{(0)}C_1^{(\pm)}\psi_1^{(\pm)}rdr = 0, \quad (30)$$

which implies that the energy of the wave magnetic field, calculated to first order in Δ, coincides with the energy calculated in the zeroth approximation. In quantum mechanics [9], this corresponds to the normalization condition for the wave function.

3.3. Dispersion Relation for MHD Waves in a Stellarator Filled Entirely with a Plasma

First, we assume that the plasma fills the entire volume of a chamber that coincides in shape with the boundary magnetic surface,

$$r = a(1 + 0.5\bar{\Delta}(a)\cos(2\theta)). \tag{31}$$

We single out the fundamental harmonics, which are proportional to $\exp(\pm i\theta)$, in the boundary condition at the metal surface to obtain the dispersion relation

$$D^{(0)2} - D^{(+)}D^{(-)} = 0, \tag{32}$$

where

$$D^{(0)} = \left\{\frac{c}{\omega}\frac{\partial\psi_1^{(0)}}{\partial r} + \mu_1\psi_1^{(0)}\right\}\Bigg|_{r=a}, \tag{33}$$

$$\begin{aligned} D^{(\pm)} = &-\frac{\bar{\Delta}ack_1^2}{\omega^4}\frac{dv^{(\mp)}}{dr} - \frac{\bar{\Delta}c^2k_1^2u^{(\mp)}}{2\omega^2} \\ &-\frac{c}{\omega}\frac{d\tilde{\psi}_1^{(0)}}{dr}\int_0^{a_p} W_1^{-1}k_1^2\psi_1^{(0)}\hat{G}_1^{(\pm)}\psi_1^{(0)}dr \\ &+ u^{(\pm)}\left[\mp\bar{\Delta}N^2 \pm \frac{\varepsilon_1^{(0)}\bar{\Delta}}{2} - \frac{\varepsilon_2^{(1)}}{2} + \frac{\mu_1\varepsilon_1^{(1)}}{2} \mp \frac{\mu_1\bar{\Delta}\varepsilon_2^{(0)}}{2}\right. \\ &\left. - \frac{\mu_1}{2}N^2\frac{d}{dr}(r\bar{\Delta})\right] - \frac{\bar{\Delta}c\psi_1^{(0)}}{2\omega r} \pm \frac{\Delta cN}{2\omega}\frac{du^{(\pm)}}{dr} \\ &\pm \frac{\mu_1Nc}{2\omega}\frac{d}{dr}(\Delta v^{(\mp)}) \pm \frac{\mu_1\bar{\Delta}c}{2\omega}\frac{d\psi_1^{(0)}}{dr}\Bigg|_{r=a}. \end{aligned} \tag{34}$$

The eigenfrequency of MHD waves can be found from dispersion relation (32) in the form

$$\omega = \omega_0 \pm \delta\omega, \tag{35}$$

where the correction $\delta\omega$ introduced by the helical ripple in an external magnetic field is equal to

$$\delta\omega = (D^{(+)}D^{(-)})^{1/2}(\partial D^{(0)}/\partial\omega)\Big|^{-1}_{\omega=\omega_0}. \tag{36}$$

When the dependence $D^{(0)}(\omega)$ is not specified analytically (e.g., when the field distributions $\psi_1^{(0)}$ and $\tilde{\psi}_1^{(0)}$ are found numerically), the derivative $\partial D^{(0)}/\partial\omega$ in (36) can be calculated perturbatively [10].

We apply the above formulas to investigate how the helical ripple in a confining magnetic field affects the frequency of small-scale FMS waves propagating in a plasma with a uniform density profile. In this case, the solution to Eqs. (14) is expressed in terms of the first-order Bessel function, $\psi_1^{(0)} = J_1(k_1r)$, and the frequency ω_0 has the form

$$\omega_0 = j_{1,s}v_A/b, \tag{37}$$

where $v_A = c\omega_{ci}/\omega_{pi}$ is the Alfvén velocity and $j_{1,s}$ is the sth root of the Bessel function: $J_1(j_{1,s}) = 0$. The correction to the frequency of these waves is equal to

$$\delta\omega = 0.25\bar{\Delta}(a)\omega_0. \tag{38}$$

3.4. Dispersion Relation for MHD Waves in a Plasma Column Separated from the Chamber by a Vacuum Gap

In present-day stellarators, the plasma column is usually separated from the cylindrical chamber by a vacuum gap. In accordance with the boundary condition at the surface of a circular metal chamber, the axial component of the magnetic field of an MHD wave in the vacuum gap has the form

$$\begin{aligned} B_z = &[P_0^{(+)}g_1(r)e^{i\theta} + P_0^{(-)}g_1(r)e^{-i\theta} + P_1^{(+)}g_3(r)e^{3i\theta} \\ &+ P_1^{(-)}g_3(r)e^{-3i\theta}]\exp(-i\omega t), \end{aligned} \tag{39}$$

where

$$\begin{aligned} g_j(r) &\equiv K_j'(\kappa_j a)I_j(\kappa_j r) - I_j'(\kappa_j a)K_j(\kappa_j r), \\ \kappa_j^2 &= j^2\alpha^2 - \omega^2/c^2. \end{aligned} \tag{40}$$

The conditions at the outermost magnetic surface with a mean radius a_p yield the dispersion relation in a form similar to (32).

We investigate the splitting of the spectra of magnetosonic waves in a plasma cylinder separated from a circular metal chamber by a narrow vacuum gap such that $|m|(a - a_p) \ll a$. The frequency of FMS waves propagating nearly perpendicular to the magnetic field ($k_A^2 \gg \kappa_1^2$) is equal to

$$\omega_0 = \pi n_r\frac{\omega_{ci}^{(0)}c}{\omega_{pi}a}\left(1 - \frac{k_A(a - a_p)}{\pi n_r}\right), \tag{41}$$

where $k_A = \omega\omega_{pi}/(c\omega_{ci})$ is the Alfvén wavenumber. The helical ripple in a magnetic field gives rise to the following correction to the frequency of such FMS waves:

$$\delta\omega = 0.25k_A^2(a - a_p)^2\bar{\Delta}(a_p)\omega_0. \tag{42}$$

The splitting of the eigenfrequency of FMS waves [see (42)] is less pronounced than that deduced in the previous subsection [see (38)], because the small parameter $\bar{\Delta}$ in (4) falls off sharply (almost exponentially) with decreasing radius, $\bar{\Delta}(a_p) < \bar{\Delta}(a)$. A smaller splitting can also be explained by the fact that the main contribution to $\delta\omega$ in (38) comes from the noncircular shape of the metal chamber, while correction (42) was derived under the assumption that the chamber is circular.

If the plasma column is separated from the metal chamber by a wide vacuum gap such that $\kappa_1(a - a_p) \gg 1$, then correction (36) to the frequency of MHD waves

becomes exponentially small, in which case the frequency of FMS waves is equal to

$$\omega = (v_A/a_p)(j_{1,k} + \kappa_1/k_A)(1 + 0.25\bar{\Delta}(a_p)). \quad (43)$$

3.5. Conclusions Regarding the Possible Splitting of the MHD Wave Spectra

The above analysis of the effect of the helical ripple in a confining magnetic field on the eigenmodes and eigenfrequencies of MHD waves under the resonance conditions (1) imposed on the axial wavelength and azimuthal wavenumber of the fundamental mode allows us to draw the following conclusions.

(i) In the resonant case, the helical ripple in a confining magnetic field gives rise to the splitting of the eigenfrequencies of MHD waves, $\omega = \omega_0 \pm \delta\omega$, if the nonreciprocity effect for these waves is insignificant. The corrections $\delta\omega$ to the eigenfrequencies are small first-order quantities, unlike in the nonresonant case, in which they are of the second order.

(ii) In the resonant case, the eigenmodes are standing waves. The positions of the nodes of a standing wave with the higher frequency $\omega = \omega_0 + \delta\omega$ coincide with those of the antinodes of a standing wave with the lower frequency $\omega = \omega_0 - \delta\omega$ and are situated at the surfaces at which the confining magnetic field is the weakest. The reason for this is that the larger the strength $|\mathbf{B}_0|$ of the uniform magnetic field, the higher the eigenfrequencies of Alfvén and FMS waves.

(iii) The superposition of two standing eigenmodes with close frequencies $\omega = \omega_0 \pm \delta\omega$ gives rise to a beat wave. The beat frequency $\delta\omega$ depends on both the external parameters (J, ω_{ci}, L, a_p, and a) and the plasma density ($k_A^2 \propto n$). Consequently, the measurements of the frequency of a beat wave with the axial wavelength $2L$ can serve to diagnose the plasma density.

(iv) The splitting of the eigenfrequency of MHD waves by the helical magnetic field can be observed experimentally. A similar effect was discovered in tokamak experiments (see, e.g., [11]): the longitudinal electric current caused the spectra of MHD waves to become nondegenerate in the sign of the axial wavenumber.

(v) In an inhomogeneous stellarator plasma, satellite Alfvén resonances (2) (in the vicinity of which both of the satellite harmonics proportional to $\exp(\pm 3i\theta)$ are converted into small-scale kinetic waves) are located deep in the plasma core, where the plasma density is higher than that near the fundamental Alfvén resonance (18) by a factor of nine. Thus, it may be expected [3] that the additional heating of a stellarator plasma in the SAR regions by MHD waves whose fundamental mode is proportional to $\propto \exp(\pm i\theta)$ will be significant.

(vi) Our results may also be useful for investigating the dispersion properties of MHD waves such that the axial wavelength and azimuthal wavenumber of the fundamental mode, whose amplitude is proportional to $\propto \exp(\pm 3i\theta - i\omega t)$, exceed those at resonance (1) by a factor of three. Taking into account not only the main term $\propto \exp il\theta$ but also the resonant term $\propto \exp 3il\theta$ in the expression for the total confining magnetic field [7] leads to a correction $\delta\omega \propto \bar{\Delta}_{3l}$, whose value is determined by (36), while the correction to the eigenfrequency introduced by the main (nonresonant) term is $\delta\omega \propto \bar{\Delta}_l^2$. Thus, we can see that these corrections may be comparable in magnitude.

4. STRUCTURE OF THE SAR AT THE PLASMA EDGE IN A STELLARATOR

The symmetry properties of the problem allow us to investigate the SAR structure by looking for a solution to Eqs. (8) in the form of a wave envelope:

$$E_r = [E_r^{(0)} + E_r^{(+1)}(r)e^{il\theta} + E_r^{(+2)}(r)e^{2il\theta}] \times \exp i(k_z z + m\vartheta - \omega t). \quad (44)$$

Here, along with the fundamental harmonic, which is excited by the antenna and is proportional to $\propto \exp ik_z z$, and the first satellite harmonic, which is proportional to $\propto \exp i(k_z - k_s)z$ and whose amplitude has a singularity $E_r^{(+1)} \propto [\varepsilon_1^{(0)} - (N_z - N_s)^2]^{-1}$ inside the SAR region in a cold plasma, we also include the second satellite harmonic, which is proportional to $\propto \exp i(k_z - 2k_s)z$. The reason for this is that because of the helical ripple in a confining magnetic field the harmonic $E_r^{(+1)}$ is most strongly coupled to $E_r^{(0)}$ and $E_r^{(+2)}$.

We analyze Eqs. (8) in the narrow layer approximation. In other words, we assume that the width δr of the resonance region is small in comparison with the characteristic dimension a^* on which the plasma density varies and impose the conditions

$$\left|\frac{dE_r^{(+1)}}{dr}\right| \gg \left|\frac{m}{r_A^{(+)}}E_r^{(+1)}\right|, \quad \left|\frac{dE_r^{(+1)}}{dr}\right| \gg \left|(k_z - k_s)E_r^{(+1)}\right|, \quad (45)$$

which imply that, in the SAR region, the variations of the fields in the radial direction are much larger than those along the poloidal and axial coordinates.

4.1. Solution to Eqs. (8) in the SAR Region

Under the above assumptions, Eqs. (8) reduce to the following coupled equations for the amplitudes $E_r^{(0)}$, $E_r^{(+1)}$, and $E_r^{(+2)}$:

$$-N_s(2N_z - N_s)E_r^{(0)} + i\varepsilon_2^{(0)}E_\vartheta^{(0)}$$
$$= (2N_z - N_s)\frac{\alpha r\bar{\Delta}c}{2\omega}\frac{dE_r^{(+1)}}{dr} + \frac{\alpha^2 r^2\bar{\Delta}^2c^2}{4\omega^2}\frac{d^2E_r^{(+2)}}{dr^2}, \quad (46)$$

$$\left[\varepsilon_1^{(0)} - (N_z - N_s)^2 + \beta\frac{d^2}{dr^2}\right]E_r^{(+1)} = A^{(+)}, \quad (47)$$

$$E_r^{(+2)} = -\frac{r\bar{\Delta}}{2l}\frac{dE_r^{(+1)}}{dr}. \quad (48)$$

For simplicity, here and below, we omit the subscript l in $\bar{\Delta}_l$ and Δ_l. The small coefficient β of the second derivative in (47) is equal to

$$\beta = \frac{c\alpha r^2\bar{\Delta}^2}{2\omega l}(N_z - N_s)\Big|_{r_A^{(+)}}. \quad (49)$$

The right-hand side of Eq. (47) varies slowly in the SAR region; in the order of magnitude, we have $A^{(+)} \sim \bar{\Delta}(N_z - N_s)^2E_\vartheta^{(0)}$.

The solution to the inhomogeneous Airy equation (47) that describes a wave carrying the energy away from the SAR region and decreases in inverse proportion to the distance from the SAR has the form

$$E_r^{(+1)} = -ik_1a^*(N_z - N_s)^{-2}A^{(+)}u_0(\xi), \quad (50)$$

where

$$u_0(\xi) = s\int_0^\infty \exp[is(t\xi + t^3/3)]dt,$$
$$\xi = k_r(r - r_A^{(+)}), \quad (51)$$
$$k_r = ((-1/\beta)d\varepsilon_1^{(0)}/dr)_{r_A^{(+)}}^{1/3} = |k_r|e^{i\psi}.$$

The propagation direction of a small-scale wave is governed by the sign of s:

$$s = \mathrm{sgn}[\mathrm{Re}(k_r)d\varepsilon_1^{(0)}/dr\big|_{r_A^{(+)}}]. \quad (52)$$

The width $\delta r \sim k_r^{-1}$ of the resonance region is determined by the helical ripple amplitude of the confining magnetic field and is equal in order of magnitude to

$$\delta r \sim a^*\bar{\Delta}^{2/3} \ll a. \quad (53)$$

Outside the SAR region, the amplitude $E_r^{(+2)}$ of the second satellite harmonic is a second-order quantity, $E_r^{(+2)} \sim \Delta E_r^{(+1)} \sim \Delta^2E_r^{(0)}$ [1]. When approaching the SAR region, the amplitude $E_r^{(+2)}$ increases more sharply than the amplitude $E_r^{(+1)}$; namely, $E_r^{(+2)} \propto [\varepsilon_1^{(0)} - (N_z - N_s)^2]^{-2}$. As a result, the amplitude of the first satellite harmonic grows more gradually. Inside the SAR region, the amplitudes of the satellite harmonics are much larger than those on the outside; in order of magnitude, we have

$$E_r^{(+2)} \sim \Delta^{1/3}E_r^{(+1)} \sim \Delta^{2/3}E_r^{(0)}. \quad (54)$$

These estimates imply that, even inside the SAR region, the satellite harmonics have a negligible impact on the radial profile $E_r^{(0)}(r)$. Near the SAR region, the amplitude $E_\vartheta^{(+1)}$ of the first satellite harmonic of the azimuthal electric field changes insignificantly:

$$\frac{dE_\vartheta^{(+1)}}{dr} \approx \frac{m + l}{r}E_r^{(+1)}. \quad (55)$$

Inside the SAR region, this component of the wave electric field remains equal in order of magnitude to that on the outside: $E_\vartheta^{(+1)} \sim \Delta E_\vartheta^{(0)}$.

In the resonance region, the amplitude $E_z^{(+1)}$ of the first satellite harmonic of the axial component of the electric field of an MHD wave has a higher order singularity than $E_r^{(+1)}$, specifically, $E_z^{(+1)} \propto [\varepsilon_1^{(0)} - (N_z - N_s)^2]^{-2}$. Nevertheless, the amplitude $E_z^{(+I)}$ remains small in comparison with $E_r^{(+I)}$, so that, in order of magnitude, we have

$$E_z^{(+1)} \sim \left(\frac{c^2\varepsilon_1^{(0)}}{\beta\omega^2\varepsilon_3}\right)^{1/3}\left(\frac{\varepsilon_1^{(0)}}{\varepsilon_3}\right)^{2/3}E_r^{(+1)}. \quad (56)$$

4.2. SAR Structure with Allowance for Collisions between Plasma Particles, the Finite Ion Larmor Radius, and Electron Inertia

With allowance for the effects of collisions, the finite ion Larmor radius, and electron inertia, the results of the previous section coincide with the results obtained in [3]. To incorporate these effects, it is sufficient to make the following replacement in Eq. (47):

$$\beta\frac{d^2}{dr^2} \longrightarrow i\varepsilon_1^{(c)} + \left(\beta + \varepsilon_T + \frac{c^2\varepsilon_1^{(0)}}{\omega^2\varepsilon_3}\right)\frac{d^2}{dr^2}. \quad (57)$$

Here, the term $i\varepsilon_1^{(c)}$ describes collisions between plasma particles [12] and the quantity ε_T accounts for the effects of the finite ion Larmor radius ρ_{Li} [13]. An analysis of (57) shows that, in studying the SAR structure, electron inertia can be neglected under the condition

$$\beta \gg c^2\varepsilon_1^{(0)}/(\omega^2\varepsilon_3), \quad (58)$$

and the finite ion Larmor radius can be ignored when

$$\beta \gg N_z^2 \rho_{Li}^2. \quad (59)$$

As the plasma temperature in the SAR region increases (all other conditions being the same), the effects of the finite ion Larmor radius and electron inertia on the SAR structure become more significant [the strong inequalities (58) and (59) weaken] and even turn out to be more important than the effect of the helical ripple in a confining magnetic field [the strong inequalities (58) and (59) change sign]. In this case, the resonance region broadens and is described by expression (3) and the amplitudes of the satellite harmonics decrease and become equal in order of magnitude to [cf. (54)]

$$E_r^{(+2)} \sim \Delta (a^*/\rho_{Li})^{2/3} E_r^{(+1)} \sim \Delta^2 (a^*/\rho_{Li})^{4/3} E_r^{(0)}. \quad (60)$$

4.3. Conclusions Regarding the Effect of the Helical Ripple in a Confining Magnetic Field on the SAR Structure

We have studied the distributions of the electromagnetic fields of MHD waves in the SAR region (2) in a cold plasma in a strong uniform axial magnetic field and a weak helical magnetic field. The results obtained can be summarized as follows.

(i) We have determined conditions (58) and (59), under which the helical ripple in the confining magnetic field $\mathbf{B}_0$ affects the SAR structure more strongly than the finite ion Larmor radius ρ_{Li} and electron inertia. In stellarators, conditions (58) and (59) can be satisfied at the plasma edge, where the deviation of the magnetic surfaces from being circular is most pronounced and the plasma is hotter than in the core.

(ii) The helical ripple in the field $\mathbf{B}_0$ does not change the RF power absorbed by the plasma in the SAR region. Our investigations generalize the analysis of Girka *et al.* [3], who studied plasma heating near the SAR and determined the absorbed power, to the case in which the effect of the helical ripple is comparable in importance to or even stronger than the effects of the finite ion Larmor radius and electron inertia [see replacement (57) and estimate (60)].

(iii) In contrast to Alfvén waves, FMS waves with the axial wavenumber $|k_z| > \omega/c$ and frequency $\omega > \omega_{ci}$ experience no fundamental AR. (The conversion and resonant absorption of FMS waves with $|k_z| < \omega/c$ and $\omega > \omega_{ci}$ in the edge plasma were studied by Girka and Stepanov [6].) However, if such FMS waves satisfy the additional condition $|k_z - k_s| < \omega/c$, then they will experience SAR (2) in a stellarator plasma. Since, in the core of a fusion plasma, we have $\omega_{pi}^2 > \omega_{ci}^2$, the point $r = r_A^{(+)}$ of this SAR lies in the plasma edge. Consequently, this SAR may give rise to undesirable heating of the edge plasma in stellarators.

(iv) Interest in studying the SAR structure in the case of a moderately rippled helical magnetic field is also associated with the following circumstance. Before proceeding to a detailed analysis of the problem, it is natural to suppose that, in the SAR region, the satellite harmonic may be larger in amplitude than the fundamental harmonic, in which case we could expect that striction nonlinearity would come into play and/or the turbulent absorption of RF power would occur via the satellite harmonic. However, a thorough investigation showed that, even in the SAR region, the amplitude $E_r^{(+1)}$ of the satellite harmonic always remains smaller than the amplitude $E_r^{(0)}$ of the fundamental harmonic [see (54)].

(v) Since, in the SAR region, the amplitudes of the fundamental harmonics of the fields of an MHD wave change only slightly, the ponderomotive potential U [14] acts exclusively to displace the point of the SAR by a small distance $\delta r_{str} = (U/T)a^*$ from the plasma axis. Thus, the initial assumption that the striction effects are insignificant is equivalent to the requirement that the influence of the nonlinear effects on the SAR structure be weaker than the influence of the helical ripple in the field $\mathbf{B}_0$.

(vi) In the nonlinear stage of growth of cyclotron waves, the ions are scattered by turbulent pulsations, so that we can speak of the effective scattering frequency, i.e., the effective collision frequency, $\varepsilon_1^{(c)} \longrightarrow \varepsilon_{l\,\mathrm{eff}}$ [15]. Since the effective frequency at which the ions are scattered by turbulent pulsations is proportional to the cube of the amplitude of the electric field of the pump wave, accounting for the amplitude $E_r^{(+1)}$ of the first satellite harmonic leads to a significant increase in $\varepsilon_{l\,\mathrm{eff}}$ inside the SAR region in comparison with that on the outside, in which case we obtain an order-of-magnitude estimate $\varepsilon_{l\,\mathrm{eff}} \longrightarrow \varepsilon_{l\,\mathrm{eff}}(1 + 1.5\bar{\Delta}^{2/3})$.

ACKNOWLEDGMENTS

This work was supported in part by the Center for Science and Technology of Ukraine, project no. 2313.

REFERENCES

1. I. A. Girka and P. K. Kovtun, Fiz. Plazmy **26**, 36 (2000) [Plasma Phys. Rep. **26**, 33 (2000)].
2. I. A. Girka, V. I. Lapshin, and K. N. Stepanov, Fiz. Plazmy **24**, 1015 (1998) [Plasma Phys. Rep. **24**, 948 (1998)].
3. I. A. Girka, V. I. Lapshin, and K. N. Stepanov, Fiz. Plazmy **23**, 23 (1997) [Plasma Phys. Rep. **23**, 19 (1997)].
4. V. V. Dolgopolov and K. N. Stepanov, Nucl. Fusion **5** (4), 276 (1965).
5. D. L. Grekov, K. N. Stepanov, and J. A. Tataronis, Fiz. Plazmy **7**, 752 (1981) [Sov. J. Plasma Phys. **7**, 411 (1981)].

6. I. A. Girka and K. N. Stepanov, Ukr. Fiz. Zh. **35**, 1680 (1990).
7. E. D. Volkov, V. E. Suprunenko, and A. A. Shishkin, *Stellarator* (Naukova Dumka, Kiev, 1983).
8. A. V. Longinov and V. A. Tsurikov, Fiz. Plazmy **16**, 39 (1990) [Sov. J. Plasma Phys. **16**, 22 (1990)].
9. L. D. Landau and E. M. Lifshitz, *Quantum Mechanics: Non-Relativistic Theory* (Nauka, Moscow, 1989; Pergamon, New York, 1977).
10. I. A. Girka and K. N. Stepanov, Ukr. Fiz. Zh. **37**, 69 (1992).
11. P. Descamos, T. Delvigne, F. Durodie, *et al.*, in *Proceedings of the 16th European Conference on Controlled Fusion and Plasma Physics, Venice, 1988* [ECA **13B**, 1053 (1988)].
12. A. I. Akhiezer, V. I. Lapshin, and K. N. Stepanov, Zh. Éksp. Teor. Fiz. **70**, 81 (1976) [Sov. Phys. JETP **43**, 42 (1976)].
13. *Plasma Electrodynamics*, Ed. by A. I. Akhiezer *et al.* (Nauka, Moscow, 1974; Pergamon, Oxford, 1975).
14. R. Klima, Czech. J. Phys., Sect. B **18**, 1280 (1968).
15. V. P. Silin, *Parametric Action of High-Power Radiation on a Plasma* (Nauka, Moscow, 1973).

Translated by I. Kalabalyk

Plasma Physics Reports, Vol. 26, No. 9, 2000, pp. 781–785. Translated from Fizika Plazmy, Vol. 26, No. 9, 2000, pp. 833–837.

PLASMA OSCILLATIONS AND WAVES

Feasibility of Using Bernstein Modes for Current Drive in Toroidal Devices

O. B. Smolyakova and M. D. Tokman

Institute of Applied Physics, Russian Academy of Sciences, ul. Ul'yanova 46, Nizhni Novgorod, 603600 Russia

Received November 25, 1999; in final form, February 22, 2000

Abstract—The feasibility of using Bernstein modes for producing electron cyclotron current drive in toroidal devices is examined. It is shown that the negative role of trapped particles may reduce upon increasing the longitudinal slowing-down factor of waves. Numerical geometrical-optics calculations of the propagation and absorption of waves were performed for the scheme in which radiation is launched from the low-field side as an ordinary wave, linearly converted into an extraordinary wave, and finally converted into Bernstein mode. An analysis is performed for medium-sized toroidal devices. Based on numerical simulation, the parameters determining the efficiency of current drive, namely, the characteristic values of the resonant energies and the longitudinal slowing-down factor of waves in the region where most of the microwave power dissipates, are found.

1. INTRODUCTION

As has already been noted (see, e.g., [1, 2]), the use of Bernstein modes (B-modes) for producing noninductive currents in toroidal devices has some advantages. First, for these waves, a significant longitudinal slowing-down factor may be achieved in the region where the energy is dissipated. The longitudinal (with respect to the constant magnetic field **B**) refractive index can attain the value $n_\parallel \approx n_\perp B_\theta/B_\varphi$, where B_φ is the toroidal magnetic field component, B_θ is the poloidal component, and $n_\perp$ is the transverse refractive index[1] (see [1, 3]). In the absorption region, $n_\perp$ can be estimated as $n_\perp \sim \beta_T^{-1}$ [1] (where β_T is the ratio of the thermal velocity v_T to the speed of light c) and the longitudinal slowing-down factor attains an appreciable value, $n_\parallel \approx \frac{1}{\beta_T}\frac{B_\theta}{B_\varphi}$ [1–3], which increases the efficiency of noninductive current drive (CD) [4–6]. Second, the absorption coefficient of the electrostatic Bernstein modes is a factor of about mc^2/T_e (where m is the electron mass and T_e is the electron temperature) higher than the absorption coefficients of the normal electromagnetic modes. Hence, in an inhomogeneous magnetic field, most of the wave power is absorbed in the region where the wave is in resonance with higher energy electrons; consequently, the efficiency of CD increases.[2]

As the device sizes increase, the traditional ("classical") method of excitation of Bernstein modes by launching the extraordinary (X) wave from the high-field side and its conversion into the B-mode in the upper hybrid resonance (UHR) region [3] becomes inefficient because of the strong cyclotron absorption of the X-mode (before it reaches the UHR region). In addition, the "inner" launching poses some technological problems. For this reason, it is worthwhile to consider the method for exciting B-modes via linear conversion from the ordinary (O) to extraordinary (X) wave and, finally, to the Bernstein mode, i.e., the so-called O–X–B mode conversion scheme proposed in 1973 [7] for heating an overdense plasma and successfully implemented in W7-AS [8]. Previously, the O–X–B mode conversion was observed in ionospheric experiments in the radio frequency range (the so-called "radio window" effect [9]).

An assessment of the CD efficiency by such a sophisticated scheme requires numerical simulation of the propagation and absorption of radiation (it was performed for the first time in [10, 11] in the model formulation of the problem).

This paper is arranged as follows. In Section 2, we consider an additional mechanism for enhancing the CD efficiency at higher $n_\parallel$ by reducing the negative effect of the trapped electrons. In Section 3, the characteristic features of the linear mode conversion scheme

[1] For Bernstein modes excited in a toroidal plasma, the toroidal component of the wave vector is naturally conserved, whereas its component lying in the plane of the minor cross section almost coincides with the transverse wave vector. The longitudinal component of the wave vector is determined by the projection of the poloidal component of the wave vector onto the field direction rather than by the toroidal component.

[2] The efficiency is proportional to the square of the resonant electron velocity v_{res}^2 [4].

1063-780X/00/2609-0781$20.00 © 2000 MAIK "Nauka/Interperiodica"

are briefly outlined. In Section 4, we present the results of numerical simulations of the propagation and absorption of radiation and estimate the CD efficiency for the O–X–B scheme. In Section 5, we draw some conclusions.

2. REDUCTION OF THE EFFECT OF TRAPPED ELECTRONS AT HIGH VALUES OF $n_\parallel$

If we ignore toroidal inhomogeneities,[3] then, for electron cyclotron CD (ECCD) at the fundamental harmonic of the gyrofrequency, all possible current components can be written in the form of the sum [5, 6]

$$j = j_{FB} + j_\parallel + j_{fr} + j_{Ok}, \quad (1)$$

where the first term j_{FB} corresponds to the Fisch–Boozer mechanism associated with the anisotropy of plasma conductivity [4], the second term $j_\parallel$ is the current associated with an increase in the longitudinal electron momentum due to both the absorption of the longitudinal momentum of electromagnetic waves [4, 6] and the ponderomotive action of the static magnetic field [6, 12], the third term j_{fr} (of negative sign) describes the current degradation associated with the neoclassical friction between trapped and passing electrons [6, 13], and the last term j_{Ok} is the Ohkawa current related to the imbalance of trapped and untrapped populations under the action of electromagnetic radiation [14]. The Ohkawa current is negative for sufficiently low values of $n_\parallel$ [4] but can change its sign as $n_\parallel$ increases[4] [1].

Within the approximation of a "flat-bottom" magnetic well [5, 6, 13, 15], following the method described in [5, 6], we write the general expression for the sums of parasitic components:

$$j_{fr} + j_{Ok} = -\frac{4e}{(4+2\alpha)} x_c \left(\frac{P_u}{D_c m} \langle v^2 \rangle_R - 2 \int_{x_c}^{1} dx \int_0^\infty dv\, v^3 f^a(v, x) \right), \quad (2)$$

where P_u is the power density absorbed by transit (other than "banana") particles, $D_c = \nu_c v_T^3$, ν_c is the Coulomb collision frequency of thermal electrons, $\alpha = (1 + Z_{\text{eff}})/2$, Z_{eff} is the effective ion charge number, x is the cosine of the electron pitch angle, v is the particle-velocity modulus, $f^a(v, x)$ is the asymmetric component of the distribution function, $x_c = (2\varepsilon/(\varepsilon + 1))^{1/2}$ is the quantity determining the boundary of the banana domain in phase space, ε is the inverse aspect ratio, and $m\langle v^2 \rangle_R/2$ is the average kinetic energy of resonant electrons.

It is evident from formula (2) that, as the antisymmetric part of the distribution function increases (provided that the values of P_u and $\langle v^2 \rangle_R$ remain unchanged), the toroidal degradation of the electron CD reduces. It is the asymmetric part of the distribution function that increases with increasing $n_\parallel$ [4], which leads not only to an increase in the current component $j_\parallel$ associated with the longitudinal wave momentum, but also to a reduction of negative toroidal effects. It should be emphasized that relation (2) is general and is valid even in the case when a "parasitic" current is only associated with the component j_{fr} (see [6]). In the case of high values of Z_{eff} (the Lorentz gas), due to the inverse dependence of f^a on the parameter $\alpha = (1 + Z_{\text{eff}})/2$, the effect of a finite value of $n_\parallel$ on the toroidal degradation of the ECCD is negligibly small [5].

3. THE SCHEME USING THE O–X–B MODE CONVERSION

In this scheme, radiation is launched as an ordinary wave from the low-field side at a certain optimal ("critical" [9]) angle. In this case, at the point where the plasma frequency ω_p is equal to the radiation frequency ω, the O-mode is completely converted into the X-mode. The critical angle is determined by the longitudinal refractive index in the region of wave conversion:

$$n_\parallel = n_{\parallel \text{opt}} = \left(\frac{\sqrt{u}}{1 + \sqrt{u}} \right)^{1/2}, \quad (3)$$

where $u = \omega_c^2/\omega^2$ and ω_c is the electron gyrofrequency. If the launching angle is not optimal, then the power conversion coefficient decreases (see, e.g., [7, 8, 16]).

Achieving a significant conversion for a wave beam with a finite angular width is a separate complicated problem; perhaps for this reason the use of the O–X–B scheme for plasma heating has long been considered to be conjectural. However, successful experiments in W7-AS [8] demonstrated that the problem of creating an appropriate beam could be solved.

4. NUMERICAL SIMULATIONS

To estimate the efficiency of noninductive CD by the O–X–B scheme, a numerical code was created and computations were performed.

A plasma was assumed to be a cylinder with the axis in the y-direction. The radial profile of the current

[3] For instance, ripples.

[4] The steady-state Ohkawa current is associated with the passage of transit particles into the "banana" region. As $n_\parallel$ increases, the angle between the lines along which quasilinear diffusion occurs and the boundary of the banana domain in phase space decreases. (In principle, at high particle energies, such a distortion in the orientation of quasilinear-diffusion lines can also be produced by relativistic effects; however, for $n_\parallel \neq 0$, this effect takes place even if the relativistic change of mass is omitted.) For a sufficiently high $n_\parallel$, quasilinear diffusion leads to the conversion of banana particles into transit particles and the Ohkawa current changes its sign (see [1]).

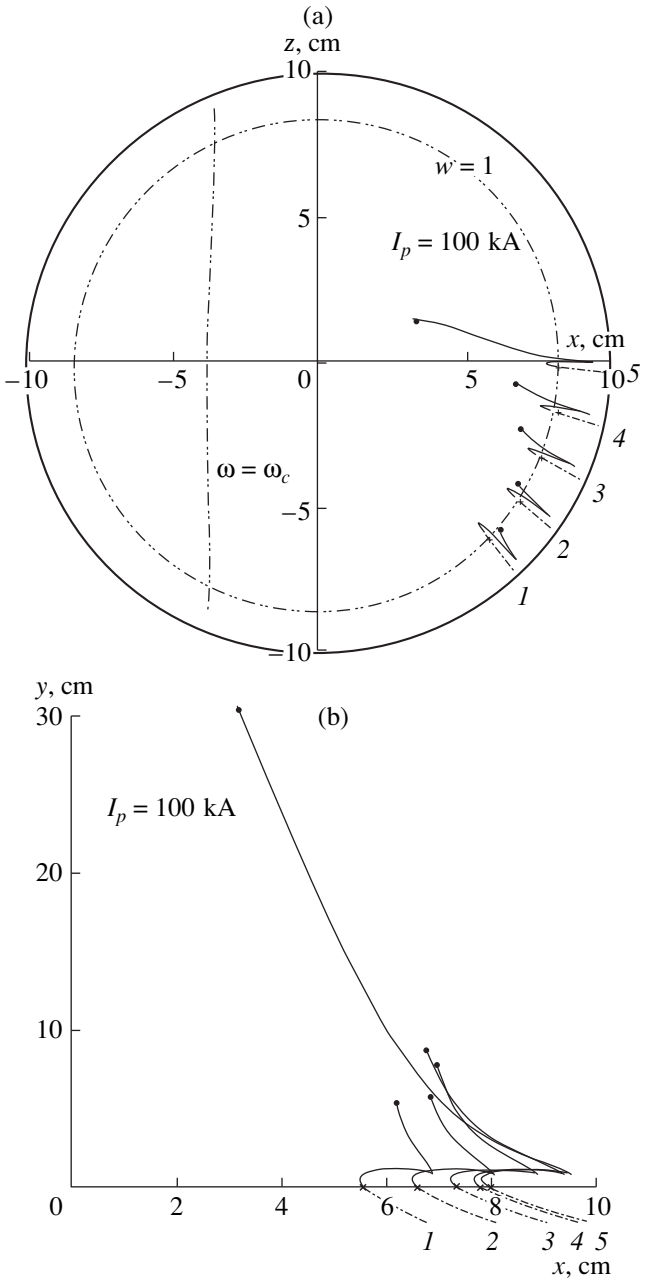

Fig. 1. Ray trajectories for I_p = 100 kA: (a) minor cross section and (b) equatorial cross section.

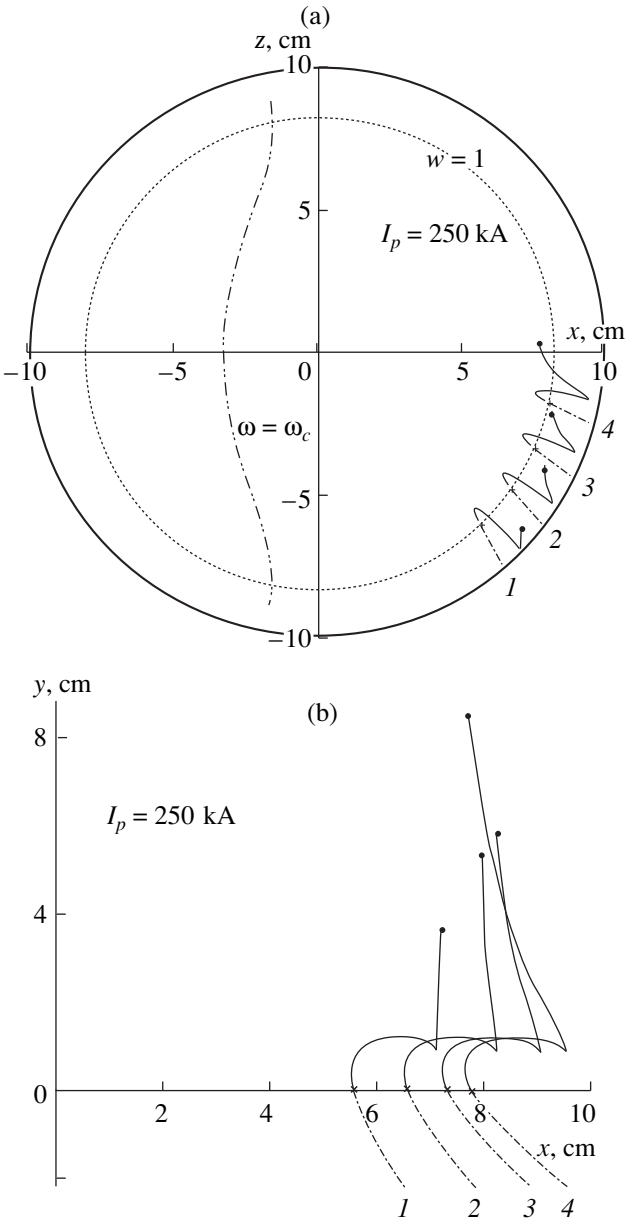

Fig. 2. Same as in Fig. 1, but for I_p = 250 kA.

density was taken to be

$$j = j_0(1 - r^2/a^2), \tag{4}$$

where r is the radial coordinate in the plane of the minor cross section and a is the minor plasma radius.

The ray trajectories and the absorbed power were calculated in a geometrical-optics approximation, the Hamiltonian of the ray trajectories being determined from the dispersion relation. For a cold-plasma approximation, we used the well-known Appleton–Hartree formula [9]. Near the UHR region, we used the dispersion relation with the "warm" correction (see [3, 17]):

$$G = (n^2 - n_o^2)(n^2 - n_x^2) - \beta_T^2 w n^6 D = 0,$$
$$D = 3\cos^4\vartheta(1-w) + \frac{6 - 3u + u^2}{(1-u)^2}\cos^2\vartheta\sin^2\vartheta \tag{5}$$
$$+ \frac{3}{1-4u}\sin^4\vartheta,$$

where ϑ is the angle between the magnetic field line and the wave vector $\mathbf{k}$, $w = \omega_p^2/\omega^2$, and n_o and n_x are the refractive indices for the ordinary and extraordinary waves in the cold-plasma approximation. For the parameter $\chi = n_\perp^2 \beta_T^2/2u$ on the order of 0.1–0.2, the Hamiltonian is determined from the conventional dispersion relation for Bernstein modes [3, 17].

When calculating the ray trajectories, the starting point on the *xz* plane was taken to lie in the cut-off region ($\omega_p = \omega$). It was assumed that the ordinary wave at this point had the wave vector $\mathbf{k}$ aligned with the magnetic field. In this case, the radiation was completely converted and then propagated as an extraordinary wave. The wave was reflected at a certain point, passed through the UHR region, and was converted into the Bernstein mode. The calculation of the ray trajectory stopped when the optical depth attained unity: $\tau \approx 1$. To determine the vacuum launching parameters, the ray trajectory of the ordinary wave was calculated from the conversion point backward to vacuum.

The relative ECCD efficiency $\eta \sim (v_{res}/v_T)^2$ is estimated for the conventional Fisch–Boozer mechanism and is determined by the parameter of the energy shift in the region where most of the power is absorbed: $Z^2 = [(1 - \sqrt{u})/n_\parallel \beta_T]^2 = (v_{res}/v_T)^2$ [4–6]. However, even with these constraints, we can demonstrate the efficiency of the O–X–B scheme for noninductive CD.

Estimates were performed for the plasma parameters typical of devices such as W7-AS, where the plasma frequency is higher than the gyrofrequency and conditions for the O–X–B mode conversion are satisfied. The major plasma radius R is equal to 105 cm, and the minor radius a is equal to 10 cm. The magnetic field B_0 in the center of the chamber varies within the range 2.2–2.4 T. The radiation frequency f is equal to 70 GHz. The maximum plasma density and temperature at the plasma center are equal to $N_0 = 1.5 \times 10^{20}$ m^{-3} and $T_0 = 500$ eV, respectively. The radial dependences of the density and temperature correspond to those in W7-AS [8]:

$$T_e = \frac{T_0}{(1 + (c_2 r/a)^{(2c_1)})}, \quad N_e = \frac{N_0}{(1 + (c_4 r/a)^{(2c_3)})}, \quad (6)$$

$$c_1 = 3.933, \quad c_2 = 1.353, \quad c_3 = 5.373, \quad c_4 = 1.294.$$

Figures 1 and 2 illustrate the set of ray trajectories that differ from each other by launching points and angles. The magnetic field in the center of the chamber is 2.4 T, which corresponds to $u_0 = \omega_c^2/\omega^2 = 0.92$. In the figures, the circles of critical density $w = \omega_p^2/\omega^2 = 1$ are depicted by dotted lines and the gyro-resonance lines $u_0 = \omega_c^2/\omega^2 = 1$ are shown by dashed-and-dotted lines. In the ray trajectories, the dashed segments correspond to the paths of the "cold" ordinary waves to the conversion points (which are marked by crosses), the solid lines show the paths of the extraordinary waves and the "warm" modes, and the heavy dots in the ray trajectories mark the points where the optical thickness τ reaches unity. Figure 1 corresponds to a total plasma current I_p of 100 kA. The longitudinal refractive index in the absorption region varies monotonically from $n_\parallel = 0.44$ for curve *5* to $n_\parallel = 1.4$ for curve *1*. In Fig. 2, corresponding to $I_p = 250$ kA, $n_\parallel$ varies from 1.01 for curve *4* to 1.84 for curve *1*.

In all of the runs, the parameter $Z^2 = [(1 - \sqrt{u})/n_\parallel \beta_T]^2 = (v_{res}/v_T)^2$ determining the relative energy of resonant electrons was $Z^2 \approx 6$; hence, the resonant electron velocity was $\sim \sqrt{6}\, v_T$. When the ordinary wave was absorbed in a plasma with similar parameters (e.g., with the same dimensions, temperature profile, and magnetic field), but with a plasma density somewhat below the critical density (i.e., when the conditions for wave propagation held), the optical thickness did not exceed unity. In this case, the resonant electron velocity was $v_{res} = v_T$ and the generation efficiency was approximately six times lower even if the dependence of the CD efficiency on $n_\parallel$ was neglected.

5. CONCLUSION

The above theoretical estimates and numerical simulations have shown that B-modes can be successfully used to obtain highly efficient CD in toroidal devices, at least in medium-sized ones, in which the O–X–B mode conversion might be an efficient method for the excitation of B-modes. The question of the methods for the excitation of Bernstein modes in large devices remains open. Another open question related to this scheme is to what extent the resonances at higher harmonics reduce the CD efficiency. These questions require further investigation.

ACKNOWLEDGMENTS

We thank E.V. Suvorov for fruitful discussions. This work was supported in part by the Russian Foundation for Basic Research, project no. 98-02-17204.

REFERENCES

1. A. G. Litvak, E. V. Suvorov, and M. D. Tokman, Phys. Lett. A **188**, 64 (1994).
2. O. B. Smolyakova and M. D. Tokman, in *Proceedings of the III International Workshop "Strong Microwaves in Plasmas," Nizhni Novgorod, 1997* (Inst. of Applied Physics, Russian Academy of Sciences, Nizhni Novgorod, 1997), Vol. 1, p. 214.
3. Yu. F. Baranov and V. I. Fedorov, Fiz. Plazmy **9**, 677 (1983) [Sov. J. Plasma Phys. **9**, 391 (1983)].
4. N. J. Fisch, Rev. Mod. Phys. **59**, 175 (1987).
5. A. Yu. Kuyanov, A. A. Skovoroda, and M. D. Tokman, Plasma Phys. Controlled Fusion **39**, 277 (1997).

6. M. D. Tokman, in *Proceedings of the 9th Joint Workshop on ECE and ECH, Borrego Springs, CA, 1995* (World Scientific, Singapore, 1995).
7. I. Prienhalter and V. Kopecky, J. Plasma Phys. **10**, 1 (1973).
8. H. Laqua, V. Erckmann, H.-J. Hartfuss, *et al.*, in *Proceedings of the 23rd EPS Conference on Controlled Fusion and Plasma Physics, Kiev, 1996* [ECA **20C**, 847 (1996)].
9. K. G. Budden, *Radio Waves in Ionosphere* (Cambridge Univ. Press, Cambridge, 1961).
10. T. Maekawa, S. Tanaka, Y. Terumichi, and Y. Hamada, Phys. Rev. Lett. **40**, 1379 (1978).
11. T. Maekawa, S. Tanaka, Y. Hamada, and Y. Terumichi, Phys. Lett. A **69**, 414 (1978).
12. P. B. Parks and F. B. Markus, Nucl. Fusion **21**, 1207 (1981).
13. J. G. Cordey, T. Edlington, and D. F. H. Start, Plasma Phys. **24**, 73 (1982).
14. T. Ohkawa, Report GA-A13847 (General Atomics Company, San Diego, CA, 1976).
15. R. H. Cohen, Phys. Fluids **30**, 2442 (1987).
16. A. A. Zharov, Fiz. Plazmy **10**, 1109 (1984) [Sov. J. Plasma Phys. **10**, 642 (1984)].
17. V. V. Zheleznyakov, *Radiation in Astrophysical Plasmas* (Yanus-K, Moscow, 1997).

Translated by N. Larionova

Plasma Physics Reports, Vol. 26, No. 9, 2000, pp. 786–791. Translated from Fizika Plazmy, Vol. 26, No. 9, 2000, pp. 838–844.

BEAMS IN PLASMA

Focusing of Heavy Ion Beams by a High-Current Plasma Lens

A. A. Goncharov, S. N. Gubarev, A. N. Dobrovol'skiĭ, I. V. Litovko, and I. M. Protsenko

Institute of Physics, National Academy of Sciences of Ukraine, pr. Nauki 144, Kiev, 03039 Ukraine

Received September 14, 1999; in final form, December 3, 1999

Abstract—Results are presented from studies of the focusing of wide-aperture low-energy (100–400 eV) and moderate-energy (5–25 keV) beams of heavy-metal ions by a high-current electrostatic plasma lens. It is found experimentally that, because of the significant electron losses, the efficient focusing of such beams can be achieved only if the external potentials at the plasma-lens electrodes are maintained constant. Static and dynamic characteristics of the lens are studied under these conditions. It is shown that, as the beam current and the electrode voltage increase, the maximum electrostatic field in the lens tends to a certain limiting value because of the increase in the spatial potential near the lens axis. The role of spherical and moment aberrations in the focusing of wide-aperture low-divergence ion beams is revealed. It is shown that, even when spherical aberrations are minimized, unremovable moment aberrations decrease the maximum compression ratio of a low-energy heavy-ion beam because of the charge separation of multiply charged ions in the focal region. At the same time, as the ion energy increases, the role of the moment aberrations decreases and the focusing of high-current heavy-ion beams by a plasma lens becomes more efficient than the focusing of light-ion (hydrogen) beams. This opens up the possibility of using electrostatic plasma lenses to control ion beams in high-dose ion implanters and high-current accelerators of heavy ions. © *2000 MAIK "Nauka/Interperiodica"*.

1. INTRODUCTION

Research on electrostatic plasma lenses (PLs) capable of focusing intense ion beams was initiated in [1, 2] (see also [3]). Experiments with low-current steady-state ion beams carried out in 1970s confirmed Morozov's concept of using the magnetic insulation of electrons and the condition that the magnetic field lines are equipotential in order to control intense plasma flows and neutralized ion beams. At the same time, it turned out that plasma-optic systems proposed for focusing ion beams operate under conditions when the voltage φ_l applied to the fixing electrodes of the lens is substantially higher than the intrinsic potential of an unneutralized ion beam ($\varphi_b = I_b/V_b$, where I_b is the beam current and V_b is the beam velocity). By the late 1970s, it became clear that, for ion beams with relatively low currents of 10–100 mA and ion energies on the order of 10 keV, when the condition $\varphi_l \geq \varphi_b$ holds, the conceptual scheme of a PL proposed by Morozov operates not under quasineutral plasma conditions (as was expected) but under conditions of overneutralization of the beam space charge, i.e., under conditions typical of a Gabor lens.

By the early 1980s, plasma ion sources generating quasi-steady repetitive pulsed beams with ion energies of tens of kiloelectronvolts and currents in the ampere range were created first for neutral injectors and later for technological applications. The challenge then arose to design plasma-optic facilities of a new generation that would be able to efficiently control the ion beams for which the condition $\varphi_l < I_b/V_b$ was satisfied. At the same time, intrinsic magnetic fields of these beams were still significantly lower than the external magnetic fields. It turned out that the conditions typical of laboratory experiments with such beams satisfied the theoretical principles of static plasma optics.

A new stage in experimental studies on electrostatic PLs began with the use of wide-aperture repetitive pulsed beams of light hydrogen ions with a current up to 2 A, an energy up to 25 keV, and a duration up to 100 μs [4, 5], which made it possible to operate with high-current quasineutral plasmas. Under these conditions, static and dynamic characteristics were studied for high-current PLs [5] in which a quasineutral medium is formed by fast ions of a passing beam and electrons from the secondary ion–electron emission. In these experiments, it was found that the magnitude of the current of the passing ion beam significantly affects the character of the electrostatic potential distribution in the PL volume and the value of the limiting electric field achievable in the lens. Thus, by varying the beam current, the configuration of magnetic field lines, the number of fixing electrodes, and the distribution of the external potential at them, it is possible to control the radial profile of the electric potential in a PL in the desired fashion and, in particular, eliminate spherical aberrations. In [6], the focusing of wide-aperture low-divergence beams of hydrogen ions was studied and a strong influence of the spherical aberrations was demonstrated. It was shown that the maximum compression ratio of such beams in the focal region is not too high (about 2–5) even with minimum spherical aberrations in the PL and that this ratio decreases as the beam current increases.

1063-780X/00/2609-0786$20.00

It was shown in [7] experimentally and theoretically that the presence of spherical aberrations may also play a positive role. By varying them, it is possible to control the radial profile of the beam at a target positioned in a given cross section on the z-axis and, in particular, to reach a uniform distribution.

In the absence of spherical aberrations, the maximum compression ratio of a low-divergence monoenergetic beam in the focal region can be limited by the field of an unneutralized space charge of the beam if $j_{\max} \le j_0 \exp(V_{r0}^2 M_b V_b / 2e\alpha I_b)$, where $V_{r0} = R_0 V_b / F$, F is the PL focal length, and α is the experimentally measured coefficient of neutralization of the beam charge in the focal region. In experiments with hydrogen ions, the measured neutralization coefficient was equal to $\alpha \le 10^{-2}$ [6]. The limitation on the maximum compression ratio of the beam is also governed by the unremovable moment aberrations arising due to the finite value of the azimuthal velocity of the fast particles of the focused beam in a PL magnetic field. Estimates of this effect [8] show that the minimum beam radius at the PL focus is limited by the value

$$R_{\min} = \frac{R_0 V_b H_0 L}{\varphi_b c \pi}, \qquad (1)$$

where R_0 is the initial beam radius, φ_b is the accelerating potential, H_0 is the magnetic field in a PL of length L, $V_b = \sqrt{ne\varphi_b / M}$, and n is the ion charge.

Now, it is clear that, under experimental conditions characteristic of the focusing of moderate-energy hydrogen-ion beams [6], a relatively low value of the maximum compression ratio of the beam may be attributed to the effects of the field of an unneutralized beam charge and moment aberrations. Estimates show that these two factors produce nearly identical effects. The aim of this paper is to study the focusing of wide-aperture repetitive pulsed beams of low-energy (100–400 eV) and moderate-energy (5–25 keV) heavy-metal ions by an electrostatic PL and investigate the static and dynamic characteristics of the PL operation under these conditions.

2. EXPERIMENTAL SETUP AND MEASUREMENT METHODS

In experiments, wide-aperture low-divergence beams of heavy-metal ions were produced with the help of a highly efficient two-chamber vacuum-arc MEVVA ion source [9]. In this source, a vacuum arc with a current up to 200 A was ignited in the cathode-material vapors. The cathodes were made of Cu, Zn, Mo, and C. Through a grid hole in the anode, the arc-discharge plasma penetrated into the second chamber of the source. A three-electrode accelerating/decelerating multiaperture ion-optical system (IOS) was used to output and form a repetitive pulsed ion beam with a pulse duration of 100 μs and a peak current up to 800 mA in the ion energy range 5–25 keV or 50 mA in the ion energy range 100–400 eV. To form moderate-energy ion beams, we used an optimized IOS with 84 individual profiled cells 4 mm in diameter; for low-energy beams, we used an optimized IOS in which 325 cells 2 mm in diameter were positioned inside a circle 5.6 cm in diameter.

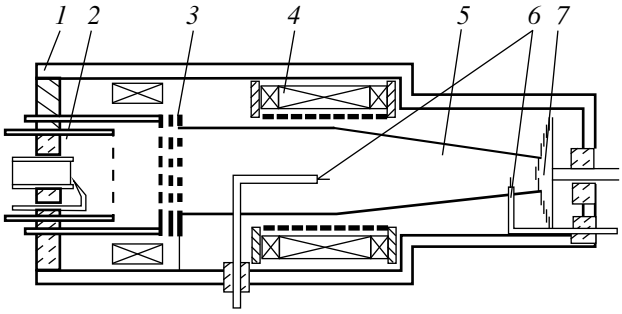

Fig. 1. Schematic of the device: (*1*) vacuum chamber, (*2*) ion source, (*3*) ion-optical system, (*4*) plasma lens, (*5*) ion beam, (*6*) probes, and (*7*) collector.

The ion source produced a low-noise ion beam at a repetition rate of 1 Hz with a sufficiently uniform density profile. The experimental setup is shown in Fig. 1. The ion source (*1*) with an IOS (*2*) was located 30 cm from the midplane of the PL. We used a nine-electrode PL (*3*) with a 70-mm-diameter entrance aperture with a length of L = 120 mm; the pulsed (τ = 0.2 ms) insulating field H_l attained 0.1 T. The maximum dc voltage applied to the central annular electrode of the PL was $\varphi_l \le +4$ kV. All the other electrodes symmetrically located around the central one were connected in pairs (first, second, and third) to the corresponding points of a voltage divider. The fourth pair of extreme electrodes was grounded.

In the experiments, we used an optimum configuration of the magnetic field lines as found experimentally in [4]. According to the equipotentiality principle ($\Phi = k\psi$, where k is the proportionality factor and ψ is the magnetic flux function), such a configuration implies the minimization of the axial magnetic tube inside which the electric field does not depend on the distribution of the external potential over the fixing electrodes.

The two-component quasineutral plasma in the PL volume consisted of fast beam ions and slow magnetized electrons and was produced due to the secondary ion–electron emission from the electrode surface bombarded by the particles from the periphery of the beam. As for the slow ions produced by the ion beam through the impact ionization of the residual gas, the experiments show that, because of the low ionization ability of heavy ions, their influence can be neglected up to gas pressures of $\sim 2 \times 10^{-4}$ torr. This pressure value is one order of magnitude higher than that in the case of focusing of hydrogen beams with the same energies. In all of the experiments, the pressure was maintained at a level

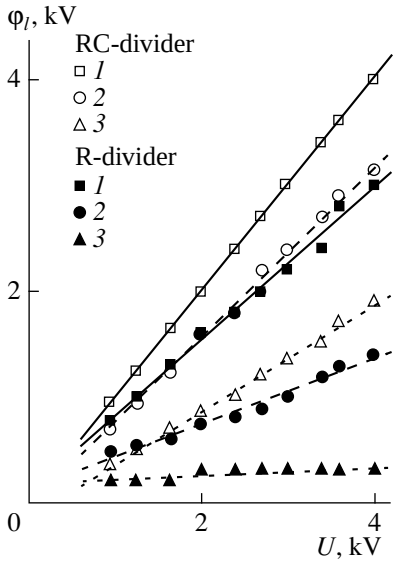

Fig. 2. Voltage applied to the lens electrodes as a function of the supply voltage of the lens for the cases of rigid and nonrigid fixation of the applied voltage for H_l = 0.1 T, I_b = 550 mA, and φ_b = 19 kV; RC-divider: (*1*) central electrode, (*2*) first pair, and (*3*) second pair; R-divider: (*1*) central electrode, (*2*) first pair, and (*3*) second pair.

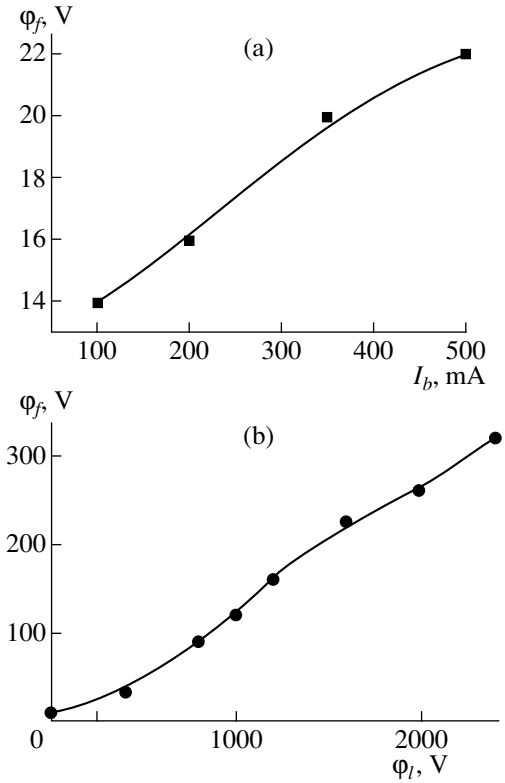

Fig. 3. Floating potential on the lens axis as a function of (a) the beam current at φ_l = 2.6 kV and (b) the central-electrode potential at I_b = 250 mA for H_l = 0.1 T and φ_b = 20 kV.

of 10^{-5} torr. The parameters of the beam and the plasma in the PL volume and drift space were measured with movable Langmuir and capacitive probes. The currents and potential were measured with sensitive Rogowski coils, sectioned collectors, and low-inductance voltage dividers.

3. EXPERIMENTAL RESULTS AND DISCUSSION

The experiments show that, unlike the case of hydrogen-ion beams, when the electron current to the PL electrodes is nearly one order of magnitude lower than the beam current, the passage of heavy-ion beams through the lens is accompanied by a substantially higher electron current to the electrodes (comparable with the beam current). It is seen from Fig. 2 that, when a resistance voltage divider (R-divider) is used, the maximum electron currents flow to the lens electrodes controlling the potential in the middle part of the beam. This evidences that the beam produces much more electrons than is needed for the rearrangement of the vacuum electric field and neutralization of the space charge of the beam. At high beam currents, it becomes almost impossible or inefficient to fix the external potentials at the PL electrodes with the help of a usual R-divider because the electric field is forced out toward the central PL electrodes (the first and second pairs). Note that forcing the electric field out from the axial region of the lens toward the periphery with increasing the beam current was first observed in experiments on the focusing of hydrogen ions [5]. It was shown in those experiments that this effect can be used to minimize spherical aberrations that naturally arise if the distribution of the external potential over the fixing electrodes of the PL is not optimized. Note also that, under these conditions, the floating potential on the axis remained at a level of 10–15 V. Our experiments show that the use of a simple RC-divider ensures that the external potentials at the PL electrodes are rigidly fixed and are equal to their vacuum values (Fig. 2). In this case, as the beam current and the potential φ_l increase, the average electric field in a high-current PL increases more slowly, because the potential on the beam axis increases due to the more intense ejection of electrons from the axial region. This gives rise to spherical aberrations adversely affecting the particle focusing. The increase in the potential on the axis occurs for different distributions of the external potential over the fixing electrodes in a wide range of beam currents. As an illustration, Fig. 3 shows the floating potential on the axis in the midplane of the PL as a function of both the beam current and the central-electrode potential for fixing-potential distributions close to the optimum ones. It is seen that there is a clear tendency toward an increase in the potential as the beam current or lens voltage increases.

It was established experimentally that, when the external-potential distribution over the fixing electrodes is close to the optimum 0-distribution found in

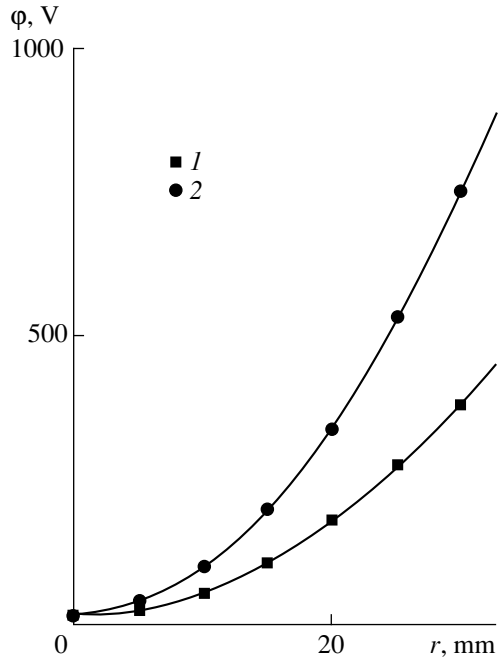

Fig. 4. Radial profile of the potential at the midplane of the lens for I_b = 250 mA, φ_b = 20 kV, and H_l = 0.1 T at φ_l = (*1*) 500 and (*2*) 1000 V.

[3] (in this case, according to the equipotentiality principle, $\Phi(z, R) \sim H_{0z}(z, 0)$), it is possible to achieve a nearly parabolic radial distribution of the potential in the midplane of the lens (see Fig. 4; the solid lines are parabolas).

Figure 5 shows the degree of compression of the focusing beam of copper ions as a function of the central-electrode potential φ_l for different values of φ_b. Measurements were carried out at the same distance z from the midplane of the PL, under conditions when spherical aberrations were minimized (i.e., with the 0-distribution). The focusing occurs at all of the beam energies, and the degree of compression rapidly increases with φ_b. Figure 6 shows the radial profiles of the ion-beam current at the probe located near the collector when the PL is switched on or off. The figure also shows the radial profile of the floating potential in the beam. It is seen that, in the region occupied by the focusing beam (for the central-electrode potential φ_l = 1 kV), the potential increases (note that, under these conditions, the central-electrode potential required for focusing the beam onto the probe is φ_l = 3.5 kV). The experiments show that the potential of an unneutralized space charge at the beam focus attains a value on the order of 120 V and increases with increasing the beam current.

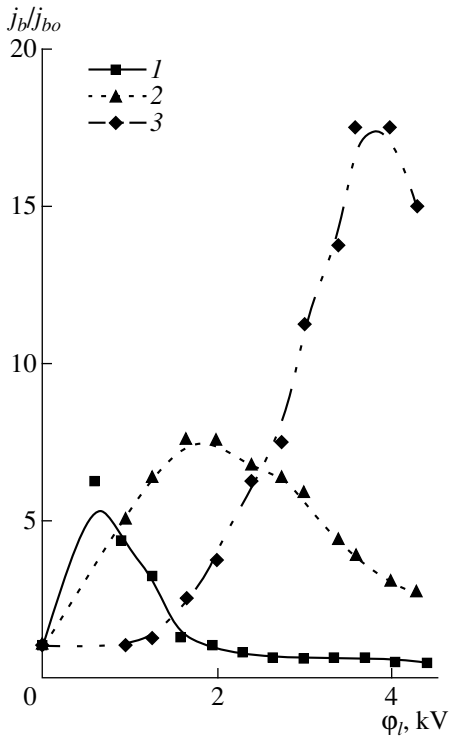

Fig. 5. Gain factor of the current density j_b on the beam axis as a function of the potential at the central electrode of the lens (z = 20 cm) for H_l = 0.1 T and different values of the accelerating voltage: U_b = (*1*) 4, (*2*) 12, and (*3*) 20 kV; j_{b0} is the current density with the lens switched off.

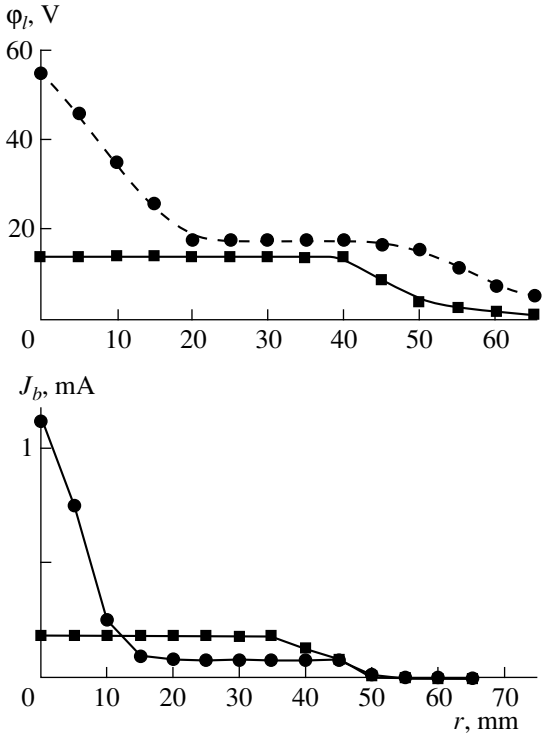

Fig. 6. Radial profile of the floating potential φ_f and the beam current to the probe for I_b = 380 mA and φ_b = 15 kV (copper ions). Squares correspond to φ_l = 0, and circles correspond to φ_l = 1 kV.

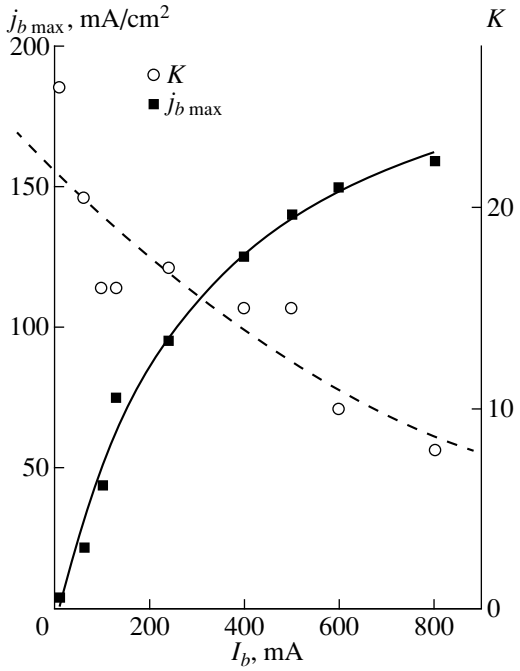

Fig. 7. Maximum current density $j_{b\max}$ at the focus (z = 28 cm) and the gain factor of the current density K as functions of the beam current for φ_l = 3 kV, φ_b = 18 kV, and H_l = 0.1 T.

Figure 7 shows the maximum beam-current density at the focus as a function of the total current flowing through the lens. The values of the compression ratio of the beam are also shown.

It is seen that, for $I_b \geq 400$ mA, there is a tendency toward a decrease in the compression ratio even though the beam-current density in the crossover continuously increases and reaches the value ~170 mA/cm^2 when the total beam current is equal to 800 mA. Apparently, this may be attributed to the observed decrease in the electric field throughout the lens with increasing both the beam current and the potential of the focused beam. We note that the role of the PL does not reduce only to focusing the beam on the target. The presence of the PL also assists the passage of the ion beam through the transport channel. It is seen from Fig. 8 that, when the PL is switched on, the total beam current at the collector increases appreciably. The measurements show that, in this case, almost the entire beam current emerging from the source is gathered by the collector. This indicates that the ion beam is somewhat divergent. This is consistent with the fact that the thin-lens formula must be taken into account in determining the PL focal length for the result to agree with the calculated value.

In our previous experiments with wide-aperture hydrogen-ion beams formed with a similar IOS, this

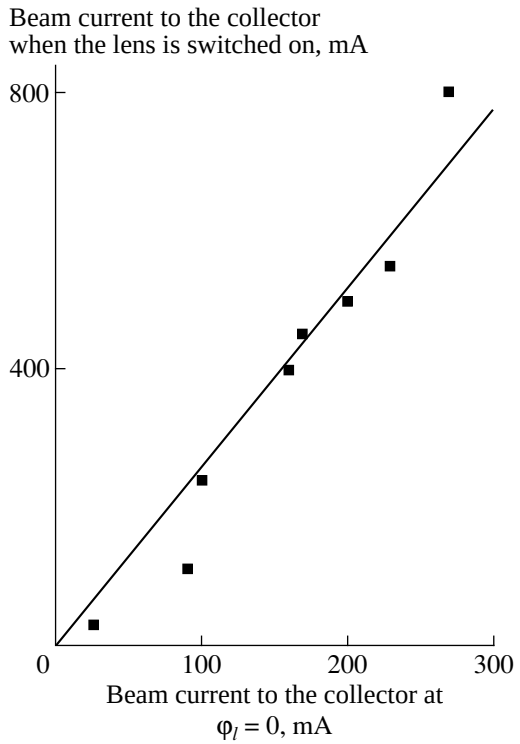

Fig. 8. Relation between the total beam currents to the collector when the lens is switched off and on for φ_l = 3.5 kV, φ_b = 18 kV, and H_l = 0.1 T.

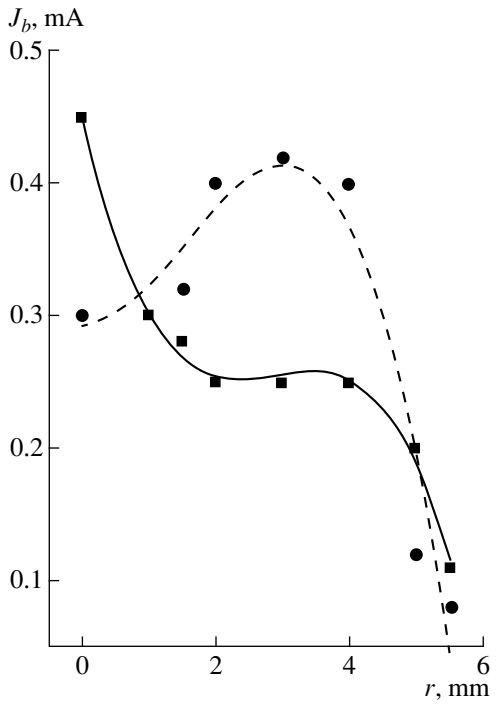

Fig. 9. Radial profiles of the beam current at the focus for different distributions of the external potential over the lens electrodes for φ_l = 200 V, φ_b = 400 V, I_b = 35 mA, and H_l = 0.1 T (Mo ions). Squares correspond to minimal spherical aberrations, and circles correspond to the presence of spherical aberrations.

effect was less pronounced because of a lower value of the initial beam divergence. Thus, these experiments demonstrate another advantage of electrostatic PLs, namely, the ability to correct imperfections of IOSs and form almost divergenceless beams.

The experiments with wide-aperture low-energy (100–400 eV) beams of heavy multiply charged ions revealed how higher order aberrations of a high-current PL (specifically, moment aberrations) affect the focusing of such beams. Experiments with Mo, Cu, and Zn ions showed that, when passing through a PL in which spherical aberrations are minimized, the beam acquires a stepped radial profile, which is especially pronounced in the focused beam (Fig. 9). At the same time, under these conditions, the profile of the focused beam of singly charged carbon ions remains monotonic. In accordance with formula (1) and the data from [10], the presence of the steps and their number can be unambiguously related to the charge composition of the ion beam produced by a vacuum-arc source, because, under these conditions, the PL makes a charge separation in the ion beam.

Thus, a high-current PL can be used to separate high-current wide-aperture ion beams by the charge-to-mass ratio. As the energy increases, the influence of the moment aberrations weakens appreciably, and, even for heavy-ion beams with energies of tens of kiloelectronvolts, their role becomes negligible. The experimental results show that the focusing of well-neutralized heavy-ions beams turns out to be significantly more efficient than the focusing of light hydrogen ions. Therefore, the maximum compression ratio in the focal region can be limited by incomplete neutralization of the beam charge because of an increase in the potential inside the beam, a possible nonmonotonic shape of the fine structure of the radial profile of the potential because of the finite width of the fixing electrodes, and collective effects in a PL.

4. CONCLUSION

The results of experimental studies of the focusing of high-current wide-aperture heavy-ion beams show that the use of electrostatic PLs for focusing and controlling such beams is much more efficient than for hydrogen-ion beams.

This shows promise for designing plasma-optic facilities intended to control the parameters of ion beams in high-dose implanters and high-current accelerators of heavy ions.

The principal results of this research were reported at the Fourth International Seminar on Plasma Electronics and New Acceleration Techniques (Kharkov, 1998), organized by Ya. B. Faĭnberg.

ACKNOWLEDGMENTS

This work was supported in part by the Science and Technology Center of Ukraine (grant no. 298) and the Ukrainian Foundation for Basic Research (project nos. 2.4/705 and 25.2/10).

REFERENCES

1. D. Gabor, Nature **160**, 89 (1947).
2. A. I. Morozov, Dokl. Akad. Nauk SSSR **163**, 1363 (1965) [Sov. Phys. Dokl. **10**, 775 (1966)].
3. O. Scherzer, *Beit. Elektronenoptik* (Berlin, 1937).
4. A. A. Goncharov, A. N. Dobrovolskii, A. V. Zatuagan, and I. M. Protsenko, IEEE Trans. Plasma Sci. **21**, 573 (1993).
5. A. A. Goncharov, A. N. Dobrovol'skiĭ, A. N. Kotsarenko, *et al.*, Fiz. Plazmy **20**, 499 (1994) [Plasma Phys. Rep. **20**, 449 (1994)].
6. A. A. Goncharov, A. V. Zatuagan, and I. M. Protsenko, IEEE Trans. Plasma Sci. **21**, 578 (1993).
7. A. A. Goncharov, A. N. Dobrovol'skiĭ, and V. F. Zadorozhniĭ, Zh. Tekh. Fiz. **67** (8), 97 (1997) [Tech. Phys. **42**, 942 (1997)].
8. A. A. Goncharov, A. N. Dobrovolsky, I. V. Litovko, *et al.*, IEEE Trans. Plasma Sci. **25**, 709 (1997).
9. I. Brown, Rev. Sci. Instrum. **65**, 3061 (1994).
10. I. Brown, Nucl. Instrum. Methods Phys. Res. B **37**–**38**, 68 (1989).

Translated by N. Larionova

Plasma Physics Reports, Vol. 26, No. 9, 2000, pp. 792–800. Translated from Fizika Plazmy, Vol. 26, No. 9, 2000, pp. 845–853.

LOW-TEMPERATURE PLASMA

Sterilization of Medical Products in Low-Pressure Glow Discharges

I. A. Soloshenko*, V. V. Tsiolko*, V. A. Khomich*, A. I. Shchedrin*, A. V. Ryabtsev*, V. Yu. Bazhenov*, and I. L. Mikhno**

**Institute of Physics, National Academy of Sciences of Ukraine, pr. Nauki 144, Kiev, 03039 Ukraine*

***Institute of Epidemiology and Infectious Diseases, Ministry of Health of Ukraine, Ukraine*

Received June 22, 1999; in final form, December 25, 1999

Abstract—Results are presented from experimental and theoretical studies of the sterilization of medical products by the plasmas of dc glow discharges in different gas media. The sterilization efficiency is obtained as a function of discharge parameters. The plasma composition in discharges in N_2 and O_2 is investigated under the operating conditions of a plasma sterilizer. It is shown that free surfaces of medical products are sterilized primarily by UV radiation from the discharge plasma, while an important role in sterilization of products with complicated shapes is played by such chemically active particles as oxygen atoms and electronically excited O_2 molecules. © *2000 MAIK "Nauka/Interperiodica".*

1. INTRODUCTION

In present-day medical practice, there is a need for cold sterilization of many thermolabile instruments and materials. Up to now, these medical products have been surface-sterilized by toxic gases such as ethylene oxide and its mixtures with chlorofluorocarbons. However, the products sterilized in this way should be aerated over a long period (up to 24 hours); moreover, they are very dangerous for the health of the involved staff and are environmentally unfriendly. In this connection, it becomes highly relevant to develop new methods for cold sterilization. One of the most important present-day alternatives to gaseous sterilization is sterilization by gas-discharge plasmas. The main advantage of the plasma sterilization technique is that the plasma, being a chemically active medium, is created during the processes of excitation, dissociation, and ionization of any gas or vapor plasma-producing media (including nontoxic media and even inert gases). Chemically active particles exist only in the course of the discharge and disappear practically instantaneously after the discharge is switched off. These two circumstances make it possible to completely solve the safety and ecological problems.

Although the idea of sterilizing medical products by gas-discharge plasmas was originated as early as the 1960s [1, 2], the efficiency of this method and the boundaries of its applicability have not been examined in detail up to now. Some aspects of this complicated problem were discussed in [3–7].

Here, we report on experimental and theoretical investigations of the physical processes that govern the efficiency of sterilization by a low-pressure gas-discharge plasma. We also describe relevant medical and biological tests. The results obtained answer the questions regarding the effectiveness of the plasma sterilization method and the boundaries of its applicability when gases that are the most interesting from a practical standpoint (air, oxygen, hydrogen, carbon dioxide, nitrogen, and argon) are used.

2. EXPERIMENTAL LAYOUT AND STERILIZATION TECHNIQUES

In our experiments, the plasma was created by dc glow discharges. The discharge current and voltage were varied over the ranges 0.05–0.7 A and 400–600 V; the working volume of the sterilization chamber ranged between 20 to 40 l. The working gases (the gases mentioned above or their mixtures) were admitted into the chamber preevacuated by a fore pump to a residual pressure of 3×10^{-3} torr. The working gas pressure was varied over the range from 5×10^{-2} to 25×10^{-2} torr. The plasma density and electron energy distribution function (EEDF) were measured by single and double Langmuir probes made of tungsten wires 50, 105, and 240 μm in diameter, the receiving sections being from 5 to 10 mm in length. The design of the probes allowed measurements over the entire chamber volume. In measuring the current–voltage (*I–V*) characteristics of the probes, the effects of discharge current pulsations were eliminated and the measurement accuracy was increased using the modified method described in [8]. The *I–V* characteristics of the probes were monitored with a specially devised programmable diagnostic system controlled by a personal computer. A complete cycle of measurements included 2048 steps synchronized with the change in the supply voltage. Our method differed from the method of [8] in that, at each step of a measurement cycle, the controlling computer

1063-780X/00/2609-0792$20.00

code specified the probe current with an accuracy of 0.1 μA and provided simultaneous measurements of the probe voltage relative to the anode, the anode voltage, and the discharge current. The results of measurements in the prescribed ranges of the discharge current and probe voltage were recorded as the dependence of the probe current on the probe voltage at a given discharge current and discharge voltage. The plasma density was computed from the electron saturation current, and the EEDF was evaluated by using special subroutines through differentiating the *I–V* characteristics twice [9] and preinterpolating (if necessary) the measured data. In the above pressure range, the plasma density was found to be essentially pressure-independent and was governed exclusively by the input power. With increasing the input power density W_d from 3×10^{-3} to 30×10^{-3} W/cm^3, the plasma density increased almost linearly from 7×10^8 to 6×10^9 cm^{-3} (Fig. 1, curve *1*), in which case the degree of plasma inhomogeneity in the working volume of the sterilization chamber was at most 25–30%. The EEDF was measured in discharges in air, oxygen, and nitrogen. In oxygen and air, the EEDF was found to be monotonic. In some regimes of a discharge in nitrogen, the EEDF was observed to be inverted in the energy range 2–4 eV because of the vibrational excitation of N_2 molecules (Fig. 2, curve *3*).

The electric field in the plasma volume is an important parameter of a gas discharge. We found that, under typical discharge conditions ($P = (4–20) \times 10^{-2}$ torr and $W_d = (3–25) \times 10^{-3}$ W/cm^3), the electric field strength varied in a range from about 0.1 to about 1.0 V/cm. The related results of measurements in a nitrogen plasma are illustrated in Fig. 3.

The UV radiation power was monitored in the following two ways. In the wavelength band 220–320 nm, the UV power was measured by a DAU-81 apparatus. In the vacuum UV and soft UV spectral bands ($120 \le \lambda < 220$ nm), the radiation power was measured by a specially developed photoresist-based technique, which consisted of the following: the exposure time of a photoresist (i.e., the time over which the exposed photoresist disappeared entirely from the substrate surface in a specially prepared solution) was uniquely determined by the fraction of UV radiation absorbed by the photoresist. The substrates with a photoresist were exposed to UV radiation from a plasma over different times and were developed. Then, we plotted the so-called characteristic curves, showing the rate at which a photoresist disappeared versus the exposure time. A comparison between these characteristic curves and those obtained from experiments carried out with sources with known powers and UV radiation spectra allowed us to determine the power of UV radiation from the discharge plasma with a sufficiently high degree of confidence. We found that the radiation intensity increased with increasing the input power density W_d (Fig. 1, curve *2*) and that the bulk of the UV power, approximately $W_S =$

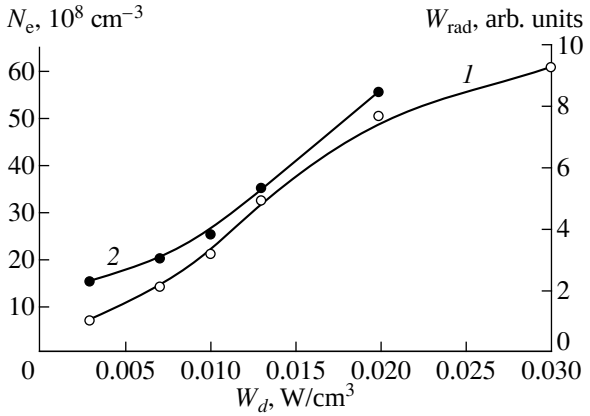

Fig. 1. (*1*) UV radiation flux density and (*2*) UV radiation power vs. the specific power input into a discharge in air at the pressure $P = 20 \times 10^{-2}$ torr.

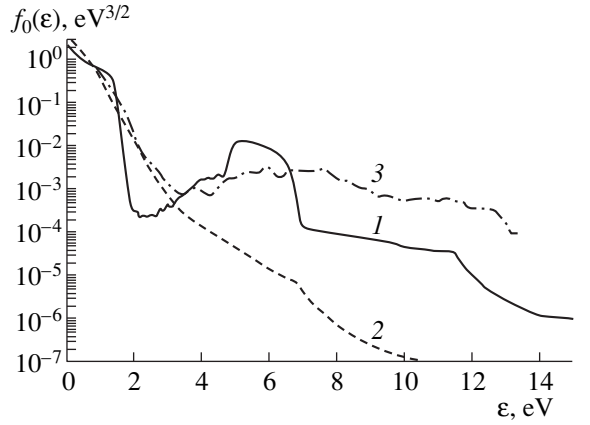

Fig. 2. Representative profiles of the EEDF calculated theoretically for (*1*) nitrogen and (*2*) oxygen and (*3*) the EEDF measured experimentally in a discharge plasma in nitrogen.

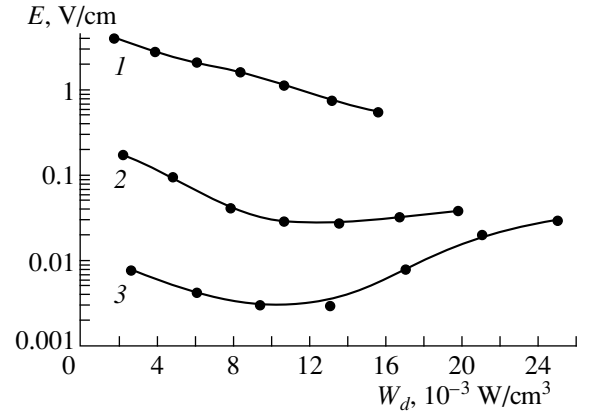

Fig. 3. Steady-state electric field in a plasma vs. the specific power input into discharges in nitrogen at different pressures P = (*1*) 2×10^{-1}, (*2*) 1×10^{-1}, and (*3*) 4×10^{-2} torr.

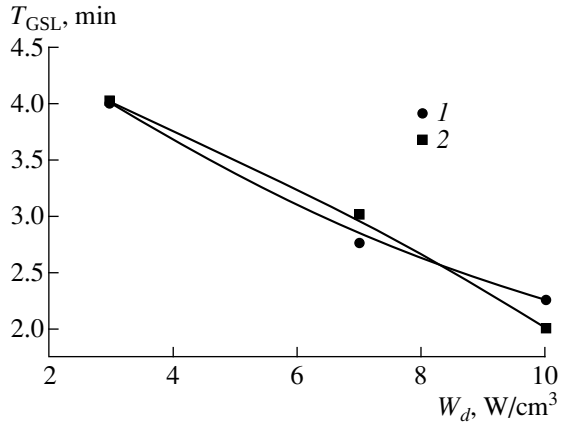

Fig. 4. Sterilization time T_{GSL} vs. the specific power input into discharges in air at two different pressures P = (*1*) 8×10^{-2} and (*2*) 20×10^{-2} torr, the initial number of the spores being 10^7.

50–100 μW/cm^2 at $W_d = (3–7) \times 10^{-3}$ W/cm^3, was emitted from the plasma at the wavelengths $\lambda \le 220$ nm.

The temperature of the sterilized products (test objects) was measured with a chromel–alumel thermocouple. The discharge regimes were chosen so that the temperature of the sterilized test objects was at most 60°C, in accordance with the requirements for sterilizing thermolabile materials.

As test objects, we used metal and glass Petri dishes with an inner surface area of about 10 cm^2. Medical and biological investigations were carried out with spores and with vegetative and viral microorganisms. The results reported below were obtained in experiments with the spores of *Bacillus subtilis,* which turned out to be the most resistant to sterilization by discharge plasmas. The inner surfaces of the Petri dishes were infected uniformly with spore-containing water suspensions. Initially, the number of spores on test objects varied between 10^5 to 10^8 (i.e., the mean surface density of the spores was 10^4–10^7 spore/cm^2). Note that the real density of microorganisms on the presterilized products is much lower (10^2–10^3 cm^{-2}); moreover, these are mostly vegetative microorganisms, which are substantially less resistant to sterilization in comparison with spores. In other words, the conditions under which we investigated sterilization by plasma were much more stringent than those prevailing in medical practice. After incubation of the spores on the test objects sterilized by plasma, we controlled the extent to which the objects were sterilized by immediately counting the number of colonies of the spores (i.e., the number of spores that survived the sterilization). Then, we plotted the survivability profiles, which reflected the number of microorganisms that remained alive versus the sterilization time. The sterilization efficiency was characterized by the time during which a guaranteed sterilization level (GSL) of 10^{-6} was achieved, i.e., the time T_{GSL} during which one of every 10^6 spores initially infected on the test objects survived the sterilization.

3. EXPERIMENTAL RESULTS

In our previous papers [6, 7] aimed at revealing the main features of sterilization by a low-pressure glow discharge plasma, we established the following:

(i) The sterilization time in discharges in all gases used in experiments is essentially independent of the gas pressure over the entire pressure range under investigation, $(8–25) \times 10^{-2}$ torr, and decreases with increasing the specific power input into the discharge (Fig. 4). Consequently, the efficiency of sterilization in discharges in each of the gases is determined by the plasma density.

(ii) The most efficient working gas is oxygen; less efficient gases in decreasing order are air, carbon dioxide, hydrogen, argon, and nitrogen.

(iii) The efficiency of sterilization by plasma decreases as the initial density of spores on the test objects is increased from 10^6 to 10^7 spore/cm^2. The reason is that, at densities of about 10^7 spore/cm^2, the spores stick together, forming lumps inside of which the spores are more resistant to plasma sterilization and thereby increase the sterilization time. Clearly, this feature of sterilization by plasma is characteristic of any plasma sterilizer.

Our main purpose here is to investigate the main sterilizing factors of low-temperature plasmas of low-pressure glow discharges: the charged plasma particles, UV radiation from the plasma, and chemically active neutral plasma particles (such as radicals and excited atoms and molecules).

To determine the relative efficiency of sterilization by charged plasma particles, we carried out experiments on the sterilization of metal test objects. Varying the potential applied to a test object, we were able to change the energy and intensity of the electron and ion fluxes onto the object, without changing the fluxes of chemically active neutral plasma particles or UV radiation from the plasma. If the charged particles play an important role in sterilization, then the sterilization efficiency should be very sensitive to the potential applied to test objects. We found that the survivability profiles obtained in experiments with metal test objects held at the anode, cathode, or floating potentials were essentially identical, thereby providing clear evidence that charged plasma particles did not affect the sterilization process.

To analyze the relative role of UV radiation from the discharge plasma, we carried out experiments with test objects that were sterilized either directly or through filters made of lithium fluoride (LiF) and a KU-1 quartz glass 3 mm thick. In the absence of filters, the objects were sterilized by the combined action of UV radiation and chemically active neutral particles, while filter-pro-

tected objects were sterilized only by UV radiation of wavelengths $\lambda \geq 120$ nm (in the case of LiF filters) and $\lambda \geq 160$ nm (in the case of quartz filters). Figure 5 shows the survivability profiles for spores during sterilization by the combined action of UV radiation and active neutral particles and exclusively by UV radiation in discharge plasmas in oxygen, air, and nitrogen. We can see that, for these gases, the profiles characterizing sterilization with and without filters are practically identical. Similar results were obtained from experiments with filters made of a KU-1 quartz glass and LiF over the entire ranges of working pressures and specific input powers W_d in discharges in all working gases. We thus conclude that the most important sterilizing factor of a discharge plasma is UV radiation. Experiments with a photoresist showed that UV radiation was emitted from plasmas at wavelengths no longer than ~220 nm. On the other hand, the fact that the experimental results obtained with the use of filters with limiting wavelengths of 160 and 120 nm are essentially the same leads to the conclusion that the lower limit on the radiation wavelength is 160 nm; in other words, sterilization by UV radiation with wavelengths in the range $160 \leq \lambda \leq 220$ nm is the most efficient.

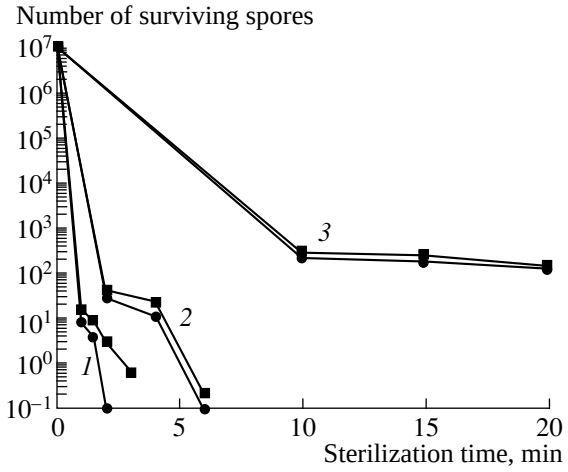

Fig. 5. Survivability profiles for the spores of Bacillus subtilis, which were obtained by counting the number of colonies during sterilization by the combined action of all of the sterilizing factors of the plasma (circles) and only by UV radiation from the plasma (squares) in discharges in (*1*) oxygen, (*2*) air, and (*3*) nitrogen at the pressure $P = 2 \times 10^{-1}$ torr and input power density $W_d = 3 \times 10^{-3}$ W/cm^3, the initial number of the spores being 10^7.

Note that the efficiency of sterilization by UV radiation from discharge plasmas is significantly higher than that by UV radiation from mercury lamps, which are routinely used in medical practice. For example, the duration of sterilization by UV radiation with the power $W_S \approx 100$ μW/cm^2 in a plasma sterilizer is five times shorter than that by UV radiation from a BUV-30 lamp with a much higher power ($W_S = 1500$ μW/cm^2). This mainly stems from the fact that the lamp emits UV radiation at significantly longer wavelengths (about 253 nm).

We point out here another important advantage of sterilization by UV radiation of plasma: since the sterilized products are immersed in the radiating plasma, the "shadowing" effect is essentially absent. Of course, this is primarily true of medical products free of holes narrower than the Debye radius of the plasma electrons (below, for brevity, the surfaces of such products will be referred to as free surfaces). The main sterilizing factor for products with complicated shapes (i.e., those with slits and holes narrower than the electron Debye radius) is chemically active neutral plasma particles rather than a more efficient UV radiation. Accordingly, it is very important to investigate the efficiency of sterilization by these particles. To do this, we developed a method aimed at studying sterilization by neutral plasma particles against the background of UV radiation, which is a more pronounced sterilizing factor. The essence of the method consists in protecting the sterilized objects by a fine metal grid, which reflected charged plasma particles because the grid cells were chosen to be narrower than their Debye radii, and by a screen, which was positioned behind the grid and was aimed at absorbing and reflecting UV radiation of the plasma. As a result, the test objects protected by both the grid and screen could be affected only by active neutral particles. We used grids with 0.01×0.01 cm cells and with a total area S_0 from 0.05 to 0.6 cm^2, the grid transmissivity being 80%. Geometrically, this system was arranged so that, over the entire range of the total grid area S_0, the particle density in the middle of a Petri dish was governed only by the balance between the particle influx through a hole of area S_0, the absorption of particles by the surface of the Petri dish, and by the particle outflux from the dish back to the discharge plasma. Consequently, as S_0 increases, the density of active neutral particles in the Petri dish should increase up to the plasma density in a certain critical area S_0. As a result, the sterilization time, which depends on the density of active particles, should decrease with increasing S_0 and should remain essentially unchanged above the critical value of S_0. Our experiments showed that the sterilization time actually decreased with increasing the hole area S_0 and became the shortest at $S_0 \geq 0.2$ cm^2. This shortest time is the time required to sterilize free surfaces by chemically active neutral plasma particles. In experiments with discharges in oxygen, nitrogen, and argon, the sterilization time was observed to depend on the hole area S_0 in an analogous manner. As in the case of discharges in air, the sterilization time was found to be the shortest at $S_0 \geq 0.2$ cm^2.

To compare the efficiency of sterilization by UV radiation from the plasma with that by chemically active neutral plasma particles, Fig. 6 shows the survivability profiles representative for discharges in oxygen and air. We can see that, in the case of discharges in air,

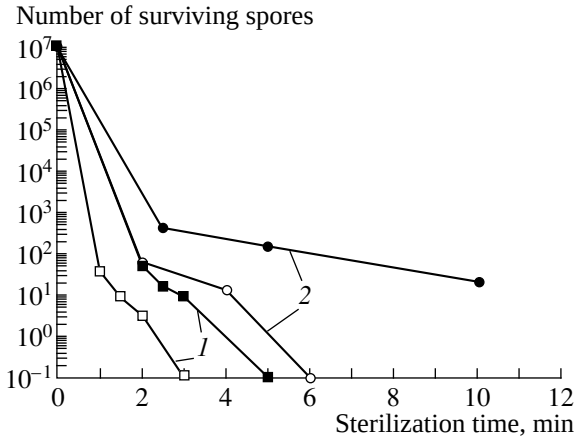

Fig. 6. Survivability profiles for the spores of *Bacillus subtilis*, which were obtained by counting the number of colonies during sterilization of free surfaces by active neutral plasma particles (closed symbols) and by UV radiation from the plasma (open symbols) in discharges in (*1*) oxygen and (*2*) air at the pressure $P = 10^{-1}$ torr and input power density $W_d = 3 \times 10^{-3}$ W/cm^3, the initial number of the spores being 10^7.

the duration of sterilization by UV radiation from the plasma is five to six times shorter than that by active neutral particles.

4. NUMERICAL MODELING

According to the experiments described above, the main role in sterilization of free surfaces is played by UV radiation, while charged plasma particles do not participate in the sterilization process (below, we will show that the plasma fluxes onto the sterilized surface are much less intense than the fluxes of UV photons and biologically active neutral particles).

The products with complicated shapes are sterilized mainly by the active neutral particles. In the case of discharges in oxygen, they are atoms, ozone molecules, and excited atoms and molecules. In the case of discharges in nitrogen, they are excited atoms and molecules.

In order to understand better what active particles are and to find the contents of the plasma, neutral plasma component, and radiation, we modeled glow discharges in nitrogen and oxygen under the operating conditions of a plasma sterilizer.

Our numerical model is based on the following kinetic equations for neutral and charged plasma components:

$$\frac{dN_i}{dt} = \sum_i k_i N_i + \sum_{i,\, j(i \le j)} k_{ij} N_i N_j + \ldots, \qquad (1)$$

where the first term on the right-hand side describes plasma processes in the approximation linear in the densities N_i of the plasma components, the second term accounts for binary collisions, and so on. The rate constants k_{ej} for binary collisions involving plasma electrons were determined from the expression

$$k_{ej} = \sqrt{\frac{2e}{m}} \int_0^\infty \varepsilon Q_{ej} f_0(\varepsilon) d\varepsilon, \qquad (2)$$

where ε is the electron energy (in units of eV), $e = 1.602 \times 10^{-12}$ erg/eV, m is the mass of an electron (in g), and $Q_{ej}(\varepsilon)$ is the cross section of the related collision process (in cm^2). The symmetric part of the EEDF, $f_0(\varepsilon)$, was found from the Boltzmann equation [10]

$$\frac{1}{n_e N}\sqrt{\frac{m}{2e}}\varepsilon^{1/2}\frac{\partial(n_e f_0(\varepsilon))}{\partial t} - \frac{1}{3}\left(\frac{E}{N}\right)^2 \frac{\partial}{\partial \varepsilon}\left(\frac{\varepsilon}{Q_T}\frac{\partial f_0(\varepsilon)}{\partial \varepsilon}\right)$$
$$-\frac{\partial}{\partial \varepsilon}\left[2\frac{m}{M}Q_T\varepsilon^2\left(f_0 + T\frac{\partial f_0(\varepsilon)}{\partial \varepsilon}\right)\right] \qquad (3)$$
$$= S_{eN} + S_{ee} + A(\varepsilon) + L(\varepsilon),$$

which was solved together with the kinetic Eqs. (1). In Eq. (3), T is the gas temperature (in units of eV); n_e is the electron density; N_i is the density of gas molecules and Q_{iT} is the relevant transport cross section; S_{eN} and S_{ee} are the integral of electron–neutral inelastic collisions and electron–electron scattering, respectively; $A(\varepsilon)$ is the ionization term describing, in particular, the source of primary electrons; the term $L(\varepsilon)$ accounts for the electrons that escape to the anode; E is the electric field strength (in V/cm); and N is the net gas density.

The integral S_{eN} of electron–molecule inelastic collisions was chosen in the form [11, 12]

$$S_{eN} = \sum_j [(\varepsilon + \varepsilon_j) Q_{ej}(\varepsilon + \varepsilon_j) f_0(\varepsilon + \varepsilon_j) - \varepsilon Q_{ej}(\varepsilon) f_0(\varepsilon)] \qquad (4)$$

for discharges in nitrogen and in the form

$$S_{eN} = \sum_j [(\varepsilon + \varepsilon_j) Q_{ej}(\varepsilon + \varepsilon_j) f_0(\varepsilon + \varepsilon_j) - \varepsilon Q_{ej}(\varepsilon) f_0(\varepsilon)] - \varepsilon Q_d f_0(\varepsilon) \qquad (5)$$

for discharges in oxygen. In (4) and (5), Q_{ej} is the cross section for excitation and dissociation of molecules by UV photons with energies ε_j and Q_d is the cross section for dissociative attachment of electrons to O_2 molecules.

The expressions for the integral S_{ee} of electron–electron scattering and for the ionization term $A(\varepsilon)$ are presented in [11]. In our model, we adopted analogous expressions, but for the gases and energies of fast electron beams used in our experiments.

Since our measurements of the potential in glow discharges showed that the applied voltage of about

450 eV dropped preferentially across the cathode sheath with a thickness of about 1 cm, we assumed that the gas in a sterilizer was ionized by a beam of fast electrons with an energy of about 450 eV. In the main discharge plasma, the electric field was almost uniform and was approximately equal to 0.1 V/cm at a pressure of ~0.1 torr. Consequently, the electrons escaping from the plasma to the anode can be described in the drift approximation. In the electron balance, we can neglect the electron losses due to electron recombination because the plasma density is low. These considerations allowed us to choose the following form of the term $L(\varepsilon)$, which describes the electrons escaping from the discharge chamber:

$$L(\varepsilon) = \frac{1}{3}\frac{E}{N^2}\frac{S_a}{V}\frac{\varepsilon}{N_i Q_{iT}(\varepsilon) + \sum_j N_j Q_{ej}(\varepsilon)}\frac{\partial f_0(\varepsilon)}{\partial \varepsilon}, \quad (6)$$

where S_a is the area of the anode surface and V is the volume of the discharge chamber.

The EEDF $f_0(\varepsilon)$ was normalized to satisfy the condition

$$\int_0^\infty f_0(\varepsilon)\sqrt{\varepsilon}\,d\varepsilon = 1. \quad (7)$$

We solved equations (1) and (2) numerically by the methods that were used and approved in [12, 13]. We assumed that the densities of all plasma components are uniform and applied the extended scheme of the kinetic processes listed in Tables 1 and 2 for nitrogen and oxygen, respectively. The UV radiation was assumed to be emitted only in transitions from the lowest resonant state to the vibrationally excited levels of the ground state. In the case of nitrogen, these transitions correspond to the Lyman–Berge–Goldfield bands. The cross sections for elastic scattering of electrons by N_2 and O_2 molecules were taken from [14–16], and the cross sections for inelastic processes were taken from [16–22]. Some of the scattering cross sections and rate constants were taken from [23, 24].

Table 1

1	$N_2 + e \longrightarrow N_2^+ + e + e$
2	$N_2 + e \longrightarrow N_2(\alpha^1\Pi) + e$
3	$N_2 + e \longrightarrow N + N + e$
4	$N_2^+ + e \longrightarrow N + N$
5	$N_2(\alpha^1\Pi) + e \longrightarrow N_2^+ + e$
6	$N_2(\alpha^1\Pi) \longrightarrow N_2 + \hbar\omega_2$
7	$N + N + N \longrightarrow N_2 + N$
8	$N + N + N_2 \longrightarrow N_2 + N_2$
9	$N + \text{wall} \longrightarrow 1/2N_2$
10	$N + e \longrightarrow N^+ + e + e$
11	$N + e \longrightarrow N(3\sigma^4P) + e$
12	$N^+ + N + N \longrightarrow N_2^+ + N$
13	$N^+ + N + N_2 \longrightarrow N_2^+ + N_2$
14	$N(3\sigma^4P) + e \longrightarrow N^+ + e + e$
15	$N(3\sigma^4P) \longrightarrow N + \hbar\omega_1$
16	$N_2 + \hbar\omega_1 \longrightarrow N_2(\alpha^1\Pi)$
17	$N + \hbar\omega_1 \longrightarrow N(3\sigma^4P)$
18	$N_2^+ + e(\text{cathode}) \longrightarrow N_2$
19	$N^+ + e(\text{cathode}) \longrightarrow 1/2N_2$
20	$e \longrightarrow$ anode
21	e–e scattering
22	Elastic scattering

5. NUMERICAL RESULTS AND COMPARISON WITH THE EXPERIMENT

Figure 2 shows representative profiles of the EEDF for discharges in nitrogen and oxygen (curves *1*, *2*). In the case of nitrogen, the EEDF is seen to be inverted ($df_0/d\varepsilon > 0$) in the energy range 2–4 eV because of the vibrational excitation of N_2 molecules; this result is confirmed by our experimental measurements (curve *3*). In the case of oxygen, the EEDF is monotonic because, first, the vibrational excitation cross section for O_2 molecules is much smaller than that for N_2 molecules and, second, in accordance with the experimental conditions, the EEDF was truncated at a low threshold energy corresponding to the electronic excitation of the molecular state $O_2(^1\Delta_g)$. Note that, to a considerable extent, the inversion of the EEDF in the case of nitrogen is also attributed to the weak electric field, which is characteristic of glow discharges at low pressures ($p \leq 0.1$ torr). In this situation, the EEDF is analogous to that observed at a certain time in a decaying plasma after switching off the electric field [8]. In the experiments with discharges in nitrogen [8], the EEDF was also observed to be inverted, which is explained by a sharp peak in the vibrational excitation cross section for N_2 molecules ($v = 1$–9) in the energy range 2–3.7 eV. At high pressures, the energy of fast electrons is too low for them to uniformly ionize the gas over the entire working volume; as a result, the electric field in the main discharge plasma increases. In this case, the EEDF becomes nearly Maxwellian and is similar in shape to that in [8, 23, 24] at the time $t = 0$ after switching-off of the electric field, because, according to (3), the electric field gives rise to diffusion in energy space.

Figures 7 and 8 depict the densities of the main plasma components versus pressure in the case of discharges in nitrogen and oxygen. It is seen from Fig. 7 that the densities of the primary products from electron–molecule reactions (i.e., plasma, atomic nitrogen

Table 2

1	$O_2 + e \longrightarrow O_2^+ + e + e$
2	$O_2(^1\Delta_g) + e \longrightarrow O_2^+ + e + e$
3	$O_2(b\,^1\Sigma_g^+) + e \longrightarrow O_2^+ + e + e$
4	$O_2(*) + e \longrightarrow O_2^+ + e + e$
5	$O_2(*) \longrightarrow O_2 + \hbar\omega_3$
6	$O_2 + \hbar\omega_3 \longrightarrow O_2(*)$
7	$O + e \longrightarrow O^+ + e + e$
8	$O_2 + e \longrightarrow O_2(^1\Delta_g) + e$
9	$O_2 + e \longrightarrow O_2(b\,^1\Sigma_g^+) + e$
10	$O_2 + e \longrightarrow O_2(*) + e$
11	$O_2 + e \longrightarrow O + O + e$
12	$O_2^+ + e \longrightarrow O + O$
13	$O_2 + e \longrightarrow O^- + O$
14	$O^- + O_2^+ \longrightarrow O + O_2 + e$
15	$O^- + O^+ \longrightarrow O + O + e$
16	$O^- + e \longrightarrow O + e + e$
17	$O^- + O_2 \longrightarrow O + O_2 + e$
18	$O^- + O \longrightarrow O + O + e$
19	$O + \text{wall} \longrightarrow 1/2O_2$
20	$O^+ + O + O \longrightarrow O_2^+ + O$
21	$O^+ + O + O_2 \longrightarrow O_2^+ + O_2$
22	$O^- + O_2(^1\Delta_g) \longrightarrow O_3 + e$
23	$O_3 + O_2(b\,^1\Sigma_g^+) \longrightarrow O_2 + O_2 + O$
24	$O_3 + e \longrightarrow O_2 + O + e$
25	$O_2(^1\Delta_g) + e \longrightarrow O + O + e$
26	$O_2(b\,^1\Sigma_g^+) + e \longrightarrow O + O + e$
27	$O_2^+ + e(\text{cathode}) \longrightarrow O_2$
28	$O^+ + e(\text{cathode}) \longrightarrow 1/2O_2$
29	$e \longrightarrow \text{anode}$
30	e–e scattering
31	Elastic scattering

and oxygen, and excited N_2 and O_2 molecules) are essentially pressure-independent. The reason for this is that, the higher the pressure of the discharge plasma, the higher the dissociation, excitation, and ionization energies at which the EEDF is truncated. Since the dissociation, excitation, and ionization rate constants k_{ej} defined in (2) are inversely proportional to the gas density, the total rate constants, which characterize the production of the corresponding components of the gas plasma and are defined as $k_{ej}N_{N_2, O_2}$, remain essentially unchanged.

Note that the densities of such biologically active components as atomic oxygen and excited oxygen molecules $O_2(^1\Delta_g)$ can be fairly high (about 10^{12} cm^{-3}). The density of the excited molecules $O_2(^1\Delta_g)$ is significantly higher than that of the excited N_2^* molecules (by three orders of magnitude) because of the low excitation energy ($\varepsilon = 0.95$ eV) of the $^1\Delta_g$ level of oxygen molecules. The densities of the secondary products from electron–molecule reactions, in particular, the number densities $N_{\hbar\omega_2}$ and $N_{\hbar\omega_3}$ of UV photons (about 10^3 cm^{-3}), are all low (Fig. 8). However, we must keep in mind that the densities do not affect the sterilization time, which is governed by the fluxes of the corresponding biologically active particles onto the substrate surface as well as by their penetrability and their sterilizing effect on the spores. The intensity $cN_{\hbar\omega_2, \hbar\omega_3}$ of the UV photon fluxes (3×10^{13} cm^{-2} s^{-1}) is more than one order of magnitude higher than the plasma flux intensity (about 10^{12} cm^{-2} s^{-1}), because the ambipolar diffusion rate in the plasma is low. The computed intensity of the UV photon flux and the computed plasma density both agree with those measured experimentally. Among the fluxes of active neutral particles, the most intense are those of oxygen atoms and excited molecules $O_2(^1\Delta_g)$ and $O_2(b\,^1\Sigma_g^+)$ (~10^{15}–10^{16} cm^{-2} s^{-1}), because the densities of these molecules are high. It is also seen from Fig. 8 that the densities of the excited nitrogen molecules increase with pressure (in contrast to the densities of the remaining neutral components). Since the sterilization efficiency is pressure-independent, we can conclude with a high degree of confidence that nitrogen plays an unimportant role in sterilization of the free surfaces of medical products. Presumably, this is attributed to the low nitrogen density (about 10^7 cm^{-3}) and low intensity (about 10^{11} cm^{-2} s^{-1}) of nitrogen fluxes.

The distributions of N_2 and O_2 molecules over vibrationally excited states are analogous to those in [23, 24]. Here, we do not focus on the vibrationally excited molecules $N_2(v)$ and $O_2(v)$, because they have the same valence as the N_2 and O_2 molecules in the ground state, which, however, do not affect the sterilization process, no matter how high their densities.

The densities of the plasma components that affect sterilization (UV photons, O atoms, and the excited molecules $O_2(^1\Delta_g)$ and $O_2(b\,^1\Sigma_g^+)$) increase linearly as the discharge current increases. This result agrees with the measurements of the sterilization time, which was found to decrease in inverse proportion to the input power as the latter was increased. In other words, the sterilization efficiency increases linearly with increasing the discharge current. Note that the computed

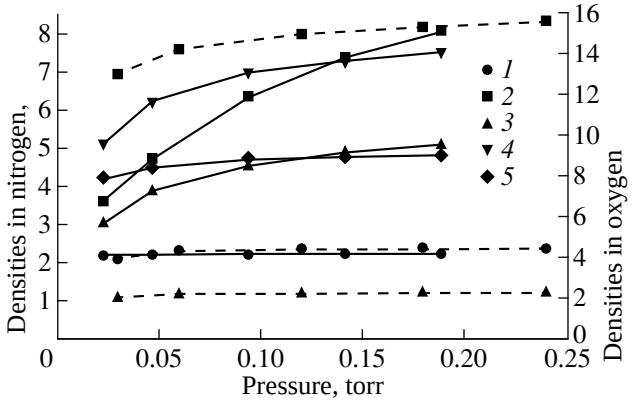

Fig. 7. Densities of the plasma components vs. pressure. The dashed curves correspond to nitrogen: (*1*) n_e, 10^8 cm^{-3}; (*2*) $N_{N_2^*}$, 2×10^9 cm^{-3}; and (*3*) N_N, 10^{12} cm^{-3}. The solid curves refer to oxygen: (*1*) n_e, 10^8 cm^{-3}; (*2*) N_O, 10^{12} cm^{-3}; (*3*) $N_{O_2(^1\Delta_g)}$, 10^{11} cm^{-3}; (*4*) $N_{O_2(b^1\Sigma_g^+)}$, 10^{10} cm^{-3}; and (*5*) $N_{O_2^*}$, 10^8 cm^{-3}.

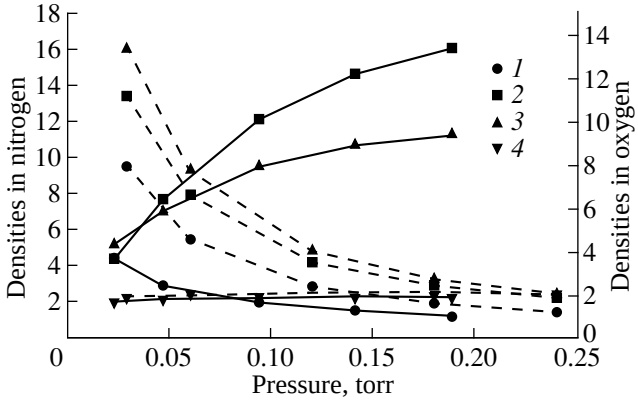

Fig. 8. Densities of the plasma components vs. pressure. The dashed curves correspond to nitrogen: (*1*) N_{N^+}, 10^4 cm^{-3}; (*2*) N_{N^*}, 10^2 cm^{-3}; (*3*) $N_{\hbar\omega_1}$, cm^{-3}; and (*4*) $N_{\hbar\omega_2}$, 10^3 cm^{-3}. The solid curves refer to oxygen: (*1*) N_{O_3}, 10^6 cm^{-3}; (*2*) N_{O^+}, 10^6 cm^{-3}; (*3*) N_{O^-}, 10^6 cm^{-3}; and (*4*) $N_{\hbar\omega_3}$, 10^3 cm^{-3}.

dependence of the plasma density on the discharge current agrees with that measured experimentally.

To conclude this section, note that, according to the results obtained, the main active particles that govern the efficiency of sterilization by discharge plasmas in oxygen and air are oxygen atoms and the excited molecules $O_2(^1\Delta_g)$ and $O_2(b^1\Sigma_g^+)$, although there are many other biologically active neutral particles in low-pressure glow discharges. This conclusion is supported primarily by a comparison between such parameters as the densities of different plasma components and the intensities of their fluxes, as well as between the dependences of these parameters on the pressure and discharge current. Since the density of biologically active particles in discharges in N_2 is much lower than that in discharges in O_2, sterilization in nitrogen requires longer time intervals in comparison with sterilization in oxygen.

6. CONCLUSIONS

The data obtained in our experiments allow us to draw the following conclusions:

(i) In the sterilization of free surfaces by discharge plasmas, the main role is played by UV radiation emitted from the plasma in the wavelength range from about 160 to about 220 nm.

(ii) The efficiency of sterilization by UV radiation from the plasma is significantly higher than that by UV radiation from sources that are routinely used in medical practice.

(iii) Medical products with complicated shapes are primarily sterilized by chemically active neutral plasma particles.

(iv) The duration of sterilization of free surfaces by active neutral particles in discharge plasmas in oxygen and air is two to six times longer than that of sterilization by UV radiation.

Our numerical modeling showed that, among the active neutral components in a discharge plasma in oxygen, the densities of oxygen atoms and oxygen molecules excited to the 0.98- and 1.64-eV energy levels are the highest. These are the particles that govern the efficiency of sterilization of medical products with complicated shapes.

The computed plasma density, EEDF, and UV radiation flux density agree well with the experimental data. This is also true for the dependences of the sterilizing factors of a discharge plasma on the discharge parameters.

ACKNOWLEDGMENTS

This work was supported in part by the Center for Science and Technology of Ukraine, project no. 57.

REFERENCES

1. W. P. Menashi, US Patent No. 3.383.163.
2. R. Bersin, US Patent No. 3.410.776.
3. L. Szu-Min, Thesis D. Sc. (University of Texas at Arlington, 1986).
4. *Proceedings of the International Kilmer Memorial Conference on the Sterilization of Medical Products, Moscow, 1989*, p. 80.

5. G. G. Shishkin and A. G. Shishkin, in *Proceedings of the 12 International Conference on Gas Discharges and Their Applications, Greifswald, 1997*, Vol. 2, p. 783.
6. V. A. Khomich, I. A. Soloshenko, V. V. Tsiolko, *et al.*, in *Proceedings of the 12 International Conference on Gas Discharges and Their Applications, Greifswald, 1997*, Vol. 2, p. 740.
7. V. A. Khomich, I. A. Soloshenko, V. V. Tsiolko, *et al.*, in *Proceedings of the Congress on Plasma Sciences, Prague, 1998*, p. 2745.
8. R. Hugon, G. Henrion, and M. Fabry, Meas. Sci. Technol. **7**, 553 (1996).
9. M. J. Druyvesteyn, Z. Phys. **64**, 790 (1930).
10. J. P. Shkarofsky, T. W. Johnston, and M. P. Bachynski, *The Particle Kinetics of Plasmas* (Addison-Wesley, Reading, 1966; Atomizdat, Moscow, 1969).
11. P. M. Golovinskiĭ and A. I. Shchedrin, Zh. Tekh. Fiz. **59** (2), 51 (1989) [Sov. Phys. Tech. Phys. **34**, 159 (1989)].
12. A. I. Shchedrin, A. V. Ryabtsev, and D. Lo, J. Phys. B **29**, 915 (1996).
13. V. P. Goretskiĭ, A. V. Ryabtsev, I. A. Soloshenko, *et al.*, Zh. Tekh. Fiz. **63** (9), 46 (1993) [Tech. Phys. **38**, 762 (1993)].
14. R. Higgins, C. J. Noble, and P. G. Burke, J. Phys. B: At. Mol. Opt. Phys. **27**, 3203 (1994).
15. R. D. Hake and A. V. Phelps, Phys. Rev. **152** (1), 70 (1967).
16. A. V. Elitskiĭ, L. A. Palkina, and B. M. Smirnov, in *Transport Phenomena in Weakly Ionized Gases* (Atomizdat, Moscow, 1975), Chap. 5.
17. J. M. Ajello, J. Chem. Phys. **53**, 1156 (1970).
18. C. J. Gillant, J. Tennyson, B. M. McLaughlin, and P. G. Burke, J. Phys. B: At. Mol. Opt. Phys. **29**, 1531 (1996).
19. J. T. Fons, R. S. Schappe, and C. C. Lin, Phys. Rev. A **53**, 2239 (1996).
20. H. C. Straub, P. Renault, B. G. Lindsay, *et al.*, Phys. Rev. A **54**, 2146 (1996).
21. E. J. Stone and E. C. Zipf, J. Chem. Phys. **58**, 4278 (1973).
22. W. Hwang, Y.-K. Kim, and M. E. Rudd, J. Chem. Phys. **104**, 2956 (1996).
23. G. Gousset, C. M. Ferreira, M. Pinheiro, *et al.*, J. Phys. D: Appl. Phys. **24**, 290 (1991).
24. V. Guerra and J. Loureiro, J. Phys. D: Appl. Phys. **28**, 1903 (1995).

Translated by G. Shepekina

Plasma Physics Reports, Vol. 26, No. 9, 2000, pp. 801–808. Translated from Fizika Plazmy, Vol. 26, No. 9, 2000, pp. 854–861.

LOW-TEMPERATURE PLASMA

Stability of the Low-Temperature States of High-Pressure Microwave Discharges

A. V. Zvonkov*, A. V. Timofeev*, and P. Handel**

**Russian Research Centre Kurchatov Institute, pl. Kurchatova 1, Moscow, 123182 Russia*

***Department of Physics and Astronomy, University of Missouri, St. Louis, MO, USA*

Received December 2, 1999

Abstract—Symmetric (planar, cylindrical, and spherical) models of microwave discharges in air are considered assuming that the deposited energy is removed via heat conduction. The characteristic features of spherical discharges are analyzed in detail, and the conditions for discharge stability are examined. It is shown that discharges in the low-temperature (unstable) state can be stabilized by varying the power of a feedback-controlled microwave source. © *2000 MAIK "Nauka/Interperiodica".*

1. INTRODUCTION

Gas discharges are a typical example of open systems through which energy is pumped continuously. The power is fed into microwave discharges by electromagnetic waves. In discharges at high (on the order of atmospheric) pressures, energy is lost primarily due to heat conduction and convection. The assumption that heat conduction dominates over convection has made it possible to develop a comparatively simple one-dimensional model of a high-pressure microwave discharge [1–3]. An analysis revealed two possible steady states of discharges at the same level of the input power: high-temperature and low-temperature states; the discharge plasma in the high-temperature state was found to occupy a much larger volume.

The question naturally arises of which of the steady states occurs in experiments. This question may be answered by means of simple qualitative considerations. At a fixed amplitude of the electromagnetic field, the energy release $\sigma|E|^2$ from a microwave discharge plasma increases with temperature according to the exponential law $\exp(-I/2T)$ (where I is the ionization potential and T is the temperature), because it is this law that describes an increase in the electron density and, accordingly, the thermal conductivity. On the other hand, the amount of energy removed from the discharge is merely a power function of temperature. We thus arrive at the conclusion that, although the energy released from the plasma can be balanced by the energy removed from it, small temperature fluctuations at a fixed electric field should grow [4]. As a result, if the temperature fluctuations grow above an equilibrium level, the discharge evolves from the low-temperature state into a high-temperature state; otherwise (if the fluctuations are negative), the discharge terminates (Fig. 1).

In experiments, the stability of a high-temperature discharge is ensured by the inverse action of the plasma on the microwave field that maintains the discharge. In plasmas with a sufficiently high temperature and density, external electromagnetic fields are screened due to the skin effect, which thus makes it possible to control the power input into the plasma during temperature fluctuations, provided of course that the skin depth is less than or comparable to the plasma dimensions. Since this condition is satisfied in high-temperature states of large-size discharge plasmas and fails to hold in low-temperature states, the only stable states are those with high temperatures.

To achieve low-temperature states requires considerable effort. We can imagine a feedback system for tuning the amplitude of incident microwaves synchronously with the temperature fluctuations. Such an external control can play the role of the natural skin effect, which ensures the stability of discharges in high-temperature states.

Here, we analyze the stability of the low-temperature states of a high-pressure microwave discharge in air and determine the negative feedback factor required for feedback stabilization of the discharge. Such dis-

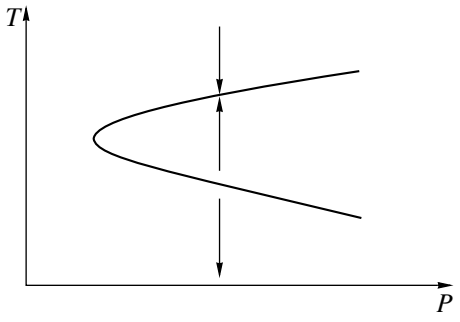

Fig. 1. Evolution of the discharge in the presence of temperature fluctuations. The arrows show how the discharge evolves, and the solid curve corresponds to the steady state of the discharge.

1063-780X/00/2609-0801$20.00 © 2000 MAIK "Nauka/Interperiodica"

charges could produce weakly ionized plasmas with a temperature of about 3–3.5 kK, which is lower than the discharge plasma temperature in high-temperature states by 1–2 kK. We may also expect that such discharges will find application in plasma chemistry.

2. STEADY STATE

The state of a weakly ionized gas in a microwave discharge at high pressures differs only slightly from a thermally equilibrium state and is characterized by a single parameter—the plasma temperature. In a discharge model in which heat conduction is assumed to dominate over convection, the spatial temperature distribution is described by the heat-conduction equation with a source term arising from microwave heating and the electromagnetic field distribution is described by the Maxwell equations with a temperature-dependent dielectric function. In the symmetric model under discussion, a planar discharge is maintained by two plane waves that are incident on the discharge from opposite sides, a cylindrical discharge is maintained by a single cylindrical wave, and a spherical discharge is irradiated uniformly in all directions with an infinite number of spherical waves.

In the steady-state case, we can switch from the heat-conduction equation to the condition for the heat flux and electromagnetic energy flux to remain in balance. The latter flux is described by the Poynting vector

$$-\lambda\nabla_r T + S_r = 0, \quad (1)$$

where r is the radial coordinate for cylindrical and spherical discharges; for a planar discharge, this is the coordinate orthogonal to the discharge plane ($r \longrightarrow x$). In the case of a spherical discharge, the energy flux S_r should be understood as the flux averaged over all partial waves. The thermal conductivity λ is represented as a sum of the conventional (λ_1) and reactive (λ_2) thermal conductivities, $\lambda = \lambda_1 + \lambda_2$. The latter accounts for the dissociation of molecules into atoms and the association of atoms into molecules in air. The coefficient λ_1 was calculated from the formula $\lambda_1(T) = 7kv_T/6\sigma = 1.4 \times 10^4\sqrt{T}$ erg/(kK s cm), where k is Boltzmann's constant, v_T is the thermal velocity of molecules, and σ is the scattering cross section. Here and below, the temperature T is expressed in kK. The coefficient λ_2 was evaluated from the dependence obtained numerically by Raizer [4] for nitrogen. In the range $T < 7.5$ kK, this dependence has the form $\lambda_2(T) = \Delta_0\ln(1 + \exp(-\Lambda_1 + \Lambda_2 T))$, where $\Lambda_0 = 0.7 \times 10^4$ erg/(kK s cm), $\Lambda_1 = 78$, and $\Lambda_2 = 18.6 \times 10^{-3}$ K^{-1}.

The propagation of the microwave field can be described by the wave equation

$$\frac{d}{dr}\mu_1\frac{dE}{dr} + \left(\frac{\omega}{c}\right)^2\mu_2 F = 0, \quad (2)$$

where the coordinate r has the same meaning as in the heat-conduction equation. In planar geometry, we have $F = E_z$, $\mu_1 = 1$, and $\mu_2 = \varepsilon$; in cylindrical geometry, we have $F = E_z$, $\mu_1 = r$, and $\mu_2 = r\varepsilon$; and, in spherical geometry, we have $F = rE_\theta$, $\mu_1 = \varepsilon(r\omega/c)^2/[\varepsilon(r\omega/c)^2 - 2]$, and $\mu_2 = \varepsilon$ (where θ is the polar angle). The plasma dielectric function has the form $\varepsilon(T) = \omega_{pe}^2(T)/\omega(\omega + i\nu(T))$, where ω is the frequency of the incident microwaves, the frequency of collisions ν between electrons and neutrals is equal to $\nu(T) = N(T)v_e(T)\sigma_e$, $N(T) = N^0T^0/T$, N^0 is the Loschmidt number, $T^0 = 0.3$ kK is room temperature, $v_e(T) = \sqrt{3kT/m_e}$, $\sigma_e = 10^{15}$ cm^2, and $\omega_{pe}^2 = 4\pi e^2 n_e(T)/m_e$. In the case of discharges in air, the electron density calculated by Protasov and Chuvashov [5] for the temperature range $4 \le T \le 5$ kK and by Aleksandrov *et al.* [6] for lower temperatures is satisfactorily described by the formula

$$n_e(T) = \begin{cases} 5.91 \times 10^{15}\exp\left(\dfrac{14.42}{T - 1.74}\right), & T \ge 1.74 \text{ kK} \\ 0, & T < 1.74 \text{ kK}. \end{cases}$$

The procedure for analyzing the steady state is outlined in Appendix 1. The results obtained in this appendix for planar, cylindrical, and spherical discharges are illustrated, respectively, in Figs. 2–4, which show the plasma temperature at the discharge center, the reflection coefficient, and the discharge dimension as functions of the microwave power fed into the discharge. The discharge dimension r_d is defined to satisfy the relationship $\int dr\, r^a n(r) = n(0)r_d^{a+1}/(a+1)$ with $a = 0$, 1, and 2 for planar, cylindrical, and spherical discharges, respectively.

The calculations showed that the discharge is initiated when the microwave input power is above a critical level and evolves into one of the two steady states, which differ in temperature and, accordingly, in density. In the high-temperature state, the microwave field penetrates into the plasma to the skin depth, while the discharge plasma in the low-temperature state is almost transparent to microwaves.

In a planar discharge, the plasma temperature in the low-temperature state is the lowest: at a microwave input power far above the critical level, it is at most ≈2.5 kK. Although the temperature profile is fairly smooth in the low-temperature state, the plasma density profile is sharply peaked near the symmetry plane, because the plasma density is an exponential function of temperature. In this case, the discharge dimension turns out to be smaller than the skin depth.

In a cylindrical discharge, the plasma temperature is higher by approximately 1 kK, in which case the discharge dimension is smaller, so that the plasma also remains transparent to microwaves.

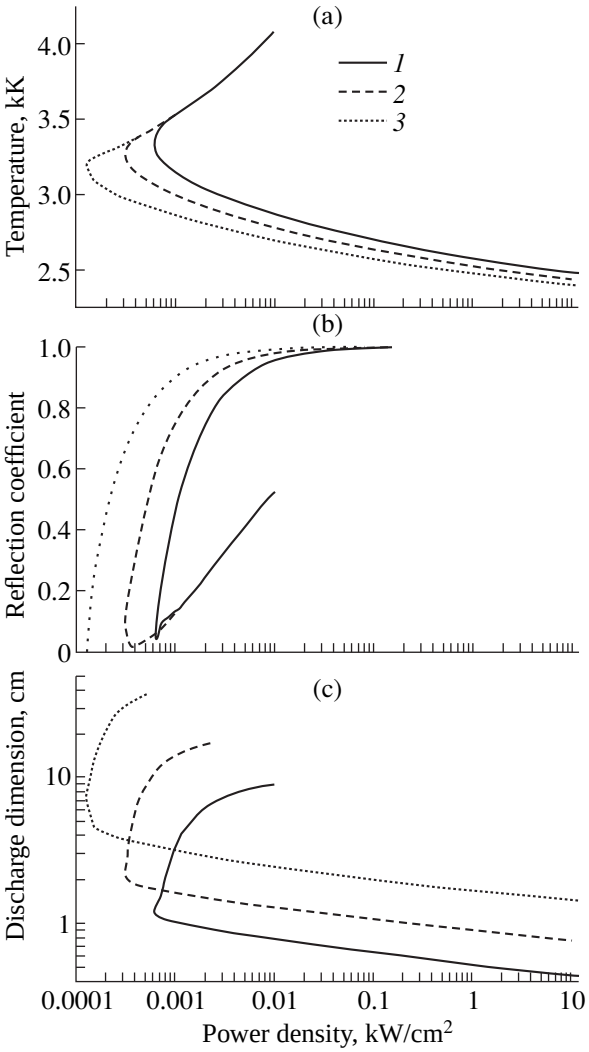

Fig. 2. (a) Central plasma temperature, (b) reflection coefficient, and (c) discharge dimension vs. the microwave power fed into a planar discharge for different sizes of the discharge chamber: r_w = (*1*) 10.7, (*2*) 21.4, and (*3*) 50 cm.

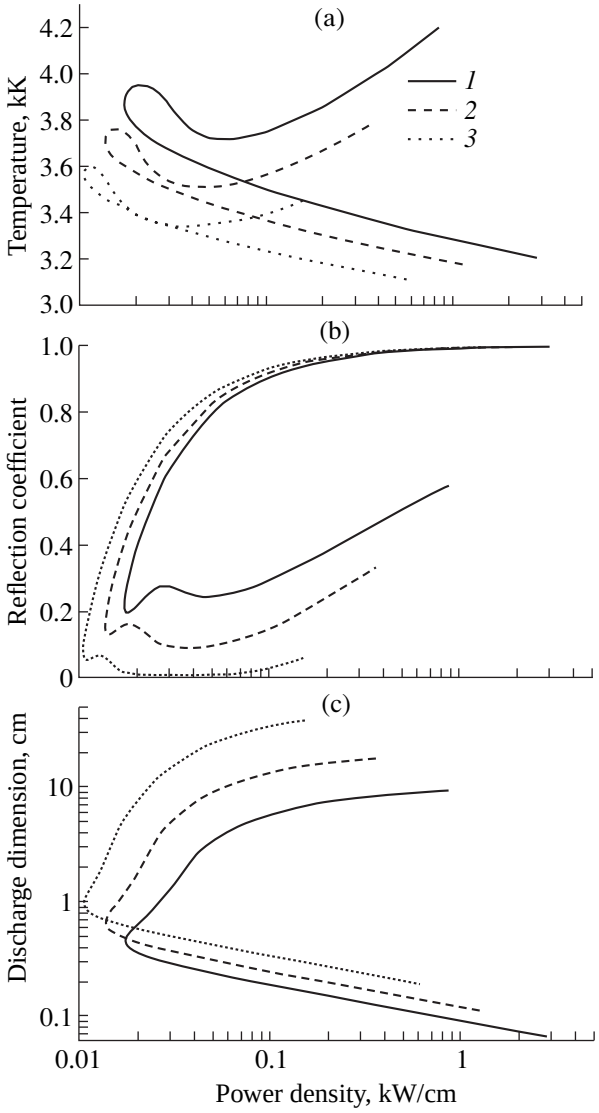

Fig. 3. The same as in Fig. 2, but for a cylindrical discharge.

In a spherical discharge, the plasma temperature in the low-temperature state is the highest and is essentially independent of both the microwave input power and the radius of the discharge chamber. The reason for this is explained in Appendix 2.

Our numerical results agree well with the results that were obtained in [1–3] by other methods of calculation. The steady spatial profiles of the temperature and electromagnetic field calculated for an unperturbed state of the discharge are used to solve the problem of the discharge stability.

3. EQUATION FOR TEMPERATURE FLUCTUATIONS

Since, in the low-temperature state, the discharge plasma does not affect the electromagnetic field distribution, the discharge dynamics is described only by the heat-conduction equation

$$c_p\rho\frac{\partial T}{\partial t} = \mathrm{div}(\lambda\nabla T) + \sigma|E|^2. \quad (3)$$

Here, the temperature dependence of the heat capacity was approximated by the formula

$$c_p(T) = \{1 - \tanh(2T - 8) + [1 + \tanh(2T - 8)]$$
$$\times 6.75\times 10^{-3}e^{1.22T}\}0.5\times 10^{10}\ \mathrm{erg/(g\ kK)},$$

which is fairly close to the numerical results obtained by Dresvin [7]. The density of a weakly ionized gas was calculated from the expression $\rho(T) = 3.53\times 10^{-4}\,T^{-1}$ g/cm^3, and the thermal conductivity was expressed in terms of the dielectric function through the relationship $\sigma(T) = -\omega/4\pi\,\mathrm{Im}\,\varepsilon(T)$.

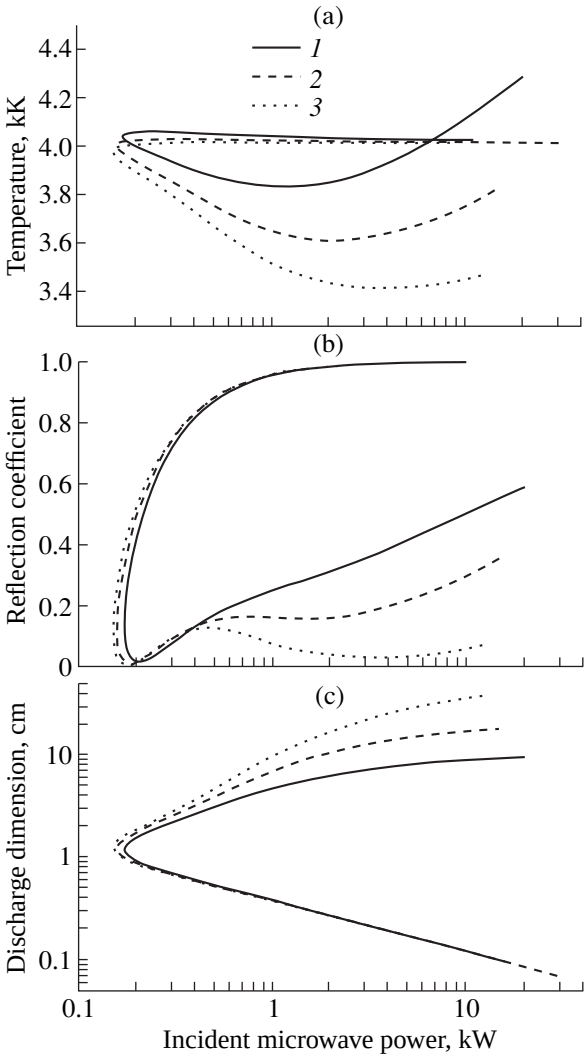

Fig. 4. The same as in Fig. 2, but for a spherical discharge.

Of course, Eq. (3) applies to sufficiently slow perturbations that, however, occur on time scales shorter than the time required for the local thermodynamic equilibrium to establish.

The external parameters of the problem were chosen in accordance with the experiments performed by Zhil'tsov *et al.* [8]: we put $\omega/2\pi = 2.45$ GHz and modeled a discharge at atmospheric pressure on a spatial interval equal to the size of the discharge chamber, which was set to be 10 cm.

The discharge stability should be analyzed by linearizing the heat-conduction equation in temperature perturbations:

$$c_p(T_0)\rho(T_0)\gamma T_1 = \mathrm{div}(\lambda(T_0)\nabla T_1) + \mathrm{div}\left(\frac{\partial\lambda}{\partial T_0}T_1\nabla T_0\right) + \frac{\partial\sigma}{\partial T_0}T_1|E_0|^2 + \sigma(T_0)|E_0|^2 f T_1(0), \quad (4)$$

where γ is the perturbation growth rate, which is in general a complex quantity. The last term, in which the quantity $T_1(0)$ is the perturbed temperature at the discharge center and f is the feedback factor, accounts for the possibility of controlling the electromagnetic field amplitude by means of feedback. Note that we neglect the delay time, which inevitably appears when the feedback system is turned on. We can do this if the time delay is insignificant in comparison with the growth time of the instability to be suppressed.

Since our model assumes only one adjustable parameter, namely, the microwave field amplitude (the field phase is unimportant), the discharge state should also be characterized by a single parameter. It is natural to take the plasma temperature at the discharge center as such a parameter. Below, we will show that, in the low-temperature state of the discharge plasma, the only growing mode is the largest scale mode, which has no node points within the spatial interval under consideration and whose amplitude is maximum near the center of the discharge or just at the center. Temperature fluctuations can in principle be measured by monitoring emission from the plasma. These considerations allowed us to assume that, in Eq. (4), the response of the feedback system (the change in the electromagnetic field amplitude) to the change in the discharge state is proportional to the plasma temperature at the discharge center. We also supplemented Eq. (4) with the following boundary conditions: $\nabla T_1 = 0$ at the discharge center and $T_1 = 0$ at the outer boundary of the discharge plasma.

The method for solving Eq. (4) is described in Appendix 3.

4. CALCULATED RESULTS AND CONCLUSIONS

The instability of the low-temperature state of the discharge is governed by an extremely strong dependence of the heat release in the discharge plasma on the plasma temperature (see the Introduction). Since, in the low-temperature state, the plasma density is peaked about the discharge center, the spatial profile of the amplitude of unstable temperature fluctuations should also be peaked centrally. In fact, our calculations show that unstable temperature perturbations are localized predominantly in the region occupied by the discharge plasma (Fig. 5). Consequently, the spatial scale on which the perturbations develop becomes shorter as the microwave input power maintaining the discharge increases; in the case of a cylindrical discharge, it turns out to be the shortest. Since the perturbation growth rate is high, the heat conduction does not have enough time to smooth out the growing temperature fluctuations. We emphasize that the above analysis applies only to the largest scale perturbation mode, which has no node points within the spatial interval under consideration; the other modes are suppressed by heat conduction.

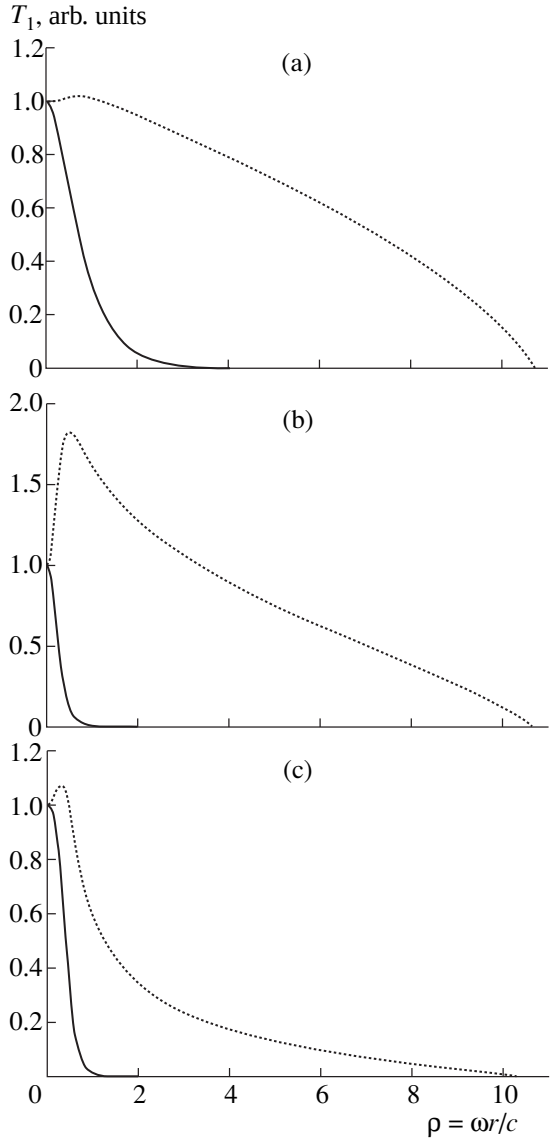

Fig. 5. Unstable temperature perturbations (solid curve) and feedback-stabilized temperature perturbations (dashed curve) in (a) planar, (b) cylindrical, and (c) spherical discharges.

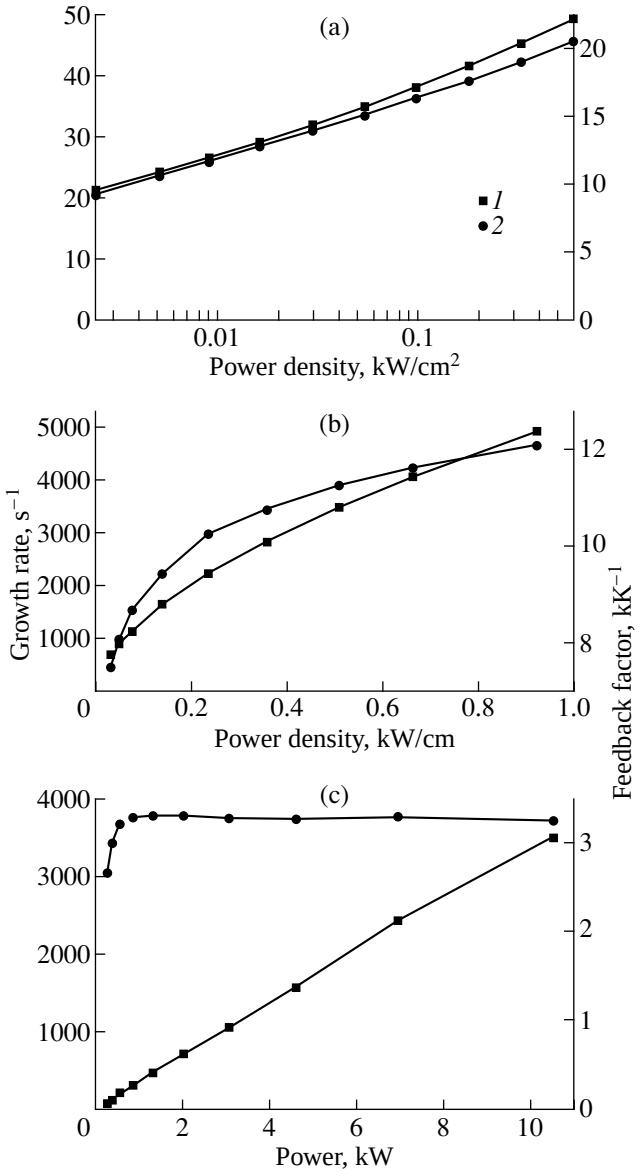

Fig. 6. (*1*) Instability growth rate in the absence of feedback and (*2*) the feedback factor required for stabilization vs. the power of microwaves incident on (a) planar, (b) cylindrical, and (c) spherical discharges.

The unstable mode can be stabilized by a negative feedback control system. Our model assumes that, at the center of the discharge, the microwave input power fluctuates in the same manner as the plasma temperature. The feedback system makes it possible to suppress fluctuations in heat release. At a critical feedback factor corresponding to the boundary of the instability domain, a slightly excessive heat release is neutralized by heat conduction, which acts to remove excessive heat toward the chamber wall. As a result, at $\gamma = 0$, feedback-stabilized temperature perturbations turn out to be smoothed out to a greater extent in comparison with unstable temperature fluctuations (Fig. 5).

Our calculations revealed that, in all types of symmetric discharges, the higher the microwave input power, the higher the instability growth rate. At the same power input, the growth rate is the highest in a cylindrical discharge, which is the smallest in dimension (Fig. 6). On the other hand, the dependence of the feedback factor required for stabilization on the input power differs strongly between different types of discharges. In the case of planar and cylindrical discharges, this dependence roughly follows the power dependence of the growth rate, while in the case of a spherical discharge the critical feedback factor reaches a saturation level at sufficiently high input powers.

Hence, we have shown that the low-temperature states of high-pressure microwave discharges can be in principle feedback-stabilized. Cylindrically symmetric discharges are likely to be most simply initiated in experiments. In cylindrical discharges, the peak in the radial temperature profile at the symmetry axis can be lowered to about 3 kK.

ACKNOWLEDGMENTS

We are grateful to V.A. Zhil'tsov, J.F. Leitner, and A.A. Skovoroda for their interest in this work.

APPENDIX 1

Transformation of the Equations for a Steady Discharge to a Form Suitable for Numerical Integration

We consider the equations describing a spherical discharge (the equations for planar and cylindrical discharges can be transformed in a similar way). The model of a spherically symmetric microwave discharge was described by Timofeev [3]. The discharge is assumed to be irradiated uniformly with waves whose electromagnetic field is described in terms of the spherical harmonic $\mathbf{E} = (E_r\cos\theta, E_\theta\sin\theta, 0)$ and $\mathbf{B} = (0, 0, B_\varphi\sin\theta)$, in which case the Maxwell equations have the form

$$\frac{2B_\varphi}{\rho} = -i\varepsilon E_r,$$

$$\frac{1}{\rho}\frac{d}{d\rho}(\rho B_\varphi) = i\varepsilon E_\theta,$$

$$\frac{1}{\rho}\left(\frac{d}{d\rho}(\rho E_\theta) + E_r\right) = iB_\varphi,$$

where the dimensionless parameter ρ is equal to $\rho = \omega r/c$.

Direct numerical integration of the Maxwell equations from the discharge center to the chamber wall is inconvenient because, in a discharge with a skinned layer, the field is an increasing exponential function of the radius. It is more expedient to introduce other, more gradual variables, e.g., the logarithm of the wave amplitude and the ratio of the field components. The variables that are most suitable for our purposes are the wave amplitude A and the wave phase Φ, which can be defined through the relationships $E_r = \frac{2}{\varepsilon}A\cos\Phi$ and $E_\theta = A\sin\Phi$. The factor $2/\varepsilon$ is introduced in order not to integrate over ε, in which case we have $B_\varphi = -i\rho A\cos\Phi$. For $\rho = 0$, the field components should satisfy the condition $E_r = -E_\theta$, under which the initial value Φ_0 is defined by the equation $\cos\Phi_0 + \frac{\varepsilon}{2}\sin\Phi_0 = 0$. In the new variables, the Maxwell equations take the form

$$(\ln A)' = \rho\sin\Phi\cos\Phi - 2\left(\cos\Phi + \frac{1}{\varepsilon}\sin\Phi\right)\frac{\cos\Phi + \varepsilon/2\sin\Phi}{\rho},$$

$$\Phi' = \rho\cos^2\Phi - 2\left(\frac{1}{\varepsilon}\cos\Phi - \sin\Phi\right)\frac{\cos\Phi + \varepsilon/2\sin\Phi}{\rho}.$$

The uncertainties in the right-hand sides at $\rho = 0$ are eliminated by expanding the functions Φ, ε, and T in powers of ρ. This procedure leads to vanishing derivatives at the discharge center: $(\ln A)' = \Phi' = 0$.

Equation (1), which implies that the total energy flux (i.e., the sum of the thermal energy flux and the wave energy flux) is constant, yields the following equation for the plasma temperature:

$$T' = -\frac{c^2}{24\pi\omega\lambda}\rho|A|^2\sinh(2\,\mathrm{Im}\,\Phi).$$

Since A and Φ are complex variables, we arrive at five real equations. It is easy to see that the plasma temperature can be evaluated without regard to the quantity $\mathrm{Im}(\ln A)$. Therefore, we need to solve only four equations. We specified the values of $\mathrm{Re}(\ln A)$ and T at the discharge center and integrated these equations by the Runge–Kutta method until the condition $T = 0.3$ kK was satisfied. Then, we varied the initial value of T or $\mathrm{Re}(\ln A)$ so as to satisfy this condition at the chamber wall. As a result, we arrived at a solution to our problem.

We also present the formulas that were used to single out the parts describing the incident and reflected waves in the solution obtained. In the representation $E_\theta = A_+a_+e^{i\rho} + A\_a\_e^{-i\rho}$ with $a_\pm = 1/\rho - 1/\rho^3 \pm i/\rho^2$, which is valid for a vacuum field [3], the first term describes the reflected wave and the second term refers to the incident wave. The amplitudes of these waves were calculated from the formula $A_\pm = \frac{A}{2}e^{\mp i\rho}[(\sin\Phi - \cos\Phi)(\rho \mp i) \mp i\rho^2\cos\Phi]$.

APPENDIX 2

Analytic Treatment of a Low-Temperature Spherical Microwave Discharge

In our calculations, a discharge in the low-temperature state is naturally characterized by high transparency and a small dimension, because, for typical discharge temperatures, we have $|\varepsilon| \gg 1$ and $\mathrm{Re}\,\varepsilon \sim \mathrm{Im}\,\varepsilon$, so that the discharge plasma is transparent to the incident microwave radiation if the plasma dimension is smaller than the radiation wavelength in the discharge. We assume that the discharge dimension ρ_d satisfies the condition $\rho_d^2\varepsilon \ll 1$ and is much smaller than the discharge chamber size ρ_w ($\rho_d/\rho_w \ll 1$). These conditions

make it possible to simplify the field equations and the heat-conduction equation, respectively.

First, we consider the heat-conduction equation. Since, in vacuum, the heat flux remains unchanged, we have $\rho^2\lambda\frac{dT}{d\rho} = -C_1$. The constant can be found by integrating the heat-conduction equation from the chamber wall to the boundary of the discharge plasma, $\int_{T_w}^{T_d}\lambda(T)dT = C_1\left(\frac{1}{\rho_d} - \frac{1}{\rho_w}\right) \approx \frac{C_1}{\rho_d}$, where the discharge radius ρ_d is assumed to be small and the temperature T_d at the plasma boundary is determined only by the dependence $\varepsilon(T)$ and is equal to the temperature at which the imaginary part of the dielectric function vanishes. Now, we can write the boundary conditions required for treating the heat-conduction equation inside the discharge plasma: $T = T_d$ and $\lambda\frac{dT}{d\rho} = -\frac{1}{\rho_d}\int_{T_w}^{T_d}\lambda\, dT$ at the boundary $\rho = \rho_d$ and $\frac{dT}{d\rho} = 0$ at the center $\rho = 0$. We impose three (rather than two) boundary conditions because the discharge radius ρ_d should also be found in solving the problem. Inside the discharge plasma, the heat-conduction equation has the form

$$\frac{1}{\rho^2}\frac{d}{d\rho}\rho^2\lambda\frac{dT}{d\rho} + \frac{c^2\,\mathrm{Im}\,\varepsilon(T)}{24\pi\omega}\left(\left|\frac{d}{d\rho}\rho E_\theta\right|^2 + 2|E_\theta|^2\right) = 0,$$

where $\mathrm{Im}\,\varepsilon(T)$ is the imaginary part of the dielectric function. Here, we used the smallness of the parameter $\rho^2\varepsilon$ to express E_r in terms of E_θ.

In the limit $\rho^2\varepsilon \ll 1$, the wave equation for E_θ reduces to

$$\frac{d}{d\rho}\rho^2\varepsilon\frac{d}{d\rho}\rho E_\theta - 2\varepsilon\rho E_\theta = 0,$$

with the boundary condition $\frac{dE_\theta}{d\rho} = 0$ at the discharge center. The field magnitude is governed by the microwave power fed into the discharge. We decompose the field into parts describing the incident and reflected waves (see Appendix 1) to obtain the condition $P_{inc} = \frac{c^3}{12\omega^2}\left|\frac{1}{\rho^2}\frac{d}{d\rho}\rho^3 E_\theta\right|^2$ (where P_{inc} is the microwave input power) at the plasma boundary $\rho = \rho_d$. Since the field component E_θ is a complex quantity, to make the problem well-posed requires that another, quite obvious boundary condition be imposed: we can specify an arbitrary value of the wave phase at the boundary of the discharge plasma.

In the above equations and boundary conditions, we switch to the dimensionless variables $x = \rho/\rho_d$ and $E = E_\theta/\sqrt{12P_{inc}\omega^2 c^{-3}}$. As a result, we arrive at the equations

$$\frac{1}{x^2}\frac{d}{dx}x^2\lambda\frac{dT}{dx} + \frac{\mathrm{Im}\varepsilon''}{2\pi c}P_{inc}\rho_d^2\left(\left|\frac{d}{dx}xE\right|^2 + 2|E|^2\right) = 0,$$

$$\frac{d}{dx}x^2\varepsilon\frac{d}{dx}xE - 2\varepsilon xE = 0$$

with the following boundary conditions:

$$\frac{dT}{dx} = 0, \quad \frac{dE}{dx} = 0$$

at $x = 0$ and

$$T = T_d, \quad \lambda\frac{dT}{dx} = -\int_{T_w}^{T_d}\lambda dT, \quad \left|\frac{1}{x^2}\frac{d}{dx}x^2E\right|^2 = 1$$

at $x = 1$.

Since the temperatures T_w and T_d are known and $\lambda(T)$ and $\varepsilon(T)$ are prescribed functions, our problem involves a single parameter, namely, $P_{\mathrm{inc}}\rho_d^2$; moreover, the number of imposed boundary conditions implies that our problem has a solution at a certain value of this parameter. Strictly speaking, since the equations are nonlinear, there may be several such values of the parameter and, thus, the problem may have different solutions corresponding to these parameter values. If we assume that the problem possesses a unique solution, then we arrive at the following conclusions: under the above assumption that the discharge is small in dimension, the central temperature is independent of the input power and remains constant and the discharge radius is inversely proportional to the square root of the input power, $\rho_d \sim 1/\sqrt{P_{\mathrm{inc}}}$, regardless of the size of the discharge chamber. These results are confirmed by numerical calculations (Fig. 4). Although, in simulations and in this appendix, the discharge dimension was determined in different ways, we obtained the same dependence of the discharge dimension on the input power because the profiles of the dimensionless temperature (and, accordingly, the dimensionless density) were the same.

APPENDIX 3

Method for Solving Eq. (4)

The nonlocal homogeneous equation (4) can formally be written as

$$\hat{L}_\gamma T_1(X) = 0, \tag{A3.1}$$

where X is the coordinate along which the discharge parameters vary; in the case of a planar discharge, it is

the coordinate orthogonal to the symmetry plane ($X = x$), and, in the case of cylindrical and spherical discharges, it is the radial coordinate ($X = r$).

In order to find the desired eigenvalue γ, we analyze how the system will respond to some external action, which can be incorporated into Eq. (A3.1) by introducing the term $C(X)$ into its right-hand side:

$$T_1(X) = \hat{L}_\gamma^{-1} C(X). \quad \text{(A3.2)}$$

For a fairly large class of perturbations, the response becomes infinite at $\gamma = \gamma_n$, where γ_n is one of the eigenvalues. We assume that the eigenvalues are nondegenerate and that, at $\gamma \approx \gamma_n$, the response can be written as

$$T_1(X, \gamma) \approx A_n T_{1n}(X) \frac{1}{\gamma - \gamma_n} + \ldots, \quad \text{(A3.3)}$$

where $T_{1n}(X)$ is an eigenfunction normalized in the proper manner and the amplitude factor A_n is governed by the external action. Expression (A3.3) can be readily derived if $\hat{L}$ is a Sturm–Liouville operator. It is natural to assume that this expression remains valid for any general operator.

The numerical procedure used to search for the eigenfunctions and related eigenvalues can be described as follows. In the plane of the complex variable γ, we chose some initial point and determined the signs of $\mathrm{Re}\, T_1(X_0, \gamma)$ and $\mathrm{Im}\, T_1(X_0, \gamma)$ for four displacements $\delta\gamma = \frac{\Delta}{\sqrt{2}}(\sigma_1 + i\sigma_2)$ from the initial point. Here, $\sigma_{1,2} = \pm 1$ and X_0 is an arbitrary point in the spatial interval under consideration except for the boundary point, at which $T_1 = 0$. If, for some of these displacements, the real and imaginary parts of $T_1(X_0, \gamma)$ calculated from (A3.3) changed sign simultaneously, then the corresponding value of γ was taken to be an approximate eigenvalue γ_n'. Otherwise, the point was displaced in the plane of the complex variable γ over the distance Δ down the gradient of $|T_1(X_0, \gamma)|$; after that, the signs of $\mathrm{Re}\, T_1(X_0, \gamma)$ and $\mathrm{Im}\, T_1(X_0, \gamma)$ were calculated again. Then, we repeated this algorithm. The eigenvalue obtained in such a manner can differ from the true eigenvalue by an amount $\delta\gamma \le \Delta$. In order to refine the numerical eigenvalue γ_n', we took it as an initial eigenvalue and repeated the above procedure with a smaller displacement Δ. For each value of γ, the nonlocal inhomogeneous differential equation (A3.2) was solved using one of the versions of the sweep method [9].

REFERENCES

1. *Low-Temperature Plasma*, Ed. by S. V. Dresvin and V. D. Rusanov (Nauka, Novosibirsk, 1992), Vol. 6.
2. V. N. Lelevkin and D. K. Otorbaev, *Experimental Methods and Theoretical Models in the Physics of Nonequilibrium Plasmas* (Ilim, Frunze, 1988).
3. A. V. Timofeev, Fiz. Plazmy **23**, 106 (1997) [Plasma Phys. Rep. **23**, 158 (1997)].
4. Yu. P. Raizer, *Gas Discharge Physics* (Nauka, Moscow, 1987; Springer-Verlag Berlin, 1991).
5. Yu. S. Protasov, S. N. Chuvashov, in *Physics of Gas-Discharge Electronic Devices: Plasma Electronics* (Vysshaya Shkola, Moscow, 1993), Part 2.
6. N. L. Aleksandrov, E. M. Bazelyan, I. V. Kochetov, and N. A. Dyatko, J. Phys. D **30**, 1616 (1997).
7. S. V. Dresvin, *Theory and Calculations of RF Plasmotrones* (Énergoatomizdat, Leningrad, 1991).
8. V. A. Zhil'tsov, J. F. Leitner, É. A. Manykin, *et al.*, Zh. Éksp. Teor. Fiz. **108**, 1966 (1995) [JETP **81**, 1072 (1995)].
9. A. A. Samarskiĭ and E. S. Nikolaev, *Methods for Solving Grid Equations* (Nauka, Moscow, 1978).

Translated by O. Khadin

Plasma Physics Reports, Vol. 26, No. 9, 2000, pp. 809–811. Translated from Fizika Plazmy, Vol. 26, No. 9, 2000, pp. 862–864.

BRIEF COMMUNICATIONS

Formation of Multiply Charged Ions in the Interaction of Laser Radiation with Targets of Various Densities

M. R. Bedilov, R. T. Khaĭdarov, and U. S. Kunishev

Research Institute of Applied Physics, Tashkent State University, Tashkent, Uzbekistan

Received May 24, 1999; in final form, November 1, 1999

Abstract—Mass, charge, and energy spectra of multiply charged ions in a plasma formed by laser heating of Ho_2O_3 and Y_2O_3 targets of various densities are investigated. The features of the formation of multiply charged oxygen and holmium (yttrium) ions at fairly low ion energies (≤50 eV) are examined. It is found that, for oxygen ions, Z_{max} is achieved at low target densities, whereas, for holmium (yttrium) ions, it is achieved at high target densities. It is suggested that these features are related mainly to nonequilibrium ionization processes in the plasma. © *2000 MAIK "Nauka/Interperiodica".*

Interest in the interaction of laser radiation with low-density (porous) targets [1–4] stems from the possibility of applying porous media to laser heating of a plasma, the formation of intense beams of nuclei and multiply charged ions, and creating plasma lasers and media for nonlinear optics. Mass-spectrometric studies of the charge and energy spectra of multiply charged ions in a plasma formed by the laser heating of targets of various densities revealed the optimum target density for which a reduction in the recombination rate in a laser plasma ensured the maximum beam intensity, charge, and energy of the ions [1, 2]. Absorption of neodymium laser radiation at a power density of 10^{14} W cm^{-2} and the energy transfer processes in porous agar-agar ($C_{14}H_{18}O_7$) targets with an average density of 1–4 mg cm^{-3} were studied experimentally by optical and X-ray techniques [3, 4]. A region with a dense high-temperature plasma efficiently absorbing laser radiation was proved to form inside a porous target.

This paper is a continuation of the previous study [1, 2] and deals with the features of the formation of low-energy multiply charged ions in the interaction of laser radiation with targets of various densities. Mass, charge, and energy characteristics of the plasma ions were determined by a mass-spectrometric method [5]. The ions emitted from the plasma in the direction $\theta = 20°$ with respect to the normal to the target surface were recorded by a spectrometer located at a distance of 100 cm from the target. The spectrometer slit width was 0.4 mm, which corresponded to a solid angle of ~10^{-4} sr. In the experiments, we used an ILTI-207 laser ($\lambda = 1.06$ μm, $E = 0.8$–1.0 J, and $\tau = 15$ ns) with a bell-shaped spatial intensity distribution and an average focal spot area of 10^{-4} cm^2, which made it possible to attain the power density q up to 10^{11} W cm^{-2} on the target surface. We investigated 5-mm-thick and 10-mm-diameter Y_2O_3 and Ho_2O_3 targets compacted from a powder with the initial mass density $n_0 = 1.2$ g cm^{-3}. Targets with mass densities of $n_1 = 1.4$ g cm^{-3}, $n_2 = 2.8$ g cm^{-3}, $n_3 = 3.2$ g cm^{-3}, $n_4 = 3.5$ g cm^{-3}, and $n_5 = 3.7$ g cm^{-3} were used. A well-known technique [6, 7] was used to prepare the targets: a block of Y_2O_3 or Ho_2O_3 was crushed into ≤30-μm pieces and then compacted at a pressure of 1–5 t/cm^2. The targets produced in such a way consisted of grains with dimensions less than 30 μm. The laser beam was incident normally to the target surface. Each experimental point was the average of the measured values obtained from five laser pulses.

Investigations of the mass spectra of the ions from a Ho_2O_3 target carried out in wide ranges of the target density ($n = n_1 - n_5$) and ion energy ($E = 20$–1000 eV) at $q = 10^{11}$ W cm^{-2} showed that the laser plasma consisted of holmium and oxygen ions; as n and E increased (at q = const), the mass composition and intensity of the ion flux changed significantly. The changes were most pronounced in the range of fairly low ion energies ($E \le 50$ eV). An increase in n at constant values of E and q resulted in a change of the mass spectra towards an increase in the content of holmium ions and a decrease in the content of oxygen ions. The charge composition within the packets of holmium and oxygen ions depended on the laser power, target density, and ion energy. The maximum charge number of oxygen ions ($Z = 4$) and the minimum charge number of holmium ions ($Z = 1$) were detected at $n = n_1$, $E = 50$ eV, and $q = 10^{11}$ W cm^{-2} (Fig. 1). An increase in n from n_1 to n_3 at the above values of q and E resulted in a decrease in the charge number of oxygen ions (from $Z = 4$ to $Z = 2$), whereas, for holmium ions, the charge number increased from $Z = 1$ to $Z = 3$. Such behavior of the charge spectra is most pronounced at $n < n_3$ and fairly low ion energies ($E \le 50$ eV) and is less pronounced at $n > n_3$ and $E > 150$ eV. The dependences of the Z_{max} of holmium ions on the target mass density n

1063-780X/00/2609-0809$20.00

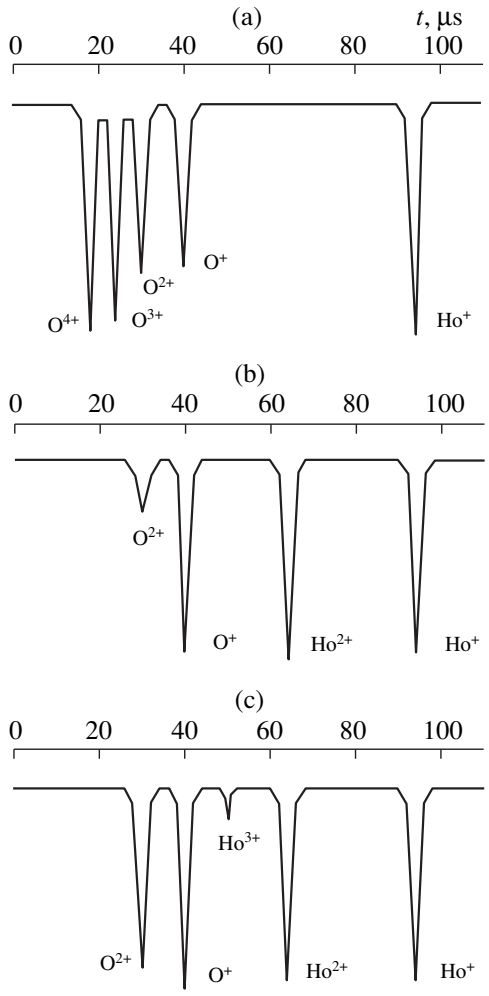

Fig. 1. Mass and charge spectra of multiply charged ions in the laser plasma obtained with a Ho_2O_3 target for $q = 10^{11}$ W cm^{-2} and an energy of 50 eV per unit charge at n = (a) n_1, (b) n_2, and (c) n_3.

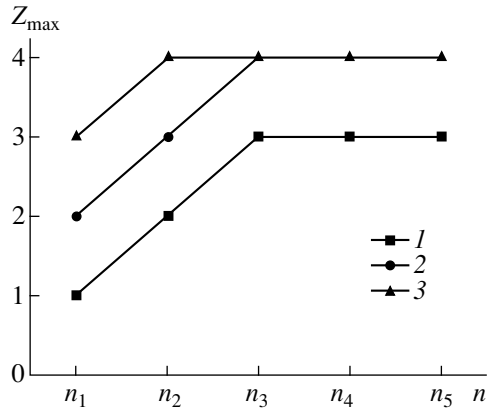

Fig. 2. Dependence of the Z_{max} of holmium ions on n for $q = 10^{11}$ W cm^{-2} at E = (*1*) 50, (*2*) 100, and (*3*) 150 eV.

are presented in Fig. 2 for E = 50, 100, and 150 eV. Note that, in the range $n < n_3$, where significant changes of the charge spectra take place, the laser pulse energy is spent mainly on heating, volume destruction, and nonequilibrium ionization of the individual target components. This is a consequence of the volume generation of a nonequilibrium plasma, which affects the ionization and recombination processes. At $n \geq n_3$, the laser energy is spent on heating, destruction of the target surface, and fairly uniform ionization of both holmium and oxygen atoms. Presumably, this is the reason why the charge spectra do not change in the range $n \geq n_3$.

The measured mass and charge spectra were used to plot the energy spectra of holmium and oxygen ions for different target densities. Typical ion energy spectra are presented in Fig. 3 for $n = n_1$ and $n = n_3$ at $q = 10^{11}$ W cm^{-2}. It is seen that, for each value of n, the energy spectra of holmium ions are five times as intense and wide as those of oxygen ions.

Thus, we have found that

(i) two ion packets in different energy ranges are clearly pronounced for all of the n values investigated;

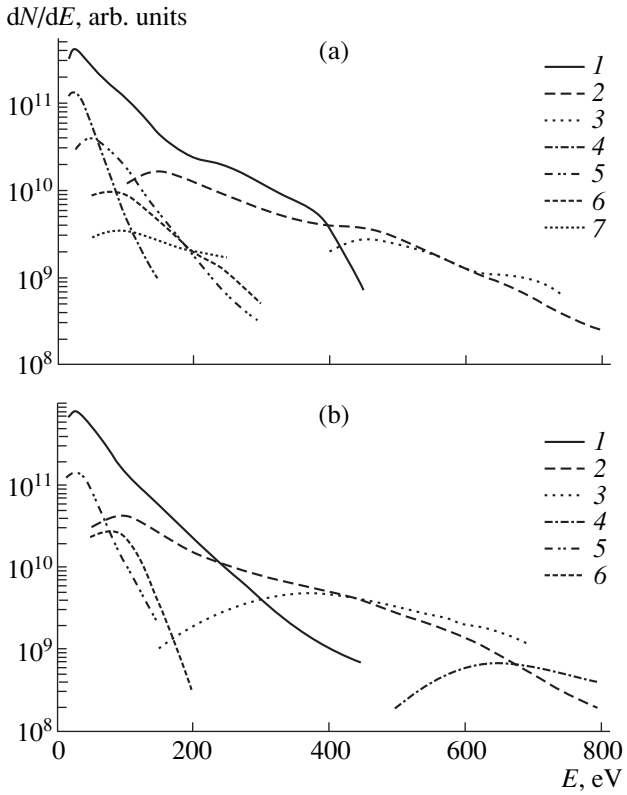

Fig. 3. Typical energy spectra of holmium and oxygen ions for $q = 10^{11}$ W cm^{-2} at (a) $n = n_1$ [(*1*) Ho^+, (*2*) Ho^{2+}, (*3*) Ho^{3+}, (*4*) O^+, (*5*) O^{2+}, (*6*) O^{3+}, and (*7*) O^{4+}] and (b) $n = n_3$ [(*1*) Ho^+, (*2*) Ho^{2+}, (*3*) Ho^{3+}, (*4*) Ho^{4+}, (*5*) O^+, and (*6*) O^{2+}].

(ii) at $n = n_1$, the packet of oxygen ions with $Z = 1$–4 is located within the range $E = 20$–400 eV; the increase in n from n_1 to n_3 leads to a substantial shrinking of the range because, in this case, the ions with $Z = 3$ and 4 are absent;

(iii) at $n = n_1$, holmium ions with $Z = 1$ occupy a fairly wide energy range ($E = 20$–450 eV); the increase in n from n_1 to n_3 results in expansion of the ion energy range toward higher energies due to the generation of holmium ions with $Z = 2$, 3, and 4; and

(iv) the nature of the energy spectra of holmium and oxygen ions for $n > n_3$ remains the same as for $n = n_3$.

Note that similar results were obtained for an Y_2O_3 target.

The results obtained can be summarized as follows:

(i) The features of the formation of mass, charge, and energy spectra of multiply charged holmium and oxygen ions are revealed. The two packets of holmium and oxygen ions are formed at a laser radiation intensity of $q = 10^{11}$ W cm^{-2}. At $n < n_3$, the mass, charge, and energy characteristics depend substantially on the target mass density; at $n \geq n_3$, such a dependence is less pronounced.

(ii) It is revealed that the ion charge number is distributed nonuniformly within both holmium and oxygen packets, especially at low target densities. Special exploration of the morphology of targets of different densities exposed to laser radiation shows that, at $n < n_3$, the target undergoes volume destruction. As the target density decreases from n_3 to n_1, the character of destruction changes (surface destruction transforms into volume destruction) and the volume of a destroyed region and the mass of the target material evaporated during the laser pulse increase. These factors influence the laser plasma formation, as well as ionization and recombination processes in the plasma. As the target density increases, the recombination rate for oxygen ions rises (the ion charge number drops from $Z = 1$–4 at $n = n_1$ to $Z = 1$–2 at $n = n_3$), whereas, for holmium (yttrium) ions, it falls (the ion charge number increases from $Z = 1$ at $n = n_1$ to $Z = 1$–4 at $n = n_3$). Note that holmium ions with $Z = 4$ are generated at $n > n_3$ with $E >$ 500 eV.

REFERENCES

1. M. R. Bedilov, R. T. Khaĭdarov, B. Kh. Yakubov, and U. S. Kunishev, Fiz. Plazmy **22**, 1151 (1996) [Plasma Phys. Rep. **22**, 1049 (1996)].
2. M. R. Bedilov, R. T. Khaĭdarov, B. Kh. Yakubov, and U. S. Kunishev, Kvantovaya Élektron. (Moscow) **23**, 835 (1996).
3. A. É. Bugrov, I. N. Burdonskiĭ, V. V. Gavrilov, *et al.*, Zh. Éksp. Teor. Fiz. **111**, 903 (1997) [JETP **84**, 497 (1997)].
4. S. Yu. Gus'kov and V. B. Rozanov, Kvantovaya Élektron. (Moscow) **24**, 715 (1997).
5. M. R. Bedilov, R. T. Khaĭdarov, and I. Yu. Davletov, Fiz. Plazmy **21**, 1007 (1995) [Plasma Phys. Rep. **21**, 952 (1995)].
6. G. S. Khodakov, in *Physics of Desintegration* (Nauka, Mocsow, 1972), p. 298.
7. W. D. Jones, *Fundamental Principles of Powder Metallurgy* (Arnold, London, 1960; Mir, Moscow, 1965).

Translated by N. Ustinovskiĭ